

Nanophotonics

Nanophotonics

Edited by
Hervé Rigneault
Jean-Michel Lourtioz
Claude Delalande
Ariel Levenson

iSTE

First published in France in 2005 by Hermes Science/Lavoisier entitled "La nanophotonique"
First published in Great Britain and the United States in 2006 by ISTE Ltd

Apart from any fair dealing for the purposes of research or private study, or criticism or review, as permitted under the Copyright, Designs and Patents Act 1988, this publication may only be reproduced, stored or transmitted, in any form or by any means, with the prior permission in writing of the publishers, or in the case of reprographic reproduction in accordance with the terms and licenses issued by the CLA. Enquiries concerning reproduction outside these terms should be sent to the publishers at the undermentioned address:

ISTE Ltd
6 Fitzroy Square
London W1T 5DX
UK

ISTE USA
4308 Patrice Road
Newport Beach, CA 92663
USA

www.iste.co.uk

© ISTE Ltd, 2006

© GET and LAVOISIER, 2005

The rights of Hervé Rigneault, Jean-Michel Lourtioz, Claude Delalande and Ariel Levenson to be identified as the authors of this work have been asserted by them in accordance with the Copyright, Designs and Patents Act 1988.

Library of Congress Cataloging-in-Publication Data

Nanophotonique. English.
Nanophotonics / Hervé Rigneault ... [et al].
p. cm.
Includes index.
ISBN-13: 978-1-905209-28-6
ISBN-10: 1-905209-28-2
1. Photonics. 2. Nanotechnology. I. Rigneault, Hervé. II. Title.
TA1520.N35 2006
621.36--dc22

2006008801

British Library Cataloguing-in-Publication Data

A CIP record for this book is available from the British Library

ISBN 10: 1-905209-28-2

ISBN 13: 978-1-905209-28-6

Printed and bound in Great Britain by Antony Rowe Ltd, Chippenham, Wiltshire.

Table of Contents

Preface	13
Chapter 1. Photonic Crystals: From Microphotonics to Nanophotonics . . .	17
Pierre VIKTOROVITCH	
1.1. Introduction.	17
1.2. Reminders and prerequisites.	19
1.2.1. Maxwell equations	19
1.2.1.1. Optical modes.	20
1.2.1.2. Dispersion characteristics	20
1.2.2. A simple case: three-dimensional and homogeneous free space	20
1.2.3. Structuration of free space and optical mode engineering	21
1.2.4. Examples of space structuration: objects with reduced dimensionality	22
1.2.4.1. Two 3D sub-spaces	22
1.2.4.2. Two-dimensional isotropic propagation: planar cavity.	24
1.2.4.3. One-dimensional propagation: photonic wire	25
1.2.4.4. Case of index guiding (two- or one-dimensionality)	26
1.2.4.5. Zero-dimensionality: optical (micro)-cavity	26
1.2.5. Epilogue	27
1.3. 1D photonic crystals	28
1.3.1. Bloch modes	29
1.3.2. Dispersion characteristics of a 1D periodic medium	30
1.3.2.1. Genesis and description of dispersion characteristics	30
1.3.2.2. Density of modes along the dispersion characteristics	32
1.3.3. Dynamics of Bloch modes.	33
1.3.3.1. Coupled mode theory	33
1.3.3.2. Lifetime of a Bloch mode.	34
1.3.3.3. Merit factor of a Bloch mode.	35
1.3.4. The distinctive features of photonic crystals	35

1.3.5. Localized defect in a photonic band gap or optical microcavity	36
1.3.5.1. Donor and acceptor levels.	37
1.3.5.2. Properties of cavity modes in a 1DPC	38
1.3.5.3. Fabry-Pérot type optical filter	39
1.3.6. 1D photonic crystal in a dielectric waveguide and waveguided Bloch modes	40
1.3.6.1. Various diffractive coupling processes between optical modes	40
1.3.6.2. Determination of the dispersion characteristics of waveguided Bloch modes	42
1.3.6.3. Lifetime and merit factor of waveguided Bloch modes: radiation optical losses	43
1.3.6.4. Localized defect or optical microcavity	44
1.3.7. Epilogue	46
1.4. 3D photonic crystals	46
1.4.1. From dream	46
1.4.2. . . . to reality	47
1.5. 2D photonic crystals: the basics.	49
1.5.1. Conceptual tools: Bloch modes, direct and reciprocal lattices, dispersion curves and surfaces	50
1.5.1.1. Bloch modes	50
1.5.1.2. Direct and reciprocal lattices	51
1.5.1.3. Dispersion curves and surfaces.	52
1.5.2. 2D photonic crystal in a planar dielectric waveguide	54
1.5.2.1. An example of the potential of 2DPC in terms of angular resolution: the super-prism effect	56
1.5.2.2. Strategies for vertical confinement in 2DPC waveguided configurations.	57
1.6. 2D photonic crystals: basic building blocks for planar integrated photonics	59
1.6.1. Fabrication: a planar technological approach.	59
1.6.1.1. 2DPC formed in an InP membrane suspended in air	59
1.6.1.2. 2DPC formed in an InP membrane bonded onto silica on silicon by molecular bonding	60
1.6.2. Localized defect in the PBG or microcavity	62
1.6.3. Waveguiding structures	64
1.6.3.1. Propagation losses in a straight waveguide	66
1.6.3.2. Bends.	67
1.6.3.3. The future of PC-based waveguides lies principally in the guiding of light	69
1.6.4. Wavelength selective transfer between two waveguides	70
1.6.5. Micro-lasers	73

1.6.5.1. Threshold power	74
1.6.5.2. Example: the case of the surface emitting Bloch mode laser	75
1.6.6. Epilogue	77
1.7. Towards 2.5-dimensional Microphotonics	77
1.7.1. Basic concepts	77
1.7.2. Applications	80
1.8. General conclusion	81
1.9. References	82
Chapter 2. Bidimensional Photonic Crystals for Photonic Integrated Circuits	85
Anne TALNEAU	
2.1. Introduction.	85
2.2. The three dimensions in space: planar waveguide perforated by a photonic crystal on InP substrate	86
2.2.1. Vertical confinement: a planar waveguide on substrate	86
2.2.2. In-plane confinement: intentional defects within the gap.	87
2.2.2.1. Localized defects	88
2.2.2.2. Linear defects	88
2.2.3. Losses.	89
2.3. Technology for drilling holes on InP-based materials	90
2.3.1. Mask generation.	90
2.3.2. Dry-etching of InP-based semiconductor materials	91
2.4. Modal behavior and performance of structures	92
2.4.1. Passive structures	92
2.4.1.1. Straight guides, taper	93
2.4.1.2. Bend, combiner.	96
2.4.1.3. Filters.	100
2.4.2. Active structures: lasers	102
2.5. Conclusion	104
2.6. References	105
Chapter 3. Photonic Crystal Fibers	109
Dominique PAGNOUX	
3.1. Introduction.	109
3.2. Two guiding principles in microstructured fibers	112
3.3. Manufacture of microstructured fibers	116
3.4. Modeling TIR-MOFs	117
3.4.1. The “effective-V model”.	117
3.4.2. Modal methods for calculating the fields	118

8 Nanophotonics

3.5. Main properties and applications of TIR-MOFs	120
3.5.1. Single mode propagation	120
3.5.2. Propagation loss	120
3.5.3. Chromatic dispersion	121
3.5.4. Birefringence	123
3.5.5. Non-conventional effective areas	124
3.6. Photonic bandgap fibers	125
3.6.1. Propagation in photonic bandgap fibers	125
3.6.2. Some applications of photonic crystal fibers	127
3.7. Conclusion	128
3.8. References	129
Chapter 4. Quantum Dots in Optical Microcavities	135
Jean-Michel GÉRARD	
4.1. Introduction	135
4.2. Building blocks for solid-state CQED	137
4.2.1. Self-assembled QDs as “artificial atoms”	137
4.2.2. Solid-state optical microcavities	139
4.3. QDs in microcavities: some basic CQED experiments	142
4.3.1. Strong coupling regime	142
4.3.2. Weak coupling regime: enhancement/inhibition of the SE rate and “nearly” single mode SE	145
4.3.3. Applications of CQED effects to single photon sources and nanolasers	150
4.4. References	154
Chapter 5. Nonlinear Optics in Nano- and Microstructures	159
Yannick DUMEIGE and Fabrice RAINERI	
5.1. Introduction	159
5.2. Introduction to nonlinear optics	160
5.2.1. Maxwell equations and nonlinear optics	160
5.2.2. Second order nonlinear processes	164
5.2.2.1. Three wave mixing	165
5.2.2.2. Second harmonic generation	166
5.2.2.3. Parametric amplification	169
5.2.2.4. How can phase matching be achieved?	170
5.2.2.5. Applications of second order nonlinearity	173
5.2.3. Third order processes	173
5.2.3.1. Four wave mixing	173
5.2.3.2. Optical Kerr effect	175

5.2.3.3. Nonlinear spectroscopy: Raman, Brillouin and Rayleigh scatterings	177
5.3. Nonlinear optics of nano- or microstructured media	177
5.3.1. Second order nonlinear optics in III–V semiconductors	178
5.3.1.1. Quasi-phase matching in III–V semiconductors.	178
5.3.1.2. Quasi-phase matching in microcavity.	179
5.3.1.3. Bidimensional quasi-phase matching	180
5.3.1.4. Form birefringence.	180
5.3.1.5. Phase matching in one-dimensional photonic crystals	181
5.3.1.6. Phase matching in two-dimensional photonic crystal waveguide.	183
5.3.2. Third order nonlinear effects	184
5.3.2.1. Continuum generation in microstructured optical fibers	184
5.3.2.2. Optical reconfiguration of two-dimensional photonic crystal slabs	184
5.3.2.3. Spatial solitons in microcavities	186
5.4. Conclusion	187
5.5. References	187
Chapter 6. Third Order Optical Nonlinearities in Photonic Crystals	191
Robert FREY, Philippe DELAYE and Gérald ROOSEN	
6.1. Introduction.	191
6.2. Third order nonlinear optic reminder.	192
6.2.1. Third order optical nonlinearities.	192
6.2.2. Some third order nonlinear optical processes.	194
6.2.3. Influence of the local field.	196
6.3. Local field in photonic crystals	198
6.4. Nonlinearities in photonic crystals	203
6.5. Conclusion	204
6.6. References	204
Chapter 7. Controlling the Optical Near Field: Implications for Nanotechnology	207
Frédérique DE FORNEL	
7.1. Introduction.	207
7.2. How is the near field defined?.	208
7.2.1. Dipolar emission	208
7.2.2. Diffraction by a sub-wavelength aperture.	212
7.2.3. Total internal reflection	213
7.3. Optical near field microscopies	217

7.3.1. Introduction	217
7.3.2. Fundamental principles	217
7.3.3. Realization of near field probes.	219
7.3.4. Imaging methods in near field optical microscopes	220
7.3.5. Feedback	222
7.3.6. What is actually measured in near field?	223
7.3.7. PSTM configuration	223
7.3.8. Apertureless microscope.	225
7.3.9. Effect of coherence on the structure of near field images	226
7.4. Characterization of integrated-optical components	227
7.4.1. Characterization of guided modes	227
7.4.2. Photonic crystal waveguides	229
7.4.3. Excitation of cavity modes	230
7.4.4. Localized generation of surface plasmons	232
7.5. Conclusion	235
7.6. References	236
Chapter 8. Sub-Wavelength Optics: Towards Plasmonics	239
Alain DEREUX	
8.1. Technological context.	239
8.2. Detecting optical fields at the sub-wavelength scale.	240
8.2.1. Principle of sub-wavelength measurement	240
8.2.2. Scattering theory of electromagnetic waves	242
8.2.3. Electromagnetic LDOS	244
8.2.4. PSTM detection of the electric or magnetic components of optical waves	246
8.2.5. SNOM detection of the electromagnetic LDOS	247
8.3. Localized plasmons	249
8.3.1. Squeezing of the near-field by localized plasmons coupling.	250
8.3.2. Controlling the coupling of localized plasmons.	251
8.4. Sub- λ optical devices	254
8.4.1. Coupling in.	254
8.4.2. Sub- λ waveguides	254
8.4.3. Towards plasmonics: plasmons on metal stripes.	255
8.4.4. Prototypes of submicron optical devices	256
8.5. References	263

Chapter 9. The Confined Universe of Electrons in Semiconductor Nanocrystals.	265
Maria CHAMARRO	
9.1. Introduction.	265
9.2. Electronic structure	266
9.2.1. “Naïf” model.	266
9.2.1.1. Absorption and luminescence spectra.	269
9.2.2. Fine electronic structure	271
9.2.2.1. Size-selective excitation.	271
9.2.2.2. “Dark” electron-hole pair	274
9.3. Micro-luminescence.	276
9.4. Auger effect	279
9.5. Applications in nanophotonics	281
9.5.1. Semiconductor nanocrystals: single photon sources	281
9.5.2. Semiconductor nanocrystals: new fluorescent labels for biology	283
9.5.3. Semiconductor nanocrystals: a new active material for tunable lasers	285
9.6. Conclusions.	286
9.7. References	287
Chapter 10. Nano-Biophotonics	293
Hervé RIGNEAULT and Pierre-François LENNE	
10.1. Introduction.	293
10.2. The cell: scale and constituents	295
10.3. Origin and optical contrast mechanisms	296
10.3.1. Classical contrast mechanisms: bright field, dark field, phase contrast and interferometric contrast.	297
10.3.2. The fluorescence contrast mechanism	298
10.3.2.1. The lifetime contrast	300
10.3.2.2. Resolving power in fluorescence microscopy	301
10.3.3. Non-linear microscopy	303
10.3.3.1. Second harmonic generation (SHG)	304
10.3.3.2. Coherent anti-Stokes Raman scattering (CARS)	305
10.4. Reduction of the observation volume	307
10.4.1. Far field methods	308
10.4.1.1. 4Pi microscopy	308
10.4.1.2. Microscopy on a mirror	309
10.4.1.3. Stimulated emission depletion: STED.	309

12	Nanophotonics	
	10.4.2. Near field methods	311
	10.4.2.1. NSOM	312
	10.4.2.2. TIRF	312
	10.4.2.3. Nanoholes	313
	10.5. Conclusion	314
	10.6. References.	314
	List of Authors	319
	Index	323

Preface

With the continuous miniaturization of electronic components over the last 50 years we have grown accustomed to the idea of micro-electronics where transistors are measured in microns, and today, with the advent of transistor grid lengths of around 10 nanometers, we are getting used to nano-electronics. Besides, we should not forget about Moore's law¹, a predictive law, according to which the length of the transistor grid is reduced by a factor of two approximately every 18 months.

The concept of nanophotonics, although not surprising, remains, however, less clearly understood by the scientific community than that of nano-electronics. Admittedly, we realize that optoelectronic components, such as the laser diode, modulators and detectors developed for the needs of optical telecommunications, are small nowadays, but there does not exist a Moore's law of optoelectronics and the most usual limit naively imagined for optics is that of wavelength, i.e. a size close to the micron for waves of the visible and near infrared spectrum.

It is, therefore, the main objective of this work to try and give a more precise overview of the rapidly emerging field of nanophotonics, wherein optical fields at the scale of a fraction of wavelength and even mainly sub-wavelength are sought to be controlled and designed.

In fact, if the optical "chip" does not exist in the liking of the electronic "chip", photonic crystals have recently led to great hopes for large-scale integration of optoelectronic components. Two-dimensional photonic crystals obtained through periodic structuring of a planar optical waveguide, in particular, have many characteristics which bring them closer to electronic micro- and nanostructures. In a simple vision, it suffices to introduce periodicity defects at suitably selected spots within the crystal to obtain the desired optical components (waveguides, bending light, micro-resonators, filters, etc.) and to pair them up with each other to form true

¹ G. Moore, founder of INTEL.

photonic circuits. Admittedly, reality is more difficult than it appears, if only for the precision needed in the manufacturing of structures. In many cases it is considered lower or equal to 10 nanometers, and then all the relevance of parallels between nano-electronics and nanophotonics become apparent. The first two chapters are thus mainly dedicated to photonic crystals in planar optics, referring to other recently published works on the subject², while focusing on the photonic components themselves, the dynamics of the photons plunged into a periodically structured medium and the prospect of obtaining high integration photonic circuits.

On the subject of two-dimensional photonic crystals radically differing from planar guided optics, Chapter 3 tackles the topic of photonic crystals fibers and, more generally, of structured fibers. Not only is the propagation of light achieved then perpendicular to the plane of periodic structuring, but also the unique production technology is based on the first assembly performed on a macroscopic scale, the final micro-nano-structures obtained by a stretching process at the second stage. It is impressive to be able “to unravel” micro-nanophotonics over distances of several kilometers! From a practical standpoint, microstructured fibers and photonic crystal fibers open up unprecedented prospects with respect to the control of the propagation mode in fiber-optics and to the control of chromatic dispersion. By controlling optical confinement, we may also easily control the processes of nonlinear optics that can be developed within these fibers.

Before the concepts of photonic circuit or fiber even appear, it should be remembered that the first studies of photonic crystals and structured materials for optics had been motivated, at the beginning of the 1980s, by the desire to control and even inhibit spontaneous emission in optoelectronic components. The largely conveyed emblematic image is that of the single transmitter in a uni-modal micro-cavity, every emitted photon being in the unique electromagnetic mode of the cavity. That aside, for the image to become reality over time, it was initially necessary to control the realization of nano-transmitters in the solid state, then to know how to combine nano-transmitters and micro-cavities. Chapter 4, in particular, deals with semiconductor quantum boxes and their association to various types of optical micro-cavities. The chapter introduces the concepts of weak and strong coupling in micro-cavity, as well as giving reports on the applications to semiconductor lasers with a very weak threshold and to single-photon micro-nanosources required for quantum cryptography.

Micro-nanostructuring of materials is also full of prospects for other active components of nonlinear optics. In fact, it is not only possible to achieve true engineering of the refraction index dispersion, but also to control the dispersion of group velocity as well as the localization of the electromagnetic field. Adapting the

² J-M. Lourtioz, H. Benisty, V. Berger, J-M. Gérard, D. Maystre, A. Tchebnokov, *Les cristaux photoniques ou la lumière en cage*, Collection Technique et Scientifique des Télécommunications, Hermès, Paris, 2003.

phase and group velocity of electromagnetic waves with very different frequencies in order to reinforce their interactions is an example of application in the case of second-order optical nonlinearities. Chapters 5 and 6 thus develop various aspects of nonlinear optics in micro- and nanostructured materials such as the second harmonic generation, the optical Kerr effect, the propagation of solitons or the mix of four degenerated waves. After a short theoretical introduction to nonlinear optics, the various effects are illustrated on the basis of experiments performed very recently.

In Chapter 7 we openly approach the field of sub-wavelength optics with the analysis techniques of near optical field. The sub- λ nature stems not only from the distances between a point and a diffracting object, but also from fading waves whose space extension may be clearly lower than that of the light wavelength. Until recently limited to particular cases, the analysis of near fields today assumes all its interest with the development of nanotechnologies and optical micro-nanodevices. Having defined the near field concept and recalled the alternatives of microscopy in the near field, this chapter thus illustrates certain recent characterizations of semiconductor micro-components in planar integrated optics.

Metallic devices involving surface or localized plasmon-polaritons are also choice objects for the studies of near fields, because these waves are not detectable in far fields. Chapter 8 is mainly dedicated to them as well as to the optical technique of microscopy by tunnel effect. The coupling between an optical wave and electric charges oscillating in a metal is a phenomenon that has been known for a long time and generally considered as a parasite, since it is dissipative over propagation lengths typically exceeding 10 microns. However, the development of micro-nanotechnologies allowed an unprecedented revival of the studies with the creation of a new set of themes known today under the name of plasmonics. The now-famous experiment of Ebbesen³ was one of the determinant elements of the renewed interest for the plasmon waves. More generally, miniaturization of metal structures appears a possible way of optical connections alongside photonic crystals.

Of a smaller size than all the devices evoked previously, including quantum box nano-transmitters, nanocrystal semiconductors composed of a few hundred to a few thousand atoms belong to the category of nano-objects of great interest for small scale optics. Developed by processes different from semiconductor quantum boxes, nanocrystals can be incorporated into transparent matrices, as they can also be grafted into biological entities. Excellent candidates for the emission of “single photons”, they are also used as biological markers and present potential applications for the creation of tunable microlasers. Chapter 9 thus makes us discover the structures of the electronic levels and the optical properties of these nano-objects which, like carbon nanotubes, still remain just as attractive for the physicist.

³ J-M. Lourtioz, H. Benisty, V. Berger, J-M. Gérard, D. Maystre and A. Chelnokov (eds.), *Photonic Crystals: Towards Nanoscale Photonic Devices*, Springer, Berlin-Heidelberg-New York, 2005.

Also dealing with small-scale objects but in a very different context, the tenth and final chapter of this book completes the review of nanophotonics by addressing the interdisciplinary topic of the nanobiophotonics. The marriage of optics and biology is certainly not completely new, because while electronic microscopy offers a nanometric solution for the study of molecular cell entities, optical techniques in turn allow a slightly invasive, even non-invasive, analysis of live cells. In particular, the chapter describes the traditional fluorescence techniques for the detection of a unique molecular entity as well as more recent techniques, building on the interactions between ultra-short optical impulses and biological environments. The emergent topic of nanophotonics aims more particularly at reducing the observation volume below the limit imposed by diffraction. The chapter shows how to achieve this goal using nonlinear optical effects or nanostructured photonic devices close to the studied biological objects.

The book that we have just briefly presented was written by internationally recognized specialists, each in their field. Thus, it constitutes a follow-up to the first spring school of the CNRS on nanophotonics held in Houches (France) in June 2003 and organized by the four coordinators of the book. It is, to our knowledge, one of the first times that such various and complementary aspects of nanophotonics have been gathered together. It would, undoubtedly, be useless to allot an exhaustive nature to the book, but students and scientists working in nanosciences would, however, still be able to find in it a rich source of information on the new fascinating and rapidly expanding field.

Jean-Michel LOURTIOZ,
Claude DELALANDE,
Ariel LEVENSON,
Hervé RIGNEAULT

Chapter 1

Photonic Crystals: From Microphotonics to Nanophotonics

1.1. Introduction

The principal motivations for the emergence of photonic crystals can be summarized in one single word, “ λ -Photonics”, which means the control of photons at the wavelength scale. The harnessing of light has always been central in the field of human endeavor: one may call to mind, for example, the destruction of the Roman fleet by the blazing mirrors of Archimedes at the siege of Syracuse in 215 BC.

Generally speaking, the harnessing of light consists of structuring the space where it is meant to be confined; but there are intrinsic limitations which are related to the undulatory nature of light and which have been formulated in the famous Maxwell equations of 1873, providing a consistent picture of the experimental data then available. These limitations lie at the heart of λ -Photonics, whose definition could be the control of photons within the tiniest possible space over the longest possible time: this implies structuring space at the wavelength scale, which is the sub-micron range for the optical domain.

Microphotonics or Nanophotonics?

The reader will have understood that the word “ λ -photonics” refers simply to Microphotonics in the optical regime. We will use the term Microphotonics throughout this chapter, given that the average size of photonic structures under

consideration is micro-metric. Yet, the size resolution to be considered for the design as well as for the fabrication of efficient practical photonic devices is the nanometer.

The nanometric control of the size of microphotonic structures is dictated by the specifications which are required for the resolution (better than one nanometer) of the operation wavelength; these constraints may be partly relaxed by the use of appropriate trimming procedures for the fine adjustment of the operation wavelength (control of the temperature, for example). But serious consequences may arise from insufficient control over the size of photonic structures, such as the unwanted mutual coupling of optical modes, and, as a result, the loss of control of photons within a confined space for the time required. For example, nanometric resolution of the size is essential for the production of resonant photonic structures with high quality factors, that is whose bandwidth is in the nanometer range or below (this terminology will be made familiar to the non-specialist reader in the course of this chapter). Finally, the relevance of the nanometric scale in active devices is twofold: first in connection with the quantum size active material (quantum wells and quantum boxes), and second, given the required resolution of its spatial localization within the microphotonic structure, whose design is meant to result in the *ad hoc* electromagnetic environment.

After this parenthesis, which, beyond semantic considerations, is meant to provide to the reader an accurate definition of the “à la mode” Micro- and Nanophotonics terms, let us resume with this introductory section.

A photonic crystal is a medium whose optical index shows a periodical modulation with a lattice constant on the order of the operation wavelength. The specificity of photonic crystals inside the wider family of periodic photonic structures lies in the high contrast of periodic modulation (generally more than 200%): this specific feature is central for the control of the spatio-temporal trajectory of photons at the scale of their wavelength and of their periodic oscillation duration.

It will be shown in section 1.2 that there are a variety of ways of structuring space, consisting of preventing the propagation of photons along one or several directions, thus resulting in photonic “objects” with reduced “dimensionality” and with photonic properties which are strongly wavelength dependent. The new avenue opened up by photonic crystals lies in the range of degrees of freedom which they provide for the control of photon kinetics (trapping, slowing down), in terms of angular, spatial, temporal and wavelength resolution.

One-dimensional photonic crystals (1DPC), which possess most of the basic physical properties of photonic crystals in general, will be discussed in section 1.3.

We will embark in section 1.4 on a short and rather frustrating trip into the elusive world of three-dimensional photonic crystals (3DPC). Sections 1.5 and 1.6 will concentrate on two-dimensional photonic crystals (2DPC), which have been the subject, so far, of most new applications in terms of device demonstrations: along these lines will be presented the essential building blocks of Integrated Photonics based on 2DPC, which is presently considered as the principal domain of applications of photonic crystals. The concepts of 2.5 D Microphotonics based on 2DPC, which can be considered as a major extension of planar technology through exploitation of the third (“vertical”) dimension, will be covered in section 1.7.

This chapter provides a vision complementary to that given in the book published by J. M. Lourtioz *et al.* (LOU 05). Concerning conceptual aspects, the present approach is more phenomenological and does not leave much room for theoretical models of photonic crystals. Particular attention is given to the changes induced by the photonic crystal on the spatio-temporal characteristics of photons immersed in the periodic medium and on similarities with phenomena observed in the case of more traditional structuring of space. As for application aspects, the present work is mainly oriented toward integrated Micro-nanophotonics: it is shown, in particular, how recent developments of 2DPC, along planar technological schemes, open the way to the production of essential building blocks for this purpose.

1.2. Reminders and prerequisites¹

1.2.1. Maxwell equations

The undulatory nature of light is expressed in terms of an electromagnetic field whose electrical $E(r,t)$ and magnetic $H(r,t)$ components, which depend on time t and space r coordinates, are given by Maxwell equations. The latter can be reduced to the so called master equation, as expressed below (in the case of an isotropic and non-absorbing medium):

$$\nabla \times \left(\frac{1}{\varepsilon(r)} \nabla \times H(r) \right) = \left(\frac{\omega}{c} \right)^2 \times H(r), \text{ with:} \quad (1)$$

¹ Section 1.2, which is a very brief and specific summary of the abundant related literature, does not include any specific references.

$$E(r) = \left(\frac{-ic}{\omega \mathcal{E}(r)} \right) \nabla \times H(r), \text{ and, } \begin{cases} H(r,t) = H(r)e^{j\omega t} \\ E(r,t) = E(r)e^{j\omega t} \end{cases} \quad (2)$$

where ω is the pulsation, $\mathcal{E}(r)$ the dielectric function of the medium and c the light velocity in vacuum. This is typically an eigenvalue/eigenvector problem.

1.2.1.1. Optical modes

Optical modes are the eigensolutions of Maxwell equations which correspond to a spatial distribution of the electromagnetic field which is stationary in the time scale.

1.2.1.2. Dispersion characteristics

These are given by the equations which relate the pulsation (eigenvalue) of optical modes to their propagation constants (eigenvector).

1.2.2. A simple case: three-dimensional and homogeneous free space

This is the simplest case, where the dielectric constant is invariant with space coordinates: the eigensolutions or eigenmodes of Maxwell equations are plane waves, with a continuous translational symmetry.

The magnetic field (as well as the electric field) can be expressed as follows:

$$H_k(r) = H_0 e^{i(k \cdot r)}, \quad (3)$$

where k is the wave-vector or the propagation constant, with $k = \frac{2\pi n}{\lambda}$, n is the optical index of the medium, and λ is the wavelength. The dispersion characteristics can be simply written as below:

$$\omega = \frac{c}{n} |k| \quad (4)$$

$\frac{c}{n}$ is the phase velocity of the optical mode; in the simple case considered here of homogeneous free space, the phase velocity coincides with energy or group velocity

$$v_g = \frac{d\omega}{dk}.$$

It is shown that the density of optical modes per volume unit and per ω unit is a continuous function of ω and is written:

$$\frac{dN}{d\omega} = \frac{\omega^2 n^3}{\pi^2 c^3} \quad (5)$$

1.2.3. Structuring of free space and optical mode engineering

Plane waves (eigensolutions of Maxwell equations in a homogeneous medium), having a theoretically infinite spatio-temporal extension, are of no practical use from the point of view of Microphotonics, whose definition we recall: *the control of photons within the tiniest possible space over the longest possible time* (or, at least, over the minimum required time interval). In other words, Microphotonics is nothing but optical mode engineering, or free space carving art, in such a way that optical modes with the appropriate spatio-temporal configuration are generated.

Lifetime or coherency time and quality factor of an optical mode

According to the above definition of Microphotonics, it appears natural to grant the optical mode a merit factor F , which quantifies the properties of the optical mode in terms of the ratio of time τ during which it remains under control (or its lifetime from the observer/user viewpoint), over the average real space volume which it fills during its lifetime.

To put it differently and more precisely, the lifetime τ is the time interval when the user may count on a coherent mode, whose phase remains deterministic, within the volume where he tries to control and confine it. The merit factor can be made dimensionless if normalized to the ratio $\frac{T}{\lambda^3}$, where T is the period of oscillation and λ is the wavelength in vacuum.

$$F = \frac{\tau}{T} \times \frac{\lambda^3}{V}, \text{ with:} \quad (6)$$

$$Q = \frac{2\pi\tau}{T},$$

where Q is the traditional quality factor of the mode.

It can be shown, straightforwardly, that the merit factor F of a plane wave is zero. Indeed, $\tau = \frac{nL}{c}$, where n is the optical index of the medium and L is the length of the wave packet processed by the user, given that the volume $V = L \times S$ of the optical mode diverges with the section S of the plane wave.

The finite lifetime of the optical mode results in a spectral widening $\delta\omega = \frac{2\pi}{\tau}$.

In the simple case of a plane wave we find:

$$\delta\omega = \frac{c}{n} \times \frac{2\pi}{L} = \frac{c}{n} \delta k \quad (7)$$

where $\delta k = \frac{2\pi}{L}$ expresses the “de-localization” of the mode in the wave-vector or reciprocal space as a result of the “localization” of the plane wave along its path over a distance L . It may be noted that equation (7) is obtained from a simple differentiation of the dispersion equation (4) of the mode (plane wave here). Therefore, although time independent and formally applying in purely stationary conditions, dispersion characteristics can provide concrete information relating to the dynamics of optical modes; we will resume this discussion regularly throughout this chapter.

Returning to the merit factor, the reader will have noticed that F is proportional to the Purcell factor, which gives the relative increase of the spontaneous recombination rate of an active medium as a result of its coupling to the optical mode, as compared to the non-structured vacuum (see Chapter 4).

1.2.4. Examples of space structuring: objects with reduced dimensionality

Let us examine a few examples of space structuring, which aims in general at the production of objects with reduced dimensionality, that is where the propagation of photons is not free in all directions at any time.

1.2.4.1. Two 3D sub-spaces

The simplest example of space structuring consists of dividing 3D free space into two 3D sub-spaces with different optical indices n_1 and n_2 , and bordered by a common infinite plane boundary (Figure 1.1).

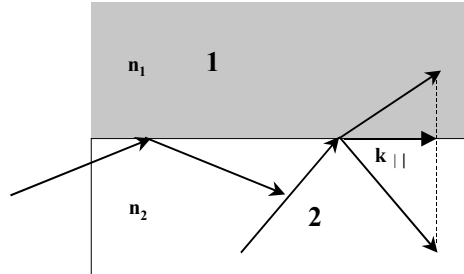


Figure 1.1. Two 3D sub-spaces with different optical indices

This system can still be simply described using plane wave type optical modes, but their propagation is bound to meet with the law of Descartes at the interface, which can be simply expressed in terms of the continuity of the wave-vector component $k_{||}$ parallel to the interface plane. Hence, if $n_2 \geq n_1$, plane waves propagating in medium 2 are subjected to total internal reflection at the interface for angles of incidence lying beyond a certain limit, and are evanescent in medium 1. This effect can be described in terms of the so called “light-line”, which is a straight line whose equation can be written $\omega = \frac{c}{n_1} k_{||}$ in $\omega(k_{||})$ coordinates: this light-line delineates a cone within which $(\omega, k_{||})$ couples are allowed inside the two media, which is where refractive coupling (communication) between plane waves of the two media is allowed (see Figure 1.2).

In other words, the inner of the cone (defined by equation $\omega = \frac{c}{n_1} k_{||}$) corresponds to the *continuum* of modes which are allowed in both sub-spaces, whereas the gray zone in Figure 1.2 is restricted solely to optical modes of sub-space 2.

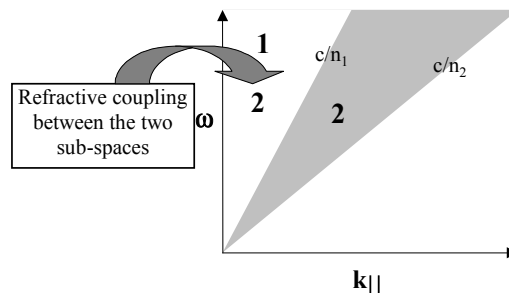


Figure 1.2. Light line and light cone in $\omega(k_{||})$ coordinates

1.2.4.2. Two-dimensional isotropic propagation: planar cavity

Figure 1.3 shows a schematic side view of an ideal planar cavity (thickness D) formed between two fully reflecting and loss-less metallic plane mirrors.

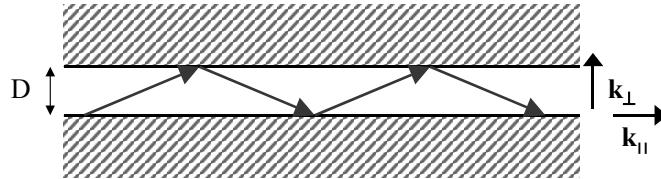


Figure 1.3. Planar cavity formed between two perfect metallic plane reflectors

Propagation is allowed along the sole directions parallel to the mirrors, with the propagation vector k_{\parallel} . Unlike in 3D free space, there is no longer a continuum of modes in $\omega(k_{\parallel})$ coordinates; one observes instead a “quantification” which manifests itself by the discrete values of the vector $k_{\perp} = \frac{p\pi}{D}$, which are required in order to meet the conditions for phase conservation after a “vertical” round trip of photons.

The general shape of the dispersion characteristics is shown in Figure 1.4.

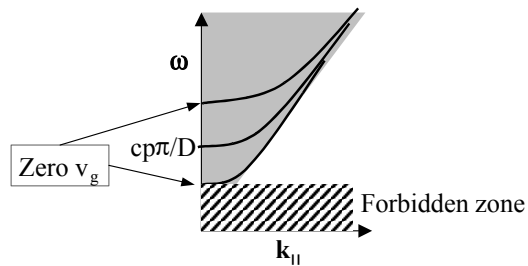


Figure 1.4. General shape of dispersion characteristics of an ideal planar cavity

The reduction in dimensionality results in clear disturbances as compared to the biblical simplicity of the case of 3D homogeneous free space. One observes, first, a forbidden frequency zone where the density of modes is zero, below the pulsation $\omega = \frac{\pi c}{D}$. In addition, curves exhibit a minimum for $k_{||} = 0$; this means that the propagation velocity of the energy or the *group velocity* v_g of photons tends to zero (whereas the density of modes remains finite and can be expressed as in a two-dimensional homogeneous medium): the optical wave is “stationary” and oscillates “vertically”. It can be shown that the merit factor F of optical modes tends to zero, in a similar way to the case of plane waves in a homogeneous medium, except for the vicinity of $k_{||} = 0$, where F tends to a finite limit which is proportional to $1/D^2$. This fact can be interpreted as the vertical confinement of photons imposed by mirrors resulting in a relative lateral “confinement” of optical modes, which cannot propagate any more for $k_{||} = 0$.

1.2.4.3. One-dimensional propagation: photonic wire

The dimensionality can be further reduced when photons are compelled to propagate along a single direction, for example inside an ideal loss-less metallic sheath (see Figure 1.5). One observes, similarly to the previous case, a forbidden frequency band below a cut off frequency where the group velocity tends to zero for $k_{||} = 0$, and where it can be shown that, in addition, the density of modes diverges when the length L of the optical wire tends to infinity.

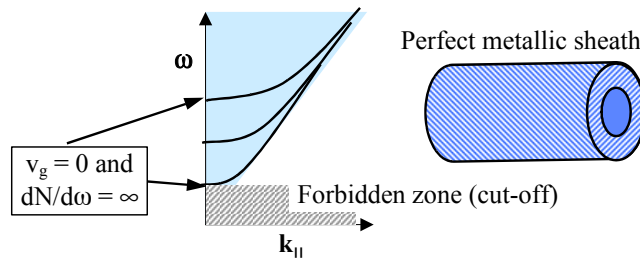


Figure 1.5. One-dimensional propagation in a perfect metallic sheath

² A full demonstration is not given here, due to limitations of space. It is based (as shown in the simple case of a plane wave) on the differentiation of the dispersion characteristics around the minimum. One finds, in particular, that the lateral extension of the optical mode during its lifetime τ is written $S = \alpha\tau$, where α is the curvature (second derivative) at the extreme (minimum here) of the dispersion characteristics. Later in this chapter, we will comment extensively on the importance of the parameter α in photonic crystals.

The confinement strengthening of optical modes manifests itself by a finite merit factor F for finite k_{\parallel} (F is proportional to the inverse of the wire section S) and by the divergence of F for $k_{\parallel}=0$, when L tends to infinity (F is proportional to $\frac{L}{S}$).

1.2.4.4. Case of index guiding (two- or one-dimensionality)

The guiding of photons is achieved in a more conventional way by trying to confine them inside material with an optical index higher than that of the surrounding medium: this is the principle classically applied in optical fibers.

The dispersions characteristics of waveguided modes share some similarities with previous cases, but they also have notable differences. First, optical modes can be kept guided as far as they are fully prevented from communicating with the surrounding medium: their dispersion characteristics are therefore confined within the area located below the light-line (see Figure 1.6). Second, confinement is not as strong as with metallic mirrors or sheaths (an evanescent portion of the electromagnetic field is allowed to extend outside the high index material): the result of this is that the cut off phenomenon is not observed (for symmetrical guiding structures), nor does the group velocity vanish.

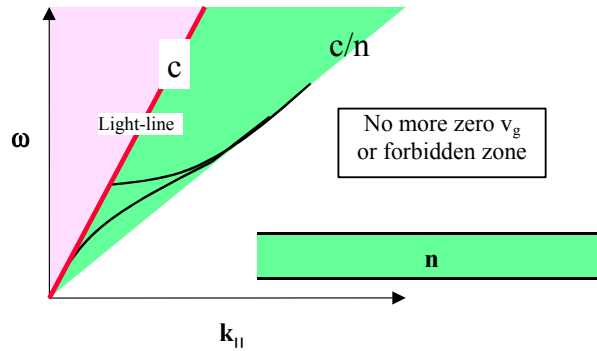


Figure 1.6. Case of index guiding: light-line

1.2.4.5. Zero-dimensionality: optical (micro)-cavity

Propagation of photons is now prevented in all directions: they are trapped in an optical cavity which can only be accessed by “resonant” modes for discrete frequencies. The spectral density of modes tends therefore to infinity at the

resonance frequencies (yet, the *average* density of modes is finite and is not changed with respect to its free space value).

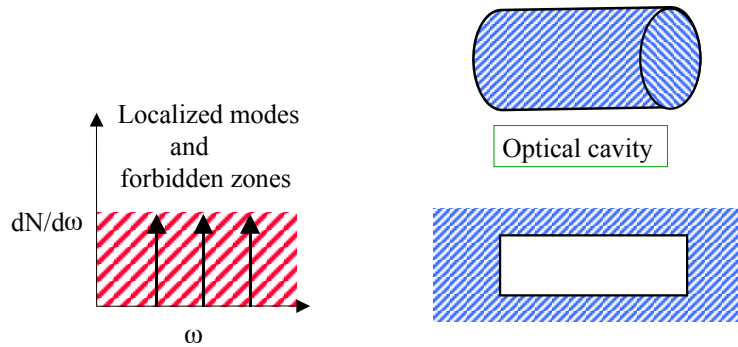


Figure 1.7. *Optical microcavity: the density of modes is a series of Dirac functions at resonance frequencies*

The merit factor of optical modes of an ideal cavity is naturally infinite, photons being confined in a finite volume for a theoretically infinite amount of time. In practice, the life of optical modes in the cavity is not infinite as a result of various “optical loss” processes: for example, a real metallic cavity will end up absorbing photons after a finite amount of time. A spectral widening $\delta\omega = \frac{1}{\tau}$ of the resonance is then observed and the density of modes $\frac{1}{\delta\omega} = \tau$ remains finite. When the optical “cage” is opened up to the external world, spectral widening extends in such a way as to overlap with the neighboring modes, and one finds again free space 3D continuum.

1.2.5. Epilogue

At the present stage, the reader should be in a comfortable position to penetrate the world of photonic crystals quite easily, whose basic ingredients have already been introduced (forbidden bands, resonance, slowing down of photons). The reader may be wondering why a periodic and high index contrast structuring of space should be at all useful in the field of photon confinement. This is the essential question that we will now try to address, given that the principal ingredients of the response can be summarized in one sentence: photonic crystals provide us with new

degrees of freedom for the control of the kinetics (trapping, slowing down, optical losses) of photons, especially in terms of angular, spatial and spectral resolutions.

1.3. 1D photonic crystals

A one-dimensional photonic crystal is a one-dimensional virtual medium, whose optical index shows periodic modulation (and it should not be viewed as a real object with reduced dimensionality in the real 3D world, as described in section 1.2.4).

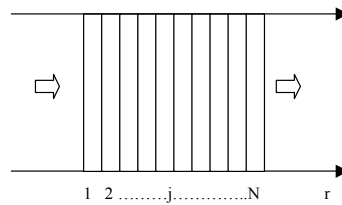


Figure 1.8. *1D photonic crystal: the direction of propagation is normal to the layer plane*

This imaginary configuration corresponds approximately to the practical situation of a periodic layer stack whose lateral dimensions are large as compared to its spatial period, given that the only relevant direction of propagation is normal to the layer plane.

Dielectric layer stacks have been around for quite some time and have been widely used and developed in optics during the last few decades to control optical signals. Modeling tools are available for the design of these periodic structures, which are based on the resolution of Maxwell equations using the so called matrix transfer technique (MAC 86). It consists of the determination, step by step, of the reflected and transmitted components of the electromagnetic field at successive interfaces and within different layers. The Bragg mirror is a famous example of such a stack layer: it consists of a periodic stack of quarter-wavelength dielectric layers, with a different optical index. It is found that this structure behaves like a mirror when operating at the configuration wavelength: reflectivity increases with the number of pair layers, and for a given number of layers, with the optical index contrast between adjacent layers. The bandwidth of the reflector also increases as a function of the index contrast. For an “infinite” number of pairs, there exist spectral bands where the propagation of photons is forbidden in the periodic medium or photonic band gaps (PBGs). The concept of PBG is therefore a pretty familiar one in the world of optics and cannot be considered as a novelty introduced by the promoters of the photonic crystal concept. The novelty lies instead in the new

viewpoint and the novel combinations brought about when regarding periodic structures as photonic crystals, that is by simply considering a photonic crystal in a similar way to crystalline materials: this is the so called solid state physics approach, with its wealth of generic concepts (YAB 1987; JOH 1987; JOA 1995).

In the following paragraphs, we will apply this approach to the analysis of 1D photonic crystals and will see that they possess most of the basic physical properties of photonic crystals in general.

1.3.1. Bloch modes

Eigenmodes of Maxwell equations in a periodic medium possess discrete periodic translational symmetry properties. According to the Bloch theorem, these modes, also called Bloch modes, can be expressed as follows:

$$\begin{aligned} H_k(r) &= e^{i(k \cdot r)} u_k(r) \quad \text{with,} \\ u_k(r) &= u_k(r + a) \end{aligned} \quad (8)$$

$u_k(r)$ can be expanded in Fourier series:

$$u_k(r) = \sum_m c_{k,m} e^{imbr}, \quad (9)$$

where $b = \frac{2\pi}{a}$ is the base vector of the so called reciprocal lattice.

The essential properties of Bloch modes are summarized below:

– Two Bloch modes whose k vector difference is $m \frac{2\pi}{a}$ (m is an integer) are equivalent: this is simply the mathematical expression of the diffraction process. As a result, dispersion characteristics (or photonic band structures) $\omega(k)$ can be fully represented in the so called first Brillouin zone (according to solid state physics terminology), in the k vector range $-\frac{\pi}{a} \leq k \leq \frac{\pi}{a}$.

– Fourier components also express the diffraction processes induced by the photonic crystal's periodic structure. It will be shown that they also hold the information regarding diffractive coupling properties of the relevant Bloch mode with other modes (for example, the “radiating” properties and loss characteristics, in case of coupling with the “radiation continuum”).

1.3.2. Dispersion characteristics of a 1D periodic medium

1.3.2.1. Genesis and description of dispersion characteristics

The genesis of dispersion characteristics is illustrated in Figure 1.9 below.

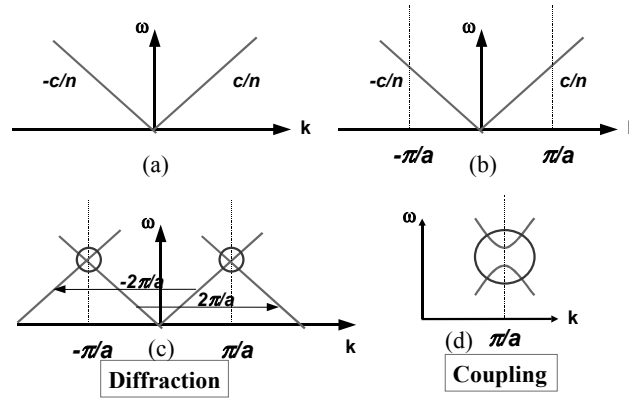


Figure 1.9. The dispersion characteristics of optical modes in a periodic medium are widely determined by diffraction processes and optical mode coupling properties

In the case of a homogeneous medium (Figure 1.9a), dispersion characteristics, standing for propagating and counter-propagating optical waves which ignore each other, are plain straight lines (equation $\omega = \pm \frac{c}{n}k$). The periodic structuring of the medium results in diffraction processes, which express themselves in terms of successive discrete translations (diffraction orders: see Figure 1.9c) of dispersion characteristics by integer numbers (positive or negative) of $\frac{2\pi}{a}$: the a periodicity of the real space has a counterpart $\frac{2\pi}{a}$ in the reciprocal propagation vector space. We see from Figure 1.9c that dispersion characteristics of back and forth optical waves cross over at coordinates $(\omega, k) = (\frac{c}{n}p\frac{\pi}{a}, \pm p\frac{\pi}{a})$: as a consequence, propagating and counter-propagating waves may be coupled through diffraction processes. Degeneracy occurs therefore at those peculiar coordinates, since two modes which propagate in opposite directions are supposed to coexist yet have the same (ω, k) coordinates.

This coexistence will not survive beyond the time required for the coupling between modes to be completed: the degeneracy will then be raised much more strongly as the coupling is more efficient. This effect is called “anti-crossing”, resulting in the opening of a PBG (Figure 1.9d), whose width increases with the coupling rate (or the inverse of the coupling time), which itself increases with the magnitude of the periodic modulation of the optical index (periodic “corrugation”).

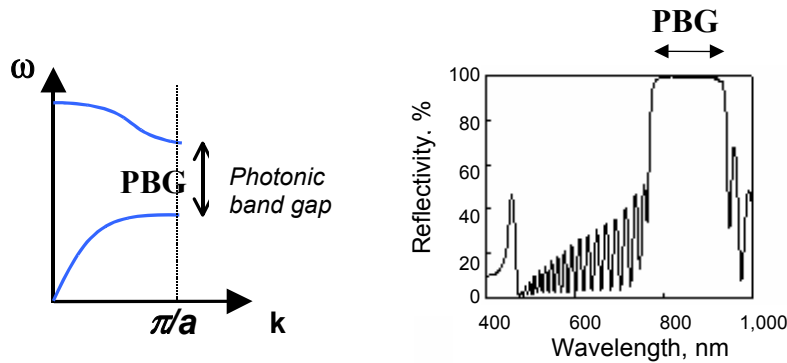


Figure 1.10. Photonic band gap (PBG) and bandwidth of a Bragg reflector

For example, anti-crossings occurring at coordinates $(\frac{c}{n} \frac{\pi}{a}, \pm \frac{\pi}{a})$, at the first Brillouin zone boundaries, correspond to the case of the Bragg reflector whose optical period is set at $\frac{\lambda}{2}$. The PBG width corresponds to that of the reflector bandwidth (Figure 1.10).

At the photonic band edges, dispersion characteristics exhibit extremes where the group velocity $\frac{d\omega}{dk}$ tends to zero. Mode coupling results there in the formation of a stationary optical wave, which cannot propagate. This situation is examined in more detail in Figure 1.11, where the electric field distributions of the stationary mode at the upper and lower band edges are shown.

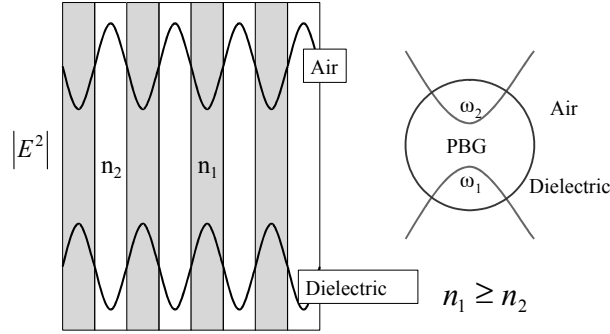


Figure 1.11. Air band and dielectric band at the photonic band edges

One may note that electromagnetic energy is concentrated principally within the low index material at the upper band edge, and vice versa at the lower band edge: this is consistent with the fact that, for a given k , photon energy decreases for increased optical index. The upper band is usually called the “air” band, whereas the lower band is called the “dielectric” band, with reference to the typical case of a photonic crystal where the low index material is air and the high index counterpart is a semiconductor dielectric.

1.3.2.2. Density of modes along the dispersion characteristics

It can easily be shown that, in a homogenous and one-dimensional medium with n as optical index, the density of modes per length and pulsation unit is constant and is expressed as $\frac{dN}{d\omega} = \frac{2n}{\pi c}$. In the presence of a periodic modulation of the optical index, this relation is simply written as follows:

$$\frac{\pi}{2} \frac{dN}{d\omega} = 1/v_g \quad (10)$$

The density of modes tends to infinity at the edges of the PBG. This is another manifestation of the existence of stationary waves whose slowing down results in the accumulation of electromagnetic energy. The density of modes is naturally zero inside the PBG.

1.3.3. Dynamics of Bloch modes

Dispersion characteristics apply in principle to periodic structures of infinite size and in stationary regime. However, the time dimension underlies the previous analysis of dispersion characteristics, especially when it comes to the coupling dynamics of optical modes and to group velocity; in addition the time dimension is inevitable in real structures of finite size. A rigorous approach would involve solving time-dependent Maxwell equations; we do not intend to analyze this aspect in detail here: intensive work in the relevant community is needed, given the ever increasing modeling requirements demanded by recent developments in the field of Microphotonics³. We will restrict ourselves to a brief discussion of optical mode dynamics, based on simple analytical relations.

1.3.3.1. Coupled mode theory

The coupled mode theory was originally proposed by Kogelnik and Shank in 1972 for the analysis of distributed feedback lasers (see also TAM 1988): this analytical theory is well suited to the modeling of microphotonic structures whose operation is essentially based on coupling phenomena between optical modes. Let us briefly recall that it is usually associated with a matrix formalism, which allows for the cascading of elementary building blocks in order to assemble more complex systems. The basic ingredients of the theory are summarized below. Coupling between two modes is described by a coupling constant $\kappa(cm^{-1})$, which depends on the magnitude of the periodic structuring of the optical index and on the overlap integral to the electromagnetic field distributions of the two modes. $L_c = 1/\kappa$ is the coupling length: in other words, enough “time” is given for coupling to occur, provided that the medium size exceeds L_c . Coupling time $\tau_c = \frac{n}{c\kappa}$, where n is the “average” optical index of the medium. The PBG opened up by coupling between two modes (see section 1.3.2) is written:

$$PBG \approx \frac{4\pi}{\tau_c} \quad (11)$$

³ Note the availability of simulation tools, which make use in particular of the FDTD (Finite Difference Time Domain) method, which allows for the 3D simulation of finite size structures in the spatial, spectral and temporal domains. There is still a long way to go, however, before efficient design tools for microphotonic devices are available.

It can also be seen that, at the photonic band edges where the group velocity is null, the curvature α (or second derivative of the dispersion characteristics) is proportional to τ_c .

1.3.3.2. Lifetime of a Bloch mode

The concept of lifetime τ of a Bloch mode in a 1D structure is meaningless unless its size L is limited (in the absence of any other loss mechanism). This aspect has already been discussed in section 1.2.3: we have shown that the limited lifetime of the mode results in a spectral widening $\delta\omega = \frac{2\pi}{\tau}$; we have also shown that it is possible to relate $\delta\omega$ (by differentiating the dispersion characteristics) to the “de-localization” of the mode in the reciprocal space $\delta k = \frac{2\pi}{L}$, which results from its “localization” in real space (the mode is allowed to extend over L).

The differentiation of the dispersion characteristics around an operation point can be written:

$$\delta\omega = v_g \delta k + \frac{\alpha}{2} (\delta k)^2 + \frac{\beta}{6} (\delta k)^3 + \dots \quad (12)$$

It can be expressed in terms of the lifetime of the mode within the structure of limited size as below:

$$\frac{1}{\tau} = v_g \frac{1}{L} + \frac{\alpha}{4\pi} \left(\frac{2\pi}{L}\right)^2 + \frac{\beta}{12\pi} \left(\frac{2\pi}{L}\right)^3 + \dots \quad (13)$$

We find, as expected, $\tau = \frac{L}{v_g}$, in a homogeneous medium, where the group velocity v_g is independent of the wavelength (and coincides with the phase velocity). In a structured medium and, in particular, around an extreme of the dispersion characteristics where the group velocity of the mode, so called slow Bloch mode, vanishes, it is found (limiting the series to the second order expansion):

$$\tau = \frac{L^2}{\pi\alpha} \quad (14)$$

The lifetime of the slow Bloch mode increases as L^2 and is proportional to the inverse of the curvature around the extreme. Note that the smaller the curvature, or the stronger the coupling between optical modes giving rise to the extreme in the dispersion characteristics, the longer the lifetime of the resulting slow Bloch mode:

the curvature α at the extreme is the relevant parameter for the description of the slowing down of photons within the periodic structure.

1.3.3.3. Merit factor of a Bloch mode

The general definition of the merit factor of an optical mode (see section 1.2.3, equation (6)) results in the following relations:

$$F = \frac{c}{v_g} = n_g, \quad (15)$$

in linear regime, where n_g is called the group optical index, corresponding to the group velocity v_g :

$$F = \frac{Lc}{\pi\alpha}, \quad (16)$$

at an extreme of the dispersion characteristics where the curvature is α .

One therefore finds that the merit factor is independent of the length of the structure in linear regime, whereas it increases linearly with the length at the extreme, steeper as the curvature at the extreme is smaller. This manifestation of the lateral “confinement” of the mode (although de-localized) should be familiar to the reader: it was discussed in section 1.2.4, concerning the behavior of optical modes in a planar cavity around the extremes of the dispersion characteristics (for $k_{\parallel} = 0$: see footnote 2). Confinement is now achieved owing to the sole presence of periodic structuring, resulting in the existence of slow Bloch modes, enabling the build-up of electromagnetic energy in a confined space, over a long period of time: it manifests itself by a *resonance* in the spectral domain, arising from the presence of (slow Bloch) modes which are intrinsically de-localized, although efficiently confined in practice.

1.3.4. The distinctive features of photonic crystals

At the present stage and from the analysis in the previous section, although restricted to 1DPC, it is possible to derive the principal characteristics that make up the distinctive features of photonic crystals, in general.

Let us remind ourselves that photonic crystals are strongly corrugated periodic structures (large magnitude of the periodic modulation of the optical index). This results in a strong diffractive coupling rate between optical modes and by significant

disturbances of the dispersion characteristics as compared to a homogeneous medium. These disturbances manifest themselves by the presence of:

- large photonic band gaps (PBG);
- flat photonic band edge extremes (where the group velocity vanishes) with low curvature (second derivative) $\alpha \approx \frac{1}{PBG}$.

These are the basic ingredients which make photonic crystals the most appropriate candidates for the production of a wide variety of compact photonic structures.

“De-localized” slow Bloch modes, discussed in the previous section, which lend themselves to the production of compact resonant structures, are one example of that matter. Another example was provided by the compact and highly reflective Bragg mirror, formed with a small number of quarter-wavelength high index contrast pairs.

We now come to the use of 1DPC, operating in the field of PBGs, for the production of compact resonant structures based on “localized” optical modes.

1.3.5. Localized defect in a photonic band gap or optical microcavity

Ideal 1D periodic structures have been considered so far. If the “crystalline” periodicity is broken locally, this results in the formation of a “localized” defect which manifests itself as a “localized” resonant optical mode within the PBG, in quite the same way as a crystalline defect introduces localized defect states in the band gap of crystalline semiconductor material. According to optics terminology, the localized defect is called an optical microcavity where the corresponding localized optical modes are confined. A well-known example is the Bragg mirror, where the optical thickness of one of its pairs is changed with respect to the quarter-wavelength configuration, as illustrated in Figure 1.12.

Cavity modes are determined by the conditions for resonance, which can be expressed as:

$$\left(\frac{2m_1}{\lambda}\right) \times 2D + \Phi_1 + \Phi_2 = p2\pi, \quad (17)$$

where $\Phi_{1,2}$ are the phases of mirror reflectivity: at resonance, photons do not experience any phase difference (modulo 2π) after a round trip in the cavity. For Bragg mirrors whose configuration wavelength corresponds to the operation wavelength (around the center of the PBG), relation (17) is simply written as:

$$D = p \frac{\lambda}{2n_1} \tag{18}$$

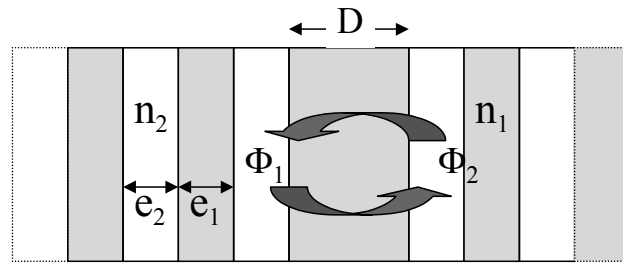


Figure 1.12. Optical microcavity formed between two Bragg reflectors

1.3.5.1. Donor and acceptor levels

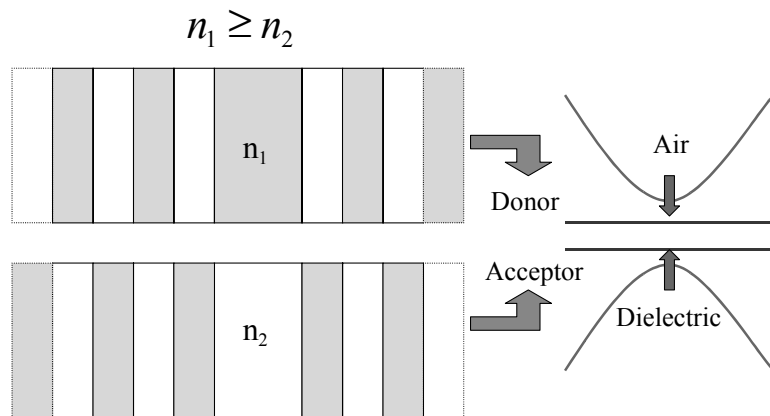


Figure 1.13. Donor or acceptor type localized state

A defect can be created, for example, by increasing the high index portion of a quarter-wavelength pair: this results in a shift in air band levels towards the PBG

and the introduction of so called donor type localized levels in the latter. When the low index portion of the pair is widened, the localized levels are acceptor-like, and originate from the dielectric band.

1.3.5.2. Properties of cavity modes in a 1DPC

A defect in a 1DPC is an object with 0 dimensionality in 1D space. Properties of localized optical modes in an 0D object have already been discussed in section 1.2.4. The spectral density of modes tends to infinity at resonance wavelengths; this is also true for the merit factor F , in the absence of any optical loss processes, which would limit the optical mode lifetime τ (which is also infinite in the absence of losses). This is not true in practice: for example, for a cavity formed between two Bragg reflectors with finite thickness, optical losses arise from the escape of photons across the mirrors whose reflectivity R is lower than 1. The lifetime of optical cavity modes and their merit factor can then be expressed as:

$$\tau \cong \frac{1}{1-R} \times \frac{nD}{c}, \quad (19)$$

$$F \cong \frac{n}{1-R},$$

where n is the optical index of the cavity material.

The density of modes is no more infinite at the resonance wavelength and the spectral response is widened as shown in Figure 1.14.

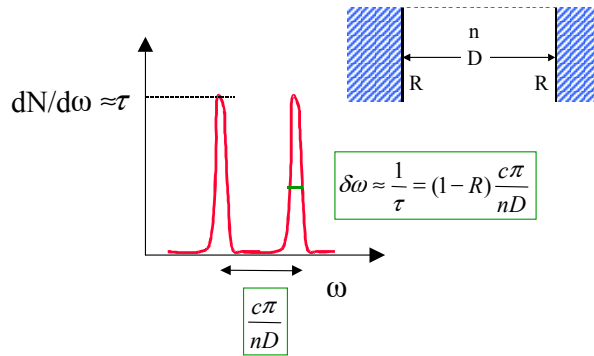


Figure 1.14. Optical mode density in a cavity formed between two reflectors

The average density of modes is $\frac{nD}{c\pi}$ (the inverse of the free spectral range between two successive cavity modes) and increases with cavity size (it is constant and equals $\frac{n}{c\pi}$, when expressed per length unit): the number of cavity modes increases therefore with size, in a given spectral range.

For $R = 0$, that is with no reflectors, optical mode density at resonance coincides with the average density of modes (which itself coincides with that of a homogeneous medium), and spectral widening corresponds precisely to the free spectral range between two cavity modes: we are back to the state continuum in 1D homogeneous free space.

1.3.5.3. Fabry-Pérot type optical filter

An optical cavity formed between two Bragg reflectors with finite thickness behaves like a wavelength selective filter. An incident plane wave is essentially reflected except for the resonant wavelength of the cavity, where it may couple with the cavity modes and be, at least in part, transmitted across the structure. If the latter is symmetrical (identical reflectors), the transmission can reach 100% at resonance wavelengths. The selectivity of the filter (spectral width of the transmission spectrum) is equal to the spectral widening $\delta\omega$, which is related to the finite lifetime of the cavity mode (see equation (19) and expression of $\delta\omega$, Figure 1.14). This type of device is usually called a Fabry-Pérot cavity filter. Filter selectivity is therefore controlled directly by the reflectivity of the Bragg mirrors (in the absence of any other source of optical losses). Wavelength tuning of the filter can be achieved simply by changing the optical thickness of the cavity (that is its physical thickness and/or its optical index). Use of photonic crystal-type Bragg reflectors, formed with high index contrast pairs, enables the production of strongly resonant, yet extremely compact, structures: a limited number of quarter-wavelength pairs is required to produce high reflectivity Bragg mirrors (SPI 98).

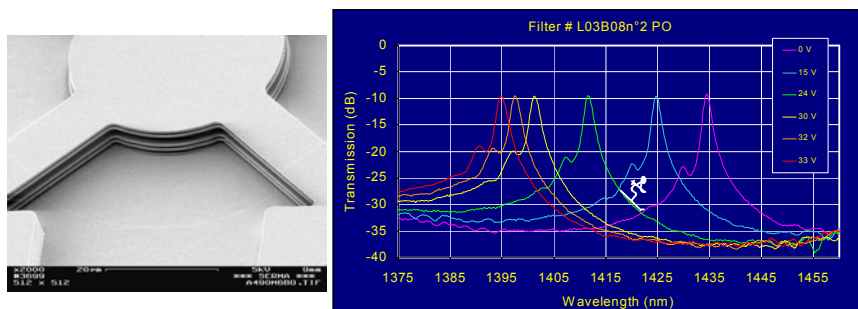


Figure 1.15. Micrograph and spectral response of a tunable Fabry-Pérot filter formed with high index contrast air-semiconductor pairs (Collaboration LEOM-ECL-CNRS/ATMEL)

Figure 1.15 shows an example of a Fabry-Pérot filter, formed with high index contrast air/semiconductor membrane pairs. This filter can be tuned by changing the thickness of the air cavity layer via electrostatic actuation. As to the selectivity of the filter, Bragg mirrors with only two quarter-wavelength pairs are sufficient to achieve a spectral bandwidth of around one nanometer.

1.3.6. 1D photonic crystal in a dielectric waveguide and waveguided Bloch modes

A 1D photonic crystal does not actually exist, in the same way that a 1D space does not exist. A closer representation of the real world would be to imagine, in 3D real space, a 1D structuring, where one would consider the sole plane waves having a propagation vector along the direction normal to the iso-optical index planes. This implies an infinite structuring depth, which is not realistic either. An additional step towards reality consists of considering a 1D structuring of a 2D object in real 3D space. The planar dielectric waveguide, where photons are so called “index guided”, already presented in section 1.2.4, is a well-known example of a 2D object. If we now admit, as a final step in non-reality, that the lateral size of the 1D structuring is infinite and that the only considered propagation is parallel to the periodic index gradient, it is possible to represent this situation with a 1D propagation in a 2D world. The dispersion characteristics $\omega(k_{\parallel})$ of optical modes in a planar waveguide free of structuring were presented in Figure 1.6. In the presence of a 1D periodic structuring, dispersion characteristics are deeply modified, as a result of a variety of coupling processes which affect the propagation of optical modes in the dielectric waveguide. The corresponding eigen waveguided modes are also called Bloch modes, and their symmetry properties along the direction of propagation are similar to those presented in the case of an ideal 1DPC (see section 1.3.1).

1.3.6.1. Various diffractive coupling processes between optical modes

We observe, first, diffractive coupling between propagating and counter-propagating waves, which may now communicate as described in section 1.3.2 in the case of an ideal 1DPC, and the resulting effects on dispersion characteristics (photonic band gap and band edge extrema, etc.). A second essential consequence of diffractive processes lies in the new channels opened up to waveguided modes for communication with radiated modes in 2D free space: this may occur as soon as the discrete translation of the dispersion characteristics induced by diffraction can shift them, at least partially, above the light-line. This can be represented by a simple geometrical operation consisting of the successive folding of dispersion characteristics around the vertical axis of equation $k_{\parallel} = \pm \frac{\pi}{a}$ and, consequently, gathering them within the first Brillouin zone (see Figure 1.16).

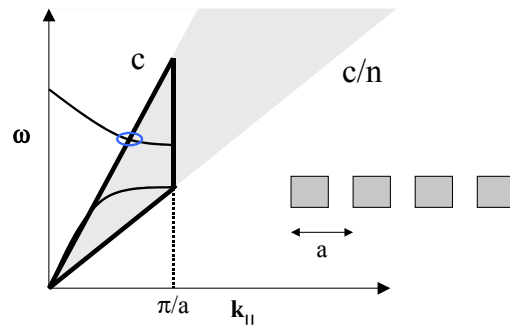


Figure 1.16. 1D photonic crystal in a dielectric waveguide: coupling processes between propagating and counter-propagating waves, and between waveguided and radiated modes

In these conditions, loss-less and pure waveguided modes correspond only to the portions of the dispersion characteristics lying within the triangular area (whose three sides are drawn in bold in Figure 1.16). For the other portions located above the light-line, the waveguided modes are “lossy”, which means that their lifetime in the waveguided state is finite: they will end up lost in the radiation continuum of the free 2D space. Note that the room available for $(\omega, k_{||})$ couples corresponding to pure waveguided modes is much larger as the effective index of the guide is higher, with respect to that of free space.

Finally, there exists a further diffractive coupling process which allows for communication between different order waveguided modes corresponding to different dispersion characteristics. These waveguided modes would otherwise ignore each other in a non-structured waveguide, since they represent eigen orthogonal solutions of Maxwell equations (applied to the uniform non-periodic waveguide). Two conditions should be met in order for the coupling to occur. First, the diffraction condition must be satisfied, that is to say that, following the translation of the relevant dispersion characteristics, there exists a crossing point, which determines the couple $(\omega, k_{||})$ where the coupling can be achieved (Figure 1.17). Second, symmetry conditions have to be met, in such a way that the overlap integral to the electromagnetic distributions of the two modes, weighted by the spatial distribution of the periodic index, is not zero. For example, if the optical index vertical distribution is even, then the sole modes with identical (even or odd) vertical symmetry will be able to couple each other (even modes in the example given in Figure 1.17). These mode coupling processes result in the opening up of new PBGs with new photonic band edge extrema, which do not necessarily coincide with the Brillouin zone boundaries, that is in the existence of slow Bloch modes at

extrema of the dispersion characteristics which do not necessarily coincide with high symmetry points ($k_{||} \neq \pm p \frac{\pi}{a}$).

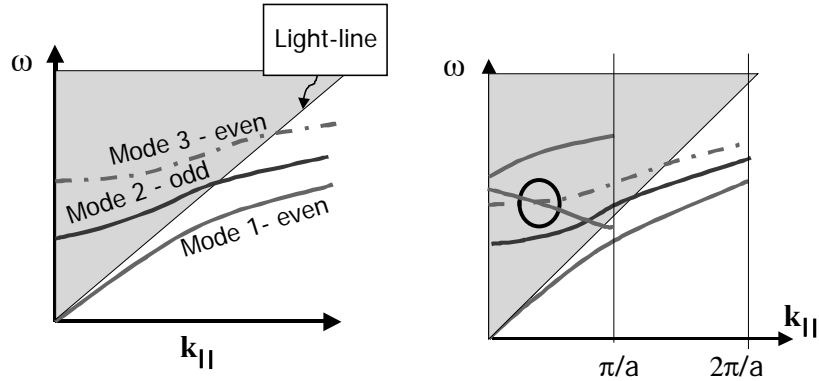


Figure 1.17. Coupling between waveguided modes of different orders (here with the same even symmetry: the only crossing point where coupling is possible is shown in the circle)

1.3.6.2. Determination of the dispersion characteristics of waveguided Bloch modes

The reader will have concluded that the dispersion characteristics or band structure of a 1DPC formed in a planar waveguide are relatively complex, given that, in addition, one obtains different characteristics for the two TE (in plane electric field and transverse magnetic field) and TM (vice versa) polarizations.

Different methods of band structure calculation are available. A simple approach, called the effective index method, provides satisfactory results: it consists of the use of an effective index for each mode (evaluated in the non-structured waveguide) and in the resolution of Maxwell equations in the periodically structured space, with the appropriate dimension (1D, for example, in the present case).

One may also consider a more rigorous method, the so called plane-wave method with “supercell”, which is used frequently (VAS 02): this consists of the resolution of Maxwell equations in a space (here 2D), periodically paved with elementary cells of rectangular symmetry, which include the waveguide and a portion of the surrounding space: the period along the direction of propagation coincides with that of the PC structuring, whereas it is large enough in the normal direction to consider that the electromagnetic field is negligible at the boundary of the supercell. This method is well suited to describing waveguided modes below the light-line.

1.3.6.3. Lifetime and merit factor of waveguided Bloch modes: radiation optical losses

The dynamics of guided Bloch modes *below the light-line* are very similar to those described in section 1.3.3 for the simple case of an ideal 1DPC: they can also be described using the coupled mode theory, and using dispersion characteristics. One may, in the same way, differentiate the dispersion characteristics in order to determine the mode lifetime and their merit factor as well, in a structure with a limited size L , thus ending up with relations (13) – (16): we remember, therefore, that their lifetime (their “time of flight”) within the structure is an increasing function of L (increases like L in linear regions of the dispersion characteristics, like L^2 at extrema with finite curvature).

As to Bloch modes which may couple to the radiated continuum, that is to say whose dispersion characteristics can be “folded” above the light-line by diffraction processes, their lifetime will be necessarily limited to a maximum value, which is their coupling time constant τ_c with radiated modes. The lifetime of Bloch modes “above the light-line” can then be written:

$$\frac{1}{\tau} = \frac{1}{\tau_g} + \frac{1}{\tau_c}, \quad (20)$$

where $\frac{1}{\tau_g}$ is given by the general relation (13), which expresses the lifetime in absence of coupling with the radiated continuum. We emphasize here the *radiation optical losses* that may significantly affect PC-based devices for integrated optics, which are meant to operate in the waveguided regime. Another way of formalizing these effects is to define the minimum distance L_c which can be explored by photons before being lost as a result of radiation losses. One find simply $L_c = v_g \tau_c$ in linear regions of the dispersion characteristics and $L_c = \sqrt{\pi \alpha \tau_c}$ at extrema, in the present case of a 1DPC formed in a planar waveguide (see equation (13)). It must be pointed out that around an extremum where the Bloch modes are slowed down, this distance can be strongly reduced in a PC, where the curvature α at an extremum can be made very weak, as discussed in section 1.3.4. This remark is of major importance, if one considers the reverse situation where one couples radiated modes to waveguided modes, that is to say when one injects photons in a waveguide from free space via diffractive coupling: it is clear that, with a PC, this function can be achieved in a very compact way, unlike with traditional diffraction gratings; we will return to this point in more detail later in the chapter (section 1.7.1).

1.3.6.4. Localized defect or optical microcavity

As in the case of an ideal 1DPC, the introduction of a defect in a 1DPC formed in a planar dielectric waveguide can result in an optical microcavity: it consists here of an object with 0 dimensionality, formed in a 1D structure (waveguided 1DPC), considered itself in a 2D space. A schematic view of the microcavity is shown in Figure 1.18, together with the corresponding dispersion characteristics: the latter are simply reduced to a horizontal straight line, which corresponds to the resonance frequency of the cavity. This results from the fact that the defect, being localized in real space, is de-localized in the k_{\parallel} vector reciprocal space and that all k_{\parallel} components are available for the cavity modes: a localized defect can therefore potentially couple with any other mode and, in particular, with the modes of the radiation continuum, using the k_{\parallel} components corresponding to points of dispersion characteristics located above the light-line (Figure 1.18).

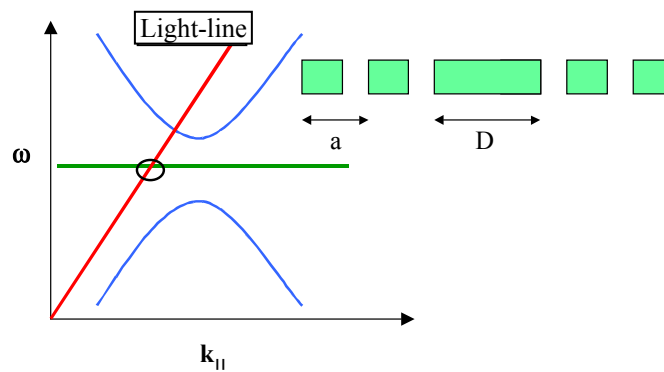


Figure 1.18. Dispersion characteristics of a localized defect or of an optical cavity: there always exist components of the k_{\parallel} vector located above the light-line

The coupling rate between the defect and another mode depends naturally on the distribution function of the k_{\parallel} Fourier components; this is true for coupling with radiated modes, which is determined by the proportion of the Fourier components located above the light-line and defining the so called radiation diagram of the defect. It is possible, in principle, to design a defect in such a way as to control the

radiation diagram⁴ in order, for example, to minimize the distribution of k_{\parallel} vectors above the light-line and, therefore, to reduce optical losses in free space.

Coupling of the cavity modes with the radiation continuum tends to reduce their lifetime, which results in the spectral widening of their resonance. Let us return to the simple case of the Fabry-Pérot cavity formed between two Bragg reflectors of limited size (which is equivalent to creating a defect in a 1DPC with limited extension) – but this time in the waveguided configuration (Figure 1.19). The lifetime τ of cavity modes is not only limited by the escape rate $\frac{1}{\tau_R}$ of photons across the Bragg reflectors (derivable from relation (19)), but also by the coupling rate $\frac{1}{\tau_c}$ with the radiated modes; it is therefore given by the relation:

$$\frac{1}{\tau} = (1 - R) \frac{c}{nD} + \frac{1}{\tau_c} \quad (21)$$



Figure 1.19. Microcavity or defect in a 1DPC, formed in a dielectric waveguide

The structure described schematically in Figure 1.19 may also be used as an optical filter in waveguided configuration. The art of the designer lies in his ability to propose configurations where optical losses are kept to a minimum, resulting in strongly resonant microcavities, useful for the production of very selective filters, as well as for the control of spontaneous emission in an active medium. We will return to this point in the section devoted to 2DPC (section 1.6.2).

⁴ Remember that the distribution of wave-vectors and the spatial distribution of the electromagnetic field relate to each other through a Fourier transformation.

1.3.7. Epilogue

We have reached the end of our discussion of the basics of one-dimensional photonic crystals. The principal concepts which hold for photonic crystals in general have been presented. The extra ingredient brought about by photonic crystals with a dimension larger than one lies essentially in the extra control of light which they may provide in terms of *angular resolution*.

The illustration given in Figure 1.20 provides a classic example of the limitations of 1D photonic crystals with respect to angular resolution: a Bragg mirror does not usually have the capacity to fully reflect the light in a given wavelength spectral range for any angle of incidence. The rest of this chapter is devoted to photonic crystals with dimensions larger than one, principally 2DPC (sections 1.5, 1.6 and 1.7), after a very brief trip into the world of 3DPC (section 1.4).

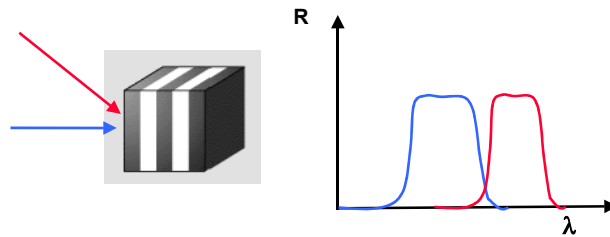


Figure 1.20. A limitation of Bragg mirrors: their transfer function depends on the angle of incidence, which usually prevents the formation of a PBG for all propagation directions

1.4. 3D photonic crystals

1.4.1. From dream ...

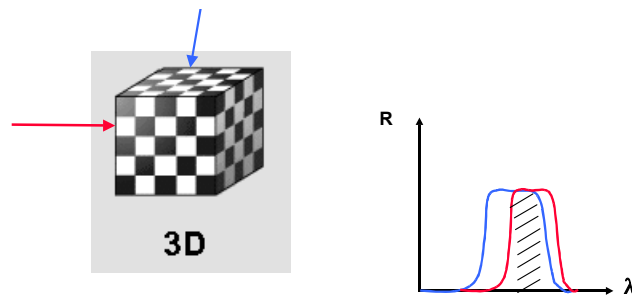


Figure 1.21. A 3D photonic crystal may behave as an omni-directional perfect reflector in a finite spectral bandwidth. As shown in the figure, there exists a range of wavelengths (cross-hatched area) where reflectivity is uniform, for several directions of propagation

A 3D photonic crystal's optical index shows high contrast periodic modulation along the three dimensions of space. The main consequence lies in the new opportunity given to the eigenstates of three dimensional space to experience strong mutual coupling via diffraction processes, whereas the plane waves, eigenmodes of the homogeneous space with continuous translational symmetry, ignore each other. Here we recall all the concepts and specifications of 1DPC analyzed in detail in section 1.3, but this time along the three dimensions of real space. As a celebrated example (this is the usual way in which 3DPC is introduced, though it is very restrictive), a 3D PC may show a full PBG for all directions of space, which means that it behaves as a perfect reflector for all angles of incidence, as illustrated in Figure 1.21.

The concept of 3DPC was introduced in 1987 by E. Yablonovitch (YAB 87) and demonstrated experimentally for the first time in the field of microwaves in a photonic crystal called "Yablonovite" (YAB 91). The initial motivation was to gain full control of the spontaneous emission of an active emitting material: for example it can be fully inhibited if the active material is inserted in a photonic crystal showing a regime of PBG in a spectral range larger than the emission spectrum of the material in homogeneous vacuum; the active material may also be inserted in an optical cavity resulting from the formation of a defect in the 3DPC (under the same principle as in the case of a 1DPC), and be left the limited choice of a few well controlled (numerical and spectral characteristics) cavity modes to take care of radiated recombination processes.

In the field of Micro-nanophotonics, the quest for the "grail", motivated by new exciting developments in the fields of Quantum Electrodynamics and of Quantum Information (very low threshold laser micro-sources, strong coupling: see Chapter 4), consists of inserting "a quantum-box" type nano-emitter in a "photonic box" or microcavity, which would accept only one optical mode in the emission spectrum of the emitter, with a perfect spectral overlap.

3DPC are potentially the best candidates for those purposes. Other brilliant applications can be contemplated, in principle, such as 3D loss-less perfect guiding of photons, by opening up a corridor across a forbidden zone, etc.

1.4.2. ... to reality

The fabrication technology of 3DPC in the optical domain is extremely complex. The only examples of mass production of such structures can be found in nature, owing to the miracles (or to the 500 millions years of research) of natural morphogenesis. Butterfly wings provide a brilliant example of nature's

achievements in this respect: their seductive colors are produced by the interaction between ambient light and their natural micro-structuring (Figure 1.22).

A great deal of technological research has been devoted to the production of artificial 3DPC. Figure 1.23 shows a few examples of recent achievements (wood-pile structure, inverse opal, 3D hole matrix similar to the famous “Yablonovite” etc. – see for example (CUI 99; LOU 05) and references therein).

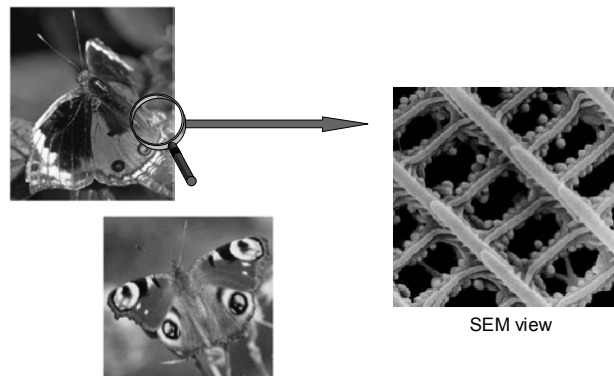


Figure 1.22. *An example of a 3D photonic structure: butterfly wings*

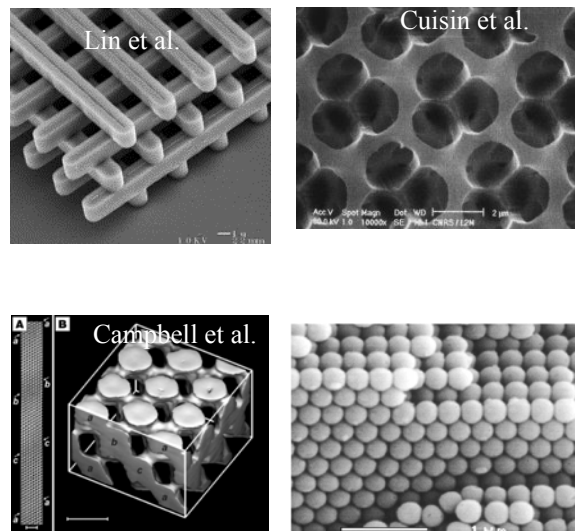


Figure 1.23. *Examples of artificial 3DPC*

However, 3DPC should be considered as laboratory objects; their transformation into high performance photonic devices is still some way ahead. As a consequence, most R&D efforts have concentrated on 2DPC, which is far more promising in terms of practical applications, at least in the short/medium range.

1.5. 2D photonic crystals: the basics

A two-dimensional photonic crystal is a virtual two-dimensional medium whose optical index is periodically modulated: such a medium should not be confused with an object with a dimensionality reduced to 2, in a real world of dimension 3, as described in section 1.2.4.

This imaginary situation could be illustrated approximately, for example, by a dielectric material dug with a periodic lattice containing deep and parallel cylindrical holes (the depth should be much larger than the lattice constant⁵), the wave propagation being considered solely along directions normal to the holes.

A cross-section of such a periodic lattice, with discrete triangular transitional symmetry, is shown in Figure 1.24.

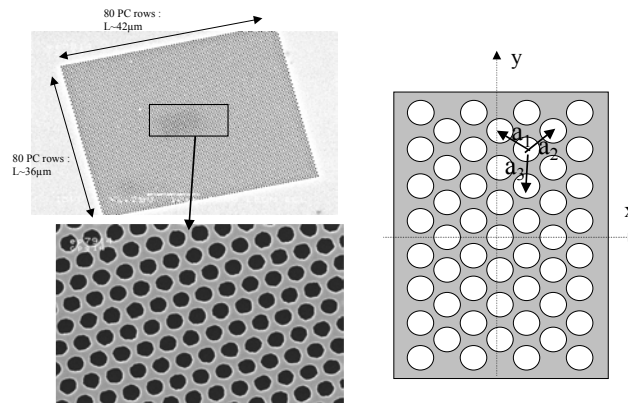


Figure 1.24. A cross-section of a 2DPC with triangular symmetry

⁵ This configuration has been realized experimentally in the so called macro-porous silicon approach (GRU 96; ROW 99).

For the rest of this chapter we will use the triangular lattice case, which is widely used (though not exclusively so) in practice as an illustrative example.

Two of the three vectors $a_j (j=1,2,3)$ in Figure 1.24 allow for a complete description of symmetry properties of the 2DPC in real space, and in particular of the permittivity of the periodic medium:

$$\varepsilon(r + a_j) = \varepsilon(r) \quad (22)$$

1.5.1. Conceptual tools: Bloch modes, direct and reciprocal lattices, dispersion curves and surfaces

In the following paragraphs we will use the conceptual tools we used for the analysis of 1DPC, now applied to 2DPC.

1.5.1.1. Bloch modes

Eigenmodes or solutions of Maxwell equations in a two dimensional periodic medium are also Bloch modes, which possess the same translational discrete periodic symmetry properties. Bloch theorem applies in the same way and the electromagnetic field is written:

$$\begin{aligned} H_k(r) &= e^{i(k \cdot r)} u_k(r) \\ u_k(r) &= u_k(r + a_j) \end{aligned} \quad \text{with,} \quad (23)$$

$u_k(r)$ can therefore be written according to a Fourier expansion:

$$u_k(r) = \sum_{m,j} c_{k,m,j} e^{i m b_j \cdot r} \quad (24)$$

where b_j is a base vector of the reciprocal lattice, described in detail in the following paragraphs, with $|b_j| = \frac{2\pi}{a} \times \frac{2}{\sqrt{3}} \approx \frac{2\pi}{a} \times 1.15$ (a is the modulus of the base vector of the direct lattice).

1.5.1.2. Direct and reciprocal lattices

Figure 1.25 shows again the triangular periodic lattice in real space and its reciprocal representation in k vector space. ΓM and ΓK stand for the two principal so called high symmetry directions of the lattice.

Any vector of the reciprocal space can be projected on the base vectors and expressed as $\sum_{m_j} m_j b_j$, where m_j is an integer.

We recall briefly the essential properties of Bloch modes, already discussed for 1DPC, but extended this time to the case of a 2DPC:

- Two Bloch modes whose k vectors differ by $\sum_{m_j} m_j b_j$ are equivalent: this is

the mathematical translation of two dimensional diffraction processes.

- Fourier components (equation (24)) include the physical reality of diffraction processes induced by the periodic structure of the photonic crystal. They also contain information about the possibility of diffractive coupling with other modes as well as about the radiating characteristics of the mode, in case of coupling with the “radiated continuum” (which we will encounter again in a real 2DPC, formed in a planar dielectric waveguide, in section 1.5.2).

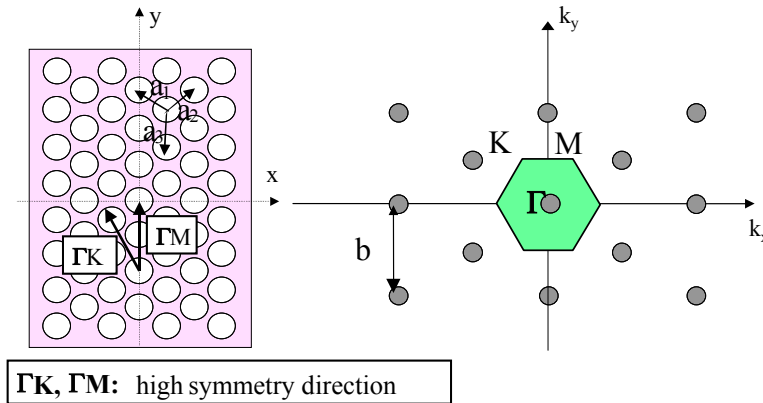


Figure 1.25. Direct and reciprocal triangular lattices. The two so called ΓM and ΓK high symmetry directions of the crystal are shown. The first Brillouin zone is included in the hexagon drawn in the reciprocal lattice. b is the module of the base vector of the reciprocal lattice

1.5.1.3. Dispersion curves and surfaces

It is appropriate here to speak in terms of dispersion surfaces $\omega(k) = \omega(k_x, k_y)$, real space being two-dimensional. In a non-structured homogeneous space, the dispersion surface is simply a conical surface (Figure 1.26), whose equation can be written:

$$\omega = c\sqrt{k_x^2 + k_y^2}, \quad (25)$$

where c is the light velocity in the homogeneous medium.

Diffraction processes induced by high index contrast 2D periodic structuring affect the dispersion surfaces significantly, in the same way as in the case of 1DPC: one also observes the formation of photonic band gaps, whose related band edges coincide with low curvature extrema of surface dispersion characteristics. These characteristics are also the result of diffractive coupling processes between optical modes, induced by periodic structuring. Dispersion surfaces (or photonic band structures) are periodic and can be fully described (folded) within the so called first Brillouin zone according to Solid State Physics terminology, corresponding to the dark gray hexagonal surface of Figure 1.25.

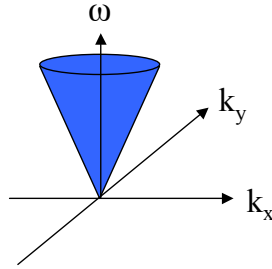


Figure 1.26. Conical surface dispersion of a two-dimensional homogenous medium

There exist various simplified representations of dispersion surfaces, whose full 3D visualization does not allow for simple extraction of essential characteristics.

One may plot, for example, iso-frequency curves (which are plain circles with $\frac{\omega}{c}$ radius in a homogeneous medium), which are the cross-section of the dispersion surface with planes of a given ω coordinate. Iso-frequency curves are no longer isotropic, as in the homogeneous space, and are subject to symmetry rules dictated by the periodic lattice, in particular along the high symmetry directions. The group velocity is now written:

$$v_g = \nabla_k \omega, \quad (26)$$

and its direction, which coincides with the direction of energy propagation, is normal to the iso-frequency curves. Thus, in general, phase velocity $v_\varphi = \left(\frac{\omega}{|k|^2} \right) k$ and group velocity do not travel in the same direction. We will comment below on the consequences, in terms of potential applications, which may result from these non-conventional properties, especially around the extrema of the dispersion characteristics.

Another widely used representation scheme (Figure 1.27) consists of plotting the dispersion characteristics along a given propagation direction of Bloch modes, obtained from the cross-section of dispersion surfaces with the plane defined by the frequency axis and the direction of propagation. This scheme is usually applied, in a concentrated yet partial manner, by restricting the propagation directions to the sole high symmetry directions ΓM and ΓK (JOA 95)⁶; for other directions (between M and K), the diagram includes only the points corresponding to the band edges or, in other words, corresponding to the Brillouin zone boundary (where optical waves propagating in opposite directions can interfere via diffractive coupling). Along high symmetry directions band edges show “full” extrema. This representation scheme is illustrated in Figure 1.27, where a full photonic band gap can be observed (for the TE polarization, gray area), at the first Brillouin zone boundary.

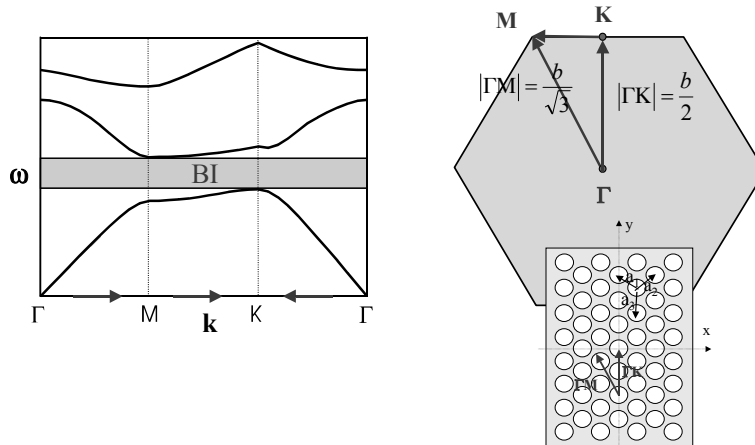


Figure 1.27. Partial representation of the dispersion characteristics of a 2DPC. The modules of the K vectors ($|\Gamma M|$ and $|\Gamma K|$) are given at the first Brillouin zone boundary for the high symmetry directions (b is the module of the base vector of the reciprocal space)

⁶ Note that this restriction may turn to an insufficient representation, especially in case of complex basic elementary structures.

The photonic band gap increases with the coupling rate between optical modes induced by the periodic structuring and, therefore, with the magnitude of its modulation, as already discussed in the case of 1DPC (section 1.3.2). In the case of a periodic array of holes in a dielectric matrix, the coupling rate increases with the “air” filling factor f (to the extent that the holes are fully defined and do not join); this is also true for the PBG as illustrated in Figure 1.28, where the band edge curves are shown as a function of f (the PBG area is white). Note the use of normalized coordinates $\frac{a}{\lambda}$, where a is the lattice parameter of the triangular lattice, for the frequency, or energy, axis (JOA 95).

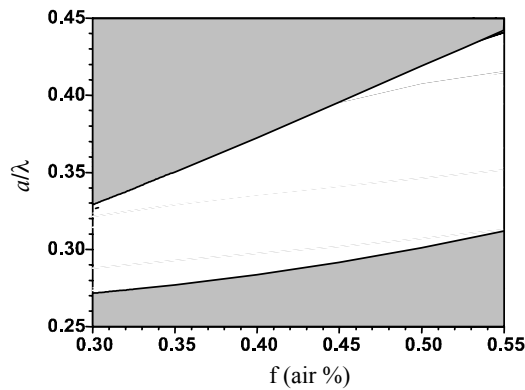


Figure 1.28. Photonic band gap as a function of the hole filling factor (from Le Vassor D’Yerville, GES, Montpellier)

1.5.2. 2D photonic crystal in a planar dielectric waveguide

Let us recall that an ideal 2DPC (two-dimensional object in a two-dimensional world) formally has no real existence and that a representation closer to reality would be to imagine, in a real 3D space, a 2D structuring of the latter, where the only directions of propagation to be considered would be along the index “gradient vector”. This implies an “infinite” shape ratio of the structuring (holes), which is not realistic either. A last step towards reality consists of considering a 2D structuring of a 2D object in 3D real space (Figure 1.29): the planar dielectric waveguide where photons are “index guided”, that is to say vertically confined by the vertical profile of the optical index, already discussed in section 1.2.4 and exploited with 1DPC (section 1.3.6), is the well known example of a 2D object, which we will again examine below.

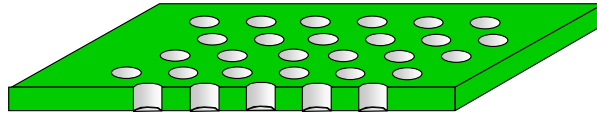


Figure 1.29. Schematic representation of a 2DPC formed in a planar dielectric waveguide

All the concepts presented in the case of 1DPC formed in a planar dielectric waveguide essentially apply to 2DPC. One finds again (and again) diffractive coupling processes and their great impact on dispersion characteristics. Figure 1.30 shows an example of dispersion characteristics (the coordinates are normalized) of a triangular 2DPC formed in dielectric membrane similar to that shown in Figure 1.29.

The light-line discussed in detail in the case of 1DPC is now a light surface or a light cone which meets the equation $\omega = c\sqrt{k_x^2 + k_y^2}$, where c is the light velocity in the surrounding homogeneous medium. In the partial representation of surface dispersions given in Figure 1.30, the light cone is also partially represented by the line which separates the radiated continuum area (gray) from the area which corresponds to loss-less Bloch modes (white). The dispersion characteristics of lossy Bloch modes (which may couple with radiated modes) are not plotted.

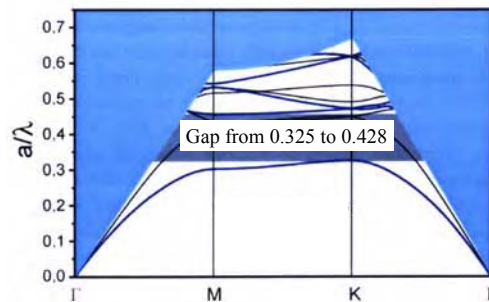


Figure 1.30. Dispersion characteristics of triangular 2DPC formed in a planar dielectric waveguide. The curves corresponding to waveguided Bloch modes below the light cone are solely represented (the area corresponding to the radiated continuum is shown in gray)

Again we encounter the concepts of lifetime and merit factor of Bloch modes and the impact of radiation losses on the latter, already discussed in section 1.3.6⁷.

⁷ The concept of lateral extension of the Bloch mode is now translated in terms of the surface of the Bloch mode. For example, if one considers an operation point at an extremum of the

In summary, all the distinctive features and virtues of photonic crystals, already discussed in the simpler context of 1DPC and allowing for a fine engineering of optical modes, that is for their slowing down, their trapping and their spectral selection, using compact structures, may apply to 2DPC. The extra “dimension” brought by 2DPC is, however, essential: its importance lies in the considerable increase in degrees of freedom offered in terms of spatial and angular resolutions.

For example, the shape of defects which can be introduced in the 2D lattice can be changed in an “infinite” number of ways: we will return to this particular aspect in the sections devoted to the building blocks of integrated photonics. Angular resolution is also a characteristic which becomes a virtue in 2DPC, opening the way to a wide range of applications, in connection for example with their non-conventional properties (dispersion, refraction), which manifest themselves at extremes of the dispersion characteristics (see for example (GRA 00)). This latter aspect is illustrated below, after a brief description of the so called super-prism effect.

1.5.2.1. *An example of the potential of 2DPC in terms of angular resolution: the super-prism effect*

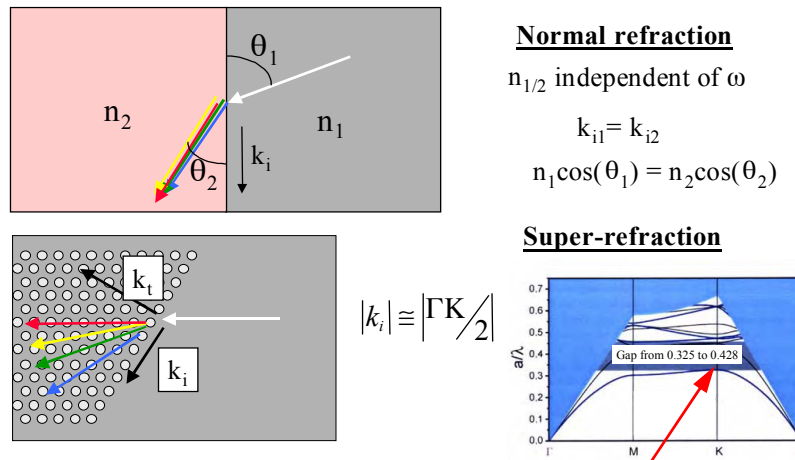


Figure 1.31. Normal refraction and super-refraction

dispersion characteristics, where the curvature is α and assumed isotropic, it can be shown easily that the maximum surface attainable by the corresponding “slow” Bloch mode is written $S_{BM} \approx \alpha \tau_c$, where $\frac{1}{\tau_c}$ is the radiation loss ratio.

“Normal” refraction, described in section 1.2.4, manifests itself by a deviation in the direction of propagation of a plane wave, when crossing the interface plane between two media with different optical indices $n_{1,2}$: this deviation is dictated by the law of Descartes, which simply expresses the conservation of the component of the propagation vector parallel to the interface plane. As a result, the angle of incidence θ_1 of the wave originating from medium 1 is related to the angle of transmission θ_2 in medium 2 through the relation given in Figure 1.31. If the index of refraction $n_{1,2}$ of both media are weakly dependent on the frequency (weakly dispersive media), then the deviation angle $\theta_1 - \theta_2$ is also weakly dependent on the frequency: the multicolor incident beam (white arrow) is only slightly dispersed in medium 2.

If medium 2 is a 2DPC, a super-refraction or super-prism effect may manifest itself, in terms of a strong angular dispersion of the multicolor incident beam impinging onto the photonic crystal.

This effect occurs when the “targeted” point of the dispersion characteristics of the 2DPC coincides with an extreme, for example the K point of the high symmetry direction ΓK , at the first Brillouin zone boundary, shown by the arrow in Figure 1.31. All that remains to be done is to adjust, on the one hand, the central frequency of the incident beam to that of the K point and, in addition, its direction in such a way as to make the projection of the incident wave-vector along the interface direction (here, the ΓK direction of the 2D PC) coincide with that of the ΓK vector (which corresponds to the retained direction of propagation in the 2DPC); in the case illustrated in Figure 1.31, this choice leads to $|k_x| \equiv \left| \frac{\Gamma K}{2} \right|$. The close proximity of the extreme results in a strong variation rate of the wave-vector in the photonic crystal as a function of frequency, and, therefore, in a strong dispersion of its propagation direction, the module of its projection being set. This phenomenon may be used for an efficient spatial separation of the different wavelength components of the multicolor incoming beam.

1.5.2.2. *Strategies for vertical confinement in 2DPC waveguided configurations*

Two approaches are used to ensure the guiding or vertical confinement of photons. In the so called “substrate” approach, vertical confinement is “weak”, which means that the vertical structuring of the optical index is achieved by a low index contrast between the dielectric cladding and core layers. Typically the core guiding layer is a semiconductor layer (through which the 2DPC is etched), epitaxied onto a semiconductor substrate, with a slightly lower optical index. A semiconductor cladding or barrier layer (with a slightly weaker optical index than the substrate) may be inserted in between for a fine adjustment of the vertical

electromagnetic distribution. This is the usual configuration for classical integrated optoelectronics based on III–V compound semiconductors. The substrate approach is therefore fully compatible with the classical technology currently in use. It enables us to take advantage of the well controlled coupling schemes between the devices and input-output optical fibers, owing to the relatively comfortable thickness (around 1–2 μm , for monomode operation in the 1.5 μm wavelength range) of the guiding or vertical confinement zone. There are drawbacks to this approach, however: it requires us first to control the fabrication of the holes of the 2DPC with a very large shape ratio; the depth of the holes must indeed exceed significantly the thickness of the guiding zone in such a way as to minimize optical losses in the semiconducting substrate (LAL 01); in addition, the large index of the cladding substrate results in a light line with a rather weak slope (like the inverse of the optical index), which leaves very little room for the pure loss-less waveguided modes, which are not allowed to couple with radiated modes below the light-line. In the so called “membrane” approach, vertical confinement is strong: guiding of light is achieved in a high index semiconductor membrane surrounded by low index cladding or barrier layers (for example an insulator such as silica, or simply air). The virtues and drawbacks of the substrate approach become precisely the drawbacks and virtues of the membrane approach: in monomode operating conditions the membrane is very thin – around a fraction of a μm ; the result of this is that low loss coupling schemes with an optical fiber are not easily achievable; however, the positive aspect of this lies in the relaxed technological constraints for the fabrication of the 2DPC (holes with an approximately uniform shape ratio). In addition, one may rely on a “reservoir” of waveguided modes below the light-line that is far more comfortable than with the substrate approach. In addition, strong vertical confinement, leading to a reduced volume of modes, results in a substantial increase in their merit factor. But the essential asset of the membrane approach will be revealed fully in section 1.7, where 2.5D Microphotonics will be briefly discussed: its rationale lies in particular in the “harmony” that is clearly apparent between the lateral structuring (2D PC) and the vertical structuring in terms of optical index contrasts. We will see that this particular feature enables us to contemplate with ease coupling between waveguided modes and radiated modes, which is otherwise considered to be a problem. The membrane approach, in this respect, enables tight control of this coupling and its full exploitation, thus opening the way to a considerable widening of the functionality provided by 2DPC, no more restricted to 2D operations but, instead, freed to the third dimension of space.

In the rest of this chapter we will concentrate on the membrane approach, which lends itself to more accessible optical objects from the conceptual point of view. A schematic view of basic building blocks for the membrane approach is shown in Figure 1.32.

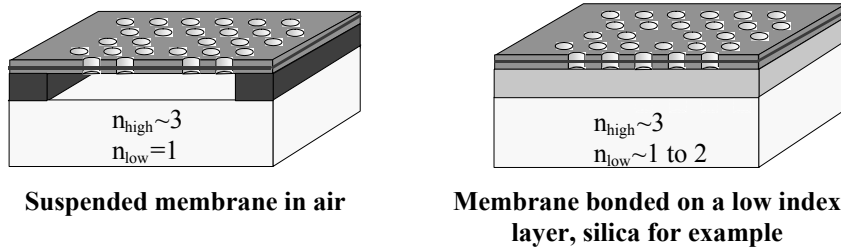


Figure 1.32. *The basic building blocks of the membrane approach*

The membrane including the 2DPC may be suspended in air: this is the “ideal” situation from the basic study point of view. For practical applications, where the thermal budget should be considered carefully, bonding of the membrane on a low index substrate (silica for example) is to be applied.

In the latter situation, advantage is also taken of improved mechanical stability as well as easier technological conditions (for the electrical contacting of the devices, for example). These two situations will be considered in the following sections.

1.6. 2D photonic crystals: basic building blocks for planar integrated photonics

1.6.1. *Fabrication: a planar technological approach*

An essential advantage of photonic integrated circuits based on 2DPC lies in their fabrication procedure which fits with the *planar technological approach*, familiar in the world of silicon microelectronics. Without sacrificing their generality, results presented as illustrations in the following sections concern essentially the cases of InP membranes either suspended in air or bonded onto silica on silicon substrate.

This latter technological approach opens up promising prospects for heterogeneous integration of optoelectronics devices based on III–V compound semiconductors with silicon microelectronic circuits. The devices are designed for operation wavelengths of InP and related materials, that is in the 1.5 μ m range.

1.6.1.1. *2DPC formed in an InP membrane suspended in air*

The heterostructure to be suspended is epitaxied on a semi-insulating InP substrate. It comprises a “guiding” InP layer with half-wavelength optical thickness (around 250nm) and may include active layers for emission or detection (for

example InAsP quantum wells or InAs based quantum box layers), located at mid-height in the InP layer. The InP layer is formed on an InGaAs sacrificial layer, which is eliminated in order to suspend the former, leaving a quarter-wavelength air gap: the elimination of the sacrificial layer is achieved by applying a wet etch surface micromachining procedure. The thicknesses of the sacrificial layer and guiding layer are chosen so as to maximize the coupling of the active layer with fundamental TE waveguided mode (monomode operation) and to inhibit the direct coupling to radiated modes. Heterostructures with quantum box layers provide a variety of interesting features, especially a weak absorption of the guided light together with a wide emission spectral range at room temperature (LET 01): these characteristics allow for the exploration of the modal properties of 2DPC in a wide spectral range (1,250–1,650nm).

The photonic crystal is fabricated using electron beam lithography, whose technological steps are described in detail in Pottier *et al.* 1999. The lattice parameter of the triangular 2DPC is about 500nm, and the filling factor of the holes ranges from 0.35 to 0.5.

1.6.1.2. 2DPC formed in an InP membrane bonded onto silica on silicon by molecular bonding

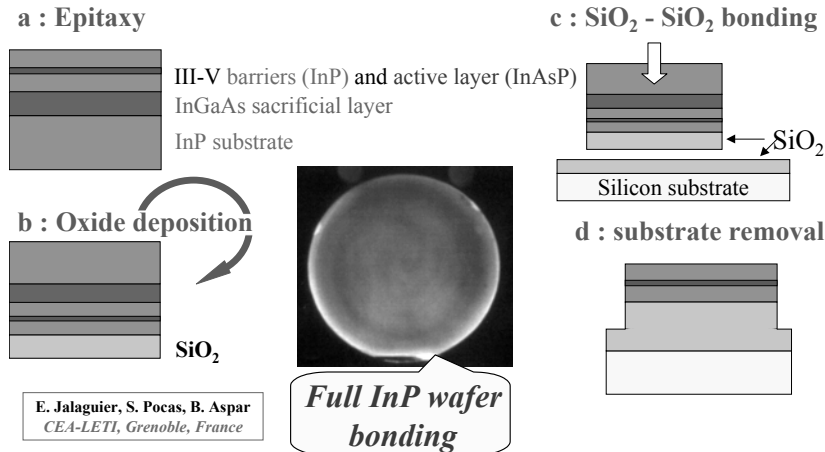


Figure 1.33. Technological steps in the molecular bonding procedure

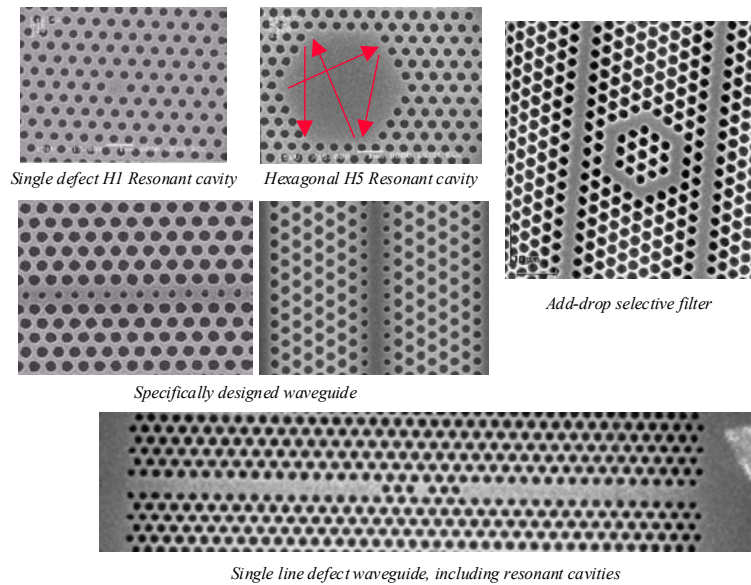


Figure 1.34. SEM micrographs of various integrated microphotonic devices based on 2DPC

The heterostructure is similar to that described above. The InP substrate, including the heterostructure, is bonded by the SiO₂-SiO₂ molecular bonding procedure (see (MON 01) for a complete description of the technological procedure, developed at CEA-LETI): a schematic view of the successive technological steps is presented in Figure 1.33, which also shows a view of a full wafer bonded InP membrane.

The InP substrate is eliminated by selective wet etching (HCl solution). The sacrificial InGaAs layer is finally etched off by selective wet etching (FeCl₃ solution). The thickness of the SiO₂ layer, below the heterostructure is around 800nm, which is enough to get rid of any significant evanescent coupling of the waveguided modes with the silicon substrate.

The fabrication of the 2DPC is then conducted as described previously.

Figure 1.34 provides a restricted sampling of the extreme variety of conceivable micro-photonic devices based on 2DPC. In the following section, we explore the principal building blocks on which they are based.

1.6.2. Localized defect in the PBG or microcavity

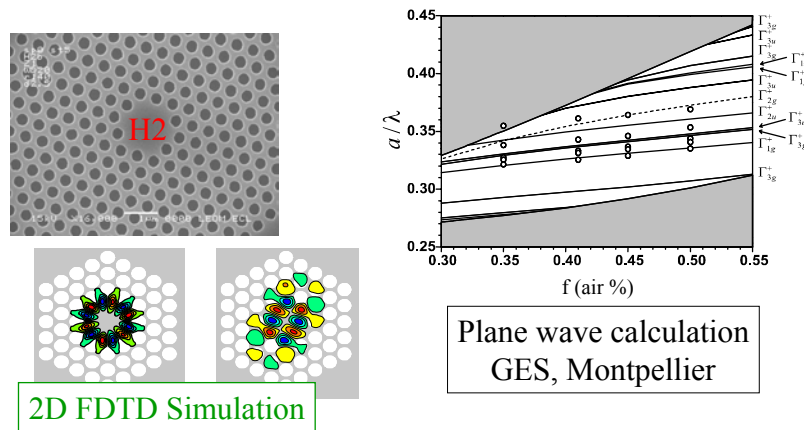


Figure 1.35. H_2 cavity: magnetic field distribution of cavity modes (2D FDTD determination) and localized states introduced in the PBG

The concept of localized defects or microcavities introduced and analyzed in detail in sections 1.3.5 and 1.3.6 devoted to 1DPC (ideal as well formed in a planar dielectric waveguide), may be extended to the case of 2DPC, as already noted in section 1.5.2. A local break in the periodic lattice constitutes a defect which behaves like a microcavity, which may trap or localize photons in space and produces localized states, allowed within the PBG energy range.

The most widely investigated defects or microcavities are obtained by the omission of a certain number of holes in the periodic lattice, such as in the particular case of H_n type hexagonal shaped cavities, n standing for the number of missing rows per side of the hexagon.

The case of the H_2 cavity is presented in Figure 1.35: the energy levels of the localized states in the PBG (white zone), or cavity modes, are calculated as a function of the hole filling factor (“plane wave” modeling realized at GES-Montpellier: (MON 03)); the experimental points are derived from photoluminescence measurements. The magnetic field distribution of two types of cavity modes (“whispering gallery” mode on the left side, transverse mode on the right side) is also shown (FDTD simulation).

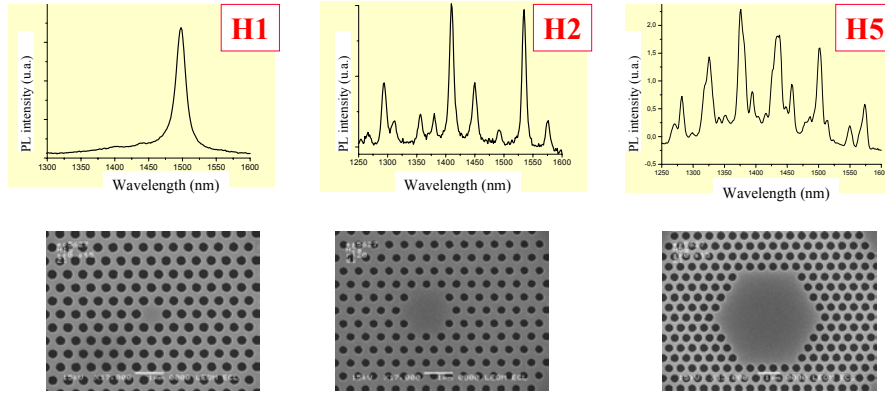


Figure 1.36. Spectral signatures of hexagonal cavities derived from photoluminescence measurements

Figure 1.36 shows the spectral distribution of the modes of hexagonal cavities with different sizes as derived from photoluminescence measurements: the latter is the manifestation of spontaneous recombination processes of the active medium, which is to a large extent controlled by the cavity modes, whose spectral density dominates the total available density of optical modes; the photoluminescence spectrum is therefore a spectral signature of the cavity modes (see (MON 03) for further details).

In the same way as in the case of cavities formed in 1DPC (section 1.3.5), we can observe that the number of modes in a given spectral range increases with the size (here the surface) of the cavity. The elementary H_1 cavity (one single missing hole) possesses only one mode (yet doubly degenerated) in the investigated spectral range.

As explained in section 1.3.6, the spectral widening $\delta\omega$ or $\delta\lambda$ of the cavity modes is like the inverse of their lifetime τ , which is principally controlled by the coupling rate $1/\tau_c$ with the radiated continuum (if the PBG area around the cavity is large enough to prevent significant lateral escape of photons, which means $\tau \cong \tau_c$). The lifetime of cavity modes varies like their quality factor Q (see equation (6)): the experimental values of Q reported in the literature are in the range of 10^2 – 10^5 . The talented designer will have the capacity to reduce the radiation of the cavity inside the light cone, that is to minimize the k vector Fourier components above the light-line (see Figure 1.18) and therefore to produce strongly “resonant” structures with high quality factors. If, in addition, the large quality factor is achieved with a small

volume cavity (hosting therefore small volume optical modes⁸), then the merit factor F of the modes, which coincides with the Purcell factor (see also Chapter 4 in this book) may be very large, which is highly desirable for exacerbating the spontaneous recombination rate of an active medium at the resonance frequency and for producing low threshold laser micro-sources.

1.6.3. Waveguiding structures

The operation of classical optical waveguides is based on *refraction* phenomena: the existence of waveguided modes is made possible by the total internal reflection processes occurring at the boundary between the guiding zone and the external world, thus confining optical modes whose dispersion characteristics are located below the light-line, as presented in section 1.2.4. Guiding structures using photonic crystals are based, in addition, if not exclusively, on diffraction phenomena, which may be exploited to channel photons within an area where the existence of modes is not forbidden.

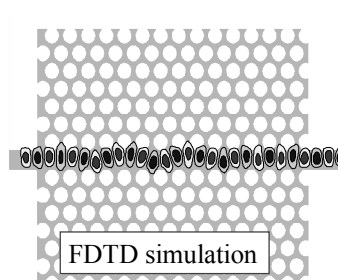


Figure 1.37. Magnetic field distribution of guided modes along a linear defect, formed by a missing row of holes in a triangular 2DPC (waveguide W_1)

We will concentrate on the case where the guiding structure is formed by a linear defect (one-dimensional structure) introduced in the 2DPC, which operates in the field of PBGs: this configuration has been the matter of a great number of studies reported in the international literature.⁹

⁸ Note that the membrane approach is attractive, in that respect, since it allows for a weak vertical extension of the optical modes, as compared to the substrate approach.

⁹ It is also possible to channel photons in a defect-free 2DPC, in permitted photonic bands, using the so called self-collimating phenomenon: this phenomenon, which is intrinsically diffractive, results from the non-isotropy of dispersion characteristics and from the fact that group velocity, which is oriented toward the propagation direction of energy, is normal to iso-frequency curves (see section 1.5.1 and, for example, (CHI 03)).

The canonical example, corresponding to the case of a linear defect simply formed by one missing row of holes (ΓK direction in this example), is shown in Figure 1.37: it is a so called W_1 waveguide. The magnetic field distribution of a waveguided mode along the guiding structure is also illustrated: it shows a periodicity which is naturally imposed by that of the 2DPC along the direction of propagation. The waveguided modes are Bloch modes with one dimension (in a three-dimensional world, if the 2DPC is formed in a dielectric membrane): their properties are very similar to those already described in section 1.3.6. Their dispersion characteristics are governed by the coupling processes induced by longitudinal 1D periodic “corrugation”, and exhibit bands where propagation is allowed, separated by PBG (so “mini-stop bands”: (OLI 01)), with photonic band edge extremes.

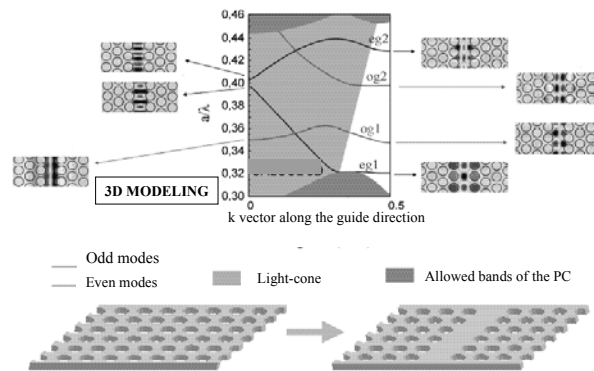


Figure 1.38. Dispersion characteristics of a W_1 waveguide (from GES, Montpellier)

The normalized dispersion characteristics of the W_1 waveguide are shown in Figure 1.38. The k propagation vector is oriented along the longitudinal direction of the guide and is limited to the first Brillouin zone. Spatial magnetic field distributions are also shown at various points in the dispersion characteristics: note that the symmetry of the modes depends heavily on the propagation conditions and on the nature of the guiding processes. For example, in the linear region, which corresponds to the fundamental mode and to a spectral range where propagation is “fast” (relatively large group velocity), the “refractive” contribution to waveguiding is rather large, as in classical waveguides (the effective index of the guiding zone, which is free of holes, is larger than that of the 2DPC): the waveguided modes are well confined within the guide. Close to the extremes, on the other hand, where the modes are slowed down, the field distribution is more spread inside the 2DPC, where photons are not allowed to stay: the principal contribution to the guiding and

confinement of photons within the guide is now taken over by diffractive processes, which are specific to photonic crystals.

1.6.3.1. Propagation losses in a straight waveguide

The reader will have noted that dispersion characteristics are partly located above the light-line (within the light cone, light gray area in Figure 1.38), which indicates that guided modes may, in these conditions, couple to the radiated continuum, and naturally result in propagation losses: the waveguided modes are so called lossy modes. This is unlike optical modes confined below the light-line, which may, theoretically, propagate without any loss. It is therefore relevant to design structures where as much room as possible is left to “fast” waveguided modes, with large group velocity, below the light-line. The simple W_1 waveguide is not very appropriate, in that respect. A possible improvement is illustrated in Figure 1.39, which shows a modified W_1 waveguide: it includes a row of shifted holes, within the core of the guiding zone! This results in a reduction in the effective index of the waveguided modes, leading to an increase in their energy as well as in the slope of the dispersion characteristics below the light-line, which turns to shift the fast fundamental mode below the light-line (GRI 03).

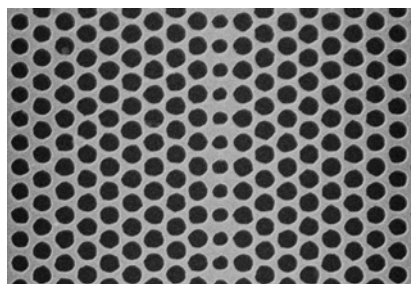


Figure 1.39. Modified W_1 waveguide in order to promote fast guiding of photons below the light-line

Constraining photons to the area below the light-line is necessary, but not sufficient in practice to ensure loss-less propagation of light: technological imperfections in the guide (promoting unwanted coupling with the radiated continuum) and the insertion of photons constitute other loss factors, which do not spare optical modes below the light-line. A number of theoretical and experimental works aimed at evaluating and minimizing losses in 2DPC-based waveguides have been reported recently in the literature. Here we will quote an elegant technique of characterization consisting of closing the two ends of guiding sections with variable lengths, thus forming linear cavities, whose resonant modes may be analyzed

spectrally (LET 01): optical losses per unit length of the guide may be derived from the quality factor of the cavity modes; in addition, it is possible to extract the dispersion characteristics of the waveguided modes from the derivation of the free spectral range of the cavity modes and to determine their kinetic properties (group velocity).

The best results reported so far (a fraction of dB/mm) are still below the performances accessible to classical optoelectronic waveguides. It turns out, however, that in the prospect of the fabrication of very compact systems, requiring photons to be transported over short distances (not exceeding a few hundred μm), these results may already be considered to be acceptable. It must also be admitted that, unfortunately, these “good” results can be obtained in rather narrow spectral bandwidths (allowed bands for fast propagation below the light-line).

1.6.3.2. Bends

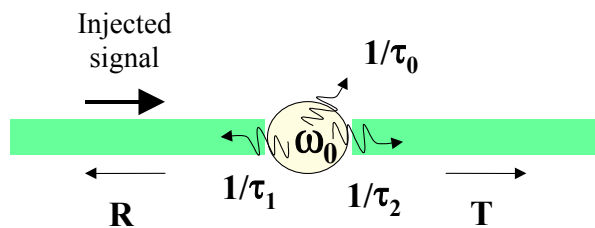


Figure 1.40. Conceptual representation of a bend

Transportation of photons necessarily implies the presence of bends to give them a chance to reach their final destination. Let us recall that 2DPC were considered to be very promising, in terms of the production of ultra-compact guides and sharp bends, after the pioneering theoretical work published by the MIT group (JOA 95). A first order argument naturally leads to the idea that PBGs do not have any alternative other than following the corridor that is opened to them when they come to a bend. The reality is different, from both conceptual and practical points of view.

A bend should indeed be viewed as a localized defect, resulting in a break in the one-dimensional periodic structure that constitutes the straight waveguide. It must be considered as a microcavity or resonator, which provides a resonant transfer of photons between the two sections of straight waveguides which are attached to it, as illustrated schematically in Figure 1.40.

This conceptual representation of a bend is general and may apply to classical guiding structures. In the classical situation, a bend may be considered as a defect

breaking the continuous (and no longer periodic) translational symmetry of the straight waveguide.

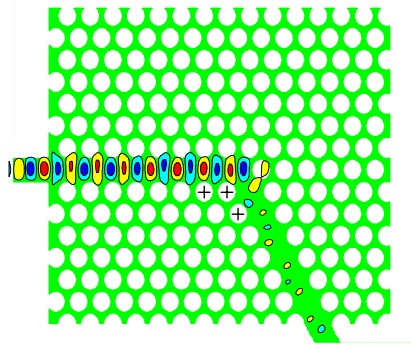


Figure 1.41. *FDTD simulation of the magnetic field distribution around a bend*

If we use a modal type terminology, the bend can be considered as hosting localized resonant modes, which, through their coupling to the input and output waveguided modes, provide the transfer of the injected signal. The coupled mode theory may be used for a relatively simple analytical description of the structure. Such simulation methods as the FDTD technique allow for a precise modeling of its behavior. Figure 1.41 shows the magnetic field distribution, obtained by 2D FDTD simulation¹⁰, provoked by the presence of a 120° bend in a W_1 waveguide. One observes that the transmission T of the input signal is strongly limited by the bend. In fact, a number of conditions have to be met in order to achieve a near-uniform transmission ratio. Let us express these conditions using the terminology of coupled mode theory:

- The transmission can be achieved only within the spectral bandwidth around the resonant frequencies of the bend, considered as a resonant cavity: this resonance must be therefore the widest possible in the spectral domain, which means that the coupling between the cavity modes (whose lifetime τ must be the smallest possible, for a maximum spectral widening) and the waveguided modes should be very strong (which is equivalent, in Figure 1.41, to minimizing the τ_1 and τ_2 time constants): it is therefore appropriate to achieve the best spectral and spatial (especially in terms of symmetry) overlaps between the cavity modes and the waveguided modes.

- The $\frac{1}{\tau_{1,2}}$ coupling rates should be identical, in order to prevent the occurrence of a finite reflection rate of the injected signal.

¹⁰ An ideal 2DPC is considered for this simulation.

– Optical losses at the bend, expressed by the ratio $\frac{1}{\tau_0}$ in Figure 1.41, as a result

of cavity mode coupling with the radiated continuum, should be minimized. If not, the transmission is reduced not only for radiated losses, but also for the reflection.

– It is advisable to operate in a monomode waveguided regime, to prevent the risk of unwanted coupling between different order orthogonal waveguided modes, promoted by the localized defect which is formed by the bend and resulting in extra reflection.

These various conditions may be summarized by the relation below:

$$\frac{1}{\tau_0} \leq \frac{1}{\tau} = \frac{2}{\tau_{1,2}} \quad (27)$$

Classical bends have the definite advantage over PC based bends that they “naturally” comply with and/or circumvent most of the previous conditions. Regarding compactness, which was argued to be a very attractive feature of PC-based bends by the MIT group, classical high index contrast refractive microwire waveguides (silicon wires on silica, for example) are strong contenders to PC waveguides: they allow for very sharp bends (bend radius around one micron), without significant theoretical losses, as a result of the evanescent coupling of waveguided modes with the radiated continuum.

May, therefore, PC-based waveguides be considered to be at all useful?

1.6.3.3. *The future of PC-based waveguides lies principally in the guiding of light*

2DPC-based waveguides are not well suited, in general, to photon transportation or to the optical transfer of information: it is more appropriate to restrict their use to the “smart” treatment of optical signals. It should not be forgotten that a guide formed in a 2DPC is itself a one-dimensional periodic structure, which behaves like a 1DPC: it is therefore advisable to exploit the natural virtues of photonic crystals which allow for tight control of the kinetics of photons, that is for their efficient slowing down and their trapping in a very limited space for a significant amount of time. It is therefore preferable to use 2DPC-based waveguides precisely under the conditions where they are inefficient light carriers, that is at operation points of their dispersion characteristics where their group velocity is limited, especially around extrema.

Figure 1.42 shows a schematic representation of the general scenario that should be followed for the use of 2DPC-based waveguides. Compact sections of “slow” PC-based waveguides, which are photon storing zones where they will stay during

the time required for the optical signal process, are connected by fast, classical refractive waveguides. The tapering transition zone between fast and slow sections is essential in the design of the whole structure: it is meant to minimize insertion losses, which manifest themselves by unwanted reflections and coupling to the radiation continuum.

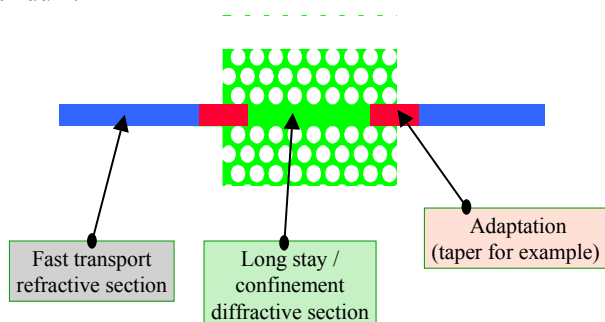


Figure 1.42. General scenario for the use of a 2DPC-based waveguide

This general scenario is expected to result in the production of a wide range of compact devices with very diverse functionality: let us mention, for example, electro- or thermo-optical modulators based on Mach-Zehnder interferometers, when full use is made of the strong phase optical index dispersion or of the large group optical index, which occurs near an extremum of the dispersion characteristics; or efficient, although compact, chromatic dispersion compensation structures; or devices making the best use of non linear phenomena, in terms of the required input optical energy, owing to strong photon confinement. The list could go on.

1.6.4. Wavelength selective transfer between two waveguides

Wavelength Division Multiplexing is today considered to be a powerful enabler for the optical transfer and treatment of information, particularly for telecommunications applications. This approach is also meant to relax high density scale integration constraints in microelectronics by opening the way to the so called Systems On Chip, combining microelectronic and microphotonic integrated circuits. In this respect, the multiplexing-demultiplexing function, which consists of adding to or dropping from a waveguide selected wavelengths, is an essential element of optical signal processing.

The principle underlying this function is presented schematically in Figure 1.43. It consists of the use of a mediator between two waveguides, which is meant to

promote the transfer of certain wavelengths from one to the other. The selected wavelengths are set by the intersections between the dispersion characteristics of the two guides with that of the mediator. Because the waveguides are meant to provide “fast” transportation of photons, the mediator should have rather flat dispersion characteristics, in such a way that their intersections with those of the fast waveguides can be well defined; this means that it should operate in the regime of slow Bloch modes, or even trapped modes (in extreme cases).

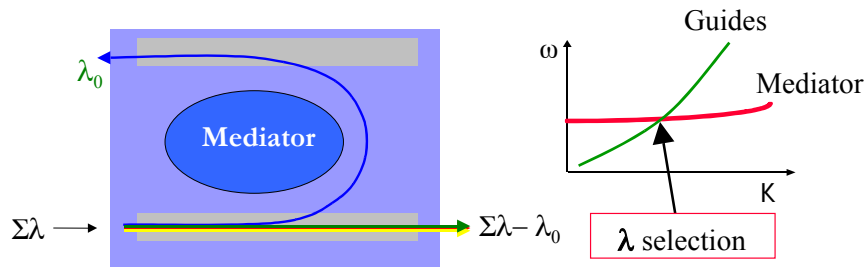


Figure 1.43. General coupling principle between two waveguides with wavelength selectivity

One can therefore contemplate the potential importance of PC-based structures for that purpose. Wavelength selectivity $\delta\lambda$ is essentially related to the lifetime or stay duration τ of optical modes in the mediator:

$$\delta\lambda \text{ proportional to } \frac{1}{\tau} = \frac{1}{\tau_0} + \frac{1}{\tau_c} \tag{28}$$

τ_c is the coupling time constant of the mediator modes with fast waveguided modes and τ_0 is the lifetime of modes related to optical losses (for example controlled by coupling with the radiation continuum and/or by absorption).

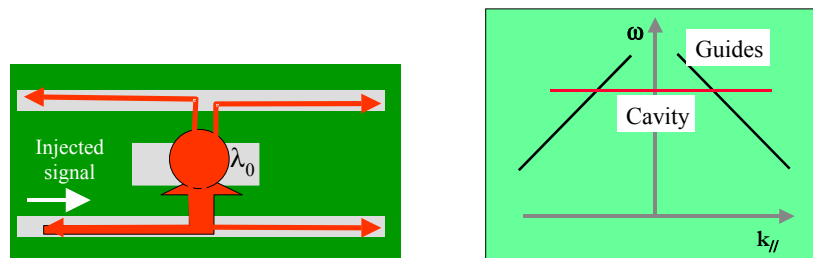


Figure 1.44. A monomode microcavity cannot provide a directional transfer of wavelengths between two waveguides

The direction of the wavelengths' selective coupling is another important characteristic of the add and drop function: it depends essentially upon the symmetry of the mediator modes, which take care of the wavelength transfer. In the simple canonical case where, for example, the mediator is formed by a monomode cavity (in the considered spectral range), the transfer cannot be directional, as illustrated in Figure 1.44. In steady state regime, the cavity mode which is generated by the coupling with the waveguided mode injected in the input waveguide is in turn coupled to both waveguides and results in counter-propagating waveguided components, as dictated by the symmetry of the structure and as allowed for by the dispersion "characteristics" of the cavity: the latter is indeed restricted to a monochromatic horizontal line, where all k_{\parallel} vectors are authorized. Consequently, the input signal is partly reflected in the input waveguide, and partly transmitted in both directions of the output waveguide¹¹.

The MIT group (FAN 98) proposed a solution to directional transfer based on the use of two degenerated cavity modes, whose symmetry properties are judiciously chosen, with the further condition that the coupling rates of each of these modes with the waveguides modes are equally balanced. These conditions are naturally met in the well known classical configuration where two refractive waveguides are resonantly coupled via a micro-disk or micro-ring type cavity (provided that the diameter is larger than the operation wavelength). Meeting these conditions with PC-based waveguides and cavities is tricky from a technological point of view, the size resolution being very high (to the order of one nanometer).

Another solution based on photonic crystals, with fewer technological constraints, consists of the use of a mediator formed by a section of "slow" waveguides, which operates around an extreme of its dispersion characteristics (HAT 05). The resonant mode of the mediator is not localized as in a microcavity, but it is a "propagating" slow Bloch mode: for this mode to retain its propagating character, its lateral extension must remain inferior to the size of the slow waveguide during its time in the mediator; it would otherwise behave like a microcavity mode, and the directionality would be lost. The slow PC-based waveguide, used around an extreme of the dispersion characteristics, enables this last constraint to be overcome, under the best compactness conditions (see sections 1.3.3 and 1.3.4, and equation

¹¹ It can be shown easily, using coupled mode theory, that in the absence of an output waveguide, the coupling of the input waveguide with the monomode cavity results in the total reflection of the input signal, if optical losses are negligible. Asano *et al.* 2003 have used this configuration to extract wavelengths from a guide by using radiation optical losses of the cavity in free space; although attractive, this approach is not expected to result in directional operation (50% at most of the input signal is extracted at resonance, the remainder being either reflected or transmitted in the input waveguide).

(14)). The operation of this type of wavelength selective and directional coupling is illustrated in Figure 1.45, with a specific example.

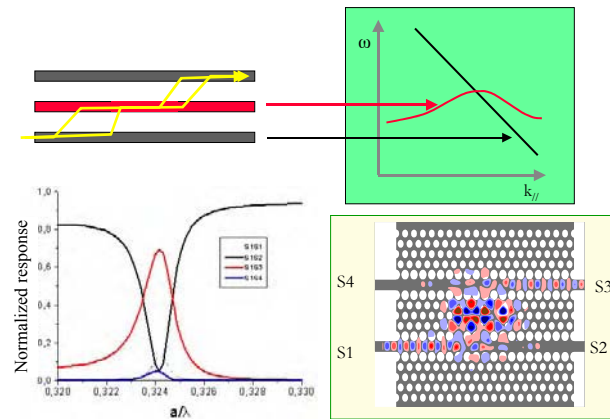


Figure 1.45. Wavelength selective and directional coupling between two waveguides: use is made of a slow Bloch mode “resonator”. The spectral response and the magnetic field distribution (2D FDTD simulation) corresponding to the specifically chosen example are also shown

1.6.5. Micro-lasers

The operation of a laser is based on the interaction between an active light emitting medium and the optical modes of a photonic structure which will have been designed to promote their mutual coupling: the objective is to reach a threshold density of photons in the active medium, for the highly coherent so called stimulated emission to overcome the poorly coherent spontaneous emission in the active medium. The general approach is to design the photonic structure in such a way as to confine optical modes within the space occupied by the active medium. The reader will have realized that the intrinsic qualities of photonic crystals, analyzed in previous sections (see particularly sections 1.3.4 and 1.5.2), make them ideal for achieving the function of photon confinement in a very compact way. Let us recall that, in general, the lateral confinement of photons can be achieved in a 2DPC, either by trapping them in a localized defect or microcavity giving rise to a localized mode within a photonic band gap, or by slowing them down in a slow Bloch mode at an extreme of the dispersion characteristics. Those two approaches result in two classes of lasers, microcavity lasers and Bloch mode lasers. Figure 1.46 shows the different types of lasers, from the point of view of their operation on dispersion characteristics.

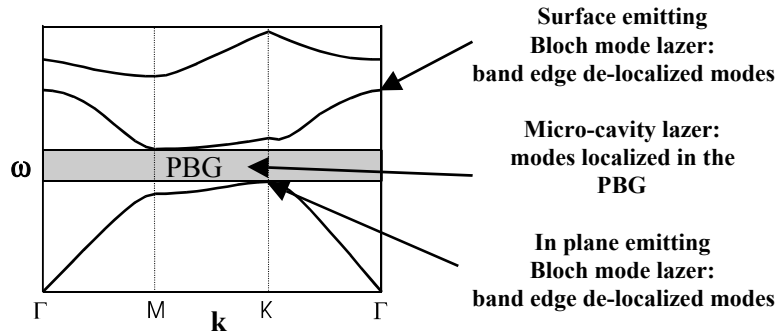


Figure 1.46. Different types of micro-lasers, as a function of their operation on dispersion characteristics

In the Bloch mode laser class¹², two types of devices can be distinguished:

- Lasers designed for in-plane emission: the operation point coincides with an extreme located below the light-line (the K point in the example in Figure 1.46; the emission is preferentially oriented toward the Γ K directions in the plane).

- Lasers designed for surface emission, that is to say in free space: the operation point coincides with an extreme located above the light-line (the Γ point in the example of Figure 1.46), resulting in vertical emission. The operation principle of this type of laser implies therefore that waveguided Bloch modes may couple to the radiated continuum; the coupling rate must however not be so strong as to “destroy” the Bloch mode resonance, that is to say, during its lifetime or its time of interaction with the active medium it must not be reduced to such an extent that the stimulated emission threshold cannot be reached. It turns out that, for reasons of symmetry, coupling with the radiated continuum may theoretically be forbidden at the Γ point, for 2DPC with specific symmetry (triangular lattice, for example): this property ensures an efficient confinement of the waveguided mode within the membrane waveguide, whereas emission close to the vertical direction is permitted.

1.6.5.1. Threshold power

The threshold power of the laser is the minimum power required for the stimulated emission to exactly compensate for all photon loss processes (absorption, optical losses).

¹² So called DFB classical lasers are also Bloch mode lasers; the novelty of 2DPC lies first in their compactness, as explained at length in this chapter, and, second, on the extra dimension that they offer.

For microcavity lasers, the threshold power is proportional to the volume of the cavity and is a decreasing function of the lifetime of the cavity mode resulting in the laser effect (LET 05). The strong lateral confinement of photons which are trapped in the localized defect within the PBG of the 2DPC, combined with the thin vertical confinement provided by the membrane approach, enables the production of microcavities whose volume does not exceed a fraction of μm^3 (for an operation wavelength around $1,5\mu\text{m}$); this opens the way for the production of very low threshold power lasers, as far as the lifetime of the cavity mode can be kept long enough, or the various sources of losses can be minimized – especially the optical losses of the cavity.

For Bloch mode lasers which operate at a band edge extreme, the threshold power is proportional to the curvature α of the dispersion characteristics at the extreme (LET 05). We see, once more, that an essential quality of photonic crystals is to offer dispersion characteristics with very low curvature band edge extremes. That the threshold power is proportional to α is a direct consequence of the fact that the lateral optical mode confinement is also proportional to α . Let us recall that the surface extension of a Bloch mode at an extreme can be written $S_{BM} \approx \alpha\tau$, where τ is its lifetime (see section 1.5.2, footnote 4).

1.6.5.2. Example: the case of the surface emitting Bloch mode laser

Experiments with the three types of micro-lasers described above have been reported in the international literature, following the pioneering work of the group at Caltech published in 1999, which concerned the production of the first microcavity laser (H_1 type) formed in an InP suspended membrane (PAI 99).

Other published works may be pointed out, such as Hwang *et al.* 2000 on microcavity lasers and Ryu *et al.* 2002 on Bloch mode lasers. The group at the Ecole Centrale de Lyon has experimented with the three types of lasers, formed in InP membranes bonded onto silica on silicon substrate (MON 01, 02; MOU 03), following the technological procedure described in section 1.6.1. Bonding of the membrane onto silica improves the thermal budget considerably as compared to the configuration where the membrane is suspended in air.

We present below, as an illustrative example, the case of surface emitting Bloch mode laser (MOU 03). The photonic crystal consists of a graphite lattice (Figure 1.47), which can be viewed as an array of H_1 coupled cavities, formed in a triangular lattice.

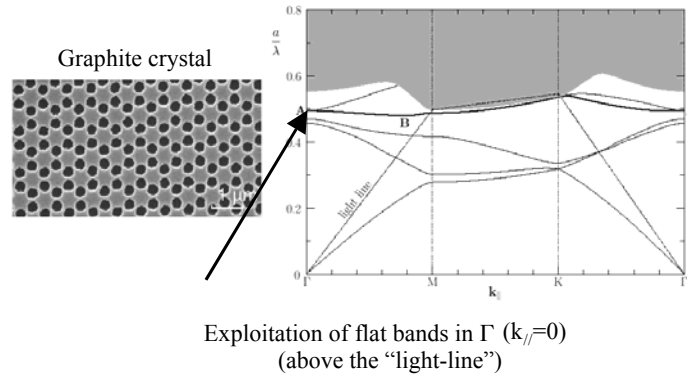


Figure 1.47. Band of a surface emitting Bloch mode laser formed in a graphite type 2DPC

This particular 2DPC exhibits band edge extremes at the Γ point with very low curvature (Figure 1.47). One of these extremes is shown in the example below.

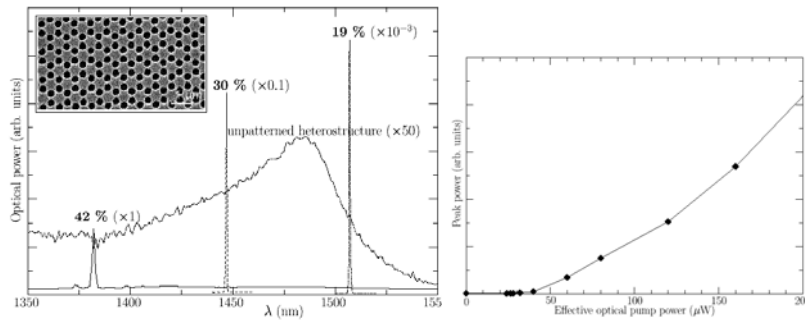


Figure 1.48. Emission spectra of the surface emitting laser formed in a graphite lattice 2DPC, for different hole filling factors (f). The plot of the emitted power versus the pumping power indicates a threshold power of $40 \mu W$ for $f=19\%$

Emission spectra of the laser are shown in Figure 1.48 for different hole filling factors f , as well as the spontaneous emission spectrum of the non-structured membrane. The device is optically pumped in a quasi-steady state regime and operates at room temperature. The peak intensity for the optimum filling factor ($f = 19\%$) is larger than the spontaneous emission power by 5 orders of magnitude. To increase f , as might be expected, the emission peak is blue shifted as a result of a reduction in the effective optical index of the membrane; at the same time, the

emission yield drops rapidly due to a decrease in the modal gain (not shown in the figure). The effective threshold pumping power, for the optimized device, is very weak and does not exceed $40\mu\text{W}$. The pumped area where the simulated emission process takes place is very limited and does not exceed 2 to $4\mu\text{m}$ in diameter: this is a clear demonstration of the outstanding ability of 2DPC to confine laterally slow Bloch modes.

1.6.6. Epilogue

Our trip into the world of 2D photonic crystals has come to an end; we should however be convinced that we have tasted some of the wide variety of landscapes that 2DPC has to offer, albeit restricted to a two-dimensional universe. The last example presented in the previous section (surface emitting laser) opens the door to an even wider range of opportunities which may be accessible when freeing 2DPC towards the third dimension. We present these new emerging developments briefly in the last part of this chapter.

1.7. Towards 2.5-dimensional Microphotonics

1.7.1. Basic concepts

Photonic devices based on 2DPC are principally aimed at forming the basic building blocks of integrated photonics and are designed for in-plane waveguided operation. We recall that these devices are very attractive from the point of view of fabrication, the technological schemes to be adopted being compatible with planar technological approaches. We recall also that the operation of photonic integrated circuits based on 2DPC may be deeply affected by optical losses resulting from unwanted diffractive coupling of waveguided modes with the radiation continuum.

This problem of optical losses, which is considered as hindering the operation of 2D photonic integrated circuits based on 2DPC, can be approached from a completely different perspective: instead of attempting to confine the light entirely within waveguide structures, 2D structures can be deliberately opened to the third space dimension by *controlling* coupling between waveguided and radiation modes. In this approach, exploitation of the optical power is achieved by accurately tailoring optical radiation into free space.

The surface emitting micro-laser (section 1.6.5) is an example of this approach: coupling between waveguided modes and radiated modes is authorized, but its rate is controlled accurately, allowing for vertical emission while retaining the strength of resonance and, therefore, achieving weak threshold power. This is a simple and

convincing illustration of a planar technological approach resulting in a photonic device freed from the bidimensional universe.

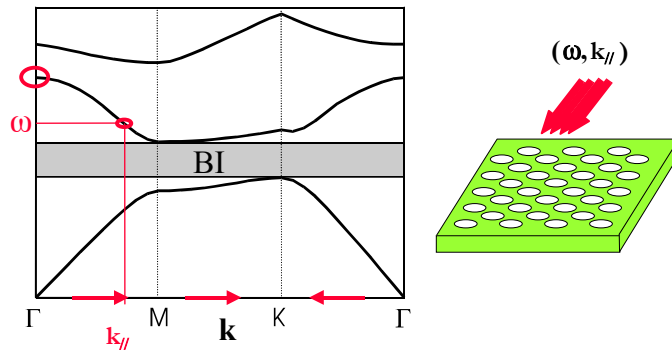


Figure 1.49. Illustration of the resonant coupling between a waveguided mode and a radiated mode

A major extension of planar technology has recently been proposed, through exploitation of the third (“vertical”) dimension by using a so called multi-layer approach, where lateral high index contrast patterning of layers would be combined with vertical 1D high index contrast patterning: here it is more appropriate to think in terms of “2.5 dimensional” photonic structures, in which there is interplay between waveguided-confined photons and radiated photons propagating through the planar multilayer structure (LET 03).

A simple illustration of this approach is the use of a plain photonic crystal membrane as a wavelength selective transmitter/reflector: when a light is shone on this photonic structure, in an out-of-plane (normal or oblique) direction, resonances in the reflectivity spectrum can be observed.

These resonances, so called Fano resonances (AST 99), arise from the coupling of external radiation to the guided modes in the structures, whenever there is a good match between the in-plane component of the wave-vector of the incident wave and the wave-vector of the guided modes (see Figure 1.49). If the lateral size of the illuminated membrane is infinite, the spectral width of the resonance is like the inverse of its lifetime τ , that is the lifetime of the waveguided mode, with $\tau = \tau_c$, where τ_c is simply the coupling time constant between waveguided and radiated

plane-wave modes¹³. In real devices, the lateral size of the illuminated area is limited, and the lifetime of the resonance is also controlled by the lateral escape rate $\frac{1}{\tau_g}$ of the waveguided mode out of this area; this escape rate should be considered as a loss mechanism for devices which are designed and intended to operate “vertically”. In these real conditions the lifetime of the resonance is written as:

$$\frac{1}{\tau} = \frac{1}{\tau_c} + \frac{1}{\tau_g} \approx \delta\omega, \quad (29)$$

where $\delta\omega$ is the spectral widening of the resonance. The ability of high index contrast PC to slow down photons and to confine them laterally, especially at the high symmetry points (or extrema) of the dispersion characteristics, as explained a number of times earlier in the chapter, allows for very good control over the lateral escape losses and results in very compact devices.

If we now consider a multilayer structure, the strong vertical 1D modulation of the optical index allows for a fine and efficient “carving” of the density and vertical field distribution of radiated modes, using a limited number of layers.

In summary, 2.5D Microphotonics, combining lateral 2DPC and vertical 1DPC, should provide a very good control over the electromagnetic environment, that is over the distribution of optical modes in 3D real space and time, at a much lower cost than the full 3D approach in terms of technological feasibility: the technological schemes to be adopted are compatible with technological approaches which are normally describable as planar.

This multi-layered or multi-level approach is familiar in the world of silicon microelectronics, when it comes, for example, to fabricating multiple levels of electrical interconnections; its usefulness in Microphotonics extends far beyond, from the viewpoint of a considerable extension of accessible functionality.

¹³ Various factors contribute to the control of the coupling time constant, such as the strength of the periodic corrugation, and the symmetry of the waveguided mode.

1.7.2. Applications

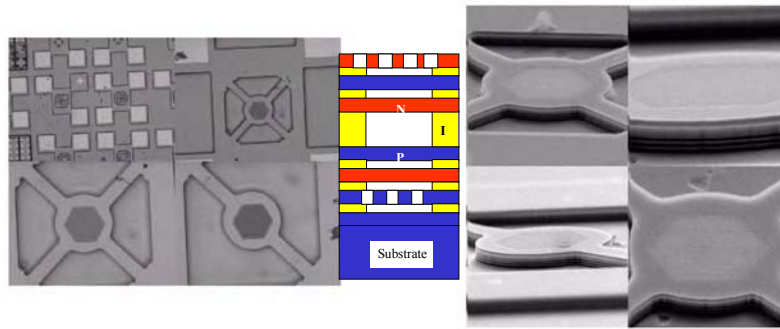


Figure 1.50. 2.5D photonic structure including several InP membranes suspended in air, with a 2DPC formed in the top membrane (SEM view)

It is clear that the exploitation of the third dimension should widen the domain of Integrated Photonics considerably. In addition to the convincing experiments with surface emitting micro-lasers mentioned above, other outstanding results have recently been published: they concern, in particular, the use of the non-linear response of a 2DPC, enabling the manipulation of Fano resonances and opening the way for new classes of compact surface addressable devices, for full optical routing and signal regeneration (RAI 03).

Other areas of Photonics should take advantage of the 2.5D Microphotonics approach. For example, the introduction of 2DPC into MOEMS (Micro Opto Electro Mechanical) devices shows great promise in terms of widening the spectrum of (electro-mechanically actuatable) optical functions, achievable with further enhanced compactness structures. Figure 1.50 gives an example of such a MOEMS 2.5D structure. These new types of photonic structures should be applied in various domains, including Optical Telecommunications (tunable or switchable wavelength selective devices, taking advantage of the extra angular resolution provided by the 2DPC), as well as the field of optical sensors: it should be noted that the sensing function should be greatly enhanced, due to the fact that the resonant “portions” of the device, i.e. those where the electromagnetic field intensity is maximum, can be very close to (or even at) the surface of the device. This is in favor of an improved sensitivity and of an easy exploitation of so called functionalized surface sensors. The “2.5D Microphotonics” approach also brings about a new opportunity, practicable in terms of technological constraints and rich in terms of extra degrees of liberty, to control the electromagnetic environment at the wavelength scale. It is

therefore the appropriate route for “physicists” looking for *ad hoc* configurations in Quantum Electrodynamics studies (coupling of active material with the electromagnetic field, threshold-less laser, directional single photon sources, combination with near optical field studies, etc.). Let us mention, finally, the great potential of 2.5D Microphotonics in biological applications, in the development of “biophotonic chips”, which would be very efficient in terms of “photonic yield”: for example, the accurate control of resonant processes at the surface of photonic microstructures should result in a considerable increase in the collection efficiency of the luminescent signal emitted by fluorescent markers used in biological chips.

1.8. General conclusion

The flow of innovations since the late 1980s created by the introduction of the concept of the photonic crystal (YAB 87; JOH 87) is still rather slow, but will no doubt accelerate in the future to an extent which is beyond our full consciousness: it was simply proposed to extend the field of optics to the three dimensions of space, which was rather confined, yet with very successful outcomes, to the one dimensional world of multilayer optical structures. It is now established that the emergence of 3D Microphotonics based on full 3DPC will be significantly delayed, as a result of technological constraints. We hope that the reader will have been convinced that, on the other hand, 2DPC are fully engaged in the process of innovation and that we are experiencing, in that respect, a truly microphotonic revolution. We have shown that 2DPC are very promising for 2D microphotonic integration; there is however a lot left to be done before 2DPC devices are fully integrated in the world of optoelectronics, especially in connection with the solutions required for the control of radiation optical losses. As for so called 2.5D Microphotonics, where 2DPC are deliberately opened up to the third dimension of space, we have seen convincing demonstrations of their ability to generate, in the short term, a wide range of photonic devices (“killer applications”) combining compactness, spatial (angular) and spectral resolution, and whose fabrication meets the standards of planar technology, familiar to the world of microelectronics.

It appears that the rising trajectory of photonic crystals will not be inhibited in the long run, provided that appropriate tools are made available for their evolution. In that respect, bottlenecks are still to be eliminated and important R&D will have to be deployed for that purpose: this is true for the modeling and design aspects (especially 3D), whose fast and efficient tools are yet to be built; the technological constraints, dictated by the necessity to control the size of the devices at the nanometer scale, are far from solved. From the latter point of view, it can be stated that we really have entered the *Nanophotonic* era.

1.9. References

- [ASA 03] Asano T, Song B-S, Tanaka Y and Noda S (2003) Investigation of channel-add/drop-filtering device using acceptor-type point defects in a two-dimensional photonic crystal slab. *Appl. Phys. Lett.* 83 (3): 407.
- [AST 99] Astratov VN, Whittaker DM, Culshaw LS, Stevenson RM, Skolnick MS, Krauss TF and De La Rue RM (1999) Photonic Band Structure Effects in the Reflectivity of Periodically Patterned Waveguides. *Phys. Rev.* B60 (24): R16255.
- [CHI 03] Chigrin DN, Enoch S, Sotomayor Torres CM and Tayeb G (2003) Self-guiding in two-dimensional photonic crystals. *Optics Express* 11(10): 1203.
- [CUI 99] Cuisin C, Chen Y, Decanini D, Chelnokov A, Carcenac F, Madouri A, Lourtioz JM and Launois H (1999) Fabrication of three-dimensional microstructures by high resolution x-ray lithography. *J. Vac. Sci. Technol.* B 17(6): 3444.
- [GRA 00] Gralak B, Enoch S and Tayeb G (2000) Anomalous refractive properties of photonic crystals. *J. Opt. Soc. Am.* A17(6): 1012.
- [GRI 03] Grillet C (2003) Micro-composants optiques à base de cristaux photoniques 2D pour l'optique intégrée. Thesis, Ecole Centrale de Lyon.
- [FAN 98] Fan S, Villeneuve PR, Joannopoulos JD and Hauss HA (1998) Channel Drop Tunneling through Localized States. *Phys. Rev. Lett.* 80 (5): 960.
- [GRU 96] Grüning U, Lehmann V, Ottow S and Busch K (1996) Macro-porous silicon with a complete two-dimensional photonic band-gap centered at 50 μm . *Appl. Phys. Lett.* 68 (6): 747.
- [HAT 05] Hattori HT, Grillet C, Letartre X, Rojo-Romeo R, Seassal C and Viktorovitch P (2005) Directional channel-drop filter based on a slow Bloch mode photonic crystal waveguide section. *Optics Express* 13: 3037.
- [HWA 00] Hwang J-K, Ryu H-Y, Song D-S, Han I-Y, Song H-W, Park H-K and Lee Y-H (2000) Room-temperature triangular-lattice two-dimensional photonic band gap lasers operating at 1.54 μm . *Appl. Phys. Lett.* 76: 2982.
- [JOA 95] Joannopoulos JD, Meade RD and Winn JN (1995) *Photonic Crystal. Molding the Flow of Light*. Princeton University Press, New Jersey.
- [JOH 87] John S (1987) Strong localisation of photons in certain disordered superlattices. *Phys. Rev. Lett.* 58: 2486.
- [KOG 72] Kogelnick H and Shank CV (1972) Coupled wave theory of distributed feedback lasers. *J. Appl. Phys.* 43: 2328.
- [LAL 01] Lalanne P and Benisty H (2001) Out of plane losses of two dimensional photonic crystal waveguides: electromagnetic analysis. *J. Appl. Phys.* 89(2): 1512.
- [LET 01] Letartre X, Seassal C, Grillet C, Rojo-Romeo P, Viktorovitch P, Le Vasseur D'yerville M, Cassagne D and Jouanin C (2001) Group velocity and propagation losses measurement in a single line photonic crystal waveguide on InP membranes. *Appl. Phys. Lett.* 79: 2312.

- [LET 03] Letartre X, Mouette J, Seassal C, Rojo-Romeo P, Leclercq J-L and Viktorovitch P (2003) Switching devices with spatial and spectral resolution combining photonic crystal and MOEMS structures. *J. Lightwave Technol.* 21(7): 1691.
- [LET 05] Letartre X, Monat C, Seassal C and Viktorovitch P (2005) An analytical modeling and an experimental investigation of 2D photonic crystal Micro-lasers: defect state (microcavity) versus band edge state (distributed feed-back) structures. *Journal of the Optical Society of America B (JOSA B)*, in press.
- [LOU 05] Lourtioz JM, Benisty H, Berger V, Gérard JM, Maystre D and Chelnokov A (2005) *Photonic Crystals: Towards Nanoscale Photonic Devices*, Springer, Berlin-Heidelberg-New York.
- [MAC 96] Macleod HA (1986) *Thin Film Optical Filters*. 2nd edition, Adam Hillger Ltd, New York.
- [MON 01] Monat C, Seassal C, Letartre X, Viktorovitch P, Regreny P, Gendry M, Rojo-Romeo P, Hollinger G, Jalaguier E, Pocas S and Aspar B (2001) InP 2D photonic crystal microlasers on silicon wafer: room temperature operation at 1.55 μm . *Electron. Lett.* 37: 764.
- [MON 02] Monat C, Seassal C, Letartre X, Regreny P, Rojo-Romeo P, Viktorovitch P, Le Vassor D'yerville M, Cassagne D, Albert JP, Jalaguier E, Pocas S and Aspar B (2002) InP based 2D photonic crystal on silicon: in-plane Bloch mode laser. *Appl. Phys. Lett.* 81: 5102.
- [MON 03] Monat C, Seassal C, Letartre X, Regreny P, Gendry M, Rojo-Romeo P, Viktorovitch P, Le Vassor D'yerville M, Cassagne D, Albert JP, Jalaguier E, Pocas S and Aspar B (2003) Two dimensional hexagonal-shaped microcavities formed in a two-dimensional photonic crystal on InP membrane. *J. Appl. Phys.* 93: 23.
- [MOU 03] Mouette J, Seassal C, Letartre X, Rojo-Romeo P, Leclercq JL, Regreny P, Viktorovitch P, Jalaguier E, Perreau P and Moriceau H (2003) Very low threshold vertical emitting laser operation in InP graphite photonic crystal slab on silicon. *Electron. Lett.* 39: 526.
- [OLI 01] Olivier S, Rattier M, Benisty H, Weisbuch C, Smith CJM, De La Rue RM, Krauss TF, Oesterle U and Houdre R (2001) Mini-stop bands of a one-dimensional system: the channel waveguide in a two-dimensional photonic crystal. *Phys. Rev. B* 63: 3311.
- [PAI 99] Painter O, Lee RK, Scherer A, Yariv A, O'Brien JD, Dapkus PD and Kim L (1999) Two-dimensional photonic band-gap defect mode laser. *Science* 284: 1819.
- [POT 99] Pottier P, Seassal C, Letartre X, Leclercq JL, Viktorovitch P, Cassagne D and Jouanin C (1999) Triangular and Hexagonal High Q-Factor 2D Photonic Bandgap Cavities on III-V Suspended Membranes. *J. Lightwave Technol.* 17: 2058.
- [RAI 03] Raineri F, Cojocaru C, Raj R, Monnier P, Seassal C, Letartre X, Viktorovitch P and Levenson A (2003) Nonlinear Optical Manipulation of Fano Resonances in 2D photonic crystal Slabs. Post Deadline CLEO 2003.

- [ROW 99] Rowson S, Chelnokov A and Lourtioz JM (1999) Two-dimensional photonic crystals in macro-porous silicon: from mid-infrared to telecommunication wavelengths (1.3-1.5 μm). *J. Lightwave Technol.* 33: 1989.
- [RYU 02] Ryu H-Y, Kwon S-H, Lee Y-J, Lee Y-H and Kim J-S (2002) Very-low threshold photonic band-edge lasers from free-standing triangular photonic crystal slabs. *Appl. Phys. Lett.* 80 (19): 3476.
- [SPI 98] Spisser A, Ledantec R, Seassal C, Leclercq JL, Benyattou T, Rondi D, Blondeau R, Guillot G and Viktorovitch P (1998) Highly selective and widely tunable 1.55 μm InP/Air-Gap micromachined Fabry-Perot filter for optical communications. *IEEE Photon. Technol. Lett.* 10: 1259.
- [TAM 88] Tamir T (1988) *Guided Wave Optoelectronics*, Springer Verlag, Berlin. Chapters 2 and 6.
- [VAS 02] Le Vassor D'Yerville M (2002) Modélisation de cristaux photoniques bidimensionnels de hauteur finie. Thesis, Montpellier II University.
- [YAB 87] Yablonovitch E (1987) Inhibited spontaneous emission in solid-state physics and electronics. *Phys. Rev. Lett.* 63: 2059.
- [YAB 91] Yablonovitch E, Gmitter TJ and Leung KM (1991) Photonic bandgap structure: the face-centered-cubic case employing nonspherical atoms. *Phys. Rev. Lett.* 67: 2295.

Chapter 2

Bidimensional Photonic Crystals for Photonic Integrated Circuits

2.1. Introduction

Within actual Photonic Integrated Circuits (PICs), light confinement is provided by the index contrast that exists between different materials and according to the geometry of a structure. This index contrast mechanism limits the desirable PIC size reduction (performances are then degraded) and the integration of optical functions. Within the periodic environment of a Photonic Crystal (PhC), light confinement can be obtained based on an intentional defect included in the PhC matrix. Devices implementing this multiple Bragg reflection mechanism may overcome these limits [LOU 05].

This chapter is an attempt to demonstrate that passive as well as active optical functions required in Telecoms networks can be fulfilled using PhC-based devices. Passive functions such as guiding, coupling and filtering as well as active functions such as emission and amplification are investigated here.

These examples demonstrate that compactness and monolithic integration can actually be reached with PhC-based devices. For the 1.3–1.5 μm Telecom wavelength domain, as emission is also addressed, all the structures reported here are fabricated on InP-based materials.

This chapter is divided into three sections:

- section 2.2 introduces the concepts that underlie device design, and explains the various performances that are expected of applications. For more in-depth exploration of the concepts, the reader is referred to Chapter 1;
- section 2.3 presents the technology required for the fabrication of 2D-PhC structures on InP substrate;
- section 2.4, the largest section, details the characterization of passive and active operating devices. Attention is paid to spectrally resolved modal behavior, as well as quantitative assessment of optical performances.

2.2. The three dimensions in space: planar waveguide perforated by a photonic crystal on InP substrate

2.2.1. Vertical confinement: a planar waveguide on substrate

For active optoelectronic functions (lasing, light amplification, fast tuning), buffer layers for carrier injection are required on both sides of the active layer. The generic vertical stack on InP substrate which is used for all the devices presented here is shown in Figure 2.1. The guided mode is vertically confined mainly in the high index layer, but spreads partly in the confinement layers, and also in the substrate.

This vertical mode confinement results from the “classical” index contrast. In the case of a GaInAsP material layer for 1.55 μm emission on InP substrate, the index contrast between the guiding layer and the buffer layers is reduced ($\Delta n/n$ only 6%), leading to a large vertical extension of the guided mode. Such large spreading has two major consequences:

- In order to intercept all the guided mode, holes have to be as deep as its vertical extension: at least 3 μm . Such deep etching technology is difficult for 200nm diameter holes (for a PhC with an air filling factor of 35%), in the case of InP-based materials.
- The PhC gap lies above the substrate light line (Figure 2.1b), so that any Bloch mode propagating in a defect which is located within the gap can radiate in the substrate; such a mode is known as a leaky mode.

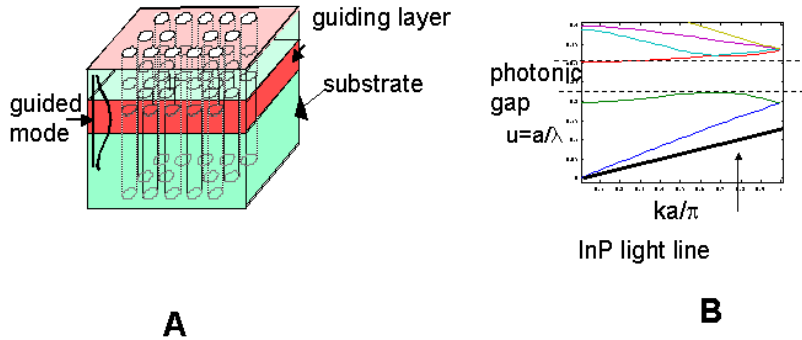


Figure 2.1. A: Planar waveguide perforated with the array of holes; B: Dispersion curve for the 2D photonic crystal calculated by the Plane Wave Expansion Method

But this large vertical deconfinement allows, as compared to the membrane case, higher coupling efficiency when light is injected from “classical” structures. This advantage is limited, as the in-plane confinement is still very strong in absolute terms. Quantitative performances and optical losses will be addressed systematically for any device, as a new device is relevant only if its power budget is reasonably mastered.

2.2.2. In-plane confinement: intentional defects within the gap

Let us now consider the high index heterostructure in which the PhC is fabricated. Here we investigate an array of holes rather than pillars, in order to generate a connected surface which will enable a metallic contact to be deposited for carrier injection. The triangular lattice gives rise to the widest gap simultaneously for both symmetry directions within the plane. We denote by ΓK the direction of the smaller period in the direct space, and by ΓM the direction of the larger period (see Chapter 1). The fabricated air filling factor is around 35%, leading to a photonic gap only for the TE polarization; TE polarization corresponds to the electric field of the optical mode being parallel to the layers’ plane. Intentional defects introduced within such a PhC matrix can support localized modes [JOA 95]. We consider here defects generated by missing holes. In such an arrangement, the region without holes has a dielectric constant larger than the PhC region, so we have to remember that for any design including this category of “defect” in the PhC, the multiple Bragg mechanism and the index contrast mechanism simultaneously confine the mode.

2.2.2.1. Localized defects

Removing a few holes while following the PhC array symmetry leads to hexagonal cavities. We denote by H1 the smallest cavity obtained by removing a single hole, as each of its sides is one period long. This H1 cavity supports a pair of degenerate modes which is efficiently included in an out-of-plane filter [AKA 03]. A larger cavity, for example the H2 cavity shown in Figure 2.2a, supports a larger number of modes. Cavity eigenmodes are calculated by the Plane Wave Expansion method ([BEN 99], and Chapter 1). We plot in Figure 2.2a the H field component amplitude for two consecutive eigenmodes of the H2 cavity; the mode on the right has its H field component confined on the boundaries, looking like a whispering gallery mode. Such a mode will be of interest for cavity-guide in-plane coupling (section 2.4.1).

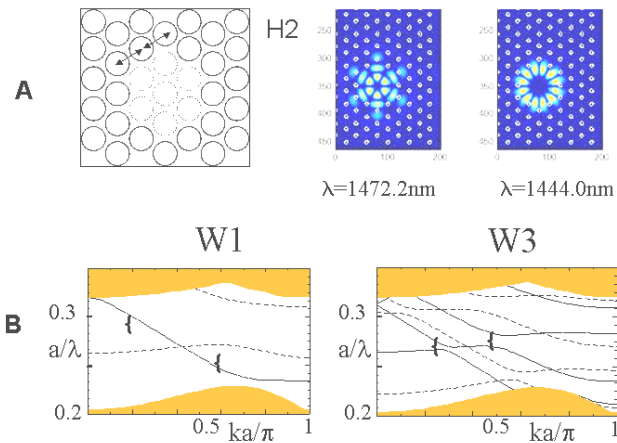


Figure 2.2. A: Schematics of an H2 cavity. Absolute value of the H field amplitude for two consecutive eigenmodes; B: Dispersion curves for W1 and W3 guides ($ff=40\%$)

2.2.2.2. Linear defects

Removing rows of holes or changing their size creates linear defects that allow Bloch modes to propagate within the gap. All the guides we will consider here are ΓK oriented, along the dense period a . They correspond to an integer number of missing rows, and are denoted by W i , for i missing rows. Previous characterizations of PhC guides have demonstrated that ΓM oriented guides are more lossy [OLI 02b].

Figure 2.2b displays the dispersion relation for W1 and W3 PhC guides. The dispersion relation plotted here corresponds to the normalized frequency $u=a/\lambda$,

versus $k_{//}$, the in-plane \mathbf{k} vector component along the symmetry direction chosen, here ΓK . The grey areas are the continuum bands. Even modes are plotted as solid lines, odd modes as dashed lines. These dispersion curves are in this case calculated using FDTD (Finite Difference Time Domain), which basically consists of a full calculation of the field components when discretizing Maxwell equations in both time and space [AGI 03]. Here we use a 2D calculation; the vertical stack is taken into account through an effective index [QIU 02a].

The W1 guide is monomode within the two wavelength domains indicated by braces below and above the odd mode. For light propagation, we will operate the W1 guide within these two domains, as it is always better to operate with a monomode guide to prevent mode mixing. This even mode exhibits a marked cut-off at the Brillouin zone edge, at $k_{//} = \pi/a$. The frequency at which this cut-off occurs is strongly dependent upon the air filling factor: thus, measuring the spectral position of this cut-off leads to an optical measurement of the filling factor.

The W3 guide is multi-mode throughout the gap. The periodicity that exists along the waveguide boundaries enables, through a contra-directional mechanism, the coupling of two modes of the same waveguide, provided that they have the same symmetry. This coupling mechanism opens a mini-gap, which is shown here by braces in the case of the two first even modes. These mini stopbands are a specific signature of propagation in a PhC guide [OLI 01]. We will see in section 2.4.1 that the spectral width of this mini stopband enables us to estimate the quality of the etched holes.

2.2.3. Losses

As has already been pointed out, all the modes supported by defects in the photonic gap are above the substrate light line, so out-of-plane losses occur through coupling to radiation modes. The amount of loss can be calculated using 3D FDTD, but this calculation is very time consuming and hardly takes into account fabrication imperfections such as non-cylindrical holes and etched surface roughness.

Benisty *et al.* proposed describing losses as a fictitious dissipation due to the air contained within the holes, thus adding an imaginary part to the dielectric constant of holes air [BEN 00]. Simulations are then performed in 2D, making their duration reasonable, and include an ϵ'' . This ϵ'' parameter is a phenomenological parameter, which is adjusted when comparing the simulation results to the measured performances. For example, the mini stopband depth and width of the W3 fundamental mode are directly related to losses [QIU 02b]. This ϵ'' parameter enables us to globally qualify the etching technology: finite hole depth, non perfect geometry, roughness (see section 2.4.1).

2.3. Technology for drilling holes on InP-based materials

Characteristic dimensions of holes required for a photonic crystal device operating in the optical domain are well below the micrometer: this technological challenge has delayed the application of PhC in the optical domain. For InP-based materials having an optical index larger than 3 and operating at $\lambda=1.55\mu\text{m}$, the gap lies at reduced frequencies around $u=0.26$, so PhC periods are close to $a=400\text{nm}$. When the air filling factor is around 35%, the holes are around 200–250nm in diameter. Vertical stacks for active functions are larger than $3\mu\text{m}$ (each buffer layer for carrier injection has to be at least $1.5\mu\text{m}$ thick in order to limit the interaction of the mode optical field with the metal of the electrode). The aspect ratio of the holes then has to be larger than 10, and closer to 20 – a real challenge in InP-based materials.

2.3.1. Mask generation

Nanometer scale features are easily fabricated using electron beam lithography. This method is very versatile, and enables the position of the holes to be changed on demand in order to investigate new structures. When structure designs are established, a lithographic mask can be generated, and deep UV lithography (248nm, 196nm) is then successfully used [BOG 02]. The advantage of such a process is that it implements the fully established and highly parallel microelectronic lithography.

Having investigated advanced structures, we have generated here all the patterns using e-beam lithography. The mask used for etching the semiconductor material is realized in two steps, described in Figure 2.3a: first, a dielectric layer is deposited on the semiconductor material (here we use SiO_2), and then an electron sensitive resist such as PMMA (PolyMethylMetAcrylate) is spin-coated on top.

PMMA is a positive resist. Holes are exposed. After development (the developer is here a solvent for the monomer which is generated when the impinging electrons break the polymer links), patterns are holes in the PMMA layer. This mask is then used to dry-etch the SiO_2 layer. When holes are correctly transferred to the underlying SiO_2 layer, the remaining PMMA is removed by plasma-ashing. This two-step mask generation is necessary as the PMMA resist is very fragile and is difficult to use for semiconductor etching (work on this area is in progress).

2.3.2. Dry-etching of InP-based semiconductor materials

Generally speaking, semiconductor materials can be etched either by wet etching – electrophile agents are then used which reveal crystallographic planes, or by dry-etching – which is a combination of physical and chemical etching within a plasma containing chemically active species and ions. Part of the etched products is evacuated by sublimation. Chlorine gas is commonly used for III–V materials plasma etching.

Here we perform dry-etching since etching holes requires a strongly anisotropic process. The larger problem when etching holes versus other sub-micrometer features such as micro-pillars or line gratings is that it is difficult to evacuate etched products from the bottom of deep holes. Because sublimation of etched products plays an important role, InP-based materials are much harder to etch than GaAs-based materials: in the case of GaAs, the etched products have comparable volatilities (Ga and As are on the same line of the periodic classification), whereas in the case of InP, the etched products have wildly different sublimation temperatures: in the case of chlorine gas, PCl_3 is volatile at room temperature, while a temperature of 200°C must be reached to evaporate InCl_3 in the same pressure conditions. Temperature is in this case a critical parameter of the etching process.

Due to the easier technology for patterning GaAs-based materials, all the fundamental PhC investigations in the 1990s were performed on GaAs structures.

Plasmas which are made denser than the one obtained in a classical Reactive Ion Etching (RIE) – Capacitive Coupled Plasma (CCP) – greatly improve the etched depth in the case of the geometry of the holes. These dense plasmas are generated either by Inductive Coupled Plasma (ICP) or by Electron Cyclotron Resonance (ECR).

Another deep-etching technique combines Ion Beam Etching (IBE) with a chemical reaction when injecting Cl_2 gas directly at the surface of the sample: this is then called Chemically Assisted Ion Beam Etching (CAIBE). This technique is still a lab technique; results presented here were obtained in the laboratory of KTH, Kista (Sweden). For the removal of etched products, the temperature is raised to 230°C [MUL 02].

Figure 2.3b shows CAIBE etched holes deeper than $3\mu\text{m}$. These holes are not perfectly cylindrical, and it is difficult to estimate the roughness of the etched surfaces. Optical characterization is needed to assess the air filling factor value correctly, and also the quality of the etched surfaces.

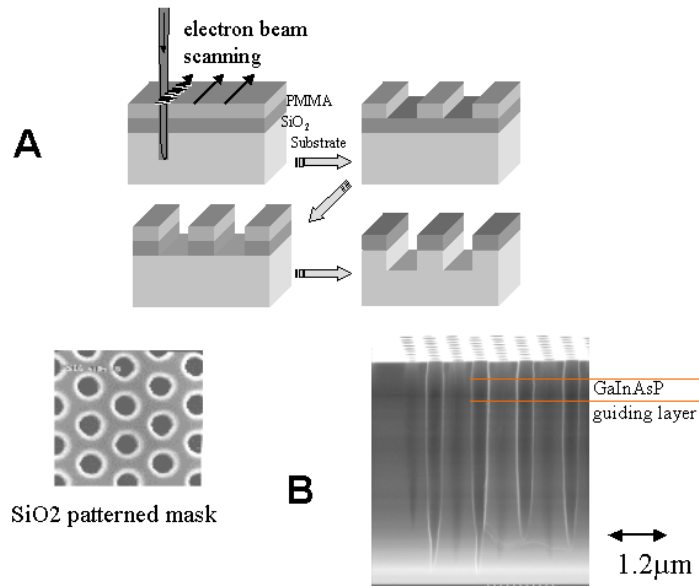


Figure 2.3. A: Mask generation in a dielectric layer using electron beam lithography; B: CAIBE etched holes in a GaInAsP semiconductor layer and buffer

2.4. Modal behavior and performance of structures

2.4.1. Passive structures

It is very important to grasp the monomode/multimode behavior of a PhC waveguide in order to understand the spectral performance of more complex PhC structures.

The characterization method used here is the so called end-fire method: the light generated by an external tunable monomode laser is injected through a micro-lensed fiber in the device. Note that this device is transparent at these wavelengths. The polarization of the injected light is maintained under tuning. The spectrally resolved transmission is measured on a wavelength domain ranging from 1,410nm to 1,590nm. Fourier transforming the transmission spectrum enables us to identify all the optical cavities existing within a structure, which are revealed by the interferences of the coherent light. The fringe contrast of each cavity is related to the internal optical losses and to the reflection coefficient amplitude of the two

reflectors that limit that cavity. We systematically use this fringe contrast measurement technique to characterize each cavity [TAL 03b].

2.4.1.1. *Straight guides, taper*

2.4.1.1.1. Straight guides

All W_i PhC waveguides, except W_1 , are multimode. In order to measure propagation losses, one must know on which mode propagation occurs. In order to undoubtedly inject the light on the fundamental mode of a W_i guide (and symmetrically collect the light exiting on the fundamental mode), each W_i is inserted between two deep ridge access guides which are monomode with a comparable modal profile. These ridges are realized during the same e-beam lithography step performed for the holes, thus their axes are aligned with the W_i guides' axes. The Scanning Electron Microscope (SEM) picture in Figure 2.4a shows a top view of the ridge access guide on the left (the white area in between two dark lines) and a W_2 Γ K waveguide on the right. The overall cavity formed by the input ridge waveguide + W_i + output ridge waveguide is limited by two cleaved facets. After calibration of propagation losses within the ridges and the reflection coefficient of the cleaved facets, measuring the transmission for different lengths of the W_i guide reveals the propagation losses within the W_i guide, and the reflection at the interfaces' ridge/ W_i [TAL 01].

Figure 2.4b displays the variation of propagation losses (overall losses including in-plane and out-of-plane losses) versus W_i guide width, reported here through the number i of missing rows. Large losses in the case of W_1 can be attributed to the strong interaction of the field with the innermost row of holes. For larger W_i , losses are reduced, and we can expect that losses will continuously reduce when i is increasing. But, the loss figure obtained for W_7 is of the same order as the one obtained for W_5 . We can demonstrate (through the width of the peak in the Fourier Transformed spectrum) that when propagating in a W_7 , even when injecting on the fundamental mode, higher order modes are excited. So part of the light is propagated on these modes, which are more lossy, leading to an overall propagation loss value larger than that which could be expected for a propagation performed only on the fundamental mode.

Following the dispersion curve of W_1 (Figure 2.2b), one can see that the even mode is slowed down when approaching the Brillouin zone edge. In a certain frequency range, no transmission is possible as no mode exists, and for even smaller frequencies, light propagation is again achieved through the continuum of optical modes. The spectral position of this cut-off is strongly dependent on the air filling factor ff . Figure 2.4c plots this cut-off for two different ff values. This optical method allows the determination of ff with an accuracy better than 1% [TAL 04b].

Turning to the multimode W3 waveguide, we refer again to the dispersion curve in Figure 2.2b. Figure 2.4d displays the transmission spectrum of a W3: the measured transmission is shown by a solid line, an FDTD simulation without losses is displayed as a dashed line, and a simulation including losses through the ϵ'' parameter is plotted in bold dashed lines, here $\epsilon''=0.10$ [SWI 01]. The mini stopband observed on the transmission spectrum is a signature of this waveguide. The ϵ'' parameter is a phenomenological parameter whose value is adjusted to fit the measured data. The smaller ϵ'' , the lower the losses. We recall here that above the substrate light-line, losses always exist through coupling vertically to radiative modes.

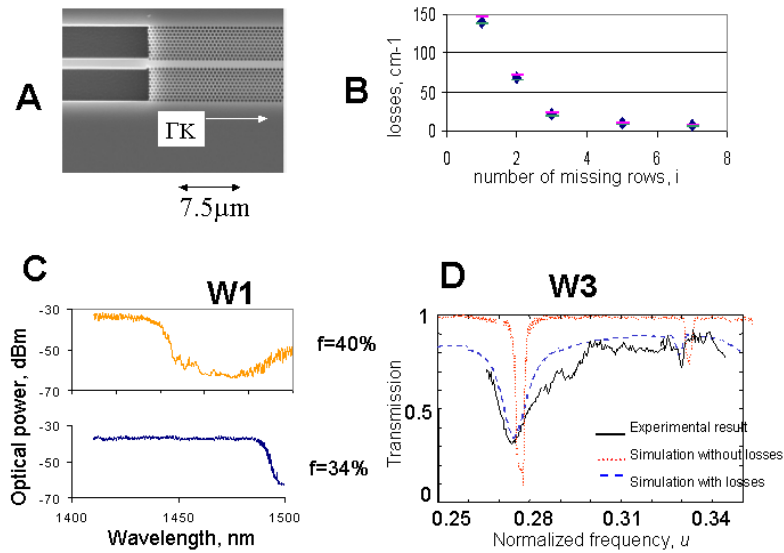


Figure 2.4. A: photonic crystal guide: Scanning Electron Micrograph (SEM) top view of a ridge access guide and a W2; B: Propagation losses versus PhC guide width, for W1; C: Cut-off of W1 mode, versus ff (air filling factor); D: Mini stopband in a W3

2.4.1.1.2. Taper

W1 waveguide is lossy, but has the advantage of being monomode. Monomode waveguides are the preferred choice for Integrated Optics devices as they prevent mode mixing; we make this choice too, and try to use W1, but on limited sections in order to minimize overall cumulative propagation losses. Such large losses for the W1 fundamental even mode stem from strong lateral confinement: Figure 2.5 displays the transverse modal profile of the fundamental mode of a ridge guide having the same confinement as the W1 mode in the refractive region. Due to this

strong lateral confinement, the mode is laterally squeezed, and thus is greatly extended vertically in the case of the low index contrast InP-material system. Such a modal shape is not at all well adapted to that of a classical monomode ridge waveguide typically 1.2 to 1.5 μm wide. A W3 waveguide is wider, and its fundamental mode is correctly adapted to the mode of a classical ridge access guide [TAL 01].

To reconcile both aspects, an original geometry has been proposed for a taper which adapts the fundamental mode of W3 to the fundamental mode of W1. This geometry is based on a continuous variation of the holes' size and depth, thus adapting the mode in both directions of the transverse plane [LAL 02]. In theory, such a geometry enables almost 100% of the light from a W3 to a W1 to be coupled, provided that we are able to produce holes with a diameter as low as 70nm.

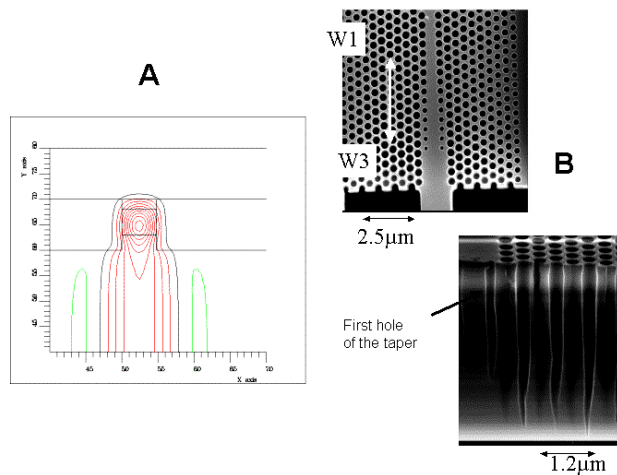


Figure 2.5. A: Optical mode confinement in a “W1-like” environment; B: SEM top view of the taper, and cross view of the first hole

Figure 2.5b displays the SEM picture of the first hole of the taper. In this fabrication run the diameter is 180nm and thus is still too large. Recent results have been obtained with a 100nm diameter hole within the taper; the coupling efficiency in that case is as high as 70% on a spectral domain larger than 80nm below the odd mode, and reflection is limited to 1% [TAL 04a].

2.4.1.2. Bend, combiner

2.4.1.2.1. Bend

The main drawback of bends realized by index contrast is the large radius of curvature required for low bending losses, which leads to very extended devices. In the case of shorter bends (large curvature), polarization conversion also occurs [VAN 96]. PhC bends have the advantage of very short bends without in-plane losses. Being in the photonic gap, there is no possibility of coupling with in-plane radiation modes. The bend geometry has to be optimized to reduce and even cancel the reflection, which is the only in-plane mechanism that can reduce the transmission. Several geometries have been investigated when moving holes in the very corner. Partly optimized designs exist for each W_i width [OLI 02a]. But one should pay attention to two points:

- 1) After the bend, the light has to exit just as it entered, on the fundamental mode; this makes it possible for bends to cascade, or for a bend to be included in a more complex PIC.
- 2) The polarization must not have been altered.

The bend breaks the symmetry of the crystal, so as soon as the guide is multimode, the bend projects the fundamental mode on all the modes supported by the guide [BEN 02, MEK 96]. FDTD simulation gives a clear view of a multimode versus a monomode propagation at the output of the bend. This multimode behavior is delicate to evidence from the far field pattern.

To follow the triangular lattice geometry, bends turn at 60° , so a practical fabricated structure with cleaved parallel facets has to include two consecutive bends. We address here point 2, investigating the effect of the bend on the polarization state. Figure 2.6 shows SEM pictures of two cascaded bends for W_3 and W_1 waveguides, again with the transmission spectra. For each PhC guide width an optimized geometry has been implemented: it corresponds to six holes moved in the case of W_3 , and one hole moved in the case of W_1 .

The external source uses a polarization maintaining fiber with a polarization rejection rate higher than 17dB. The light is injected on the TE polarization, using a polarization maintaining fiber, and is analyzed at the output of the collecting fiber through a polarizer. This enables the power level at the output to be measured for both polarizations.

For W_3 bends, we can see in Figure 2.5a that the power level on TM is only 10dB smaller than the one on TE: this means that part of the light injected on the TE polarization is now collected on TM; some polarization conversion has occurred in this bend. In the case of W_1 bends, the measured TM level at the output is 17dB

lower than the TE one, which is the source rejection. No polarization conversion (or below 17dB) has occurred.

In conclusion we could say that W1 is lossy, but it is monomode and no polarization conversion occurs in the bend, whereas W3 has lower propagation losses, but some polarization conversion occurs in a bend.

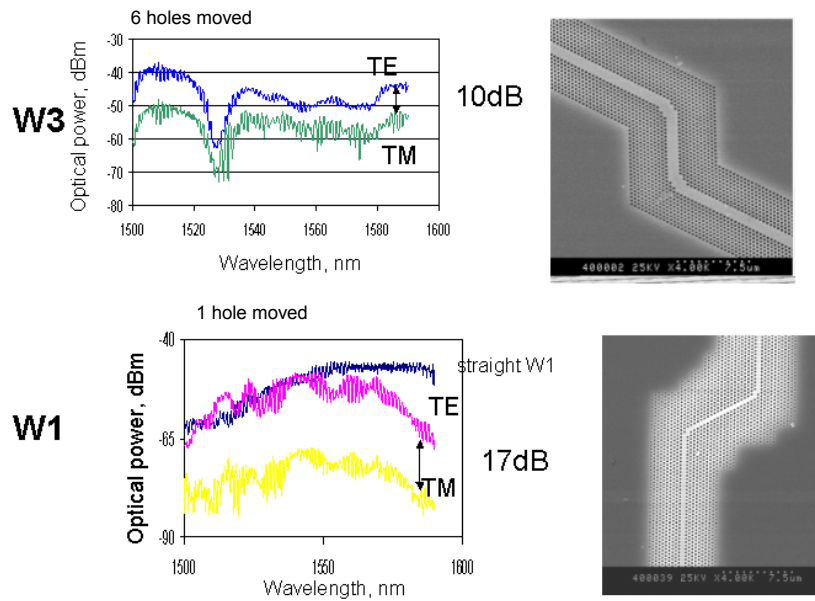


Figure 2.6. Double bend in W1 and W3 PhC guides: on the left, optical transmitted power versus wavelength for both TE and TM polarizations; on the right, an SEM picture of each double bend

The best bend design ideally combines a wide PhC guide, e.g. W3 in the straight sections (for low propagation losses), and a narrow PhC guide, e.g. W1 in the very bend, which does not produce polarization conversion, and excites only the fundamental mode of the wide guide at the exit. We have realized such a bend including tapers between the straight W3 sections and the W1 bend [TAL 04a].

The FDTD simulation in Figure 2.7a shows that the light exits here on the fundamental mode of the W3. The fabricated structure (SEM picture in Figure 2.7b with the detail of the bend and the access taper) demonstrates losses as low as 1.5dB

per bend, when compared to a straight deep ridge (plotted as a dashed line), on a 30nm wide spectral range.

It is clear from the SEM picture that there is room for improvement in the fabrication – taper holes have to be as small as 70nm in diameter, as previously stated. Performance will consequently be improved.

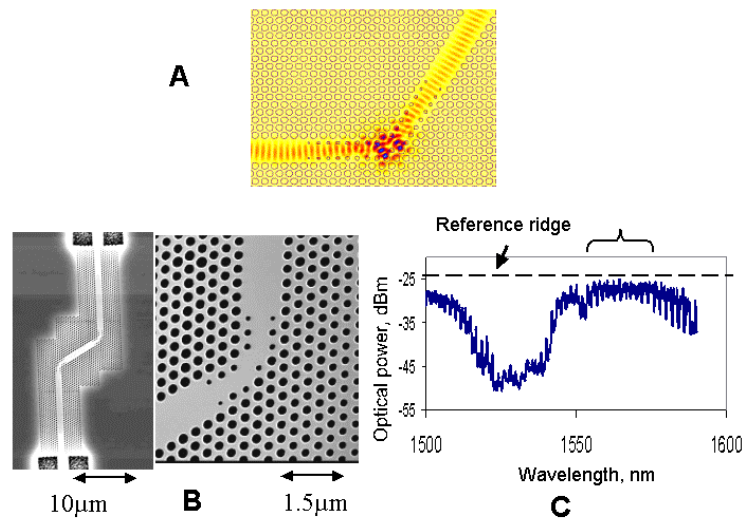


Figure 2.7. A: FDTD simulation ($2D+\epsilon''$) of a bend including a taper; B: SEM pictures: general overview, and detail of the fabricated bend; C: Measured optical transmitted power – the straight guide is plotted as a reference

2.4.1.2.2. Y branching combiner

Optical signal processing will require more complicated circuits such as interferometers (Mach-Zhender ...). A generic building-block is a combiner, in which at least two optical paths have to be combined (divided).

Figure 2.8a is an SEM picture of a two-branch combiner fabricated with W1 guides and including a taper at each input and at the output. Different geometries have been investigated for the combining region. The design rule followed here is to limit the excitation of higher order modes in the enlarged section. The best result is the one obtained on the structure shown on the enlarged SEM picture of the combining region, when adding a single hole of the same size with respect to a canonical design. Symmetry considerations are used to optimize this design.

Transmissions plotted in Figure 2.8b show that both entrances C1 and C2 have the same power budget, which is 3dB lower than that of a bend [TAL 04b]. This is the same performance as a “classical” Y junction, but for a combiner which is 100 times smaller (10^4 in area footprint). The remaining oscillations on both the C1 and C2 spectra arise from the interference fringes due to the reflection at the cleaved facets which have no anti-reflective coating. The cut-off at 1,540nm is the signature of the W1 guide.

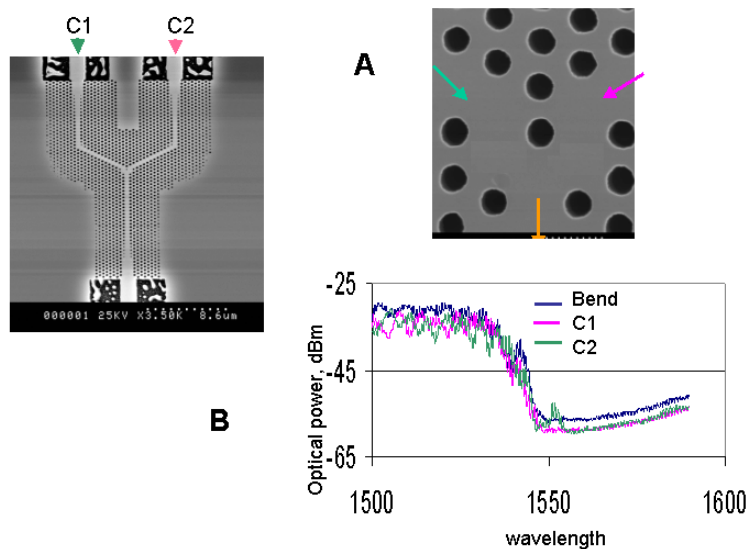


Figure 2.8. A: SEM pictures of a Y combiner: general overview, and detail of the combining section; B: Measured transmission spectra for both entrances – the bend alone is plotted as a reference

General rules for designing PhC guiding structures are based on symmetry considerations and modal shapes. It is not possible here to resolve the inverse problem as it is commonly done for 1D Bragg mirrors, where the stack of layers can be calculated to provide a spectral reflectance defined beforehand.

Attempts are now made to obtain the best geometry using genetic algorithms: the parameters are the holes' positions and sizes, a figure of merit is defined, and the algorithm produces the geometry that allows the best fit for this figure. Very little understanding of PhC physics is required to define such structures, though some optimal guiding geometries have been produced [HAK 05]. This approach is

probably time consuming, and is limited to guiding structures. Resonant structures, as we will see below, are based mainly on mode shaping.

2.4.1.3. *Filters*

Let us recall that in Wavelength Division Multiplexing (WDM) networks, wavelengths are typically spaced at 0.8nm intervals (100GHz at 1.55 μ m), or even lower intervals (from 50 to 25GHz). A directive filter makes it possible to add or drop one wavelength selected among all the transmitted wavelengths. The filter rejection has to be better than 25dB. These requirements can be fulfilled for a filter having a quality factor Q larger than 2,000.

The designs of filters, including PhC structures, can be based on the co-directional coupling mechanism, as in classical filters, channeling the light from one waveguide to another through a resonator. Specific designs implementing the contra-directional coupling that exists in PhC waveguides can also be produced.

2.4.1.3.1. Co-directional coupling

Before fabricating a fully-fledged filter (guide + resonator + guide), we will investigate a drop structure which includes a cavity coupled to a guide. We want to demonstrate that one wavelength, which corresponds to a resonant mode of the cavity, is missing after transmission.

Figure 2.9a shows the SEM picture of an H2 cavity coupled to a W3 guide. The transmission spectrum, after filtering the fringes due to the overall resonator limited by the two cleaved facets, shows a dip at 1,440nm, and the quality factor is 200. The light is co-directionally coupled from the refractive mode of W3 to the whispering gallery mode of H2 (see section 2.2.2, Figure 2.2a).

The filter in Figure 2.9b couples an H7 cavity to a W3 guide. The epitaxial layers used for this design include quantum boxes on GaAs whose luminescence is excited by optical pumping. In the case where the cavity is separated from the guide by two rows of holes, the light is extracted from the guide, with a quality factor of 800 (spectrometer limited), through the slow mode of the mini stopband, as represented by the dark arrows [SMI 00].

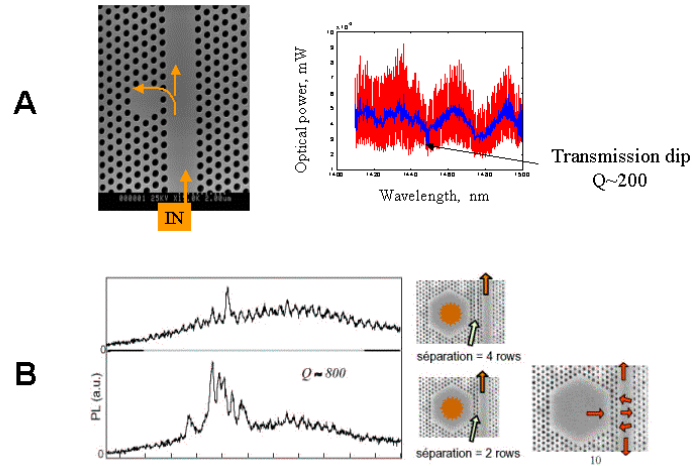


Figure 2.9. A: Guide-cavity coupling through the gallery mode;
 B: Guide-cavity coupling through the slow mode of the mini stopband

2.4.1.3.2. Contra-directional coupling

Within a multimode PhC waveguide, the mini stopband is the result of contra-directional coupling between two modes of this guide, through the periodicity of the PhC guide itself. When the design makes it possible to collect the light on the backward mode, this wavelength is dropped from the forward mode, over the spectral domain of the mini stopband.

The structure proposed by Qiu *et al.* [QIU 03] includes 2 PhC guides: one is a W1, the other is a W0.8; both are separated by one row of holes (Figure 2.10a). Coupling between these two guides creates a mini stopband, visible on the dispersion curve. The optical spectrum measured on the collection guide (drop) is compared to the calculated one. Light is correctly transferred and the quality factor is $Q=150$, again limited by out-of-plane losses (device on InP substrate).

Benisty *et al.* have proposed a structure based on the slow mode of the mini stopband of a W5 guide or similar (Figure 2.10b). This structure also includes quantum boxes on GaAs for characterization. Both transmissions measured on the incident guide (bar) and on the transferred guide (cross) are displayed as bold lines in Figure 2.10b; the calculated transmissions are plotted as grey lines [OLI 03]. The quality factor Q is 150, again limited by the out-of-plane losses.

All these results show that it is difficult to reach the desired Q value when operating on a substrate. FDTD simulations including out-of-plane losses through the ϵ'' parameter clearly evidence that any efficient in-plane wavelength selective mechanism loses its effectiveness when including out-of-plane losses, even a low level of losses. On the other hand, quality factors as large as 100,000 have recently been reached for membrane structures on SOI material [AKA 05]. Design rules for efficient resonators are based on modal shape analysis taking into account the light cone.

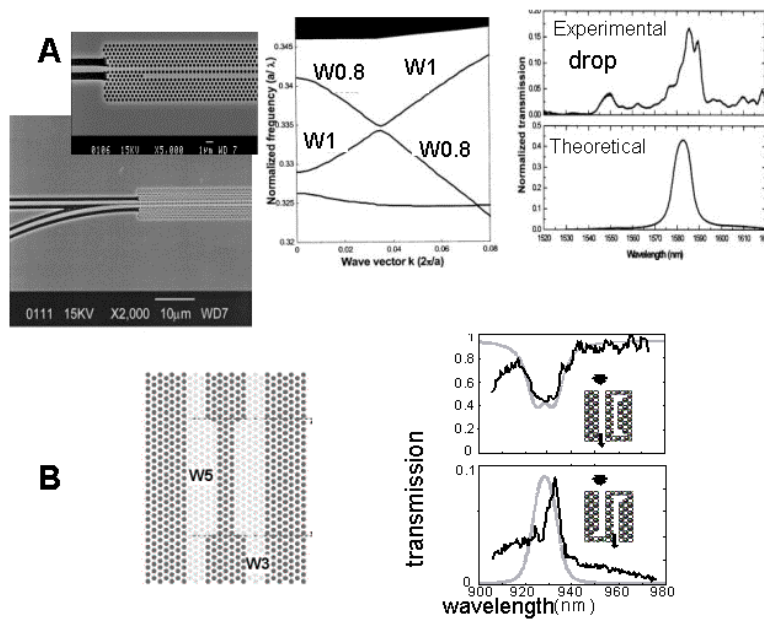


Figure 2.10. A: Contra-directional coupling, through the mini stopband, in the W1/W0.8 system; B: Measured transmission of coupling through the mini stopband of W5

2.4.2. Active structures: lasers

PICs fulfilling all the optical functions will require active functions, such as emission, amplification or fast tunability obtained through carrier injection or biasing. Injecting carriers or biasing a deeply etched structure with holes is very difficult.

A laser is a good example of an “active function”. The threshold current offers reliable information about surface recombination due to all the defects produced during etching, while external efficiency is related to optical losses for the lasing mode. One can also take advantage of the periodicity inherent in the PhC to reach monomode operation.

Here we present results on full-PhC edge-emitting lasers, operating on continuous wave under electrical injection at room temperature.

In the structure presented in Figure 2.11a, spectral selectivity is provided by coupling 40 cavities of size H7 [HAP 01], following the proposal of the so called CROW (Coupled Resonator Optical Waveguide) [OLI 01 and references therein]. Coupling such a large number of cavities ensures a very large side mode suppression ratio (SMSR) for the resonant mode.

The design proposed in Figure 2.11b has no holes in the axis of the cavity. In this case, monomode behavior is achieved by adding another periodicity on the PhC matrix: one hole is added every six holes along the W5 Γ K guide. This additional periodicity folds the dispersion curve and allows the fundamental mode to be folded within the gap, to the 10th order.

This behavior is “DFB-like”, but without losses on the other orders as they lie outside of the gap. This laser also has a PhC rear mirror calculated to have its maximum efficiency at the lasing wavelength [LAB 99]. The measured SMSR was found to be 25dB, and the external efficient reached 0.17 W/A; these performances are comparable to devices actually implemented in optical networks [TAL 03a].

These results demonstrate that PhC structures are efficient for active optical functions. As amplification can be obtained on the same electrical scheme, a PhC amplifier can be included along with a passive PhC function, leading to a full PhC-based PIC demonstrating an overall power budget of 0dB.

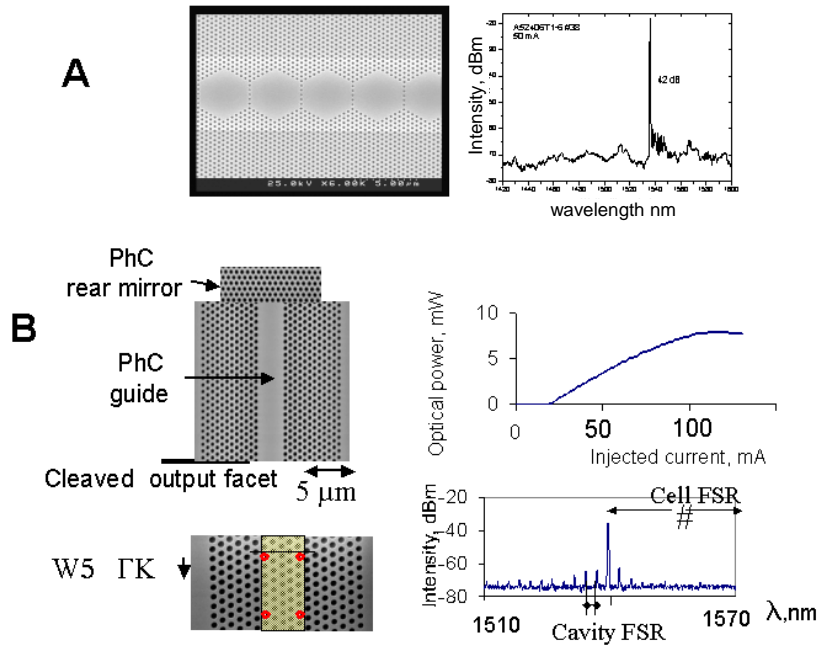


Figure 2.11. Lasing operation of full photonic crystal lasers. A: Coupled cavity structure (CROW) showing a very large rejection; B: “DFB-like” laser, showing a large rejection, and a large external efficiency $\eta=0.17$

2.5. Conclusion

This chapter has discussed several passive and active devices based on photonic crystals. These devices can be introduced as building blocks in Photonic Integrated Circuits. Substrate-based structures are found to be adequate to obtain lasing emission or amplification, but when resonant performances are required, the limitation which is inherent as a result of losses through out-of-plane radiation modes is not acceptable for WDM applications.

Photonic crystals also have interesting properties outside the photonic gap, related to the particular curvature of dispersion bands, such as the super-prism effect [KOS 98] or autofocussing.

The nanotechnology required for these devices has been intensively developed, and has enabled the fabrication of structures including holes with diameters smaller than 100nm. Investigations are currently in progress to estimate the ultimate

performances of PhC structures within the limits of today's technology (lithography accuracy, etching quality).

2.6. References

- [AGI 03] Agio M "Optical properties and wave propagation in semiconductor-based two-dimensional photonic crystals" PhD, University of Pavia, Italy
- [AKA 03] Akahane Y, Mochizuki M, Asano T, Tanaka Y and Noda S (2003) "Design of a channel drop filter by using a donor-type cavity with high-quality factor in a two-dimensional photonic crystal slab" *Appl. Phys. Lett.* 82: 1341
- [AKA 05] Akahane Y, Asano T, Takano H, Song BS, Takana Y and Noda S (2005) "Two-dimensional photonic-crystal-slab channel-drop filter with flat-top response" *Optics Express* 13: 2512
- [BEN 96] Benisty H (1996) "Modal analysis of optical guides with two-dimensional photonic band-gap boundaries" *J. Appl. Phys.* 79: 7483
- [BEN 99] Benisty H, Weisbuch C, Labilloy D, Rattier M, Smith CJM, Krauss TF, De La Rue R, Houdré R, Oesterle U, Jouanin C and Cassagne D (1999) "Optical and confinement properties of two-dimensional photonic crystals", *J. Light Technol.* 17: 2063
- [BEN 00] Benisty H, Labilloy D, Weisbuch C, Smith CJM, Krauss TF, Cassagne D, Béraud A and Jouanin C (2000) "Radiation losses of waveguide-based two dimensional photonic crystals: positive role of the substrate" *Appl. Phys. Lett.* 76: 532
- [BOG 02] Bogaerts W, Wiaux V, Taillaert D, Beckx S, Luyssaert B, Bienstman P and Baets R (2002) "Fabrication of photonic crystals in Silicon-on-Insulator using 248nm deep UV lithography" *IEEE J. Sel. Top. Quant. Elec.* 8: 928
- [HAK 05] Hakansson A and Sanchez-Dehesa J (2005) "Inverse designed photonic crystal de-multiplex waveguide coupler" *Optics Express* 13: 5440
- [HAP 01] Happ TD, Markard A, Kamp M and Forchel A (2001) "Single-mode operation of coupled-cavity lasers based on two-dimensional photonic crystals" *Appl. Phys. Lett.* 79:4091
- [JOA 95] Joannopoulos JD, Meade RD and Winn JN (1995) *Photonic Crystals*. Princeton University Press, Princeton, NJ
- [KOS 98] Kosak H, Kawashima T, Tomita A, Notomi M, Tamamura T, Sato T and Kawakami S (1998) "Superprism phenomena in photonic crystals" *Phys. Rev. B* 58: r10097
- [LAB 99] Labilloy D, Benisty H, Weisbuch C, Krauss TF, Cassagne D, Jouanin C, Houdré R, Oesterle U and Bardinal V (1999) "Diffraction efficiency and guided light control by two-dimensional photonic-bandgap lattices" *IEEE J. Quant. Electron.* 35: 1045

- [LAL 02] Lalanne P and Talneau A (2002) “Modal conversion with artificial materials for photonic-crystal waveguides” *Optics Express* 10: 354
- [LOU 05] Lourtioz JM, Benisty H, Berger V, Gérard JM, Maystre D and Tcheltnokov A (2005) *Photonic Crystals: Towards Nanoscale Photonic Devices*, Ed. Springer, Berlin, Heidelberg, New York
- [MEK 96] Mekis A, Chen JC, Kurland I, Fan S, Villeneuve PR and Joannopoulos JD (1996) “High transmission through sharp bends in photonic crystal waveguides” *Phys. Rev. Lett.* 77: 3787–90
- [MUL 02] Mulot M, Anand S, Carlström CF, Swillo M and Talneau A (2002) “Dry etching of photonic crystals in InP-based materials” *Physica Scripta*, T101: 106–9
- [OLI 01] Olivier S, Rattier M, Benisty H, Weisbuch C, Smith CJM, De La Rue RM, Krauss TF, Oesterle U and Houdré R (2001) “Mini-stopbands of a one-dimensional system: the channel waveguide in a two-dimensional photonic crystal” *Phys. Rev. B* Brief Report 63: 113311
- [OLI 02a] Olivier S, Benisty H, Weisbuch C, Smith CJM, Krauss TF, Houdré R and Oesterle U (2002) “Improved 60° bend transmission of submicron-width waveguides defined in two-dimensional photonic crystals” *IEEE, J. Lightwave. Technol.* 20: 1198–1203
- [OLI 02b] Olivier S, Benisty H, Smith CJM, Rattier M, Weisbuch C and Krauss TF (2002) “Transmission properties of two-dimensional photonic crystal channel waveguides” *Optical and Quantum Electronics* 34: 171–181
- [OLI 03] Olivier S, Benisty H, Weisbuch C, Smith CJM, Krauss TF, Houdré R and Oesterle U (2003) “All-Photonic crystal add-drop filter exploiting low group-velocity modes” WeB1.2, conference ECIO
- [QIU 02a] Qiu M (2002) “Effective index method for heterostructure-slab-waveguide-based two-dimensional photonic crystals” *Appl. Phys. Lett.* 81: 1163
- [QIU 02b] Qiu M, Jaskorzynska B, Swillo M and Benisty H (2002) “Time-domain 2D modelling of slab-waveguide-based Photonic Crystal devices in the presence of radiation losses” *Microwaves and Optical Tech. Lett.* 34: 387
- [QIU 03] Qiu M, Mulot M, Swillo M, Anand S, Jaskorzynska B, Karlsson A, Kamp M and Forchel A (2003) “Photonic crystal optical filter based on a contra-directional waveguide coupling” *Appl. Phys. Lett.* 83: 5121
- [SMI 00] Smith CJM, De La Rue RM, Rattier M, Olivier S, Weisbuch C, Krauss TF, Houdré R and Oesterle U (2000) “Coupled guide and cavity in a two-dimensional photonic crystal” *Appl. Phys. Lett.* 78: 1487
- [SWI 01] Swillo M, Qiu M, Mulot M, Jaskorzynska B, Anand S and Talneau A (2001) “Characterisation and modeling of InP/GaInAsP photonic-crystal waveguides” ECOC 2001
- [TAL 01] Talneau A, Legouezigou L and Bouadma N (2001) “Quantitative measurement of low propagation losses at 1.55µm on planar photonic crystal waveguides” *Opt. Lett.* 26: 1259–61

- [TAL 03a] Talneau A, Mulot M and Anand S (2003) "CW monomode operation of efficient full-photonic crystal lasers at 1.55 μm " PDTh 4.2.1: 44–5, ECOC 2003; also *Appl. Phys. Lett.* (2004) 85: 1913
- [TAL 03b] Talneau A, Mulot M, Anand S and Lalanne P (2003) "Compound cavity measurement of transmission and reflection of a tapered single-line photonic-crystal waveguide" *Appl. Phys. Lett.* 82: 2577–2579
- [TAL 04a] Talneau A, Agio M, Soukoulis CM, Mulot M, Anand S and Lalanne P (2004) "High bandwidth transmission of an efficient photonic crystal mode converter" accepted at the PECS V conference, Kyoto, March
- [TAL 04b] Talneau A, Mulot M, Anand S, Olivier S, Agio M, Kafesaki M and Soukoulis CM (2004) "Modal behavior of single-line photonic crystal guiding structures on InP substrate" *Photonics and Nanostructures – Fundamentals and Applications*
- [VAN 96] Van Dam C, Spiekman LH, Van Ham FPGM, Groen FH, Van der Tol JJGM, Moerman I, Pascher WW, Hamamcher M, Heidrich H, Weinert CM and Smit MK (1996) "Novel compact polarization converters based on ultra short bends" *IEEE Phot. Technol. Lett.* 8: 1346–48

Chapter 3

Photonic Crystal Fibers

3.1. Introduction

Thanks to the great strides taken at the very beginning of the twenty-first century, a large number of active and passive functions (emission, reception, filtering, wavelength multiplexing-demultiplexing ...) can be operated by means of photonic integrated circuits (PICs). Thus, as demonstrated in the preceding chapter, the necessary basic elements are now available for designing advanced integrated functions for high bit rate optical transmissions. However, to take full advantage of this progress, high quality connections with optical fibers must be achieved. The transmission fibers themselves must also exhibit higher and higher levels of performance. The connection between PICs and standard optical fibers usually involves a taper for adjusting the size of the mode. This is followed by a diffraction grating engraved in the circuit for extracting light. The measured coupling efficiency is higher than 25% and can potentially exceed 80% [MCN 03; TAI 03].

A considerable increase in the transmission bit rate into one single optical fiber has already been made possible, thanks to two major breakthroughs over the past 20 years: first, since 1985, the use of fibers operating in the single mode regime in the spectral bandwidth of the highest transparency of silica (around 1,550nm), and secondly, since 1990, the all-optical amplification of spectrally multiplexed high bit rate signals into rare earth doped fibers.

Nevertheless, there is still much to be done – in particular, increasing further the bit rate of optical communication around 1,550nm, and for many other applications

at different wavelengths, novel fibers must be designed in order to reduce, cancel or compensate for chromatic dispersion at the operating wavelength. Indeed, the only means of significantly changing chromatic dispersion is to act on the contribution of the guide to this parameter: this means that one must imagine fibers in which the confinement of the guided mode spectrally evolves in a radically different way from that observed in usual fibers.

In order to meet this need, a new generation of optical fibers with specific micro or nano-structuration of the cladding, known under the generic designation of “photonic crystal fibers” (PCFs), has been conceived. As we will see below, a particular class of PCFs guides light by means of a photonic bandgap effect similar to that used in photonic crystals described in the preceding chapter. With these fibers, low loss propagation of light can be achieved in a hollow core provided that the submicrometric structuration of the cladding is perfectly controlled over long lengths (tens or hundreds of meters, indeed kilometers). These fibers are not designed to perform particular new functions, unlike PICs. Their main job is to provide propagation properties over long distances that cannot be obtained with other guides. In other words, they have a complementary role to play in the field of photonics.

The history of photonic crystal fibers concretely begins in 1995, when a group of British researchers under the direction of Philip St J. Russell (Optical Research Center in Southampton, later University of Bath) decided to exploit, in the domain of optical fibers, the concept of photonic band gap already implemented for confining light in periodic bidimensional semi-conductor structures [BIR 95]. The sought result is a guiding effect due to a transverse Bragg resonance into the cladding of the fiber. In other words, it is a 2D application of the principle of Bragg fibers with 1D periodical cladding theoretically demonstrated by Yeh *et al.* in 1978 [YEH 78].

The optical cladding of Bragg fibers is made of a stack of transparent layers with alternately high and low indices. It can efficiently confine light in the core, even if the index of this core is lower than the minimum index of the layers of the cladding, since the usual total internal reflection principle is not involved in the guiding mechanism [BRE 00b; FIN 99]. In particular, the core may be filled with air (hollow core). Obviously, the transmission bandwidth of such a fiber is limited to the transverse resonance bandwidth of the cladding [BRE 00a]. For a given pair of materials constituting the layers of the cladding, the central wavelength of the transmission bandwidth decreases with the thickness of the layers. For example, light can be guided in the near infrared (around 1,550nm) in a hollow core Bragg fiber whose cladding is made of 35 alternate layers of glass (As_2Se_3) and polymer (PEI) having refractive indices respectively equal to 2.82 and 1.66 at 1,550nm. In

order to guide light in this spectral bandwidth, the thickness of the layers must be equal to 270nm and 470nm respectively [KUR 04].

In Russell's project, the concentric layers with alternate high and low indices constituting the resonant optical cladding of the Bragg fibers are replaced by a hexagonal or a triangular lattice of air holes running along the axis, in a pure silica medium (Figure 3.1).

Because of the regular micro-structuration of the cladding, an optical wave launched into the core experiences a periodic modulation of the surrounding medium whatever the considered direction in the transverse plane. By analogy with photonic crystals designed to guide light into semi-conductor media, these microstructured fibers have been called "photonic crystal fibers". However, this novel type of optical waveguide differs radically, due to the fact that the light does not propagate any more perpendicularly to the invariant direction of the lattice (z direction), but parallel with this direction. This peculiarity must be pointed out because photonic bandgaps in fibers made of silica and air could not exist in other conditions. Indeed, in the case of a wave propagating perpendicularly to the hole axis, one could obtain a photonic bandgap whatever the polarization only if the air fraction (denoted f) was higher than 0.66 and, above all, if the index contrast was at least equal to 2.66; that is to say if it was higher than the 1.45 index contrast existing between air and silica [VIL 92].

These requirements are considerably reduced if we consider an optical wave whose wave vector has a non-zero axial component β . In this case, with an index contrast equal to only 1.45 and a sufficient air fraction, there are bandwidths where, for a given value β , one cannot find any pair of transverse components (k_x , k_y) whatever the considered polarization. The propagation of an optical wave at a wavelength in one of these bandwidths, through the periodic structure, is thus impossible: these bandwidths are photonic bandgaps. Then, if a defect set into the structure (hole with a size different from the others, or lake of hole) allows the existence of a mode with a propagation constant β , this mode must remain confined to this defect that behaves as the optical "core" of the fiber (Figure 3.1).

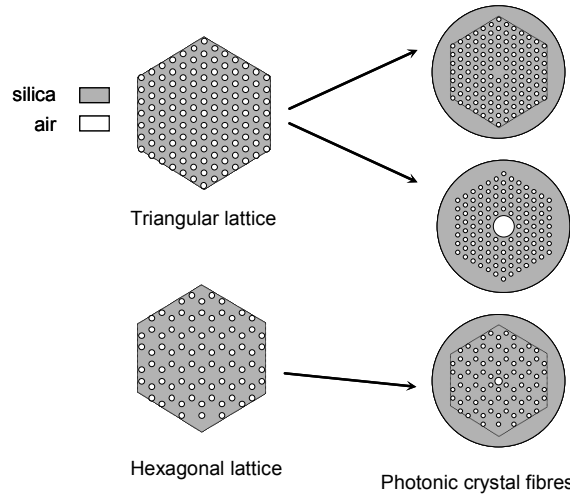


Figure 3.1. Cross-sections of photonic crystal fibers based on a triangular or hexagonal lattice of holes

3.2. Two guiding principles in microstructured fibers

The two main geometrical parameters of photonic crystal fibers are the diameter of the holes (d) and the spacing between two adjacent holes, called the “pitch” and denoted by Λ . These two dimensions are related to the air fraction f by $f \approx 0.91(d/\Lambda)^2$. The photonic bandgaps in the cladding of a triangular lattice air/silica photonic crystal with a 45% air-filling fraction can be identified in Figure 3.2 by means of $k\Lambda$ (grey zones), where k is the modulus of the wave vector in the vacuum [BIR 95]. These wavelengths are those likely to be guided into the core of the fiber. In the considered example, they exist for values of β greater than $7/\Lambda$.

However, it is necessary to distinguish two types of spectral bandwidths whose wavelengths cannot propagate into the cladding. The first one (the grey triangle on the right at the bottom of Figure 3.2) corresponds to wavelengths guided into the core by virtue of the total internal reflection principle. These wavelengths comply with the relation $\beta > k_0 n_{\text{eg}}$ where n_{eg} is the effective index of the fundamental mode able to exist in the heterogeneous cladding whose extension is supposed to be infinite. n_{eg} , which for simplicity’s sake will be referred to as “cladding effective index”, is given by:

$$n_{\text{eg}}^2 = \frac{\iint n^2 |E|^2 dS}{\iint E^2 dS} - \frac{\iint \left| \frac{dE}{dr} \right|^2 dS}{k^2 \iint E^2 dS} \quad (1)$$

where E is the electric field; n is the index of the silica (n_s) or of the medium filling the holes (n_a) depending on the considered point of the cross-section; S is the area of an elementary cell of this cross-section; and r is the distance to the center of the fiber. For these wavelengths there exists no possible refraction angle between the core and the cladding. In other respects, there are also four other narrow bandwidths, at shorter wavelengths, due to the true guiding by the Bragg resonance in the photonic crystal. These bandwidths are obtained for all the polarizations of the electromagnetic field, for values of the product $k\Lambda$ comprised between 8 and 12. Thus, for obtaining bandwidths in the near infrared or the visible, the pitch must be 1 to 2 μm . This means that it is far larger than that necessary in planar guided optics. The explanation lies once again in the fact that light propagates in the direction of invariance of the crystal and not following the plan of periodicity [BIR 04].

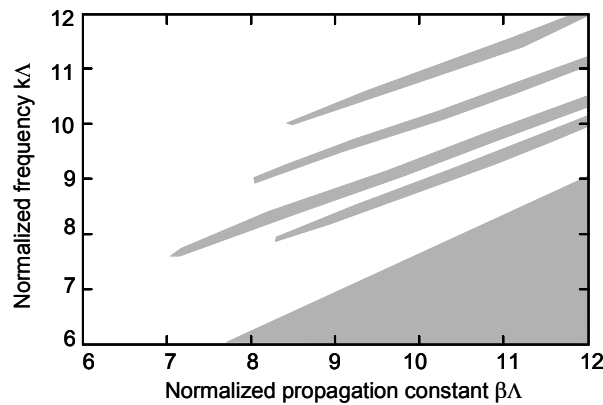


Figure 3.2. Photonic bandgaps in a triangular lattice air/silica photonic crystal with a 45% air-filling fraction [BIR 95]

The very first fiber manufactured to obtain a guiding effect in an air/silica photonic crystal consisted of one silica rod surrounded by narrow air holes with somewhat different diameters (0.2 to $1\mu\text{m}$), spaced at approximately $2.3\mu\text{m}$ intervals. A single mode was guided at different wavelengths from 337nm to 1,550nm, so one could think that the attempt was successful [KNI 96]. However, more careful study shows that this fiber cannot exhibit photonic bandgaps because the air-filling fraction into the cladding is too weak. The single mode guiding observed over a surprisingly large bandwidth is in fact easily explained by the two following considerations:

- n_{eg} , the effective index of the heterogeneous medium constituting the optical cladding, that is the result of a balance between the index of the air and the index of the silica, is necessary lower than that of the pure silica core (see section 3.4). The observed guiding effect is then simply due to the total internal reflection (TIR) at the

frontier between the cladding area and the core area whose limits are not physically located. The fiber behaves as a step index fiber with a numerical aperture equal to $NA=(n_s^2-n_{eg}^2)^{1/2}$. The core radius can be stated as $a_{eq}=0,64\Lambda$: indeed, one can show that the propagation constants of the modes of the step index fiber described by these opto-geometrical parameters are very close to those of the corresponding modes of the microstructured fiber [BRE 00c];

– as the extension of the field into the holes depends heavily on the wavelength, one can suspect that, considering equation 1, n_{eg} do not vary conventionally with respect to the wavelength. For example, for wavelengths significantly longer than d and Λ , the field largely spreads into the holes and, in a first approximation, it can be considered as a plane wave propagating into a medium having its index equal to $n_{eg}=[f.n_a^2 + (1-f).n_s^2]^{1/2}$. On the contrary, the shorter the wavelengths, the more the field avoids the air holes so that the effective index of the cladding asymptotically tends towards that of silica, under the form [REE 02]:

$$n_{eg} \approx \left(n_s^2 - \frac{d}{\Lambda} \left(\frac{\lambda}{\Lambda} \right)^2 \right)^{1/2} \quad (2)$$

The above relation shows that the numerical aperture proportionally decreases with the wavelength. The spatial normalized frequency $V=k.a_{eq}.NA$, that is in fact the Fresnel number in one dimension associated to the guided beam divided by 2π , gives one an indication of the number of spatial samples in this beam, that is to say, of the number of modes that can be guided. V tends from lower values towards a limit V_{lim} that depends only on the ratio d/Λ (Figure 3.3). When V_{lim} is lower than the cut-off spatial frequency of the second mode (2.405 when $a_{eq}=0.64\Lambda$), the fiber remains theoretically single mode whatever the wavelength [BIR 97]. This property can be fulfilled even with very large core fibers [KNI 98a]. However, as the effective index of the cladding approaches that of silica, the efficiency of the guiding decreases and the bend loss increases [SOR 01]. This drawback limits the single mode bandwidth that can actually be used.

The non-usual spectral dependence of the effective index of the cladding, due to the heterogeneous nature of the medium, also strongly influences the effective index and the chromatic dispersion of the fundamental mode propagating into the core. By choosing d and Λ carefully, one can adjust the effective area of the mode over a large range of values. The birefringence may also be adjusted by acting on the symmetry of the structure. Considering these features, one can easily understand that microstructured fibers guiding light due to the total internal reflection principle exhibit attractive propagation properties, even if the well known guiding principle has been exploited for years in standard fibers. As we will see below, these

properties open the way for novel applications in very diverse domains such as telecommunications, metrology, spectroscopy and non-linear optics. This is the main reason for the intensive research that has been undertaken since 1996 in numerous laboratories in the industry (Corning, Lucent Technologies, Alcatel, NTT-Ibaraki ...) and in the universities (University of Bath, ORC in Southampton (UK), TUD Lyngby (Denmark), IRCOM Limoges (France), University of Sydney (Australia) ...). Bodies such as Crystal Fiber (Denmark), specially devoted to their fabrication and distribution, have also been created in recent years. It is natural to devote space to them in this chapter.

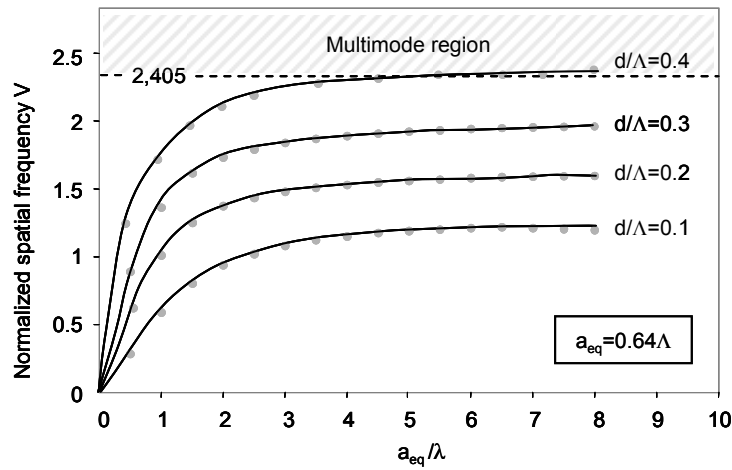


Figure 3.3. Spectral dependence of the spatial normalized frequency showing that the microstructured fibers remain single mode whatever the wavelength for weak values of the d/Λ ratio

Before continuing, it is worth noting that the label “photonic crystal fiber”, wrongly attributed to the very first microstructured fiber from the University of Bath in 1996, has since been used in most publications to refer to the microstructured fibers that guide light following the total internal reflection principle. In this chapter, to avoid confusion, such fibers will be called “air/silica microstructured optical fibers” or, for simplicity’s sake, “TIR-MOFs”. The label “photonic crystal fibers” (PCFs) will be reserved for those guiding due to a photonic bandgap (PBG) in the cladding.

3.3. Manufacture of microstructured fibers

The technical process generally implemented in manufacturing microstructured fibers (TIR-MOFs or PCFs) is quite similar to that used for conventional silica fibers. In both cases, the fiber is drawn at a high temperature (between 1,800 and 2,000°C) from a preform set in a vertical furnace at the top of a drawing tower. However, preforms are elaborated following very different techniques. On the one hand, the preform of a usual fiber can be described as a pure silica rod with a diameter of few centimeters, in the center of which a doped silica region is incorporated. Due to the dopants (Al, Ge, P ...) the index of the doped region is higher than that of the silica, and this region is intended to become the core of the fiber. The creation of this kind of preform necessitates the implementation of complex physico-chemical techniques, such as MCVD, OVD or VAD. The index profile of the drawn fiber is a homothetical reduction of that of the preform.

Preforms of MOFs are obtained by carefully stacking an assembly of pure silica capillary tubes and rods having a diameter of about 2mm. This assembly is inserted into a maintaining tube that constitutes the initial preform whose diameter is a few centimeters (Figure 3.4a). The general arrangement of the lattice of holes in the preform, i.e. the number and distribution of these holes, must be maintained throughout the drawing process. But contrary to the case of classical fibers, the final cross-section of an MOF does not systematically result from a simple homothetical reduction of that of the preform. Numerous parameters, including the temperature of the furnace, the pressure inside the tubes and the speed of the drawing operation, have a significant influence on the shape and size of the holes in the fiber, and on those of the possible residual interstices between these holes (Figure 3.4b and c).

The used methods, so called “stack and draw methods”, enable a large variety of MOFs to be manufactured; they are characterized by the distribution of the holes in the lattice (triangular or hexagonal), the dimension of the core, the air-filling fraction (in other words the ratio d/Λ) and the number of rings of holes. These parameters are chosen with respect to the targeted application. In order to obtain performing MOFs, the following conditions must be met:

- very high purity silica rods and tubes, perfectly desiccated, must be used, with the lowest possible rugosity at the silica/air interface, to reduce propagation loss;
- the nominal dimensions of d and Λ must be respected because the effective area of the guided mode, its chromatic dispersion and the birefringence are very sensitive to these parameters;
- the cross-section must not be varied axially – this is absolutely vital for achieving low propagation losses, especially in the case of hollow core PCFs [VEN 02].

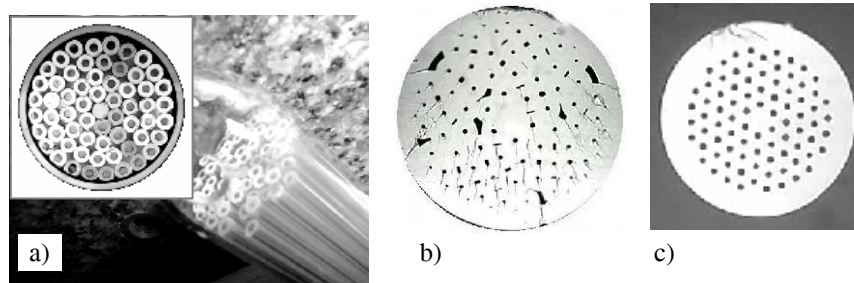


Figure 3.4. Photographs of cross-sections: A: a preform of an MOF; B and C: an MOF drawn with unsuitable (b) and inadequate (c) drawing parameters (photographs from IRCOM)

3.4. Modeling TIR-MOFs

As is the case whatever the type of guide, the main goal when modeling the propagation of light into microstructured fibers is to determine the effective index of each mode together with the spatial distribution of the associated electromagnetic field. The chromatic dispersion is deduced from the variations in the effective index versus the wavelength, whereas the field distribution enables the effective area, the confinement loss and the splice loss to be calculated.

3.4.1. The “effective- V model”

With the so called “effective- V model”, one seeks *at each wavelength* the opto-geometrical parameters of a step-index fiber whose propagation characteristics are identical to those of the studied MOF (equivalent step-index fiber) [BIR 97]. The index of the core of this fiber is that of pure silica, n_s . The index of the cladding is the highest effective index associated with a mode able to propagate in the silica/air structure when the latter is supposed to be infinite and free from all geometrical defects. This mode is known as the “fundamental space filling mode”. Among the modes of the infinite structure, the fundamental space filling mode is the one with the largest part of its energy located in the silica. One calculates n_{eg} by solving the Maxwell equations over an elementary cell that is a rectangle whose two opposite angles are the centers of neighboring holes. By duplicating this cell using symmetries versus its edges, the whole silica/air structure is reconstituted. The effective indices of the modes of the MOF are very close to those of the corresponding modes of the equivalent step-index fiber having a core radius equal to 0.64λ . Thus, by replacing the MOF with its equivalent step-index fiber at each

wavelength, one can easily determine the spectral single mode propagation domain, the chromatic dispersion and the bend loss of this MOF. The effective-V model is very easy to implement but, as it cannot bring about distribution of the guided mode, it is of limited utility.

3.4.2. Modal methods for calculating the fields

Modal methods consist of calculating the components of the electromagnetic fields of the guided modes due to the resolution of the wave equation, taking into account the actual index profile of the fiber that is supposed to be invariant along its axis. Generally, vector formulations are preferred to scalar ones, which are acceptable only if the index difference between the core and the cladding is very low (weak guidance approximation). This condition is rarely respected in MOFs, especially those with a large air-filling fraction in the cladding.

One method involves solving the wave equation by replacing the expressions of the electromagnetic field and the index profile by their decomposition over a properly chosen base of functions. They can be:

- trigonometric functions (Galerkin method) [KIM 00];
- cosine functions for the periodic region of the index profile and Hermite-Gauss type localized functions for the central area and the fields [MON 99, 00];
- Hermite-Gauss functions exclusively for both the index profile and the fields.

This last choice is generally the most judicious because the decrease in the field is suitably described by means of a minimal number of localized functions, allowing a quick convergence of calculations and a lower memory requirement of the computer.

The finite element method is based on the resolution of the Maxwell equations at each node of a triangular grid previously operated over the index profile of the fiber [NED 86]. In order to guarantee a proper description of the fields, the regions close to the core where the amplitude variations are significant necessitate fine mesh (length of the edge of a mesh between two successive nodes $< \lambda/5$). The distant regions where the amplitude of the field is sufficiently weak can be described by means of larger meshes in order to optimize the necessary memory. This optimal management of the dimensions of the meshes enables us to model fibers with larger diameters [PEY 03a]. When modeling perfectly symmetrical MOFs, the mesh can only be operated over a $\pi/6$ angular sector and one can then use symmetries in order to reconstitute the grid over the whole fiber. This technique, which provides a grid with the same symmetry as the modeled structure, strongly limits the “numerical” birefringence [PEY 03b]. However, when modeling actual MOFs, the mesh must be directly operated over the whole cross-section and the symmetry of the grid is no

longer guaranteed. In this case, the numerical birefringence appears to be somewhat higher. By setting electric or magnetic short-circuits along two perpendicular radial directions, the electric or magnetic field respectively is cancelled along these directions, providing a means of choosing the direction of polarization of the studied mode. Moreover, by setting a real impedance along a circular contour around the last ring of holes, the confinement loss due to the evanescent part of the field beyond this limit can be calculated. The results of this evaluation cannot be considered as absolute because they depend upon the value of the impedance. However, when the real impedance is replaced by a perfect matched layer (PML) that is a virtual surrounding medium avoiding any reflection, the order of magnitude of the computed confinement loss becomes realistic [BER 94; YU 04]. The finite element method is somewhat difficult to implement, but it has been shown to be particularly reliable, especially for accurately modeling actual MOFs by taking into account their geometrical imperfections.

The multipole method conceived in the 1980s is a modal method that has been adapted to MOFs since the year 2000 by French and Australian research groups (respectively at the Fresnel Institute in Marseille and at the School of Physics in Sydney) [KUH 02; WHI 02]. It is a rigorous vectorial method in which the field near a given hole (hole n^j), decomposed in the Fourier-Bessel series, is seen as the sum of three contributions: an incident exciting field (monochromatic plane wave), the field diffracted by the hole n^j and moving away from this hole, and the field diffracted by all the other holes towards the hole n^j . The formulation of the problem, too complicated to set out here, leads to a matrix system $[M][B]=0$, where $[B]$ is the vector associated with the electromagnetic field of a mode of the structure and $[M]$ is the generalized diffraction matrix of this structure. Very clear and didactic descriptions of this method can be found in both English and French [KUH 02; LOU 05]. From a practical point of view, one can recall that it could model any index profiles of MOF unless the circles surrounding neighboring holes intersect. This limitation particularly concerns PCFs with a very large air-filling fraction. Diffraction matrices can be calculated analytically for circular holes. For holes with different sections, they generally necessitate the use of complicated integral or differential methods and this considerably increases the computation time.

There are other, less efficient, modal methods:

- the equivalent average index method, which is a very approximate method consisting of replacing the considered MOF with an “equivalent” fiber with a revolution symmetry of its index profile [PEY 02a; RAS 03];
- the biorthogonal method, based on the decomposition of the fields in a set of plane waves, applies only to perfectly symmetrical structures [FER 99; SIL 98].

Finally, before ending this section, mention must be made of the beam propagation method (BPM), which is not a modal method. Thanks to successive alternate incrementations of the field in the direct space and in the conjugated one, the evolution of the input field along the propagation axis is described. In particular, one can observe the setting up of the fundamental mode in a single mode fiber and one can also evaluate the confinement loss [FOG 02]. BPM is mainly devoted to the study of propagation in guides whose profiles vary along the axis, such as tapers, fused couplers and splices. In order to study MOFs, it is necessary to use a vectorial formulation because of the high index contrast existing at the silica/air interfaces.

As was shown above, a large number of numerical tools are available for modeling the propagation into MOFs. However, one must avoid systematically relying on the numerical results without question because all the methods operate in the frame of work hypothesis and/or approximations that must be known or taken into account. In other words, as the authors of Chapter 2 in [LOU 05] say: “it should be stressed that beginners need to be extremely cautious before considering numerical results as valid, especially when they do not know the theoretical and numerical foundations of the code used for obtaining these results”.

3.5. Main properties and applications of TIR-MOFs

3.5.1. *Single mode propagation*

The possibility of single mode propagation over a very wide range of wavelengths into TIR-MOFs, provided that the ratio d/Λ is lower than a limit (about 0.35), has already been mentioned above (section 3.2). This property is of great interest to stellar interferometry by optical fibers which exploits the whole spectrum from the visible to the infrared [PEY 02b]. It also allows efficient amplification into rare earth doped fibers with a large active area (see section 3.5.5) [HIL 03].

3.5.2. *Propagation loss*

In a TIR-MOF, the confinement of the guided field into the core must be achieved by a sufficient number of rings of holes, depending on d/Λ . If this condition is not fulfilled, the field can spread beyond the microstructured cladding and it behaves as a leaky mode with very high loss. For example, with $d/\Lambda=0.4$ ($\Lambda=2.3\mu\text{m}$), the confinement loss at $\lambda=1,550\text{nm}$ increases from 10^{-2}dB/m to 10dB/m when the number of rings is reduced from 6 to 4 [WHI 01].

As with classical fibers, the bend loss of MOFs becomes significant at long wavelengths, because the extent of the field in the cladding area increases with λ . But, contrary to standard fibers, one can also note an increase in the bend loss at

short wavelengths because the guiding becomes too weak (see section 3.2). One can consider that, at short wavelengths, the loss remains negligible so long as the curvature radius remains very large as compared to $R_c = \Lambda^3/\lambda^2$ [BIR 97]. Thus, MOFs can theoretically be used over only a limited spectral range. Nevertheless, with standard packaging conditions, the available bandwidth is large enough to enable all the applications in the usual transmission windows of silica [SOR 01].

Other causes of loss are absorption by the silica and diffusion at the silica/air interfaces. Thanks to great progress in material synthesis and in fabrication techniques (see section 3.3), the attenuation coefficient decreased to 0.28 dB/km at 1,550 nm at the end of 2003, very close to the current figure of 0.14 dB/km in silica [TAJ 03]. Even if this attenuation remains higher than that of standard fibers (about 0.15 dB/km at 1,550nm), it is possible to use TIR-MOFs in optical links with the aim of taking advantage of other propagation characteristics that cannot be provided by classical fibers.

3.5.3. Chromatic dispersion

The chromatic dispersion of one mode of a guide (denoted D_c) can be expressed as a function of the spectral dependence of the effective index, as follows:

$$D_c = -\frac{\lambda}{c} \frac{d^2 n_e}{d\lambda^2} \quad (3)$$

n_e is the effective index of the mode, depending on the index of the core, on that of the cladding and on the fraction of the field respectively located in each of these two areas of the guide. Its spectral dependence expresses both that of the two media (cause of the dispersion of the material) and that of the radial extent of the field (from which the dispersion of the guide rises).

In classical fibers, the dispersion of the material in the core and in the cladding is that of silica. It can be modified, though only a very small amount, by adding dopants, but this should dramatically increase the absorption in the material. Thus, in order to modify the chromatic dispersion of the fundamental mode – taking D_c into account is of interest only in the single mode regime – one can only modify the dispersion of the guide. This can be achieved by acting on the spectral evolution of the confinement via the design of a more or less complicated index profile [AUG 02; MEU 03]. Nevertheless, the index difference between the core and the cladding remains constant and this considerably limits the possibility of adjusting the dispersion. In particular, the dispersion can be cancelled only at wavelengths longer than 1,300nm and it can be flattened only over a reduced spectral bandwidth.

On the contrary, the index difference between the core and the cladding in MOFs can significantly change with the wavelength because of the strong spectral dependence of n_{eg} , already mentioned. One can guess that the spectral evolution of the confinement and, consequently, of the effective index originates from a much finer alchemy. Opportunities to modify the chromatic dispersion over a given spectral bandwidth by adjusting the opto-geometrical parameters of the fiber increase. But, except in certain cases, the prediction of the evolution of $D_c(\lambda)$ can be obtained only with the calculation of n_e over the whole considered bandwidth, by means of one of the methods mentioned above (see section 3.4).

Flattened D_c over a wide spectral range is one of the non-conventional dispersion characteristics that MOFs can exhibit [FER 00]. For example, chromatic dispersion is lower than 1.2ps/(nm.km) from 1,000nm to 1,600nm in a fiber comprising 11 rings of holes where $d=0.58\mu\text{m}$ and $\Lambda=2.59\mu\text{m}$ [REE 02]. Potential applications are first of all optical communications based on the wavelength division multiplexing (WDM) technique. Nevertheless, one must stress the fact that the value of chromatic dispersion is particularly sensitive to very weak variations in opto-geometrical parameters. Indeed, a discrepancy of 10nm in the holes' diameters, or of 100nm in the pitch, induces a significant reduction in the low dispersion spectral bandwidth (1,250–1,450nm in this case). The consequence is that very tight control of the manufacturing process is required to obtain fibers having the desired dispersion characteristics.

It is also possible to cancel chromatic dispersion at wavelengths shorter than 1,300nm in MOFs. To reach this goal, the negative (normal) dispersion of the material must be compensated for using a positive (abnormal) dispersion of the guide obtained when a large index difference between the core and the cladding strongly confines the field over the considered bandwidth. Thus, MOFs with their dispersion cancelled at short wavelengths are fibers having a large air-filling fraction in the cladding together with a narrow guiding area for preserving the single mode nature of the propagation. Chromatic dispersion can be cancelled at very short wavelengths, in which case dispersion of the material is considerable. For example, an MOF with a 0.5 μm diameter core surrounded by holes 50 times larger has its chromatic dispersion cancelled at 560nm where the dispersion of the material still reaches $-360\text{ ps}/(\text{nm.km})$ [KNI 00].

These applications are mainly in the field of non-linear optics because, around the zero dispersion wavelength, one can obtain constructive non-linear interactions over long lengths of fibers and consequently create appreciable effects, among which are the following:

- frequency generation producing large continua in MOFs when excited with short pulses centered at wavelengths close to the zero dispersion wavelength [FEV 01; PRO 01; RAN 00; WAD 04]. A technique for generating even more

extended continua (from the UV to 1,700nm) is to pump the MOF with a two wavelength laser, the two pumping wavelengths being situated on both sides of the zero dispersion wavelength of the fiber [CHA 04]. This result from a complicated cascade of non-linear effects involving stimulated Raman diffusion, self phase modulation, cross phase modulation and four wave mixing. The main applications are in the domains of bright wide spectrum sources for medical imaging, WDM systems and metrology [HOL 00];

- cross phase modulation used in all optical commutation systems [SHA 02a];
- four wave mixing for designing parametric oscillators [SHA 02b].

3.5.4. Birefringence

It is well known that guides having a rotational symmetry of $2\pi/m < \pi$ are isotropic. TIR-MOFs with a perfectly organized triangular lattice of holes that have a $\pi/6$ symmetry of their structure abide by this rule. If we consider only the geometrical effects, these MOFs are then theoretically free from any birefringence (we recall that birefringence is defined as $B = n_{ex} - n_{ey}$ where n_{ex} and n_{ey} are the effective indices of the two perpendicular polarizations of the fundamental mode) [STE 01]. In other words, n_{ex} and n_{ey} are theoretically identical even if the field distribution is made different in the two polarizations by compliance with the conditions of continuity at the silica/air interfaces [PEY 03b].

Actually, the geometry of the cross-section of a MOF can never be perfectly symmetrical and its slight imperfections can cause notable shape birefringence. For giving an order of magnitude, B can reach $1.5 \cdot 10^{-4}$ at 1,550nm, corresponding to a beat length $L_b = \lambda/B$ in the order of one centimeter, if the diameter of the holes varies within a range of only $\pm 1\%$ and if their position versus their nominal location is shifted by $\pm 0.5\%$ [LIB 01]. The contribution of possible internal stress to the birefringence seems to be minor and is not clearly established. However, thanks to excellent control of the manufacturing process, one can reduce birefringence to very low values, corresponding to beat lengths of several tens of meters [NIE 02].

Due to the stack technique for manufacturing preforms, it becomes easy to elaborate structures having a single diametrical symmetry to induce a very high shape birefringence. One can deform the hexagonal shape of the core (Figure 3.5a and b) or conceive of an arrangement of holes with different diameters (Figure 3.5c and d) [MEL 03; ORT 00]. The measured birefringence is equal to a few 10^{-3} ($L_b < 4\text{mm}$ at 1,550nm); that is to say it is at least as high as that of most classical polarization maintaining fibers (PANDA, bow tie, ...). Because of their potentially low cost of fabrication, highly birefringent MOFs can be considered to be good candidates for all the applications that require operation with only one polarization, especially those involving techniques based on interferometry.

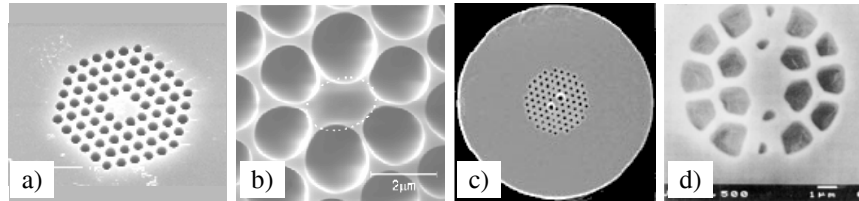


Figure 3.5. Cross-sections of highly birefringent MOF: with a non-hexagonal core (fibers from Alcatel (a) and Crystal Fiber (b)); involving holes with different diameters (fibers from Crystal Fiber (c) and Blaze Photonics (d))

3.5.5. Non-conventional effective areas

Single mode propagation into TIR-MOFs is guaranteed whatever the wavelength, provided that the ratio d/λ remains lower than a limit in the order of 0.36 (see section 3.2). Thus, it can be obtained in fibers whose core diameter 2λ is far larger than the wavelength. As an example, only the fundamental mode can propagate in a $22\mu\text{m}$ diameter core at the 458nm wavelength [KNI 98a]. But in these conditions, the numerical aperture is obviously very small and the propagation loss as well as the bend loss becomes high. The attractive feature of such fibers is that, for a given guided power, the power density decreases because of the large effective area of the mode (a few hundred μm^2) and this enhances the power threshold at which appreciable non-linear effects appear.

On the other hand, with a large air-filling fraction in the cladding area, one obtains a much higher index differential between the core and the cladding than that reachable in classical fibers. This makes it possible to efficiently confine, into a small core, a field whose effective area does not exceed a few μm^2 . Then, even with low guided power, high power density can be reached by inducing significant non-linear Kerr effects. The applications principally deal with the frequency generation already mentioned in section 3.5.3 together with soliton propagation [CRI 04].

An increase in the numerical aperture with the wavelength induces a spectral evolution of the effective area of the guided mode that is slower in MOFs than in standard fibers. By doping the core with rare earth, one can take advantage of this relative stability for designing efficient fiber amplifiers even if the pump and the signal wavelengths are very distant. Indeed, it becomes possible to obtain an optimal overlap of both the pump and the signal wavelengths with a somewhat extended doped area without affecting the single mode nature of the propagation at the two wavelengths. One of the main applications of this feature is erbium-doped amplifiers pumped at 980 nm and operating at $1,550\text{ nm}$ [HIL 03].

3.6. Photonic bandgap fibers

3.6.1. Propagation in photonic bandgap fibers

As explained in section 3.2, the propagation of light in true photonic crystal fibers (PCFs) is based on a transverse resonance in the cladding that makes the transverse propagation of light impossible at certain wavelengths; in other words, it is based on the existence of photonic bandgaps in the cladding. As the conditions of total internal reflection are no longer required, the index of the core can be lower than the effective index of the cladding n_{eg} . This gives an opportunity for novel applications than could not be implemented by other means. Indeed, the core can be constituted with any transparent material, in particular air or other gas, whose optical properties can be exploited. The general structure of a PCF is shown in Figure 3.6 [CRE 99, SAI 03].

The method proposed by Pendry [PEN 94] makes it possible simply to evaluate the transmission bandwidth of PCFs. This finite element type method solves the Maxwell equations at the nodes of a square mesh of a structure, for small incidence angles. (A detailed description of the method can be found in [LOU 05].) In order to identify the photonic bandgaps and to describe the modes of the PCFs, one can also implement the method based on the decomposition of fields over a set of plane waves [BAR 99; BRO 00; POT 03], or a vectorial finite element method in which the edges of the elementary cells are curved for a better description of the geometry of the holes [SAI 03]. The main practical lesson that can be learnt from the simulations is that obtaining significant photonic bandgaps in silica/air fibers is possible only if the air-filling fraction is higher than 70% ($d/\Lambda > 0.88$). Obviously, the width of the bandgap for a given value of β increases with the air-filling fraction. For practical applications, f must exceed 80% ($d/\Lambda > 0.95$), implying that the cladding must be composed of very large holes separated by a narrow partition of silica. The use of materials with an index higher than that of silica, such as telluride or chalcogenide glasses whose indices in infrared are respectively in the range 1.8–2.3 and 2.4–2.7, enables substantial bandwidths with a lower air-filling fraction to be created (in the order of 60%, i.e. $d/\Lambda > 0.81$) [POT 03]. As expected, the confinement loss of the mode is reduced as the air-filling fraction in the cladding is increased and as the number of rings of holes is increased. To indicate some orders of magnitude, it is divided by 1,000 when f increases from 73% to 80%; for $f = 80\%$, it decreases from 100dB/m to 0.01dB/m when the number of rings of holes is increased from 4 to 12 [SAI 03]. At least, the shape of the central hole has a great influence on the confinement loss. It is shown that this loss is significantly reduced if the cross-section of the central hole is close to that depicted in Figure 3.6, instead of a perfect hexagon.

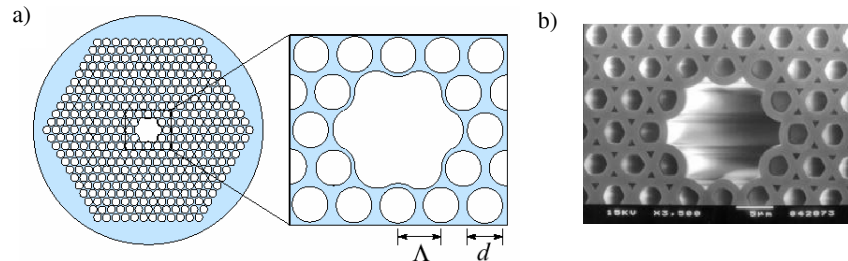


Figure 3.6. Cross-section of a hollow core PCF. A: general shape [SAI 03]; B: fiber manufactured at the University of Bath [CRE 99]

The very first demonstration of guiding in a hollow core PCF, in 1998, was not really convincing because the holes were organized following a hexagonal matrix that allowed the field to spread out of the core and relocate in the silica interstices at the close periphery of this core [KNI 98b]. On the contrary, a triangular lattice of holes effectively confines the field in the hollow core [CRE 99]. The very high loss measured in the first manufactured PCFs (1999–2000) were essentially due to a lack in the axial uniformity of the fiber that randomly shifts the position of the bandgap along the propagation [WES 00, 01]. A second cause of loss is the coupling of light from the core to the silica (surface modes) that is made minimal by the use of a large section hollow core surrounded by a microstructured cladding with very narrow silica partitions [DIG 04]. The thickness of these partitions must remain smaller than $\lambda/10$.

Over the course of a few years, advances in manufacturing techniques have made it possible to reduce propagation loss considerably [VEN 02; HAN 03; MAN 04]. Figure 3.7 shows the cross-section of a PCF whose propagation loss is reduced to less than 2dB/km over a 10nm spectral width around 1,565nm, due to scrupulous adherence to the above conditions. The elementary motives in the cladding have a $3.9\mu\text{m}$ diameter and the thickness of the silica partitions is about 120nm.

These promising results allow one to dream that, in the near future, the loss of hollow core PCFs will be reduced, over a large spectral range, under the 0.15 dB/km threshold imposed by Rayleigh diffusion in conventional fibers. In such fibers, the power threshold over which significant non-linear effects appear should be 100 times higher than in usual fibers. They are obviously of great interest for the transmission of signals at wavelengths strongly absorbed by the silica (UV and far IR) and for the guiding of high power pulses without spectral distortions.

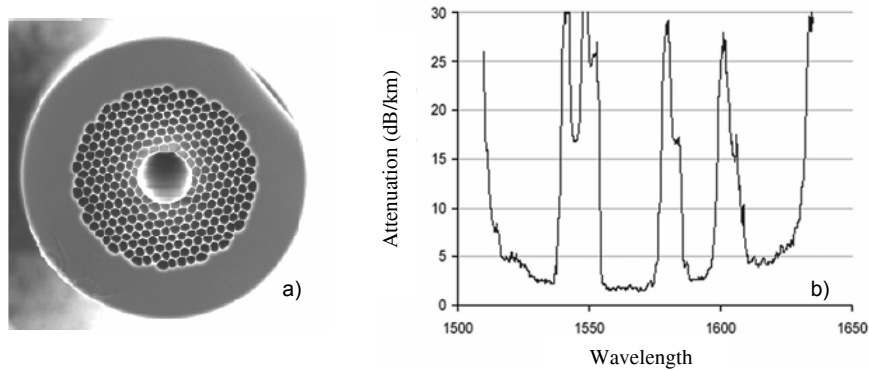


Figure 3.7. *A: Microscope Electronic Beam picture of the cross-section of a PCF whose core is realized by removing the central rod and the two first rings of capillaries in the structure; B: spectral attenuation of this fiber [MAN 04]*

3.6.2. Some applications of photonic crystal fibers

It is well known that very small objects (from atoms to micro-particles) can be trapped in the area of highest power density of a light beam and moved under the action of the radiation pressure of light. By launching the trapping beam into the hollow core of a PCF, micro-objects can be guided over a long distance in the center of this core, while following the curvature of the fiber, without any contact with the lining, and directed precisely towards the desired destination. In the first experiment that has proven the validity of this process, 5 μm diameter polystyrene balls were guided by a continuous beam from an argon laser ($\lambda=514\text{nm}$, $P=80\text{mW}$) over 15cm at a speed of 1cm/s in the center of the 20 μm diameter core of a PCF ($d=3\text{--}4\mu\text{m}$, $f=75\%$, attenuation=5dB/m at 514nm) [BEN 02b]. The length over which particles are guided can potentially exceed 100 meters in a fiber with lower attenuation, such as that shown in Figure 3.7. This opens up new horizons for all the applications that necessitate moving micro-objects to a precise location without any contact: for example, biology (handling of viruses and bacteria), chemistry and atomic physics.

By filling the hollow core of a PCF with a highly non-linear gas, one can obtain significant effects with a very low pumping level, due to the very long lengths of interaction between the light and the gas along the fiber. As an example, in the core of a PCF filled with hydrogen under pressure, a pulsed laser beam generates Stokes and anti-Stokes lines with a necessary energy in each pulse two orders of magnitude lower than that required by other techniques (interaction in a capillary or in the waist of a focused beam). With pulses of only 800 nJ/6 ns, a 30% conversion efficiency in

the Stokes line is measured at the output of only a few centimeters-long sample of PCF [BEN 02a].

A PCF can also guide, over several meters, femtosecond soliton pulses with a peak power of several megawatts. In order to achieve this, certain conditions must be fulfilled. First, the chromatic dispersion of the mode of the fiber must cancel at a wavelength close to the central wavelength of the pulse. Second, the propagation must operate in a material having a very low non-linear coefficient. Finally, no Raman effect may appear because it should quickly shift the spectrum of the pulse out of the transmission bandwidth of the fiber. These conditions are met in a PCF with a 13 μ m diameter core ($f=94\%$) filled with rare gas (xenon) and with its chromatic dispersion cancelled at 1,425nm [OUZ 03]. Gaussian soliton pulses (5.5 MW/75 fs), centered at 1,470nm, have been demonstrated to be properly guided over a 2m length of fiber. The applications are principally in the domains of spectroscopy, biology and medicine.

Finally, in order to achieve novel functions by means of fibers similar to PCFs, one can draw inspiration from the numerous components based on MOFs with very large holes filled with different media proposed by Kerbage and Eggleton (*hole assisted fibers*) [EGG 01]. Indeed, the core of a PCF can be filled with different liquids (liquid crystal, amplifying medium, biological medium, liquid whose optical properties are modified by an outer event such as the application of an electric field or a change in temperature ...). Obviously, even if the structure of the PCF is preserved, the operating guiding principle in this case is likely to become the TIR because of the higher index of medium in the core. Notwithstanding this, making the guided light wave interact with the liquid inserted into the core of the fiber opens the way to a multitude of applications: switches, tunable attenuators, tunable lasers, intrinsic sensors, biosensors for the analysis of sub-microliter samples, etc. [LAR 03].

3.7. Conclusion

Since their quasi-fortuitous invention in 1996, interest in microstructured fibers guiding light following the total internal reflection principle has increased considerably. Such infatuation is due to the novel propagation properties of these fibers that open the way to a large number of applications not realizable with more conventional fibers, in particular for telecommunications and non-linear optics. Furthermore, the manufacturing technique of preforms that consist of stacking simple silica tubes and rods makes it possible to conceive structures with opto-geometrical characteristics much more varied than those made possible through CVD-type techniques.

Photonic crystal fibers operating by virtue of transverse resonance in cladding have also raised many hopes, especially since their ability to guide light in a hollow core over long distances has been experimentally demonstrated. This has been made possible by a spectacular improvement in fabrication techniques over the first years of the 21st century. The very first applications reported at the end of this chapter take advantage of the fact that, contrary to the case of all other fibers, the light wave can remain confined and propagate in low index media such as a vacuum, gas or certain liquids. The very long lengths of interaction between light and the medium inserted into the core enable us to efficiently exploit the optical properties of this medium: transparency, high or low non-linear coefficients, etc.

With TIR-MOFs and PCFs, it has thus been shown that nanostructures could be realized and maintained longitudinally invariant in fibers over several hundreds of meters, even kilometers. Moreover, in another register, optical fibers can also form the basic element of short length nanostructures used in particular for near field analysis techniques. Indeed, the different techniques of near field microscopy are based on the use of probes consisting of a short sample of tapered fiber for making a sharp point (metallized or not) whose end is 50 to 200nm in diameter. In this case too, control of the geometry of the structure (shape of the tip, dimension of the nano-opening) is particularly critical. This issue is treated in detail in the Chapter 7.

Considering the great efforts that the large laboratories have made to improve the performance of micro- and nanostructured fibers, one can predict that significant progress will be made shortly, in the early years of the twenty-first century, in particular in the fields of telecommunications, metrology and opto-biology. Even though the results already obtained are numerous and convincing, they are perhaps only the beginnings of a true revolution in the field of guided optics.

3.8. References

- [AUG 02] AUGUSTE J.L., BLONDY J.M., MAURY J., MARCOU J., DUSSARDIER B., MONNOM G., JINDAL R., THYAGARAJAN K., PAL B., "Conception, realization, and characterization of a very high negative chromatic dispersion fiber", *Optical Fiber Technology*, 8, p. 89-105, 2002.
- [BAR 99] BARKOU S.E., BROENG J., BJARKLEV A., "Silica-air photonic crystal fiber design that permits waveguiding by true photonic bandgap effect", *Optics Letters*, 24, p. 46-48, 1999.
- [BEN 02a] BENABID F., KNIGHT J.C., ANTONOPOULOS G., RUSSELL P.ST.J., "Stimulated Raman scattering in hydrogen-filled hollow-core photonic crystal fiber", *Science*, 298, p. 399-402, 2002.
- [BEN 02b] BENABID F., KNIGHT J.C., RUSSELL P.ST.J., "Particle levitation and guidance in hollow-core photonic crystal fiber", *Optics Express*, 10, p. 1195-1203, 2002.

- [BER 94] BERENGER J.P., "A perfectly matched layer for the absorption of electromagnetic waves", *Journal of Computational Physics*, 114, p. 185-200, 1994.
- [BIR 95] BIRKS T.A., ROBERTS P.J., RUSSELL P.ST.J., ATKIN D.M., SHEPHERD T.J., "Full 2-D photonic bandgaps in silica/air structures", *Electronics Letters*, 31, p. 1941-1943, 1995.
- [BIR 97] BIRKS T.A., KNIGHT J.C., RUSSELL P.ST.J., "Endlessly single-mode photonic crystal fiber", *Optics Letters*, 22, p. 961-963, 1997.
- [BIR 04] BIRKS T.A., BIRD D.M., HEDLEY T.D., POTTAGE J.M., RUSSELL P.ST.J., "Scaling laws and vector effects in bandgap-guiding fibres", *Optics Express*, 12, p. 69-73, 2004.
- [BRE 00a] BRÉCHET F., LEPROUX P., ROY P., MARCOU J., PAGNOUX D., "Analysis of bandpass filtering behaviour of singlemode depressed-core-index photonic – bandgap fibre", *Electronics Letters*, 36, p. 870-872, 2000.
- [BRE 00b] BRÉCHET F., MARCOU J., PAGNOUX D., ROY P., "Complete analysis of the propagation characteristics into photonic crystal fibers by the finite element method", *Optical Fiber Technology*, 6, p. 181-191, 2000.
- [BRE 00c] BRÉCHET F., ROY P., MARCOU J., PAGNOUX D., "Single-mode propagation into depressed-core photonic-bandgap fibre designed for zero-dispersion propagation at short wavelengths", *Electronics Letters*, 36, p. 514-515, 2000.
- [BRO 00] BROENG J., BARKOU S.E., SONDERGAARD T., BJARKLEV A., "Analysis of air-guiding photonic bandgap fibers", *Optics Letters*, 25, p. 96-98, 2000.
- [CHA 04] CHAMPERT P.A., COUDERC V., LEPROUX P., FÉVRIER S., TOMBELAINE V., LABONTÉ L., ROY P., FROEHLI C., "White-light supercontinuum generation in normally dispersive optical fiber using original multi-wavelength pumping system", *Optics Express*, 19, p. 4366-4371, 2004.
- [CRE 99] CREGAN R.F., MANGAN B.J., KNIGHT J.C., BIRKS T.A., RUSSELL P.ST.J., ROBERTS P.J., ALLAN D.C., "Single mode photonic band gap guidance of light in air", *Science*, 285, p. 1537-1539, 1999.
- [CRI 04] CRISTIANI I., TEDIOSI R., TARTARA L., DEGIORGIO V., "Dispersive wave generation by solitons in microstructured optical fibers", *Optics Express*, 12, p. 124-135, 2004.
- [DIG 04] DIGONNET M.J.F., KIM H.K., SHIN J., FAN S., KINO G.S., "Simple geometric criterion to predict the existence of surface modes in air-core photonic-bandgap fibers", *Optics Express*, 9, p. 1864-1872, 2004.
- [EGG 01] EGGLETON B.J., KERBAGE C., WESTBROOK P.S., WINDELER R.S., HALE A., "Microstructured optical devices", *Optics Express*, 9, p. 698-713, 2001.
- [FER 99] FERRANDO A., SILVESTRE F., MIRET J.J., ANDRÈS P., ANDRÈS M.V., "Full-vector analysis of a realistic photonic crystal fiber", *Optics Letters*, 24, p. 276-278, 1999.

- [FER 00] FERRANDO A., SILVESTRE E., MIRET J.J., ANDRÈS M.V., “Nearly zero ultraflattened dispersion in photonic crystal fibers”, *Optics Letters*, 25, p. 790-792, 2000.
- [FEV 01] FÉVRIER S., ALBERT A., LOURADOUR F., ROY P., PAGNOUX D., BARTHÉLÉMY A., “Fibres optiques non linéaires microstructurées pour source lumineuse blanche d’impulsions femtosecondes”, *Proceedings of COLOQ 2001*, Rennes, 2001.
- [FIN 99] FINK Y., RIPIN J., SHANHUI F., CHIPING C., JOANNOPOULOS J.D., THOMAS E.L., “Guiding optical light in air using an all-dielectric structure”, *Journal of Lightwave Technology*, 17, p. 2039-2041, 1999.
- [FOG 02] FOGLI F., SACCOMANDI L., BASSI P., BELLANCA G., TRILLO S., “Full vectorial BPM modeling in index-guiding photonic crystal fibers and couplers”, *Optics Express*, 10, p. 54-59, 2002.
- [HAN 03] HANSEN T.P., BROENG J., JAKOBSEN C., VIENNE G., SIMONSEN H.R., NIELSEN M.D., SKOVAGAARD P.M.W., FOLKENBERG J.R., BJARKLEV A., “Air guidance over 345m of large-core photonic bandgap fiber”, *Proceedings of Optical Fiber Conference*, paper PD4, Atlanta, 2003.
- [HIL 03] HILAIRE S., ROY P., PAGNOUX D., BAYART D., “Large mode Er^{3+} - doped photonic crystal fibre amplifier for highly efficient amplification”, *Proceedings of European Conference on Optical Communications*, paper We4.P13, Rimini, 2003.
- [HOL 00] HOLSWARTH R., UDEM T., HÄNSCH T.W., KNIGHT J.C., WADSWORTH W.J., RUSSELL P.ST.J., “Optical frequency synthesizer for precision spectroscopy”, *Physical Review Letters*, 85, p. 2264-2266, 2000.
- [KIM 00] KIM J., CHUNG Y., PAEK U.C., KIM D.Y., “A new numerical design tool for holey optical fibers”, *Optoelectronics and communications conference*, paper 12B3-3, Chiba Japon, 2000.
- [KNI 96] KNIGHT J.C., BIRKS T.A., RUSSELL P.ST.J., ATKIN D.M., “All-silica single-mode fiber with photonic crystal cladding”, *Optics Letters*, 21, p. 1547-1549, 1996.
- [KNI 98a] KNIGHT J.C., BIRKS T.A., CREGAN R.F., RUSSELL P.ST.J., DE SANDRO J.P., “Large mode area photonic crystal fibre”, *Electronics Letters*, 34, p. 1347-1348, 1998.
- [KNI 98b] KNIGHT J.C., BROENG J., BIRKS T.A., RUSSELL P.ST.J., “Photonic band gap guidance in optical fibers”, *Science*, 282, p. 1476-1478, 1998.
- [KNI 00] KNIGHT J.C., ARRIAGA J., BIRKS T.A., ORTIGOSA-BLANCH A., WADSWORTH W.J., RUSSELL P.ST.J., “Anomalous dispersion in photonic crystal fibres”, *IEEE Photonics Technology Letters*, 12, p. 807-809, 2000.
- [KUH 02] KUHLMEY B., WHITE T.P., RENVERSEZ G., MAYSTRE D., BOTTEN L.C., MARTIJN DE STERKE C., MCPHEDRAN R.C., “Multipole method for microstructured optical fibers II: implementation and results”, *Journal of Optical Society of America*, B 10, p. 2331-2340, 2002.
- [KUR 04] KURIKI K., SHAPIRA O., HART S.D., BENOIT G., KURIKI Y., VIENS J.F., BAYINDIR M., JOANNOPOULOS J.D., KINK Y., “Hollow multilayer photonic bandgap fibers for NIR applications”, *Optics Express*, 8, p. 1510-1517, 2004.

- [LAR 03] LARSEN T.T., BJARKLEV A., HERMANN D.S., BROENG J., “Optical devices based on liquid crystal photonic bandgap fibres”, *Optics Express*, 11, p. 2589-2596, 2003.
- [LIB 01] LIBORI S.B., KNUDSEN E., BJARKLEV A., SIMONSEN H.R., “High-birefringent photonic crystal fiber”, *Proceedings of Optical Fiber Conference*, paper TuM2, Anaheim, 2001.
- [LOU 05] LOURTIOZ J.M., BENISTY H., BERGER V., GÉRARD J.M., MAYSTRE D. and TCHELNOKOV A. (2005) *Photonic Crystals: Towards Nanoscale Photonic Devices*, Ed. Springer, Berlin, Heidelberg, New York.
- [MAN 04] MANGAN B.J., FARR L., LANGFORD A., ROBERTS P.J., WILLIAMS D.P., COUNY F., LAWMAN M., MASON M., COUPLAND S., FLEA R., SABERT H., “Low loss (1.7dB/km) hollow core photonic bandgap fiber”, *Proceedings of Optical Fiber Conference*, post-dead line paper PDP24, Anaheim, 2004.
- [MCN 03] MCNAB S.J., MOLL N., VLASOV Y.A., “Ultra-low loss photonic integrated circuit with membrane-type photonic crystal waveguides”, *Optics Express*, 22, p. 2927-2939, 2003.
- [MEL 03] MÉLIN G., CAVANI O., GASCA L., PEYRILLOUX A., PROVOST L., RÉJEAUNIER X., “Characterization of a polarization maintaining fibre”, *Proceedings of European Conference on Optical Communications*, paper We1.7.4, Rimini, 2003.
- [MEU 03] MEUNIER J.P., *Physique et technologie des fibres optiques*, Chapter 5, Hermès, Paris, 2003.
- [MON 99] MONRO T.M., RICHARDSON D.J., BRODERICK N.G.R., BENNETT P.J., “Holey optical fibers: an efficient modal model”, *Journal of Lightwave Technology*, 17, p. 1093-1102, 1999.
- [MON 00] MONRO T.M., RICHARDSON D.J., BRODERICK N.G.R., BENNETT P.J., “Modeling large air fraction holey optical fibers”, *Journal of Lightwave Technology*, 18, p. 50-56, 2000.
- [NED 86] NEDELEC J.C., “A new family of mixed finite element in R^3 ”, *Numer. Math.*, 50, p. 57-81, 1986.
- [NIE 02] NIEMI T., LUDVIGSEN H., SCHOLDER F., LEGRÉ M., WEGMULLER M., GISIN N., JENSEN J.R., PETERSSON A., SKOVGAARD P.M.W., “Polarization properties of single-moded, large-mode area photonic crystal fibers”, *Proceedings of European Conference on Optical Communications*, paper 1.9, Copenhagen, 2002.
- [ORT 00] ORTIGOSA-BLANCH A., KNIGHT J.C., WADSWORTH W.J., ARRIAGA J., MANGAN B.J., BIRKS T.A., RUSSELL P.ST.J., “Highly birefringent photonic crystal fibers”, *Optics Letters*, 25, p. 1325-1327, 2000.
- [OUZ 03] OUZOUNOV D.G., AHMAD F.R., MÜLLER D., VENKATARAMAN N., GALLAGHER M.T., THOMAS M.G., SILCOX J., KOCH K.W., GAETA A.L., “Generation of megawatt optical solitons in hollow-core photonic crystal band-gap fibers”, *Science*, 301, p. 1702-1704, 2003.
- [PEN 94] PENDRY J.B., “Photonic band structures”, *Journal of Modern Optics*, 41, p. 209-229, 1994.

- [PEY 02a] PEYRILLOUX A., FÉVRIER S., MARCOU J., BERTHELOT L., PAGNOUX D., SANSONETTI P., "Comparison between the finite element method, the localized function method and a novel equivalent averaged index method for modelling photonic crystal fibres", *Journal of Optics A: Pure and Applied Optics*, 4, p. 257-262, 2002.
- [PEY 02b] PEYRILLOUX A., PAGNOUX D., REYNAUD F., "Evaluation of photonic crystal fiber potential for fiber linked version of stellar interferometers", *Proceedings of SPIE conference "Astronomical Telescopes and Instrumentation"*, Hawaii, 2002.
- [PEY 03a] PEYRILLOUX A., Modélisation et caractérisation des fibres microstructurées air/silice pour applications aux télécommunications optiques, Thesis, University of Limoges, 2003.
- [PEY 03b] PEYRILLOUX A., CHARTIER T., HIDEUR A., BERTHELOT L., MELIN G., GASCA L., PAGNOUX D., ROY P., "Theoretical and experimental study of the birefringence of a photonic crystal fiber", *Journal of Lightwave Technology* 21, p. 536-539, 2003.
- [POT 03] POTTAGE J.M., BIRD D.M., HEDLEY T.D., BIRKS T.A., KNIGHT J.C., RUSSELL P.ST.J., "Robust photonic band gaps for hollow core guidance in PCF made from high index glass", *Optics Express*, 11, p. 2854-2861, 2003.
- [PRO 01] PROVINO L., DUDLEY J.M., MAILLOTTE H., GROSSARD N., WINDELER R.S., EGGLETON B.J., "Compact broadband continuum source based on microchip laser pumped microstructured fibre", *Electronics Letters*, 37, p. 558-560, 2001.
- [RAN 00] RANKA J.K., WINDELER R.S., STENTZ A.J., "Visible continuum generation in air-silica microstructure optical fibers with anomalous dispersion at 800nm", *Optics Letters*, 25, p. 25-27, 2000.
- [RAS 03] RASTOGI V., CHIANG K.S., "Holey optical fiber with circularly distributed holes analysed by the radial effective-index method", *Optics Letters*, 28, p. 2449-2451, 2003.
- [REE 02] REEVES W.H., KNIGHT J.C., RUSSELL P.ST.J., ROBERTS P.J., "Demonstration of ultra-flattened dispersion in photonic crystal fibers", *Optics Express*, 10, p. 609-613, 2002.
- [RUS 01] RUSSELL P.S.J., "Holey new fibers", *Tutorial in Optical Fiber Conference*, TuL1, Anaheim, 2001.
- [SAI 03] SAITOH K., KOSHIBA M., "Leakage loss and group velocity dispersion in air-core photonic bandgap fibers", *Optics Express*, 11, p. 3100-3109, 2003.
- [SHA 02a] SHARPING J.E., FIORENTINO M., KUMAR P., WINDELER R.S., "All-optical switching based on cross phase modulation in microstructure fiber", *IEEE Photonics Technology Letters*, 14, p. 77-79, 2002.
- [SHA 02b] SHARPING J.E., FIORENTINO M., KUMAR P., WINDELER R.S., "Optical-parametric oscillator based on four-wave mixing in microstructure fiber", *Optics Letters*, 27, p. 1675-1677, 2002.
- [SIL 98] SILVESTRE F., ANDRÈS M.V., ANDRÈS P., "Biorthonormal-basis method for the vector description of optical-fibre modes", *Journal of Lightwave Technology* 16, p. 923-928, 1998.

- [SOR 01] SORENSEN T., BROENG J., BJARKLEV A., KNUDSEN E., BARKOU LIBORI S.E., "Macro-bending loss of photonic crystal fibre", *Electronics Letters*, 37, p. 287-289, 2001.
- [STE 01] STEEL M.J., WHITE T.P., MARTIJN DE STERKE C., MCPHEDRAN R.C., BOTTEN L.C., "Symmetry and degeneracy in microstructured optical fibers", *Optics Letters*, 26, p. 488-490, 2001.
- [TAJ 03] TAJIMA K., ZHOU J., NAKAJIMA K., SATO K., "Low water peak photonic crystal fiber", *Proceedings of European Conference on Optical Communications*, paper PD34, Rimini, 2003.
- [TAI 03] TAILLAERT D., CHONG H., BOREL P.I., FRANSEN L.H., DE LA RUE R., BAETS R., "A compact two-dimensional grating coupler used as a polarization splitter", *IEEE Photonics Technology Letters*, 9, p. 1249-1251, 2003.
- [VEN 02] VENKATARAMAN N., GALLAGHER M.T., SMITH C.M., MÜLLER D., WEST J.A., KOCH K.W., FAJARDO J.C., "Low loss (13dB/km) air core photonic band-gap fibre", *Proceedings of European Conference on Optical Communications*, paper PD1.1, Copenhagen, 2002.
- [VIL 92] VILLENEUVE P.R., PICHÉ M., "Photonic band gaps in two-dimensional square and hexagonal lattices", *Physical Review*, B 46, p. 4969-4972, 1992.
- [WAD 04] WADSWORTH W.J., JOLY N., KNIGHT J.C., BIRKS T.A., BIANCALANA F., RUSSELL P.S.T.J., "Supercontinuum and four-wave mixing with Q-switched pulses in endlessly single-mode photonic crystal fibres", *Optics Express*, 12, p. 299-309, 2004.
- [WES 00] WEST J.A., FAJARDO J.C., GALLAGHER M.T., KOCH K.W., BORRELLI N.F., ALLAN D.C., "Demonstration of IR-optimized air-core photonic band-gap fiber", *Proceedings of European Conference on Optical Communications*, p. 41-42, Munich, 2000.
- [WES 01] WEST J.A., VENKATARAMAN N., SMITH C.M., GALLAGHER M.T., "Photonic crystal fibres", *Proceedings of European Conference on Optical Communications*, paper Th A22, Amsterdam, 2001.
- [WHI 01] WHITE T.P., MCPHEDRAN R.C., DE STERKE C.M., "Confinement losses in microstructured optical fibers", *Optics Letters*, 26, p. 1660-1662, 2001.
- [WHI 02] WHITE T.P., KUHLMEY B., MCPHEDRAN R.C., MAYSTRE D., RENVERSEZ G., MARTIJN DE STERKE C., BOTTEN L.C., "Multipole method for microstructured optical fibers I: formulation", *Journal of Optical Society of America*, B 10, p. 2322-2330, 2002.
- [YEH 78] YEH P., YARIV A., MAROM E., "Theory of Bragg fiber", *Journal of Optical Society of America*, 68, p. 1196-1201, 1978.
- [YU 04] YU C.P., CHANG H.C., "Yee-mesh based finite difference eigenmode solver with PML absorbing boundary conditions for optical waveguides and photonic crystal fibers", *Optics Express*, 12, p. 6165-6177, 2004.

Chapter 4

Quantum Dots in Optical Microcavities

4.1. Introduction

Since 1990, Cavity Quantum ElectroDynamics (CQED) has become a major source of inspiration for basic research in optoelectronics [BUR 95; WEI 96; DUC 96; BEN 98]. In the 1980s, a beautiful series of experiments on atoms in microwave and optical cavities had demonstrated that optical processes – including spontaneous emission (SE) – can be deeply modified using a cavity to tailor the emitter-field coupling [HAR 89].

Among other effects observable in the so called “weak coupling regime”, the modification of the emission diagram, the enhancement or inhibition of the SE rate, the funneling of SE photons into a single mode and the control of the SE process on the single photon level are particularly attractive for applications in optoelectronics. For very high-Q (i.e. weakly damped) cavities, SE can even become a reversible process, in the so called “strong-coupling regime”.

Improving control over spontaneous emission processes in optoelectronic devices was recognized in the mid-1980s as a promising avenue for improving the performance of light emitting diodes and laser diodes. In lasers, for instance, photons that are spontaneously emitted into the lasing mode(s) act as seeds for amplification by stimulated emission. Conversely, SE into other modes is useless and even detrimental, as it consumes a significant amount of the injected electron-hole pairs.

By increasing the fraction β of the SE that is coupled to the lasing mode, one can reduce (roughly in inverse proportion) the threshold current of the laser. Novel devices based on full spontaneous emission control have also been proposed. In the $\beta=1$ limit, all photons (be they emitted by SE or by stimulated emission) are funneled into the lasing mode. This device, known as “thresholdless laser” [YOK 92; BJO 91], would act as an ideal converter of electrical signals into optical signals. Another attractive device is the single mode single photon source, which is able to generate on demand light pulses containing a single photon prepared in a well defined quantum state (spatial mode, polarization ...). Such a source can be obtained by placing a single quantum emitter (atom, ion, quantum dot ...), able to generate photons one by one, into a single mode optical microcavity.

High quality solid-state microcavities became widely available in the early 1990s, and have since brought about major achievements, such as the observation of strong coupling for quantum wells in planar cavities [WEI 92], the fabrication of high-efficiency microcavity LEDs which exploit SE angular redistribution [DEN 97], and low-threshold vertical-cavity surface emitting lasers [HUF 97] or microsphere lasers [SAN 96]. However, the emission spectrum of solid-state emitters is usually spectrally broad, which has long been a major hindrance to the observation of several important CQED effects.

Because of their “atomic-like” properties, self-assembled semiconductor quantum dots (QDs) are particularly well suited to performing solid-state CQED experiments. By placing one or a few QDs in semiconductor optical microcavities, one can for instance obtain the first clear demonstrations, in a solid-state system, of the Purcell effect [GER 98; GRA 99; GAY 98; GAY 01; KIR 01; MOR 01a; SOL 01; VUC 03] and of the strong coupling regime for a single discrete emitter [REI 04; YOS 04; PET 05]. A single-mode solid-state source of single photons based on a single QD in a pillar microcavity has also been developed [MOR 01a; SAN 02; OLI 05]. This device is the first optoelectronic component whose operation actually relies on CQED, through the Purcell effect, and has a strong application potential in the field of quantum communications and quantum information processing.

In this chapter, we first briefly present in section 4.2 some relevant properties of QDs as well as available single mode semiconductor microcavities. Basic CQED effects observed in the weak and strong coupling regimes are discussed in section 4.3. Finally, well-established as well as more prospective applications of these CQED effects in the field of nano-optoelectronics and quantum information processing are finally discussed in section 4.4.

4.2. Building blocks for solid-state CQED

4.2.1. Self-assembled QDs as “artificial atoms”

Solid-state CQED experiments have until now generally been performed on InAs/GaAs QDs in GaAs/GaAlAs microcavities. We will concentrate our attention on this very mature system, although other QDs, such as II–VI self-assembled QDs [ROB 05], QDs formed by interface fluctuations in quantum wells [BRU 94; HOU 03; PET 05] and semiconductor nanocrystals [FAN 00; ART 01] are also potentially interesting in this context.

It has been known since 1985 [GOL 85] that strained-layer epitaxy can be used to build defect-free nanometer scale InAs rich clusters in GaAs, which constitute potential traps for both electrons and holes. These self-assembled QDs support well-separated discrete electronic states and exhibit a single narrow emission line ($\ll kT$) under weak excitation conditions [MAR 94]. A linewidth close to the limit imposed by the exciton radiative lifetime ($\sim 1 \mu\text{eV}$) has been observed at 2K [BAY 02; KAM 02].

This makes it possible to exploit fully the potential of high Q cavities for SE control. When the temperature is raised, electron-phonon interaction causes the onset of a broadband line related to elastic acoustic phonon-exciton interactions as well as a broadening of the zero-phonon line [BES 01; BOR 01; MAT 01; FAV 03]. At 300K, the first of these effects is dominant and single QDs exhibit a lorentzian emission line, whose linewidth can be as large as 5 to 10 meV.

Due to the strong 3D electronic confinement in QDs, few-particle Coulomb effects dominate single QD emission spectra under high excitation conditions [LAN 98; GeER 99a]. For instance, “exciton” and “biexciton” lines, into which photons are emitted when the QD contains respectively one or two electron-hole pairs, are separated by typically one to three meV for InAs QDs (see Figure 4.1). This splitting varies from QD to QD and from one laboratory to another, a fact that highlights the high sensitivity of these effects to the precise shape and size of the QD. Under non-resonant pumping, the QD emission is influenced by the fluctuating charge distribution in its surroundings, which entails a significant broadening of the exciton and multi-exciton lines. This effect, as well as the phonon-related ones, shows that a single QD cannot in general be considered an *isolated* artificial atom. This implies that CQED experiments with QDs have to be performed (in most cases) at low temperature, and puts severe limits on the implementation of CQED effects in optoelectronic devices as discussed in section 4.5.

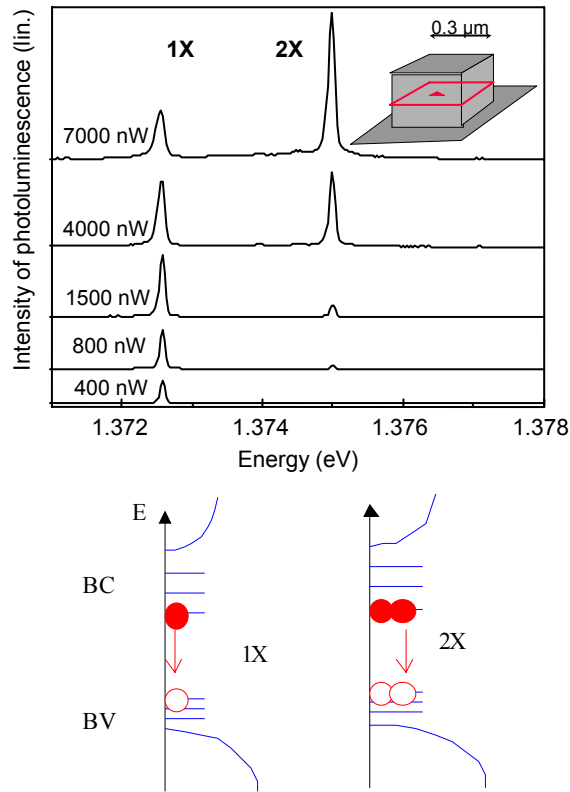


Figure 4.1. Photoluminescence spectra obtained at 4K for a single InAs QD, isolated in an etched mesastructure, as a function of excitation power. Schematic view of the density of states of the valence band (VB) and conduction band (CB) and of the QD state filling by electrons and holes, for exciton and biexciton recombination events

Self-assembled QDs also display a large electric dipolar moment d for their fundamental optical transition, providing efficient coupling to the electromagnetic field. Due to the compressive strain experienced by InAs, this dipole is (randomly) oriented in the xy epilayer plane. Absorption experiments on InAs QD arrays have shown that the oscillator strength per QD is in the order of 10 [WAR 97]; this corresponds to values for d_x (or d_y) around $9 \cdot 10^{-19} \text{C}\cdot\text{m}$, which is ten times larger than typical values for atoms emitting in the same wavelength range. This feature is reflected by the rather short radiative lifetime ($\sim 1 \text{ ns}$) of InAs QDs in bulk GaAs.

The peak emission wavelength of InAs QD arrays can be chosen – typically in the $0.9\text{--}1.5\mu\text{m}$ range at 10 K – since the average size of the QDs depends

reproducibly on the growth conditions in molecular beam epitaxy [GER 95]. Such QDs display a high radiative quantum yield ($\eta \sim 1$), provided that carrier thermoemission is negligible. This corresponds to $T < 100$ to 200 K depending on their average size. This excellent yield is due to the trapping of excitons in the defect-free QDs, which prevents further diffusion towards non-radiative recombination centers [GER 96a]. This trapping is obviously the key to the observation of intrinsic properties for QDs in etched microcavities, which present free surfaces close to the QDs under study.

Though moderate, size fluctuations lead to a significant dispersion of QD bandgaps within arrays, revealed by the inhomogeneous broadening of QD arrays emission lines (~ 15 to 100 meV). This feature constitutes at first sight a major difficulty when one wants to place a single QD in resonance with a discrete cavity mode. This difficulty can however be turned to some extent into an asset. Instead of placing a single QD inside the cavity (which is in practice rather tricky [BAD 05]), it is possible to insert a collection of a few hundred QDs, which are statistically all different due to size fluctuations. The detuning between the cavity mode and the center of the QD distribution can easily be adjusted so that a single QD on average is resonant with the cavity mode. Fine tuning of the resonance can then be obtained using small temperature changes [KIR 01].

Finally, let us mention a major practical advantage of QDs for applications: unlike atoms, QDs can be pumped in a non-resonant way, by exciting the GaAs barrier. This opens a route toward compact, electrically pumped optoelectronic devices exploiting CQED effects on QDs.

4.2.2. Solid-state optical microcavities

Early CQED experiments have been performed in the microwave spectral-range, for which perfectly reflecting mirrors based on superconductors can be used to define the electromagnetic cavity. Such perfect mirrors have no equivalent in the optical spectral range, since metallic mirrors entail significant losses upon reflection. Metals are therefore usually not used to build optical microcavities, with the remarkable exception of the demonstration of both SE rate enhancement ($\times 3$) and inhibition ($\times 0.7$) at room temperature for a quantum well inserted a planar microcavity defined by Ag mirrors, by varying the cavity thickness [BOU 00]. However, the absorption of a large part of the emitted light by the output mirror puts strong limitations on this approach. Planar microcavities are commonly defined by placing the “cavity” layer, which contains the emitting species, between two transparent dielectric mirrors. Such mirrors exploit distributed Bragg reflection, and are usually made by stacking one-quarter-wavelength thick layers of two different dielectric materials. For such structures, the electromagnetic field penetrates inside

the mirror upon reflection, which increases very significantly the effective thickness of the cavity. Only minor modifications of the spontaneous emission rate ($\pm 20\%$) have been observed experimentally for rare earth atoms in dielectric cavities [VRE 93] as well as quantum wells in the weak coupling regime [TAN 95], in accordance with theoretical expectations.

The implementation of zero D (or 0D) optical microcavities, able to confine light in all three dimensions of space on the wavelength scale, is the key to observing stronger modifications of SE dynamics as discussed in the next section. In order to achieve such a confinement, two basic effects can be used independently or in combination. The first one is total internal reflection in high-refractive index dielectrics, which has long been used to realize 1D waveguides such as optical fibers as well as to provide 0D confinement in silica microspheres [SAN 96; ART 01], microdisks [MCC 92; FUJ 00; GAY 01] (Figure 4.2b) or torroid-shaped microcavities [ARM 03]. The second effect is distributed Bragg reflection (basically an interference effect) which is commonly used for instance to build high-reflectivity optical dielectric coatings. This concept has been extended to the multi-dimensional case through the development of 2D and 3D photonic crystals [YAB 87; YAB 93]. Pillar microresonators [JEW 89; GER 96b] (Figure 4.2a) exploit both waveguiding along the micropillar axis and Bragg reflection for vertical confinement. Another approach, illustrated by Figure 4.2c, consists of defining a cavity surrounded by a 2D photonic crystal (which ensures lateral confinement) from a thin semiconductor membrane (which ensures in-plane waveguiding) [PAI 99; PAR 04; YOS 04].

These examples highlight the diversity of the strategies that can be used to achieve 0D confinement of light on the wavelength scale using only dielectric material. One should note at this stage that these cavities do not constitute perfect “photonic dots”. Besides their discrete resonant modes, which are confined in all 3 dimensions of space, they also sustain a continuum of non-resonant modes. The recent development of 3D photonic crystals in the optical spectral range changes, at least conceptually, this state of affairs [NOD 00]. Inside such a structure, the density of non-resonant modes can be decreased to arbitrarily small values by increasing the crystal size, while the introduction of a defect of tailored size/shape makes it possible to introduce high Q resonant mode(s) at a specific wavelength within the stop-band of the photonic crystal.

An optical microcavity confines light in both space and time. In order to compare the respective assets of these 0D microcavities for CQED, let us consider two important figures of merit: the cavity quality factor $Q = \omega / \Delta\omega$ and the modal volume V . Typical values for some semiconductor microcavities are shown in Figure 4.2. These microcavities concentrate – for resonant modes – the electromagnetic field within a remarkably small volume. One can note for instance

that, for an electromagnetic energy equal to $\hbar\omega/2$ (in other words, for the vacuum field), the amplitude of the field at the mode antinode is in the order of 10^5 V/cm for a mode volume $V=(\lambda/n)^3$ and $\lambda=1\ \mu\text{m}$. Their cavity Q however remains relatively small, in spite of significant recent progress [GAY 01; YOS 04]. Let us recall at this point that Q is simply proportional to the photon lifetime inside the cavity; this time is for instance close to 0.6 ps for $Q=1,000$ and $\lambda=1\ \mu\text{m}$. Silica microspheres [SAN 96] and microtores [ARM 03] display very different properties when their diameter is large enough ($\sim 100\ \mu\text{m}$); they manifest huge cavity Q s as large as 10^9 , but their modal volume V is much larger than $(\lambda/n)^3$ ($V\sim 1,000(\lambda/n)^3$). When their diameter is in the order of few micrometers, their Q s and V s are more similar to those of semiconductor microcavities [ART 01].

To conclude, many approaches can be used to build a 0D optical microcavity. Owing to their different merits, these microcavities present advantages in different contexts. High Q microspheres or microtores constitute an ideal system for realizing very low threshold lasers [SAN 96; KIP 04], whereas low volume semiconductor microcavities are better suited to the observation of the Purcell effect or of the strong coupling regime, provided an appropriate emitter, such as a single QD at low temperature, is implemented.

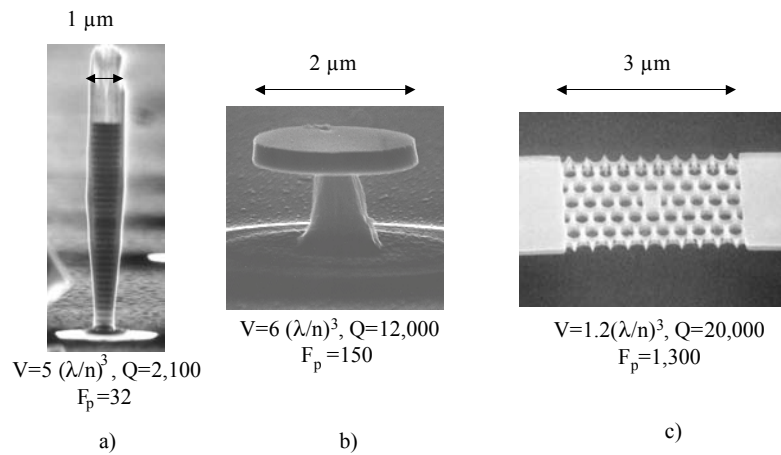


Figure 4.2. Micrographs obtained by scanning electron microscopy for some 0D semiconductor microcavities fabricated at CNRS/LPN. The typical values for Q and V are taken from [GER 98] for GaAs/AlAs micropillars (a), [GAY 01] for microdisks (b), and [YOS 04] for photonic crystal microcavities (c)

4.3. QDs in microcavities: some basic CQED experiments

4.3.1. Strong coupling regime

Ideally, the strong coupling regime is achieved when a two level system, which is initially in its excited state, is coupled resonantly and exclusively with a single resonant mode of a loss-less electromagnetic cavity. In such a case spontaneous emission becomes a reversible process. Since emitted photons cannot leak out of the cavity, they are reabsorbed by the emitter. The coupled emitter-cavity system describes a Rabi oscillation whose angular frequency is given by:

$$\hbar\Omega = \left| \vec{d} \cdot \vec{\mathcal{E}}(\vec{r}_e) \right| \quad (1)$$

where \vec{r}_e is the emitter's location, $\vec{\mathcal{E}}$ is the field amplitude when the electromagnetic energy in the cavity mode is $\hbar\omega$, and \vec{d} is the dipolar electric moment of the emitter. The eigenstates of the coupled system are mixed exciton-photon states, whose energies are split by $2\hbar\Omega$.

In practice, this regime will be observable only if all decoherence mechanisms are slower than the Rabi oscillation. Such possible decoherence mechanisms include for instance the escape of the photon out of the cavity, and the SE into other non-resonant modes (if any). In solid state systems, other phenomena can play a dominant role for the emitter, such as homogeneous broadening due to electron-electron or electron-phonon interactions.

For solid-state microcavities, the strong coupling regime was first observed for quantum wells inserted inside a high Q planar microcavity [WEI 92]. At low temperature, the elementary excitations of the quantum well are excitons, electron-hole pairs which are bound by their mutual Coulomb attraction. Excitons move freely within the plane of the quantum well, so that their eigenstates are plane waves, characterized by their in-plane wave vector $k_{//}$. Similarly, the planar cavity is a 2D photonic system. Since $k_{//}$ is conserved during an optical transition, one sees that each exciton state is coupled to a single optical mode, which leads to the strong coupling regime. Numerous studies have been devoted to this system over the last ten years. In practice, the analogy with the standard "single atom in a cavity" model system for CQED is rather limited. For quantum wells in planar cavities, mixed exciton-photon states, which are called *microcavity polaritons*, form bands and the dynamic properties of the system are dominated by additional effects such as polariton-polariton scattering or phonon-polariton scattering [LES 98; SEN 99; SAB 01].

Due to their discrete electronic levels, single QDs enable one to work in close analogy with atomic CQED. Figure 4.3 displays the expected Rabi splitting for a single InAs QD located at the mode antinode, as a function of the modal volume V [GER 03]. The expected Rabi splitting can be in the order of $100\mu\text{eV}$, ie much larger than usual values for single atom CQED; this is a consequence of the combination of an emitter having a large dipole, and of a cavity with very small modal volume.

Remarkably, the expected Rabi splitting is much larger than the typical linewidth of a single InAs QD at low temperature (few μeV to few tens of μeV). On the other hand, the cavity Qs of semiconductor microcavities were until recently too small to allow observation of the vacuum Rabi splitting for a single QD. Let us note that in such a regime, for which decoherence is mostly due to cavity damping, the necessary condition for observing the strong coupling regime is written [AND 99]:

$$4\hbar\Omega > \Delta E_{cav} \quad (2)$$

where ΔE_{cav} is the linewidth of the mode of the “empty” cavity (i.e. before coupling with the emitter is established). In order to present condition (2) graphically, we compare in Figure 4.3 state of the art values of ΔE_{cav} obtained for various microcavities to the expected value of $4\hbar\Omega$ for a QD located at the mode antinode.

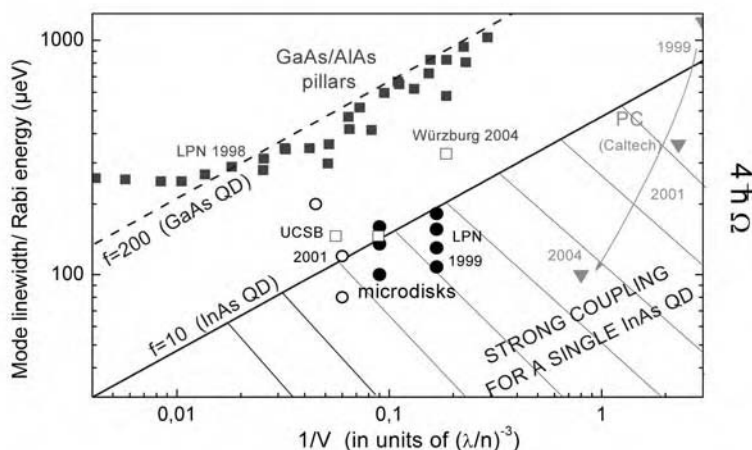
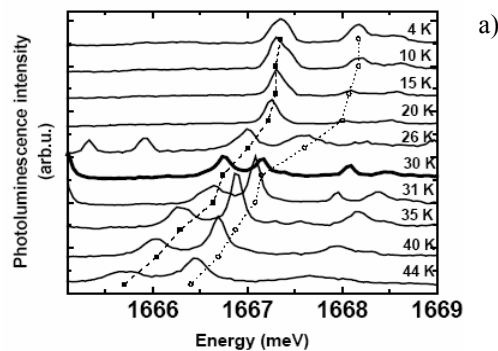


Figure 4.3. Theoretical estimate of $4\hbar\Omega$ (i.e. twice the Rabi splitting) for a single InAs QD or a single GaAs QD formed by an interface defect of a quantum well, located at the antinode of a cavity mode of volume V . This estimate is compared to experimental values of the cavity mode linewidth for micropillars [GER 98; REI 04], microdisks [GAY 01; KIR 01], and photonic crystal microcavities [PAI 99; YOS 04]

New design rules led recently to a spectacular improvement in the cavity Qs of photonic crystal microcavities. Such microcavities now have the greatest potential in this context, due to the combination of a modal volume which is close to the ultimate limit for a dielectric cavity ($V \sim (\lambda/2n)^3$) as well as the highest Qs ($Q \sim 20,000$ per $V = (\lambda/n)^3$). As a result, such cavities have made it possible to observe very recently, for the first time, the strong coupling regime for a single InAs Q [YOS 04].

Another promising approach consists of increasing the oscillator strength of the QD. QDs formed by monolayer fluctuations of the thickness of a GaAs/AlAs quantum well are particularly attractive in this context [AND 99]. For appropriate growth conditions, such interface defects can be much larger than the Bohr radius of the exciton. In such a case, confined excitons couple more strongly to light, and exhibit a large oscillator strength (a few hundreds instead of 10 for a single InAs QD). Experimentally, the strong coupling regime has been achieved by placing such a GaAs QD in a high Q microdisk [PET 05] (see Figure 4.4), as well as large InGaAs QDs in pillar microcavities [REI 04].

In these three successful experiments, the Rabi splitting is typically 1 to 3 times larger than the linewidth of the cavity mode. In other words, the system describes only few Rabi oscillations due to the strong decoherence related to cavity damping. Figure 4.3 tells us, however, that for a large oscillator strength QD ideally located in a high Q photonic crystal microcavity, the coupled system could produce as many as 100 Rabi oscillations before being destroyed, which creates very interesting opportunities. Such strongly coupled cavity-QD systems could for instance be used in the future to realize single QD lasers [GER 03] or to demonstrate quantum logical gates based on coherent optical manipulations [IMA 99].



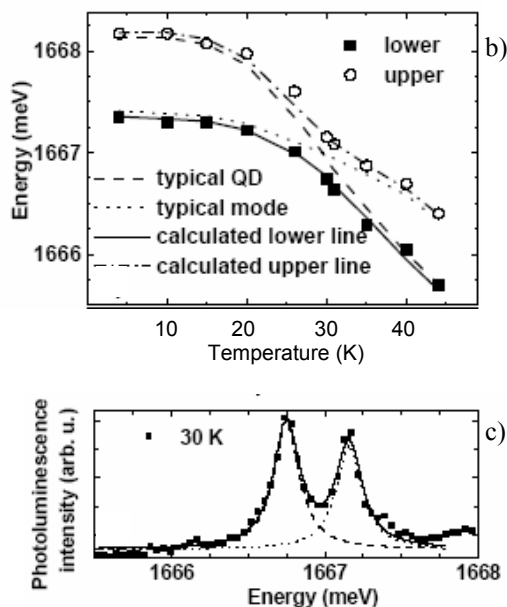
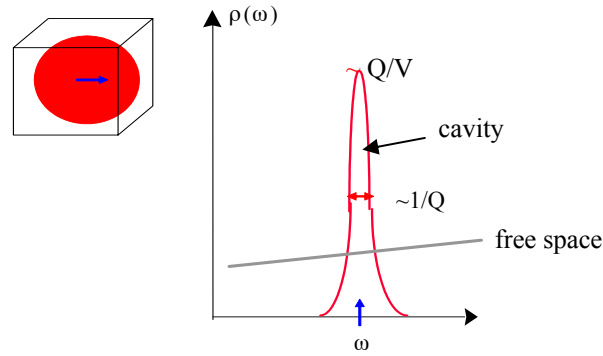


Figure 4.4. Strong coupling regime for a single GaAs QD in a microdisk (from [PET 05]). (a) MicroPL spectra for various temperatures T in the 4–44K range. (b) Peak energies of two emission lines as a function of T . As long as they are well separated spectrally, these lines exhibit different energy shifts, respectively typical of a QD emission line and of a microdisk whispering gallery mode. Close to 30K, the QD enters in resonance with the cavity mode; the clear “anticrossing” behavior of these two lines demonstrates that the QD-cavity system is in the strong coupling regime. (c) Blow-up of (a), showing the PL spectrum at 30K. As expected for a strongly coupled QD-cavity system on resonance, the two exciton-photon modes exhibit the same intensities and spectral linewidths

4.3.2. Weak coupling regime: enhancement/inhibition of the SE rate and “nearly” single mode SE

As shown in the previous section, it is relatively difficult to achieve a strong coupling regime for a single QD. In general, QDs in microcavities are in the weak coupling regime, ie SE remains an irreversible process as when the emitter is in free space. The SE rate, which is given by Fermi’s Golden Rule, is proportional to the density of modes per unit volume. It can therefore be tailored to a large extent by modifying the density of electromagnetic modes to which the emitter is coupled, as suggested by Purcell as early as 1946 [PUR 46].



	Free space	Cavity
Mode density	$\frac{\omega^2 V_{\text{norm}} n^3}{\pi^2 c^3}$	$\frac{2Q}{\pi\omega}$
Volume	V_{norm}	V
Dipole/field overlap	1/3	1

Figure 4.5. Schematic representation of the density of modes per unit volume related to one discrete mode of a 0D cavity and for free space

Let us consider more specifically an emitter in a strongly damped 0D microcavity. In such a case we have $\Delta E_{\text{cav}} > \Delta E_{\text{em}}$; the emitter, which is quasi-monochromatic on the scale of the mode linewidth, sees a continuum of electromagnetic modes, as when it is in a homogeneous dielectric medium or in free space (Figure 4.5).

By comparing the density of modes per unit volume for both cases (and taking into account the fact that the emitter is coupled in free space to one third of the modes, which have a polarization vector parallel to its dipole), one sees that the SE rate in the cavity is enhanced/inhibited by a factor F_p , with respect to the SE in a homogeneous dielectric medium of refractive index n :

$$F_p = \frac{3Q(\lambda/n)^3}{4\pi^2 V} \quad (3)$$

It is essential to note that this “Purcell factor” F_p is a cavity figure of merit, related to one specific mode. It expresses the SE rate of an *ideal* emitter, referenced to its value in free space. This dimensionless number depends solely on the mode volume V^1 – normalized by the wavelength in the material λ cubed – and on the cavity mode quality factor Q . This ideal emitter is optimally coupled to the cavity mode, i.e. is located at the antinode of the mode and has a dipole vector which is aligned with the local polarization vector of the field. Furthermore, it is quasi-monochromatic and perfectly matched spectrally with the cavity mode. If the emitter cannot be treated as quasi-monochromatic (for instance when it experiences a strong homogeneous broadening due to dephasing mechanisms), it is necessary to replace $1/Q$ by $1/Q+1/Q_{em}$ in equation (3) (the quality factor of the emitter is defined by $E/\Delta E_{em}$).

The Purcell effect or *enhancement* of the SE rate was first spectacularly observed (x500) for Rydberg atoms located inside microwave cavities [HAR 89]. Although high- F_p semiconductor microcavities have been available since the early 1990s, its observation in the solid-state was somewhat delayed due to the spectral broadness of usual solid-state emitters. Indeed, for spectrally broad emitters, $1/Q \ll 1/Q_{em}$, so that the Purcell effect is smeared out. Using QDs at low temperature as artificial atoms was therefore the key to observing a strong Purcell effect in a solid-state system [GER 98; GRA 99; GAY 01; SOL 01; KIR 01; MOR 01].

The Purcell effect was first observed by performing time resolved photoluminescence experiments on collections of QDs inserted inside micropillars (x5 [GER 98]), microdisks (x13 [GAY 01]), and structures very close to vertical-cavity surface emitting lasers (x2.3 [GRA 99]). In such experiments, the SE rate enhancement factor is much smaller than the Purcell factor F_p (30 for pillars, 120 for microdisks), since the QDs are randomly distributed, both spatially and spectrally, with respect to the cavity mode. When the number of QDs coupled to the mode is large enough (~30 at least), one can easily account quantitatively for the magnitude of the Purcell effect by realizing a statistical averaging, assuming random spectral and spatial distributions of the QDs [GER 98, 03].

¹ In this expression, V represents the effective volume of the mode, which is usually much smaller than the physical volume of the microcavity. This figure of merit quantifies the suitability of the cavity for the spatial confinement of the electromagnetic field. It is defined as the volume of a cavity defined by Born-von Karmann periodic boundary conditions (inside which the electromagnetic field is uniform), for which the vacuum field would have the same maximum amplitude as for the cavity in question.

More recently, single QDs inserted in a micropillar [MOR 01; SOL 01] or in a microdisk [KIR 01] have also been studied. As an example, Figure 4.6 displays some time resolved photoluminescence spectra obtained for three QDs located in the core of a $1\mu\text{m}$ diameter micropillar. For such a pillar, one can compare directly the properties of QDs which are in resonance or out-of-resonance with its fundamental resonant mode. Out-of-resonance QDs, which are only coupled to the continuum of non-resonant modes of the pillar cavity, display a radiative lifetime which is very close to the one of similar QDs inserted in bulk GaAs (~ 1.3 ns). In spite of the modest Purcell factor of the pillar under study ($F_p=6$), a clear enhancement of the SE rate is observed for the QD1, which is perfectly matched spectrally with the cavity mode. As expected, the magnitude of the Purcell effect can be stronger for a single QD than for a collection of QDs, as soon as the former is reasonably well coupled (spatially and spectrally) to the cavity mode.

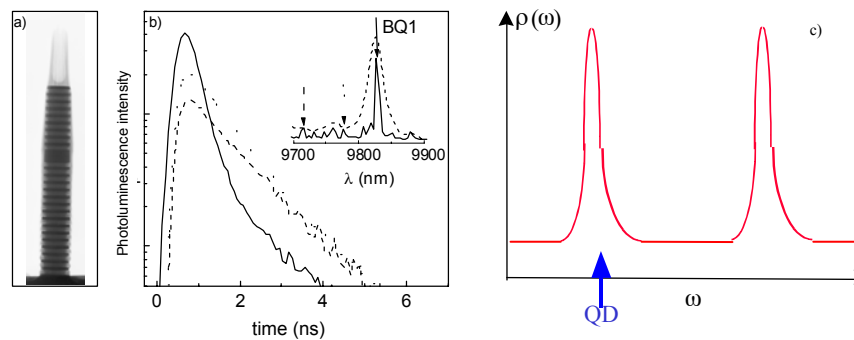


Figure 4.6. (a) Scanning electron micrograph obtained for a GaAs/AlAs micropillar containing QDs in its core (diameter: $1\mu\text{m}$). (b) Time-resolved photoluminescence decay curves (log scale) measured for three QDs located in this micropillar, after excitation by a pulsed excitation of the GaAs barrier by a laser. Two photoluminescence spectra obtained for this micropillar are also shown in the inset. Under weak optical excitation (solid line), single QD emission lines are spectrally resolved. Under strong excitation (dashed line), each QD experiences strong homogeneous broadening; the spectrum then reflects the density of modes of the cavity [MOR 01]. (c) Schematic representation of the density of modes per unit volume for a micropillar

An intrinsic difficulty in the analysis of such experiments is related to the fact that their precise location in the cavity is not known, likewise the radiative lifetime they would exhibit in bulk GaAs [GAY 03]. Earlier, we implicitly assumed that this lifetime is similar for QDs having similar bandgaps, which is generally well verified. In order to demonstrate unambiguously the occurrence of the Purcell effect for a single QD, it is however better to play with the spectral detuning of the cavity-QD

system so as to compare the behavior of a given QD when it is in or out of resonance with the cavity mode. Temperature tuning, which affects essentially the QD bandgap, has made it possible to evidence a strong Purcell effect for a single InAs QD in a microdisk (x6) [KIR 01], or in a micropillar (x5) [VUC 03].

Until now, the Purcell effect has only been observed at relatively low temperatures ($T < 50\text{K}$). The homogeneous broadening of the QD line, related to electron-phonon interaction, is a major hindrance in view of applications of the Purcell at 300K, for instance to realize ultrafast light emitting diodes. In the mid-term, the Purcell effect will more likely be used to collect efficiently the SE into a single mode [GER 98], rather than utilized for its ability to fasten SE dynamics. Let us indeed consider the density of modes per unit volume related to a 0D microcavity, such as a micropillar (Figure 4.6c). Such a microcavity supports a continuum of unconfined modes, besides its set of discrete resonant cavity modes. However, if a resonant mode has a large Purcell factor, its contribution to the density of modes per unit volume can be much larger than for all the non-resonant modes together. For an emitter in resonance in the cavity, the Purcell effect enhances *selectively* the SE rate into the resonant cavity mode, and funnels dynamically most emitted photons into that specific mode.

Let us consider for instance the QD1 which is studied in Figure 4.6. Its SE rate into the continuum of non-resonant modes (estimated using the SE rate of QD2 and QD3 which are out of resonance) is in the order of $1/(1.3) \text{ ns}^{-1}$, whereas its total SE rate is $1/(0.4) \text{ ns}^{-1}$. The fraction of the SE which is coupled to the fundamental mode of the pillar is therefore $\beta = 1 - (0.4/1.3) \sim 0.7$. For micropillars displaying higher Purcell factors ($F_p > 30$), β s in excess of 95% could be achieved in this way [GER 98; SOL 01], which brings about very interesting opportunities in the field of nanolazars or single photon sources.

The Purcell effect can also be used to control the polarization of spontaneously emitted photons. The dipole of InAs QDs has two similarly strong components along the x and y in-plane directions. As a result, the emission of such QDs is in general essentially unpolarized². This property is not affected by QD insertion inside axi-symmetrical micropillars, since their fundamental mode displays two-fold polarization degeneracy related to the equivalence of x and y directions. Some shape birefringence can be introduced by designing micropillars with an elliptical cross-section. Elliptical micropillars present a non-degenerate pair of fundamental modes, which have linear polarizations along crossed directions [GAY 98]. When a single

² High resolution microphotoluminescence experiments performed on a single QD reveal a fine splitting of the exciton line related to the QD asymmetry [BAY 99]. In such a case, the two components of this doublet exhibit crossed linear polarizations and similar intensities, when the QD is surrounded by bulk GaAs.

QD is inserted into such a micropillar, its emission exhibits a strong linear polarization degree (in excess of 90% in the best cases), which is defined by the polarization of the resonant mode to which it is preferentially coupled, due to the Purcell effect [MOR 01].

Finally, let us discuss briefly recent experiments demonstrating SE inhibition for QDs in 0D microcavities. As shown by the behavior of out-of-resonance QDs (see e.g. Figure 4.6), this effect cannot be observed in standard micropillars, since the density of non-resonant modes is comparable to that of bulk GaAs. This can be traced back to the fact that GaAs/AlAs Bragg mirrors designed to operate at a certain wavelength have a good reflectivity only for a limited angular range ($\pm 20^\circ$ typically around normal incidence, when seen from the cavity layer). Several strategies can be used to reduce significantly the density of non-resonant modes. In the spirit of Yablonovitch's initial proposal [YAB 97], inverse opal 3D photonic crystals have been used to inhibit the SE from semiconductor nanocrystals [LOD 04]. For self-assembled QDs, a decrease in the SE rate by a factor as large as 10 has been observed in metal-coated micropillars [BAY 01], due to the suppression of the continuum of leaky modes entering/exiting the micropillar through its sidewalls. Although they do not display a complete photonic bandgap, 2D photonic crystals are highly reflective (and, therefore, suppress non-resonant modes) over a very large solid angle for laterally propagating light. Strong SE inhibition has been observed for both collections of InAs QDs ($\times 0.5$) [KRE 05] and single QDs ($\times 0.2$) [ENG 05] in 2D GaAs photonic crystals. When a single QD is coupled to a cavity mode in such structures, it experiences both the Purcell effect, which enhances the SE into one resonant cavity mode, and an inhibition of its SE rate into the continuum of leaky modes. These combined effects ensure an excellent single-mode collection of the QD emission ($\beta > 0.97$), which is very attractive in view of the development of high efficiency single photon sources, as discussed in the next section.

4.3.3. *Applications of CQED effects to single photon sources and nanolazars*

These CQED effects open an avenue toward the development of novel optoelectronic devices, displaying original functionalities. We will first review the recent fabrication of single-mode Solid-State Sources of Single Photons (S4P), before discussing potential developments in the field of nanolazars.

A single photon source is a device that is able to generate on demand a light pulse containing one and only one photon. For usual light sources, on the other hand, the number of photons in a given pulse is ill defined; this is for instance the case for a thermal source, such as a light bulb ($\Delta N \sim \langle N \rangle$), or for a laser source ($\Delta N = \langle N \rangle^{1/2}$). Presently, the development of single photon sources is in general motivated by their potential application to quantum key distribution, which uses

encoding of the information on the state of a quantum system (i.e. a photon or an entangled pair of photons) to ensure a perfect confidentiality of a communications channel [BEN 92]. Numerous experimental demonstrations of quantum key distribution have already been achieved, both in the lab and on public telecommunications networks. The oldest protocol for QKD, which relies on the encoding of binary information on the polarization state of single photons, is still a good compromise in terms of complexity and efficiency. Until recently, attenuated lasers were used as approximate sources of single photons, due to the lack of real single photon sources. In practice, the attenuation must be very strong (average number of photons per pulse $\langle N \rangle \ll 1$) in order to reduce to an acceptable level the proportion of multiple-photon pulses, which could be exploited by an eventual eavesdropper. Simple models show that the replacement of a weak coherent source by a true single photon source would make it possible to increase the length of secure transmission channels based on optical fibers from 30 to 100 km typically, or to increase the bit rate (for a constant transmission length) by two orders of magnitude [BRA 00]. In the longer term, a nearly perfect single photon source could also be used as standard (for light flux, or energy), or even quantum computers using single photons as physical supports for quantum bits [KNI 01].

Two main strategies can be followed to build an S4P. One can firstly implement a Coulomb blockade in semiconductor nanostructures: if one injects exactly one electron and one hole in a quantum well or QD, it will emit one photon (at most) [KIM 99]. This approach seems however restricted to a low temperature operation range ($T < 0.1$ K until now). A second approach consists of using a single emitter, which supports discrete electronic levels. Single photon generation has recently been reported for a single molecule [BAS 92; LOU 00], a color center in diamond [KUR 01; BRO 00], a semiconductor nanocrystal [MIC 00a], and a single self-assembled QD [MIC 00b; SAN 01]. Among these solid-state emitters, only QDs have enabled the demonstration of an *electrically pumped* S4P [YUA 02] as well as of a *single-mode* S4P [MOR 01], which is able to generate single photons with very high efficiency, prepared with a well defined spatial mode and polarization. This possibility is particularly interesting in practice for quantum key distribution, since it is necessary, prior to polarization encoding of the information, to prepare the photons in a reference state. When using a source of unpolarized photons, half of the photons are lost during this preliminary preparation stage.

The operation of the single mode S4P relies on two basic functions: the generation of photons one by one, and their preparation in a well defined quantum state. Since a QD can trap several electron-hole pairs (and can, in such a case, re-emit several photons within an arbitrarily short delay), a specific protocol must be used to ensure that photons are really emitted one by one on demand. The strong Coulomb interaction between charge carriers trapped inside QDs is particularly helpful in this context. Figure 4.7 depicts a simple protocol that was proposed a few

years ago [GER 99b], which has been validated experimentally by numerous groups [MIC 00; SAN 02; MOR 01]. A QD, which has been isolated by convenient means, is excited non-resonantly through pulsed optical or electrical pumping of the barrier material. Several electron-hole pairs are rapidly captured by the QD and relax down to their lowest electronic states within a few tens of picoseconds. A sequential recombination of these pairs then occurs, until the QD is “empty”. At each stage of this radiative cascade, one photon is emitted at a specific energy X_n , which depends on the number n of electron-hole pairs still present in the QD. Spectral filtering can therefore be used to prepare light pulses containing a well defined number of photons. By selecting for instance the X_1 QD emission line, a single photon is prepared, whereas a filtering of both X_1 and X_2 lines makes it possible to prepare a strongly correlated pair of photons [MOR 01b]. Because this pumping scheme is non-resonant, electrical pumping can also be achieved [YUA 02; OLI 05].

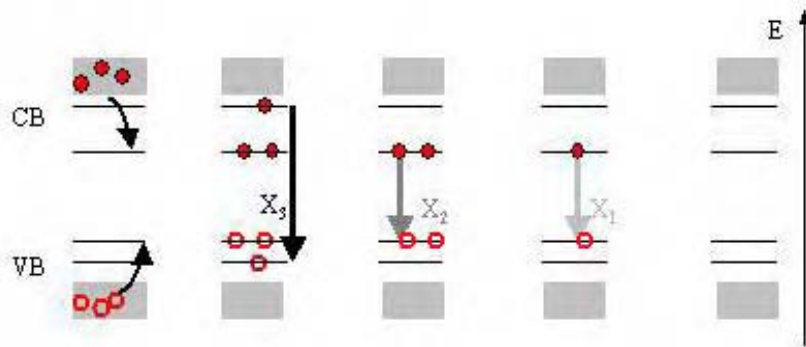


Figure 4.7. Schematic illustration of a radiative cascade in a QD, and of the protocol that is used to generate single photon pulses [GER 99b]

As a result of their particular fabrication process, self-assembled QDs are inserted in a bulk semiconductor, whose refractive index is large. Therefore, most of the QD SE usually remains trapped within this matrix due to total internal reflection at the semiconductor-air interface. By inserting the QD in a microcavity, one can greatly improve extraction efficiency, and prepare these photons, as described in section 4.3, with a well defined mode and polarization due to the Purcell effect. Detailed studies performed at CNRS/LPN [MOR 02], Stanford University [PEL 02] and CEA Grenoble [OLI 05] have confirmed that such an S4P, although not perfect, already presents very attractive properties in view of its application to QKD. Interestingly, the probability of emitting one photon is already as high as 40%, and the probability of emitting two or more photons is reduced by one to two orders of

magnitude, when compared to a weak coherent source of similar intensity. Short term studies in this field aim at developing a “plug and play” S4P for QKD, which will combine electrical pumping and a singlemode emission within the 1.3 μm telecom window. In the future, novel microcavity designs based for example on photonic crystals could be implemented to increase S4P efficiency further [GER 04]. One a more fundamental note, QD SE dynamics becomes faster than emitter decoherence processes when the Purcell effect is strong enough. In such a case, each single photon emission event is identical. In such a regime, the QD emits indistinguishable single photons [SAN 02, VAR 05] which opens up many novel opportunities in the field of quantum information processing.

Improved SE control is also likely to improve microlasers significantly, and should in particular make it possible to reduce their threshold current by several orders of magnitude [GER 03]. A first approach would exploit an ultimately small microcavity ($V \sim (\lambda/2n)^3$) built from a photonic crystal structure. For such a cavity, a strong Purcell effect can be obtained even for spectrally broad emitters. Let us consider for instance a state-of-the-art InAs QD array, having an inhomogeneous spectral linewidth in the order of 15 meV ($Q_{em} \sim 60$). The expected SE rate enhancement factor is close to 20 and the SE coupling coefficient β is around 0.95. This approach is probably the most promising one to date for approaching the regime of “thresholdless lasing” at room temperature, and for reducing the threshold current of laser microsources below 1 μA at 300K, as compared to at least 30 μA today [HUF 97]. It is also possible, at least in principle, to build a laser with an active medium restricted to a single QD, and to reduce the threshold current further, down to 10 pA [PEL 99]. Here however, the QD line must be narrow enough to warrant a good coupling of the QD to the cavity mode, which requires operation at a low temperature ($T < 100\text{K}$) [GER 03]. Although major technological difficulties must be faced, for example to ensure the electrical pumping of these microlasers, these estimates show that the implementation of CQED effects will greatly modify the physics of laser diodes, and bring them close to their ultimate properties. On the application side, very low threshold microlasers working at 300K could be of use in realizing dense optical interconnections embedded in integrated electronic circuits, or remote optical sensors for the environmental or biomedical domains.

This chapter is based in large part on research work conducted by the author in collaboration with CNET and CNRS/LPN researchers in Bagnaux between 1990 and 2002. The contributions of numerous colleagues including B. Gayral, E. Moreau, B. Sermage, I. Abram, I. Robert, J. Y. Marzin, P. Senellart, E. Peter, J. Bloch, A. Lemaître, L. Ferlazzo, V. Thierry-Mieg and C. Dupuis are gratefully acknowledged.

4.4. References

- [AND 99] L.C. Andreani, G. Panzarini, J.M. Gérard, *Phys. Rev. B* 60, 13276 (1999)
- [ARM 03] D.K. Armani, T.J. Kippenberg, S.M. Spillane, K.J. Vahala, *Nature* 421, 925 (2003)
- [ART 01] M.V. Artemyev, U. Woggon, R. Wannemacher, H. Jaschinski, W. Langbein, *Nano Letters* 1, 309 (2001)
- [BAD 05] A. Badolato, K. Hennessy, M. Atatüre, J. Dreiser, E. Hu, P.M. Petroff and A. Imamoglu, *Science* 308, 1158 (2005)
- [BAS 92] Th. Basché *et al.*, *Phys. Rev. Lett.* 69, 1516 (1992)
- [BAY 99] M. Bayer *et al.*, *Phys. Rev. Lett.* 82, 1748 (1999)
- [BAY 01] M. Bayer, T.L. Reinecke, F. Weidner, A. Larionov, A. Mc Donald, A. Forchel, *Phys. Rev. Lett.* 86, 3168 (2001)
- [BAY 02] M. Bayer, A. Forchel, *Phys. Rev. B* 65, 041308 (2002)
- [BEN 92] C.H. Bennett, G. Brassard, A.K. Eckert, *Sci. Am.* 267, 50 (1992)
- [BEN 99] For a review, see *Confined Photon Systems: Fundamentals and Applications*, H. Benisty, J.M. Gérard, R. Houdré, J. Rarity, C. Weisbuch (eds), Springer, Heidelberg (1999)
- [BES 01] L. Besombes, K. Kheng, L. Marsal, H. Mariette, *Phys. Rev. B* 63, 155307 (2001)
- [BJO 91] G. Björk *et al.*, *IEEE-J. Quant. Electron.* 27, 2386 (1991)
- [BOR 01] P. Borri, W. Langbein, S. Schneider, U. Woggon, R.L. Sellin, D. Ouyang, D. Bimberg, *Phys. Rev. Lett.* 87, 157401 (2001)
- [BOU 00] G. Bourdon, I. Robert, R. Adams, K. Nelep, I. Sagnes, J.M. Moison, I. Abram, *Appl. Phys. Lett.* 77, 1345 (2000)
- [BRA 00] G. Brassard, N. Lütkenhaus, T. Mor, B.C. Sanders, *Phys. Rev. A* 85, 1330 (2000)
- [BRO 00] R. Brouri *et al.*, *Opt. Lett.* 25, 1294 (2000)
- [BRU 94] K. Brunner, G. Abstreiter, G. Böhm, G. Tränkle, G. Weimann, *Phys. Rev. Lett.* 73, 1138 (1994)
- [BUR 95] For a review, see *Confined Electrons and Photons, New Physics and Applications*, E. Burstein and C. Weisbuch (eds), NATO ASI Series B340, Plenum Press, New York (1995)
- [DEN 97] H. De Neve, J. Blondelle, P. Van Daele, P. Demeester, R. Baets, *Appl. Phys. Lett.* 70, 799 (1997)
- [DUC 96] For a review, see *Quantum Optics of Confined Systems*, M. Ducloy and D. Bloch (eds), NATO ASI Series E314, Kluwer, Dordrecht (1996)
- [ENG 05] D Englund *et al.*, *Phys. Rev. Lett.* 95, 013904 (2005)
- [FAN 00] X. Fan, P. Palinginis, S. Lacey, H. Wang and M.C. Lonergan, *Opt. Lett.* 25, 1600 (2000)

- [FAV 03] I. Favero, G. Cassabois, R. Ferreira, D. Darson, C. Voisin, J. Tignon, C. Delalande, G. Bastard, P. Roussignol, J.M. Gérard, *Phys. Rev. B* 68, 233301 (2003)
- [FUJ 00] M. Fujita, R. Ushigome, T. Baba, *Electron. Lett.* 36, 790 (2000)
- [GAY 98] B. Gayral, J.M. Gérard, *Appl. Phys. Lett.* 72, 1421 (1998)
- [GAY 01] B. Gayral, J.M. Gérard, B. Sermage, A. Lemaître, C. Dupuis, *Appl. Phys. Lett.* 78, 2828 (2001)
- [GER 95a] J.M. Gérard, *Topics of Applied Physics*, 30, 269 in [BUR 95]
- [GER 95b] J.M. Gérard, J.B. Génin, J. Lefebvre, J.M. Moison, N. Lebouché, F. Barthe, *J. Crystal Growth* 150, 351 (1995)
- [GER 96a] J.M. Gérard, O. Cabrol, B. Sermage, *Appl. Phys. Lett.* 68, 1113 (1996)
- [GER 96b] J.M. Gérard, D. Barrier, J.Y. Marzin, R. Kuszelewicz, L. Manin, E. Costard, V. Thierry-Mieg, T. Rivera, *Appl. Phys. Lett.* 69, 449 (1996)
- [GER 98] J.M. Gérard, B. Sermage, B. Gayral, E. Costard, V. Thierry-Mieg, *Phys. Rev. Lett.* 81, 1110 (1998)
- [GER 99a] J.M. Gérard, A. Lemaître, B. Legrand, A. Ponchet, B. Gayral and V. Thierry-Mieg, *J. Crystal Growth* 201/202, 1109 (1999)
- [GER 99b] J.M. Gérard, B. Gayral, *J. Lightwave Technol.* 17, 2089 (1999)
- [GER 03] J.M. Gérard in “Single Quantum Dots: Fundamental, Applications and Novel Concepts”, *Topics of Applied Physics* 90, P. Michler (ed), Springer, Heidelberg (2003)
- [GER 04] J.M. Gérard, B. Gayral, *Proceedings of SPIE* vol. 5361, 88–95 (2004)
- [GOL 85] L. Goldstein, F. Glas, J.Y. Marzin, M.N. Charasse, G. Le Roux, *Appl. Phys. Lett.* 47, 1099 (1985)
- [GRA 99] L.A. Graham, D.L. Huffaker, D.G. Deppe, *Appl. Phys. Lett.* 74, 2408 (1999)
- [HAR 89] S. Haroche, D. Kleppner, *Physics Today* 42, 24 (1989)
- [HOU 03] J. Hours, S. Varoutsis, M. Gallart, J. Bloch, I. Robert, A. Cavanna, I. Abram, F. Laruelle, J.M. Gérard *Appl. Phys. Lett.* 82, 2206 (2003)
- [HUF 97] D.L. Huffaker, D. Deppe, *Appl. Phys. Lett.* 71, 1449 (1997)
- [IMA 99] A. Imamoglu, D. Awschalom, G. Burkard, D.P. Di Vincenzo, D. Loss, M. Sherwin and A. Small, *Phys. Rev. Lett.* 83, 4204 (1999)
- [JEW 89] J. Jewell, A. Scherer, S.L. McCall, Y.H. Lee, S. Walker, J.P. Harbison, L.T. Florez, *Electron. Lett.* 25, 1123 (1989)
- [KAM 02] C. Kammerer *et al.*, *Phys. Rev. B.* 66, R041306 (2002)
- [KIM 99] J. Kim, O. Benson, H. Kan, Y. Yamamoto, *Nature* 397, 500 (1999)
- [KIR 01] A. Kiraz, P. Michler, C. Becher, B. Gayral, A. Imamoglu, L. Zhang, E. Hu, *Appl. Phys. Lett.* 78, 3932 (2001)
- [KLO 00] F. Klopff, J.P. Reithmaier, A. Forchel, *Appl. Phys. Lett.* 77, 1419 (2000)

- [KNI 01] E. Knill, R. Laflamme, G. Millburn, *Nature* 409, 46 (2001)
- [KRE 05] A. Kress, F. Hofbauer, N. Reinelt, M. Kaniber, H. Krenner, R. Meyer, G. Böhm, J. Finley, *Phys. Rev. B* 71, 241304 (2005)
- [LOD 04] P. Lodahl *et al.*, *Nature* 430, 654 (2004)
- [LOU 00] B. Lounis, W.E. Moerner, *Nature* 407, 491 (2000)
- [LES 98] Le Si Dang, D. Heger, R. André, F. Bœuf, R. Romestain, *Phys. Rev. Lett.* 73, 716 (1998)
- [MAR 94] J.Y. Marzin, J.M. Gérard, A. Izraël, D. Barrier, G. Bastard, *Phys. Rev. Lett.* 73, 716 (1994)
- [MAT 01] K. Matsuda, K. Ikeda, T. Saiki, H. Tsuchiya, H. Saito, K. Nishi, *Phys. Rev. B* 63, 121304 (2001)
- [MCC 92] S.L. McCall, A.F.J. Levi, R.E. Slusher, H.H. Houch, N.A. Whittaker, A.C. Gossard, J.H. English, *Appl. Phys. Lett.* 60, 289 (1992)
- [MIC 00a] P. Michler, A. Kiraz, C. Becher, W. Schoenfeld, P.M. Petroff, L. Zhang, E. Hu, A. Imamoglu, *Science* 290, 2282 (2000)
- [MIC 00b] P. Michler, A. Imamoglu, M. Mason, P. Carson, G. Strouse, S. Buratto, *Nature* 406, 968 (2000)
- [MOR 01a] E. Moreau, I. Robert, J.M. Gérard, I. Abram, L. Manin, V. Thierry-Mieg, *Appl. Phys. Lett.* 79, 2865 (2001)
- [MOR 01b] E. Moreau, I. Robert, L. Manin, V. Thierry-Mieg, J.M. Gérard, I. Abram, *Phys. Rev. Lett.* 87, 183601 (2001)
- [MOR 02] E. Moreau, I. Robert, L. Manin, V. Thierry-Mieg, J.M. Gérard, I. Abram, *Phys. E* 13, 418 (2002)
- [NOD 00] S. Noda, K. Tomoda, N. Yamamoto, A. Chutinan, *Science* 289, 604 (2000)
- [OLI 05] S. Olivier *et al.*, *Proceedings of ECIO'05*, Grenoble 2005
- [PAI 99] O.J. Painter, A. Husain, A. Scherer, J.D. O'Brien, I. Kim, D. Dapkus, *J. Lightwave Technol.* 17, 2082 (1999)
- [PAR 04] H. G. Park, S.H. Kim, S.H. Kwon, Y.G. Ju, J.K. Yang, J.H. Baek, S.B. Kim, Y.H. Lee, *Science* 305, 1444 (2004)
- [PEL 99] M. Pelton, Y. Yamamoto, *Phys. Rev. A* 59, 2418 (1999)
- [PEL 02] M. Pelton, C. Santori, J. Vuckovic, B. Zhang, G. Solomon, J. Plant, Y. Yamamoto, *Phys. Rev. Lett.* 89, 233602 (2002)
- [PET 05] E. Peter, P. Senellart, D. Martrou, A. Lemaître, J. Hours, J.M. Gérard, J. Bloch, *Phys. Rev. Lett.* 95, 067401 (2005)
- [PET 05] Petroff and A. Imamoglu, *Science* 308, 1158 (2005)
- [PUR 46] E.M. Purcell, *Phys. Rev.* 69, 681 (1946)
- [REI 04] J.P. Reithmaier *et al.*, *Nature* 432, 197 (2004)

- [ROB 05] I.C. Robin *et al.*, *Appl. Phys. Lett.* 87, 233114 (2005)
- [SAB 01] M. Saba, C. Ciuti, J. Bloch, V. Thierry-Mieg, R. André, Le Si Dang, S. Kundermann, A. Mura, G. Bongiovanni, J.L. Staehli, B. Deveaud, *Nature* 414, 731 (2001)
- [SAN 96] V. Sandoghdar, F. Treussart, J. Hare, V. Lefèvre-Seguin, J.-M. Raimond, S. Haroche, *Phys. Rev. A* 54, R1777 (1996)
- [SAN 01] C. Santori, M. Pelton, G. Solomon, Y. Dale, Y. Yamamoto, *Phys. Rev. Lett.* 86, 1502 (2001)
- [SAN 02] C. Santori, D. Fattal, J. Vuckovic, G. Solomon, Y. Yamamoto, *Nature* 419, 594 (2002)
- [SEN 99] P. Senellart, J Bloch, *Phys. Rev. Lett.* 82, 1233 (1989)
- [SOL 01] G. Solomon, M. Pelton, Y. Yamamoto, *Phys. Rev. Lett.* 86, 3903 (2001)
- [TAN 95] K. Tanaka, T. Nakamura, W. Takamatsu, M. Yamanishi, Y. Lee, T. Ishihara, *Phys. Rev. Lett.* 74 3380 (1995)
- [VAR05] S. Varoutsis *et al.*, *Phys. Rev. B* 72, 041303 (2005)
- [VRE 93] A.M. Vredenberg, N.E.J. Hunt, E.F. Schubert, D.C. Jacobson, J.M. Poate, G.J. Zydzik, *Phys. Rev. Lett.* 71, 517 (1993)
- [VUC 03] J. Vuckovic, D. Fattal, C. Santori, G. Solomon, Y. Yamamoto, *Appl. Phys. Lett.* 82, 3596 (2003)
- [WAR 97] R.J. Warburton, C.S. Dürr, K. Karrai, J.P. Kotthaus, G. Medeiros-Ribeiro, P.M. Petroff, *Phys. Rev. Lett.* 79, 5282 (1997)
- [WEI 92] C. Weisbuch, M. Nishioka, A. Ishikawa, Y. Arakawa, *Phys. Rev. Lett.* 69, 3314 (1992)
- [WEI 96] *Microcavities and Photonic Bandgaps: Physics and Applications*, C. Weisbuch and J. Rarity (eds), NATO ASI series E324, Kluwer, Dordrecht (1996)
- [YAB 87] E Yablonovitch, *Phys. Rev. Lett.* 58, 2059 (1987)
- [YAB 93] E. Yablonovitch, *J. Opt. Soc. Am.* B10, 283 (1993)
- [YOK 92] H. Yokoyama *et al.*, *Science* 256, 62 (1992)
- [YOS 04] T Yoshie *et al.*, *Nature* 432, 200 (2004)
- [YUA 02] Z. Yuan, B.E. Kardynal, R.M. Stevenson, A.J. Shields, C.J. Lobo, K. Cooper, N.S. Beattie, D.A. Ritchie, M. Pepper, *Science* 295, 102 (2002)

Chapter 5

Nonlinear Optics in Nano- and Microstructures

5.1. Introduction

One year after the invention of the laser [MAI 60], the observation of second harmonic generation [FRA 61] was the starting point for a new field in optics: nonlinear optics. This observation constituted a demonstration of the possibility of changing the wavelength of a laser via a second order nonlinear process. Since that time, nonlinear optics has grabbed the attention of many researchers and the progress made in this domain can be measured by looking at some of the very important resulting applications. For example, many commercial tunable laser sources are based on the use of nonlinear processes such as parametric oscillations or parametric amplification. One can also cite the use of the optical Kerr effect, a third order nonlinear effect, in optical fiber communications systems in order to compensate chromatic dispersion and propagate optical solitons. However, breakthroughs are still awaited in nonlinear optics, especially their capability to be used for ultrafast data processing for future optical integrated circuits.

On the other hand, in the domain of nano- and microtechnologies, the tremendous progress achieved in material processing, such as in growing, lithography and etching, are revolutionizing optoelectronics and integrated optics because they enable the fabrication of nano- and microstructures that can be used to manufacture completely new miniaturized optical components [JOA 97].

Using microstructures presenting a periodic modulation of the refractive index was proposed as soon as the first steps were taken in nonlinear optics to obtain greater nonlinear interactions. The first proposals aimed at using these structures to achieve the phase matching condition that is necessary to get efficient second order nonlinear interactions [BLO 70; ZIE 75]. Despite pioneering experiments [ZIE 76], it is only since the 1990s that the study of nonlinear effects in microstructured materials has become a very active research domain [BAL 99; FIO 98; GOL 99; JAN 93; MAR 97; RAN 00; TRU 95; WAD 00]. Structuring the matter at the scale of the wavelength of the light enables the engineering of its dispersion properties, such as phase and group velocity [ZHE 00]. This possibility can be used, for instance, to make optical waves at very different wavelengths propagate in a very dispersive medium at the same phase velocity to fulfill the phase matching condition and at low group velocities to obtain greater nonlinear interactions.

This chapter describes the marriage of nonlinear optics and nano-microstructured materials. It is organized in the following way:

- In section 5.2, the general concepts of nonlinear optics are introduced, starting with Maxwell's equations. We describe briefly some of the second order nonlinear processes like second harmonic generation and parametric amplification as well as some of the third order nonlinear phenomena like non-degenerated four wave mixing, optical Kerr effect and Raman, Brillouin and Rayleigh scattering.
- In section 5.3, some examples of the literature on how the nano- or microstructuration of matter can be used to enhance nonlinear interactions are given.

5.2. Introduction to nonlinear optics

5.2.1. Maxwell equations and nonlinear optics¹

Assuming a medium without free charges, nonlinear optics phenomena can be described in a classical way with Maxwell's equations:

$$\begin{aligned} \nabla \cdot \mathbf{D}(\mathbf{r}, t) &= 0 & \nabla \cdot \mathbf{B}(\mathbf{r}, t) &= 0 \\ \nabla \times \mathbf{E}(\mathbf{r}, t) &= -\frac{\partial \mathbf{B}(\mathbf{r}, t)}{\partial t} & \nabla \times \mathbf{H}(\mathbf{r}, t) &= \frac{\partial \mathbf{D}(\mathbf{r}, t)}{\partial t} \end{aligned} \quad (1)$$

$\mathbf{E}(\mathbf{r}, t)$ is the electric field, $\mathbf{H}(\mathbf{r}, t)$ is magnetic excitation, $\mathbf{D}(\mathbf{r}, t)$ is the displacement vector and $\mathbf{B}(\mathbf{r}, t)$ is magnetic induction. The medium response to the excitations $\mathbf{E}(\mathbf{r}, t)$ and $\mathbf{H}(\mathbf{r}, t)$ is given by the constitutive relations that read in an ideal dielectric medium:

¹ For more detail see [BUT 90].

$$\mathbf{D}(\mathbf{r},t) = \epsilon_0 \mathbf{E}(\mathbf{r},t) + \mathbf{P}(\mathbf{r},t) \quad \mathbf{B}(\mathbf{r},t) = \mu_0 \mathbf{H}(\mathbf{r},t) \quad (2)$$

where $\mathbf{P}(\mathbf{r},t)$ is the induced polarization vector, and ϵ_0 and μ_0 are void permittivity and permeability respectively. From these equations, we can obtain the following propagation equation for the electromagnetic field:

$$\nabla \times \nabla \times \mathbf{E}(\mathbf{r},t) + \frac{1}{c^2} \frac{\partial^2 \mathbf{E}(\mathbf{r},t)}{\partial t^2} = -\mu_0 \frac{\partial^2 \mathbf{P}(\mathbf{r},t)}{\partial t^2} \quad (3)$$

Because the considered materials are without free charges, they can be modeled by an assembly of charged particles linked to each other. When a weak electric field is applied, these particles behave like dipoles oscillating at the exciting field frequency. This implies a linear dependence of the polarization on the electric field. The polarization is characterized by the linear susceptibility $\chi^{(1)}$ of the medium which is a second order tensor:

$$\mathbf{P}^L(\mathbf{r},t) = \epsilon_0 \int_{-\infty}^{+\infty} \chi^{(1)}(\mathbf{r},t;\tau) : \mathbf{E}(\mathbf{r},\tau) d\tau \quad (4)$$

This constitutes the linear response of the material. Let us assume now that the electric field is intense enough to obtain an anharmonic response of the oscillating charges of the material. It is convenient to decompose this response in the consecutive powers of the electric field:

$$\mathbf{P}^{NL}(\mathbf{r},t) = \sum_{i=2}^{\infty} \mathbf{P}^{(i)}(\mathbf{r},t) \quad (5)$$

with:

$$\mathbf{P}^{(i)}(\mathbf{r},t) = \epsilon_0 \int_{-\infty}^{+\infty} d\tau_1 \dots \int_{-\infty}^{+\infty} d\tau_i \chi^{(i)}(\mathbf{r},t;\tau_1, \dots, \tau_i) : \mathbf{E}(\mathbf{r},\tau_1) \dots \mathbf{E}(\mathbf{r},\tau_i) \quad (6)$$

$\chi^{(i)}$, the i^{th} order susceptibility, is a $(i+1)^{\text{th}}$ order tensor. Thus, the total macroscopic polarization reads as the sum of a linear term and a nonlinear term:

$$\mathbf{P}(\mathbf{r},t) = \mathbf{P}^L(\mathbf{r},t) + \mathbf{P}^{NL}(\mathbf{r},t) \quad (7)$$

In the frequencies space, the relation between $\mathbf{P}(\mathbf{r}, \omega)$ and $\mathbf{E}(\mathbf{r}, \omega)$ becomes simpler:

$$\begin{aligned} \mathbf{P}(\mathbf{r}, \omega) = & \varepsilon_0 \chi^{(1)}(\mathbf{r}, -\omega; \omega) : \mathbf{E}(\mathbf{r}, \omega) \\ & + \sum_{i=2}^{\infty} \varepsilon_0 \chi^{(i)}(\mathbf{r}, -\omega; \omega_1, \dots, \omega_i) : \mathbf{E}(\mathbf{r}, \omega_1) \cdots \mathbf{E}(\mathbf{r}, \omega_i) \end{aligned} \quad (8)$$

With for each value of i :

$$\omega = \sum_{p=1}^i \omega_p \quad (9)$$

Note that ω_p frequencies can be positive, negative or null. The relation between $\mathbf{E}(\mathbf{r}, \omega)$ and $\mathbf{E}(\mathbf{r}, t)$ reads:

$$\mathbf{E}(\mathbf{r}, \omega) = \int_{-\infty}^{+\infty} \mathbf{E}(\mathbf{r}, t) e^{j\omega t} dt \quad \text{et} \quad \mathbf{E}(\mathbf{r}, t) = \frac{1}{2\pi} \int_{-\infty}^{+\infty} \mathbf{E}(\mathbf{r}, \omega) e^{-j\omega t} d\omega \quad (10)$$

We can now write the propagation equation for the electric field oscillating at ω frequency:

$$\nabla \times \nabla \times \mathbf{E}(\mathbf{r}, \omega) - \frac{\omega^2}{c^2} \varepsilon(\mathbf{r}, \omega) : \mathbf{E}(\mathbf{r}, \omega) = \omega^2 \mu_0 \mathbf{P}^{\text{NL}}(\mathbf{r}, \omega) \quad (11)$$

where:

$$\varepsilon(\mathbf{r}, \omega) = 1 + \chi^{(1)}(\mathbf{r}, -\omega; \omega) \quad (12)$$

The nonlinear polarization appears like a source term in the propagation equation (11). In general, this equation is difficult to solve. In order to be able to discuss the nonlinear effects and to extract some general rules, the following hypotheses are considered:

- The nonlinear medium is assumed to be homogenized, which means that the dielectric constant does not depend on the variable \mathbf{r} .
- All the electromagnetic waves are propagating collinearly in the z -direction.
- All the waves interacted nonlinearly are propagating in one sense.

– The waves are assumed to be plane, linearly polarized and oscillating in plane normal to propagation direction. As a consequence, the problem becomes scalar and the transverse nature of electric fields ensures the condition: $\nabla \cdot \mathbf{E}(\mathbf{r}, \omega) = 0$.

The propagation equation (11) now reads:

$$\frac{\partial^2 E(z, \omega)}{\partial z^2} + \frac{\omega^2}{c^2} \epsilon(z, \omega) E(z, \omega) = -\omega^2 \mu_0 P^{NL}(z, \omega) \quad (13)$$

Let us suppose:

$$E(z, \omega) = \frac{1}{2} A_\omega(z) e^{jk_\omega z} + cc \quad (14)$$

where $k_\omega = n_\omega \omega / c$ with n_ω the refractive index at ω frequency. cc corresponds to the complex conjugate. The n^{th} order nonlinear polarization reads:

$$P^{(n)}(z, \omega) = \frac{1}{2} p_\omega^{(n)}(z) e^{jk_{NL} z} + cc \quad (15)$$

with:

$$k_{NL} = \sum_{p=1}^n k_{\omega_p} \quad (16)$$

By injecting (14) and (15) in (13), and by taking into account the n^{th} order nonlinear polarization only, we obtain:

$$\frac{\partial^2 A_\omega(z)}{\partial z^2} + 2jk_\omega \frac{\partial A_\omega(z)}{\partial z} = -\omega^2 \mu_0 p_\omega^{(n)}(z) e^{j\Delta k z} \quad (17)$$

The quantity $\Delta k = k_{NL} - k_\omega$ is called the phase mismatch. We will see later in this chapter that this term plays a crucial role in second order processes.

Because all waves are traveling in one sense, we can apply the slowly varying envelope approximation:

$$\left| \frac{\partial^2 A_\omega(z)}{\partial z^2} \right| \ll \left| 2k_\omega \frac{\partial A_\omega(z)}{\partial z} \right| \quad (18)$$

Thus, the propagation equation of the electric field envelope reads:

$$\frac{\partial A_\omega(z)}{\partial z} = \frac{j\omega \mu_0 c}{2n_\omega} p_\omega^{(n)}(z) e^{j\Delta k z} \quad (19)$$

This supposes that the envelope does not depend on the time variable. In the case where the propagation of ultrashort pulses is considered, this description is not adapted. Time dependence must also be taken into account in the slowly varying envelope approximation:

$$\left| \frac{\partial^2 p_\omega^{(n)}(z,t)}{\partial t^2} \right| \ll \left| 2\omega \frac{\partial p_\omega^{(n)}(z,t)}{\partial t} \right| \ll \left| \omega^2 p_\omega^{(n)}(z,t) \right| \quad (20)$$

We can show that the propagation equation reads:

$$\left(\frac{\partial}{\partial z} + \frac{1}{v_g} \left| \frac{\partial}{\partial t} \right. \right) A_\omega(z,t) = \frac{j\omega}{2n_\omega \epsilon_0 c} p_\omega^{(n)}(z,t) e^{j\Delta k z} \quad (21)$$

where $v_g = \frac{\partial \omega}{\partial k}$ is the group velocity.

In a general way, the nonlinear polarization appears as a perturbation term in the propagation equation of the light. Second and third order nonlinear effects are discussed below.

5.2.2. Second order nonlinear processes

The propagation equation of a monochromatic wave at ω pulsation was established in the last paragraph when n th order nonlinear polarization term was considered (17). Let us now consider the second order term of nonlinear susceptibility. The second order nonlinearity of a material enables the coupling of three electromagnetic waves. In a corpuscular description, this means that three different photons at angular frequencies ω_1 , ω_2 and ω_3 are interacting. Energy conservation imposes a condition on their energy:

$$\hbar\omega_3 = \hbar\omega_1 + \hbar\omega_2 \quad (22)$$

The electric fields associated to these pulsations read:

$$E(z, \omega_i) = \frac{1}{2} A_i(z) e^{jk_i z} + cc \quad (23)$$

$i = 1, 2, 3$

If n_i is the refractive index at ω_i pulsation, the wave vector modulus is $k_i = n_i \omega_i / c$.

5.2.2.1. Three wave mixing

Preliminary note concerning second order nonlinear tensors

Generally, second order nonlinear polarization reads:

$$P_i^{(2)}(\omega_m) = \sum_{jk} \sum_{np} \chi_{ijk}^{(2)}(-\omega_m; \omega_n, \omega_p) E_j(\omega_n) E_k(\omega_p) \quad (24)$$

$i = x, y, z \quad \omega_m = \omega_n + \omega_p \quad m = 1, 2, 3$

$E_j(\omega_n)$ are the Cartesian components of the electric field $\mathbf{E}(\omega_n)$. Several simplifications occur in the expression of nonlinear susceptibility when the following properties of materials are taken into account:

- Symmetry rules. Note that the second order nonlinear susceptibility is null for centrosymmetrical materials.
- Medium transparency. This gives the Kleinman relations that induce the non-dispersive nature of nonlinear susceptibility.

As a consequence, second order nonlinear susceptibility is represented by a 3x6 matrix (d_{jk}) that couples $P_i^{(2)}(\omega_m)$ to terms of the form $E_j(\omega_n) E_k(\omega_p) + E_k(\omega_n) E_j(\omega_p)$.

Further, the problem is assumed to be scalar, as it was when equation (13) was established. For this, we introduce the effective nonlinear susceptibility $\chi^{(2)}$ that describes nonlinear interaction. To each frequency corresponds a nonlinear polarization term:

$$\text{– for } \omega_3 : P^{(2)}(z, \omega_3) = \frac{1}{2} \varepsilon_0 K \chi^{(2)}(-\omega_3; \omega_1, \omega_2) A_1(z) A_2(z) e^{j(k_1 + k_2)z} + cc$$

$$- \text{ for } \omega_2 : P^{(2)}(z, \omega_2) = \frac{1}{2} \epsilon_0 K \chi^{(2)}(-\omega_2; -\omega_1, \omega_3) A_1^*(z) A_3(z) e^{j(k_3 - k_1)z} + cc$$

$$- \text{ for } \omega_1 : P^{(2)}(z, \omega_1) = \frac{1}{2} \epsilon_0 K \chi^{(2)}(-\omega_1; -\omega_2, \omega_3) A_2^*(z) A_3(z) e^{j(k_3 - k_2)z} + cc$$

with: $K = 2^{l+q-2} r$ where $l=1$ if $\omega_m \neq 0$ otherwise $l=0$, q and r are respectively the numbers of null frequencies and permutations in the list of the $\omega_{n,o,p}$. For example, if the considered frequencies are non-null and all are different: $K = 2^{1+0-2} \times 2! = 1$.

Thanks to the nonlinear polarization expressions, we can now write the propagation equations for the different spectral components of the electric field envelope:

$$\begin{cases} \frac{dA_1(z)}{dz} = \frac{j\omega_1}{2cn_1} \chi^{(2)} A_2^*(z) A_3(z) e^{j\Delta kz} \\ \frac{dA_2(z)}{dz} = \frac{j\omega_2}{2cn_2} \chi^{(2)} A_1^*(z) A_3(z) e^{j\Delta kz} \\ \frac{dA_3(z)}{dz} = \frac{j\omega_3}{2cn_3} \chi^{(2)} A_1(z) A_2(z) e^{-j\Delta kz} \end{cases} \quad (25)$$

$\Delta k = k_3 - k_2 - k_1$ is the phase mismatch between a field and induced polarization at the same frequency.

5.2.2.2. Second harmonic generation

Let us now consider the simplest case of three wave mixing: second harmonic generation (SHG). Now, we have $\omega_1 = \omega_2 = \omega$ and $\omega_3 = 2\omega$.

In this case, the equations system (25) is simplified and becomes:

$$\begin{cases} \frac{dA_\omega(z)}{dz} = \frac{j\omega}{2n_\omega c} \chi^{(2)} A_{2\omega}(z) A_\omega^*(z) e^{j\Delta kz} \\ \frac{dA_{2\omega}(z)}{dz} = \frac{j\omega}{2n_{2\omega} c} \chi^{(2)} A_\omega^2(z) e^{-j\Delta kz} \end{cases} \quad (26)$$

Note the $1/2$ factor coming from the frequencies' degeneracy ($K = 2^{1-0-2} \times 1! = 1/2$). Figure 5.1 depicts the quantum diagram of second harmonic generation when no field is in resonance with the nonlinear material.

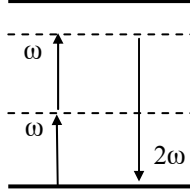


Figure 5.1. Quantum diagram of second harmonic generation. Full lines correspond to real energy level and dotted lines symbolize the start and end states of the virtual transitions

A_ω is called the fundamental field (F) envelope and $A_{2\omega}$ the second harmonic field (SH) envelope. The usual configuration is the generation of an SH wave from an F wave incident on a nonlinear medium, meaning that two photons of the F field are taken to generate one photon of double energy.

When the second harmonic generation efficiency is not very high ($\leq 10\%$), the fundamental wave can be considered undepleted. In this case, the F field intensity is constant and the equation describing SH field envelope propagation can easily be integrated. Thus, the SH field intensity reads:

$$I_{2\omega}(z) = \frac{1}{2} n_{2\omega} c \epsilon_0 |A_{2\omega}(z)|^2$$

$$I_{2\omega}(z) = \frac{2\pi^2}{\epsilon_0 c \lambda^2} \frac{1}{n_\omega^2 n_{2\omega}} [\chi^{(2)}]^2 I_\omega^2(0) \left[\frac{\sin(\Delta k z/2)}{\Delta k/2} \right]^2 \quad (27)$$

$I_\omega(0)$ is the F field intensity and λ its wavelength. The efficiency of second harmonic generation over a distance L is defined as the ratio between the SH and F intensities:

$$\eta(L) = I_{2\omega}(L)/I_\omega(0) \quad (28)$$

From (26) and (27), it can easily be seen that, when Δk is non-null, i.e. when nonlinear polarization and the generated second harmonic do not travel in the medium with the same phase velocity, conversion efficiency varies periodically with the distance (see Figure 5.2a). It reaches its maximum value at the propagation distance $L_c = \pi/\Delta k = \lambda/4(n_{2\omega} - n_\omega)$, called the coherence length. This length corresponds to the maximal distance over which the generated SH interfere constructively with the nonlinear polarization. As the phase mismatch increases, the coherence length as well as the conversion efficiency decreases.

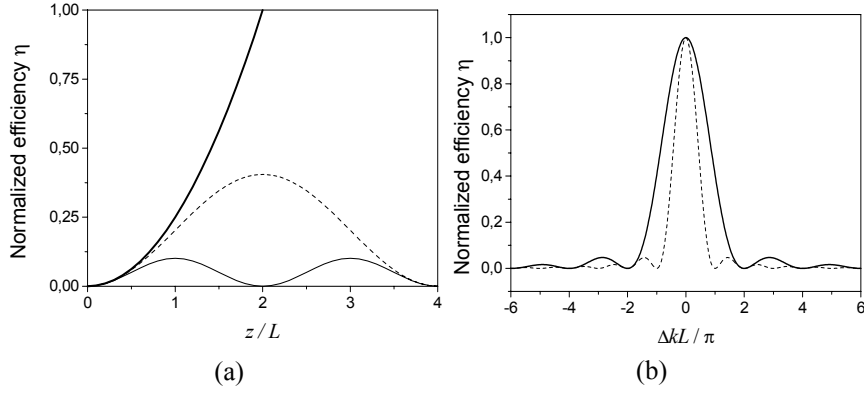


Figure 5.2. Figure 5.2a depicts conversion efficiency as a function of the propagation distance z (normalized to L) for different cases: $\Delta kL=\pi$ (thin full line), $2\Delta kL=\pi$ (dotted line) and $\Delta kL=0$ (phase matching) (thick full line). Figure 5.2b represents phase matching curves (efficiency versus phase mismatch) for a length of interaction L (full line) and for $2L$ (dotted line). It should be noted that as the interaction length is increased, the phase matching curve becomes narrower

Optimal conversion efficiency is obtained when the phase mismatch is null, i.e. when all the induced dipoles by the F field oscillate in phase with the generated SH in all the points of the nonlinear medium. SH intensity grows in this case as the interaction length squared (Figure 5.2a).

Note: SH generation for ultrashort Gaussian pulses of duration τ .

In this case, the following equation has to be solved:

$$\left(\frac{\partial}{\partial z} + \frac{1}{v_g} \bigg|_{2\omega} \frac{\partial}{\partial t} \right) A_{2\omega}(z, t) = \frac{j\omega}{2n_{2\omega}c} \chi^{(2)} A_{\omega}^2(z, t) e^{-j\Delta kz} \quad (29)$$

It can be shown that beyond the length defined as:

$$l = \frac{\tau}{\frac{1}{v_g} \bigg|_{2\omega} - \frac{1}{v_g} \bigg|_{\omega}} \quad (30)$$

SH average intensity no longer grows quadratically with the length; it grows linearly.

5.2.2.3. Parametric amplification

A parametric amplifier is a quadratic nonlinear medium (length L) in which two waves are injected. One of these two waves, the pump, is sufficiently intense to transfer a part of its own energy to a weaker signal injected with a frequency ω_1 or ω_2 .

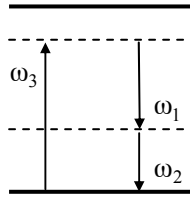


Figure 5.3. *Quantum diagram of parametric amplification. One pump photon with frequency ω_3 is changed in a photon with the frequency and in the mode of the signal (ω_1) and in an idler photon (ω_2)*

A third wave is generated (the idler) to satisfy energy conservation. In order to simplify equation (25), we define a quantity proportional to the photons' flow at the angular frequency ω_i :

$$|\xi_i(z)|^2 = n_i \frac{|A_i(z)|^2}{\omega_i} \quad (31)$$

Consequently, (25) becomes:

$$\begin{cases} \frac{d\xi_1(z)}{dz} = jg\xi_2^*(z)\xi_3(z)e^{j\Delta kz} \\ \frac{d\xi_2(z)}{dz} = jg\xi_1^*(z)\xi_3(z)e^{j\Delta kz} \\ \frac{d\xi_3(z)}{dz} = jg\xi_1(z)\xi_2(z)e^{-j\Delta kz} \end{cases} \quad (32)$$

with:

$$g = \frac{\chi^{(2)}}{2c} \sqrt{\frac{\omega_1 \omega_2 \omega_3}{n_1 n_2 n_3}} \quad (33)$$

In the following, the field at ω_1 frequency is the signal, the field at ω_2 the idler, and the field at ω_3 the pump. As the pump is much more intense than the two other fields, $\xi_3(0)$ is assumed constant. The pump phase at $z = 0$ is considered as null. When $G = g\xi_3(0)$, the solution of equations system (32) reads:

$$\begin{cases} \xi_1(z) = \left\{ \xi_1(0)ch(bz) + \frac{j}{b} \left[G\xi_2^*(0) - \frac{\Delta k}{2} \xi_1(0) \right] sh(bz) \right\} e^{j\frac{\Delta k z}{2}} \\ \xi_2(z) = \left\{ \xi_2(0)ch(bz) + \frac{j}{b} \left[G\xi_1^*(0) - \frac{\Delta k}{2} \xi_2(0) \right] sh(bz) \right\} e^{j\frac{\Delta k z}{2}} \end{cases} \quad (34)$$

The parametric gain by length unit is then given by:

$$b = \sqrt{G^2 - (\Delta k/2)^2} \quad (35)$$

Just like conversion efficiency in the GSH, this gain is maximized when phase matching reaches ($\Delta k = 0$). In this case it grows linearly with incident pump power.

5.2.2.4. How can phase matching be achieved?

We have just seen how important it is to achieve the phase matching condition to obtain efficient nonlinear second order processes. In the following, two methods of obtaining phase matching are described.

5.2.2.4.1. Phase matching by birefringence

Phase matching is usually obtained using the property that most second order nonlinear materials have: birefringency. Two ways of obtaining phase matching in a birefringent material are generally distinguished:

– Type I phase matching: in this case, the two photons at ω frequency are identically polarized (either along the ordinary axis or along the extraordinary axis). The second harmonic photon is then generated along the perpendicular polarization. The propagation direction is chosen so that the relation $n_e(2\omega) = n_o(\omega)$ is verified for a uniaxial negative crystal and $n_o(2\omega) = n_e(\omega)$ for a uniaxial positive crystal.

– Type II phase matching: the two photons of the fundamental field are perpendicularly polarized and the SH photon is polarized along the extraordinary (ordinary) axis for the uniaxial negative (positive) crystals. The phase matching condition reads in the case of the uniaxial negative crystal:

$$n_e(2\omega) = \frac{1}{2}[n_o(\omega) + n_e(\omega)].$$

The main drawbacks of this method are, firstly, that it is impossible to implement it in isotropic materials (like III–V semiconductors), and secondly, that it is not always possible to reach the greatest coefficients of the nonlinear tensor like the d_{33} of LiNbO₃.

5.2.2.4.2. Quasi-phase matching

One way to overcome the problems of phase matching obtained by birefringence is to use quasi-phase matching [ARM 62; FEJ 92]. This approach consists of periodically modulating (Λ is the period) the value of the nonlinear coefficient of the material².

Let us consider this in the context of SHG. Taking into account the spatial variations of nonlinear susceptibility, the evolution equation of the second harmonic envelope (26) becomes:

$$\frac{dA_{2\omega}(z)}{dz} = \frac{j\omega}{2n_{2\omega}c} \chi^{(2)}(z) A_{\omega}^2(z) e^{-j\Delta kz} \quad (36)$$

As nonlinear susceptibility is a periodical function, it can be written as a Fourier sum:

$$\chi^{(2)}(z) = \sum_{n=-\infty}^{n=+\infty} d_n e^{jK_n z} \quad \text{où} \quad K_n = n \frac{2\pi}{\Lambda} \quad (37)$$

We obtain:

$$\frac{dA_{2\omega}(z)}{dz} = \frac{j\omega}{2n_{2\omega}c} A_{\omega}^2(z) \sum_{n=-\infty}^{n=+\infty} d_n e^{j(K_n - \Delta k)z} \quad (38)$$

² Frequently, the solution consists of changing the sign of nonlinear susceptibility with a period equal to the coherence length. Indeed, during propagation over this distance the fundamental wave and the nonlinear polarization are phase-shifted by π . The change in the sign of susceptibility allows them to interfere constructively (Figure 5.4a).

The phase matching condition is consequently somewhat relaxed. If, for instance, $K_p = \Delta k$, it is obvious that after the integration of equation (38), the d_p term becomes dominant as the other terms of the sum oscillate quickly. Thus, the second harmonic field value after propagating over a distance L reads:

$$A_{2\omega}(L) = \frac{j\omega}{2n_{2\omega}c} d_p A_{\omega}^2(0)L \quad (39)$$

The phase matching condition is verified for the d_p component.

Note that quasi-phase matching also makes it possible to obtain an SH intensity which grows quadratically with the propagation length. However, efficiency is reduced by the d_p factor which is equal to $2/\pi$ in the optimal case.

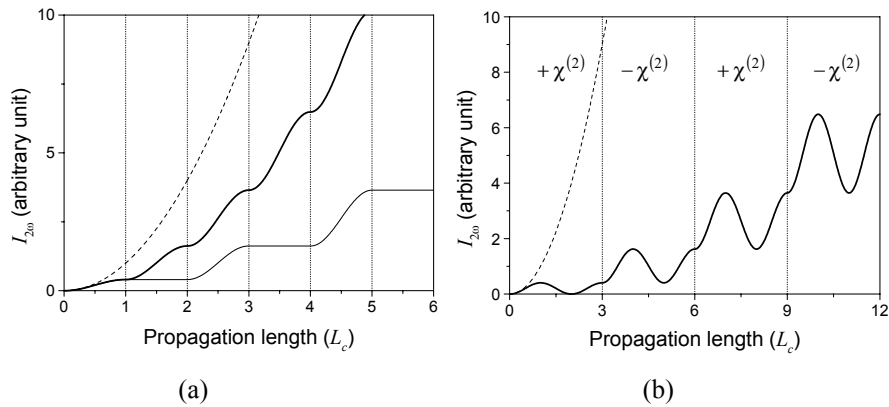


Figure 5.4. (a) The SH conversion efficiency as a function of the propagation distance normalized to the coherence length in the case of quasi-phase matching of the first order ($\Lambda=2L_c$). The thin curve corresponds to the case where the susceptibility is cancelled over a coherence length. The thick curve corresponds to the case where nonlinear susceptibility is periodically inverted (optimal case). (b) An example of quasi-phase matching of the third order ($\Lambda=6L_c$). The evolution of SH intensity in the case of a bulk phase matched material is plotted on the two diagrams as dashed lines

5.2.2.5. *Applications of second order nonlinearity*

Second order nonlinear effects are involved in numerous applications. Here are some examples:

Second harmonic generation is used to obtain laser sources at wavelength that are not available with “standard” sources.

Parametric amplification leads to a parametric gain for the signal field. Using parametric material in a resonant cavity (at least for signal frequency), a parametric oscillator can be obtained. This kind of source is equivalent to a laser source in which stimulated emission is replaced by parametric emission. Parametric sources can be widely spectrally tunable by changing the phase matching conditions with an exterior parameter like temperature or light incident angle on the nonlinear crystal.

There is also a quadratic phenomenon which is the parametric equivalent to spontaneous emission: parametric fluorescence. This effect consists of the spontaneous creation in the nonlinear crystal of two photons with frequency ω_1 et ω_2 from one photon at ω_3 . This phenomenon can be used in light sources for quantum cryptography protocols.

In section 5.3, we will describe how the nano- or microstructuration of materials with a strong nonlinear coefficient enables the fabrication of compact integrated light sources.

5.2.3. *Third order processes*

This section is dedicated to the study of the effects associated with the third order term of nonlinear susceptibility. This term depends on the cube of electric field amplitude. As a consequence, a large number of different phenomena of nonlinear optics are expected to occur. Namely, considering that the nonlinear tensor $\chi^{(3)}$ order is 4, the number of possible interactions is 3^4 .

5.2.3.1. *Four wave mixing*

Let us consider the coupling of four monochromatic waves of frequency ω_1 , ω_2 , ω_3 , ω_4 in a material having a third order nonlinear susceptibility³.

³ Third order nonlinear susceptibility is non-null in all materials. This is not the case for second order nonlinear susceptibility.

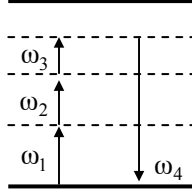


Figure 5.5. Energy diagram of a four wave mixing process (sum frequency)

Energy conservation is written:

$$\hbar\omega_4 = \hbar\omega_1 + \hbar\omega_2 + \hbar\omega_3 \quad (40)$$

In this case, the polarization term at ω_m frequency is given by the following relation:

$$P_i^{(3)}(\omega_m) = \sum_{jkl} \sum_{nop} \chi_{ijkl}^{(3)}(-\omega_m) E_j(\omega_n) E_k(\omega_o) E_l(\omega_p) \quad (41)$$

$$i = x, y, z \quad \omega_m = \omega_n + \omega_o + \omega_p \quad m = 1, 2, 3, 4$$

where $\chi_{ijkl}^{(3)}$ and $E_j(\omega_n)$ are respectively the Cartesian components of the third order nonlinear tensor and of the electric field amplitude at ω_m frequency.

If the problem is assumed to be scalar, as previously, the nonlinear polarization for each wave reads:

$$\begin{aligned} - P^{(3)}(z, \omega_4) &= \frac{1}{2} \varepsilon_0 K \chi^{(3)}(-\omega_4; \omega_1, \omega_2, \omega_3) A_1(z) A_2(z) A_3(z) e^{j(k_1+k_2+k_3)z} + cc \\ - P^{(3)}(z, \omega_3) &= \frac{1}{2} \varepsilon_0 K \chi^{(3)}(-\omega_3; -\omega_1, -\omega_2, \omega_4) A_1^*(z) A_2^*(z) A_4(z) e^{j(-k_1-k_2+k_4)z} + cc \\ - P^{(3)}(z, \omega_2) &= \frac{1}{2} \varepsilon_0 K \chi^{(3)}(-\omega_2; -\omega_1, -\omega_3, \omega_4) A_1^*(z) A_3^*(z) A_4(z) e^{j(-k_1-k_3+k_4)z} + cc \\ - P^{(3)}(z, \omega_1) &= \frac{1}{2} \varepsilon_0 K \chi^{(3)}(-\omega_1; -\omega_2, -\omega_3, \omega_4) A_2^*(z) A_3^*(z) A_4(z) e^{j(-k_2-k_3+k_4)z} + cc \end{aligned}$$

with: $K = 2^{l+q-3} r$ where $l=1$ if $\omega_m \neq 0$ otherwise $l=0$, q and r are respectively the numbers of null frequencies and permutations in the list of the

$\omega_{n,o,p}$. The propagation equation for each wave can now be deduced by casting these terms of polarization in (17).

5.2.3.2. Optical Kerr effect

In the nonlinear optics formalism, the optical Kerr effect corresponds to a third order susceptibility of the form $\chi^{(3)}(-\omega; \omega, -\omega, \omega)$.

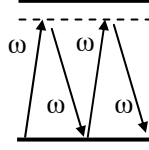


Figure 5.6. Energy diagram of the optical Kerr effect

In this case, three different triplets of frequencies are obtained: $(\omega, -\omega, \omega)$, $(-\omega, \omega, \omega)$ and $(\omega, \omega, -\omega)$. The K coefficient equals to $2^{1+0-3} \times 3 = 3/4$ and the nonlinear polarization reads:

$$P^{(3)}(z, \omega) = \frac{3\epsilon_0}{8} \chi^{(3)}(-\omega; \omega, -\omega, \omega) A_\omega(z) A_\omega^*(z) A_\omega(z) e^{jk_\omega z} + cc \quad (42)$$

Using this relation in (13), we can define an intensity dependent effective refractive index $N(z, \omega)$ as:

$$N(z, \omega) = n_\omega + N_2(\omega) I(z, \omega) \quad (43)$$

where n_ω is the linear refractive index, $I(z, \omega)$ is the electromagnetic wave intensity and $N_2(\omega)$ is the nonlinear refractive index given by:

$$N_2(\omega) = \frac{3\chi^{(3)}(-\omega; \omega, -\omega, \omega)}{4n_\omega^2 c \epsilon_0} \quad (44)$$

Thus, the refractive index depends linearly on electromagnetic wave intensity: it is the *optical Kerr effect*. Numerous different physical phenomena can create this effect, for instance: thermal effects, electronic polarization, atomic transition saturation, and free-carriers population variation in semiconductors.

Applications

Among all the nonlinear processes, the optical Kerr effect is certainly one of the most important for applications. Indeed, this effect is involved in a great number of phenomena such as:

– Self-focussing and self-defocussing: This comes from nonlinear refractive index variation in space. For example, if we consider the propagation of an electromagnetic wave that has a Gaussian transverse spatial distribution in intensity in a Kerr medium, the induced refractive index change follows this spatial distribution, the change being maximal where the intensity is maximal. If N_2 is positive, the medium acts like a converging lens and self-focussing occurs. When N_2 is negative, self-defocussing is expected. Self-focussing can be used to compensate diffraction and to obtain spatial solitons.

– Self-phase modulation: Let us consider the propagation of a pulse in a Kerr medium. The propagation equation of the electric field envelope $A(z, t)$ reads:

$$\left(\frac{\partial}{\partial z} + \frac{1}{v_g} \left| \frac{\partial}{\partial t} \right. \right) A_\omega(z, t) = \frac{j}{2} \omega n_\omega \varepsilon_0 N_2(\omega) |A_\omega(z, t)|^2 A_\omega(z, t) \quad (45)$$

Here, the second order term of dispersion $\frac{\partial^2 k}{\partial \omega^2}$ is neglected. If $\xi = t - z/v_g$ where v_g is the group velocity, the solution of the propagation equation is:

$$A_\omega(z, \xi) = A_\omega(0, \xi) \exp\left(\frac{j}{2} \omega n_\omega \varepsilon_0 N_2(\omega) |A_\omega(0, \xi)|^2 z \right) \quad (46)$$

This represents a constant-intensity pulse that accumulates a supplementary phase ϕ as it propagates through the medium. After a distance L this phase reads:

$$\phi = \frac{1}{2} \omega n_\omega \varepsilon_0 N_2(\omega) |A_\omega|^2 L \quad (47)$$

Because ϕ depends on the temporal distribution of intensity, the pulse broadens spectrally. Self-phase modulation is presently used in optical fiber transmission systems to compensate chromatic dispersion of silica in order to propagate temporal solitons.

– Four wave mixing degenerated in frequency: Two powerful pump waves at ω frequency interfere to create a nonlinear refractive index grating. A third wave of weak intensity (probe at ω frequency) is then partially diffracted by the grating that gives birth to a fourth wave. More details on this phenomenon can be found in Chapter 6.

5.2.3.3. Nonlinear spectroscopy: Raman, Brillouin and Rayleigh scatterings

Nonlinear spectroscopy constitutes a fundamental application of nonlinear optics for the study of excitations in natural media (atoms, solids ...) and their dynamics. The principle relies on the stimulated scattering of light by matter: a laser of weak intensity (probe at ω_s) propagates through a medium pumped by an intense second laser (pump at ω). Pump photons are scattered in probe photons through nonlinear effects. The probe intensity is measured as a function of frequency detuning δ between the pump and the probe.

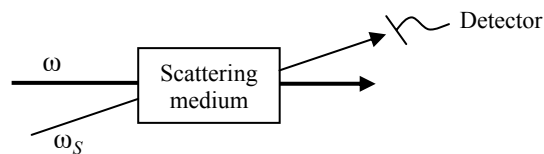


Figure 5.7. Principle of nonlinear spectroscopy based on stimulated scattering. A probe wave at ω_s frequency is detected after propagating through a medium pumped by another wave at ω frequency

The nonlinear effects generally associated with nonlinear spectroscopy are:

- stimulated Raman spectroscopy: δ is an optical frequency (for instance 13THz for silica optical fibers);
- stimulated Brillouin scattering: δ is an acoustic frequency (≈ 11 GHz for silica optical fibers);
- stimulated Rayleigh scattering: $\delta = 0$. Here, it is an elastic diffusion process.

5.3. Nonlinear optics of nano- or microstructured media

Some examples of applications of third order nonlinear optics in nano- or microstructures are described in this section.

5.3.1. Second order nonlinear optics in III–V semiconductors

Second order nonlinear susceptibilities of III–V semiconductors are very high. Moreover, they are widely used in optoelectronics. These two features make them very attractive for achieving integrated parametric sources. Unfortunately these materials are optically isotropic and the standard techniques of birefringent phase matching cannot be used to compensate their strong chromatic dispersion. Using some examples, we will show in this section how the nano- or microstructuration of their optical properties enables the realization of phase matching.

5.3.1.1. Quasi-phase matching in III–V semiconductors

For a fundamental wavelength at $1.55\mu\text{m}$, the coherence length of AlGaAs is around $1.6\mu\text{m}$. As a consequence, in order to fabricate quasi-phase matched III–V semiconductors, it is necessary to be able to modulate their nonlinear susceptibility with a period of about one micrometer. This value has to be compared to $20\mu\text{m}$ for ferroelectric materials to understand why this kind of operation can be difficult. To achieve the periodical inversion of susceptibility, several methods have been demonstrated. Here we describe one method which seems to be very promising [YOO 95]. Two substrates of GaAs oriented along the crystallographic axis [001] are bounded using an interface formed by two 20nm thick layers made in $\text{In}_{50\%}\text{Ga}_{50\%}\text{P}$.

After the bounding the upper substrate is removed by selective chemical etching, and the process is stopped by an AlGaAs layer. A grating is patterned into the semiconductor by photolithography followed by etching. A periodical substrate is obtained on which three AlGaAs layers are then grown. One can observe on Figure 5.8a the result obtained after the process: a structure presenting a periodical inversion of the crystallographic axis is shown (interface visible between the two parts of the crystal with opposed orientation). This inversion leads to a periodical change of the sign of nonlinear susceptibility. A ridge waveguide is then defined by chemical etching in order to guide the light efficiently (Figure 5.8b).

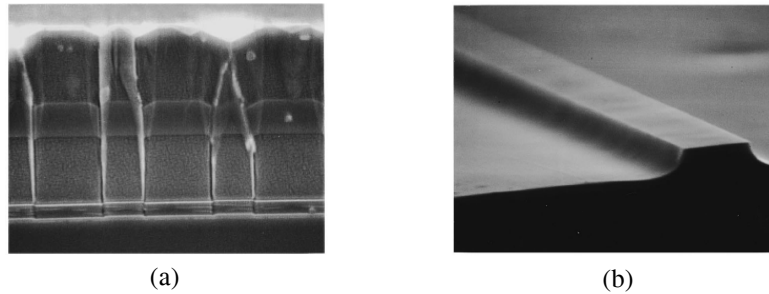


Figure 5.8. Scanning electronic micrographs from [YOO 95]. (a) The periodical inversion of the sign of nonlinear susceptibility. (b) The whole nonlinear ridge waveguide

5.3.1.2. Quasi-phase matching in microcavity

An alternative method to domain inversion consists of using a doubly resonant microcavity (for F and SH frequencies) [ROS 95]. The microcavity is designed in such a way that for each reflection onto the mirrors, the F and SH fields which are phase-shifted by π during their propagation in the medium are resynchronized. The authors of [SIM 97] reported the first achievement of such a microcavity in III–V semiconductors (Figure 5.9).

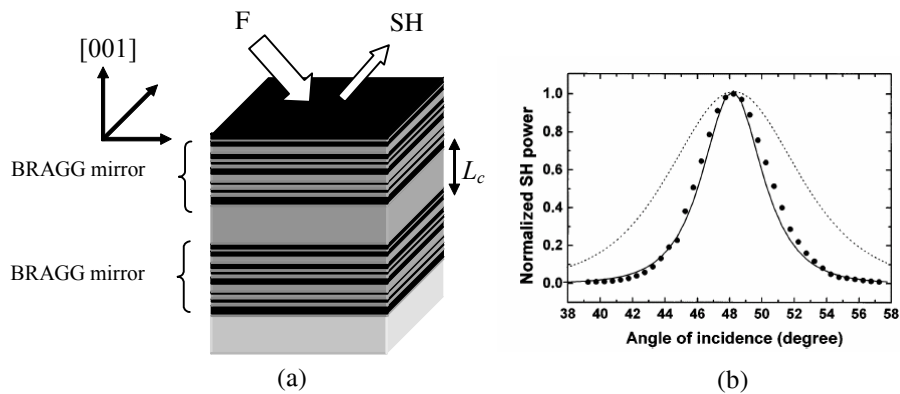


Figure 5.9. (a) A doubly resonant microcavity made of AlGaAs optimized for SHG. (b) The generated SH from this microcavity as a function of the incident angle. The dashed curve is deduced from a simulation considering a simply resonant cavity. The experimental observation of the decrease of FWHM of this curve confirms the doubly resonant regime

The use of non-periodical Bragg mirrors makes it possible to obtain a doubly resonant structure (at F and SH frequencies) as well as the quasi-phase matching condition. Note that, because the F field is resonant, conversion efficiency increases proportionally to cavity finesse.

5.3.1.3. Bidimensional quasi-phase matching

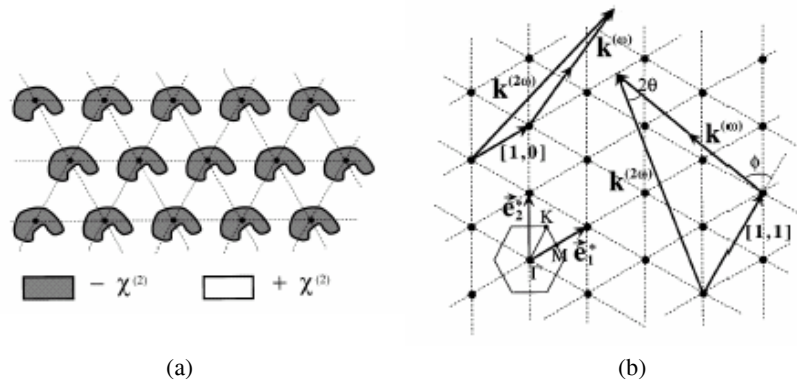


Figure 5.10. (a) Representation of a nonlinear photonic crystal in real space.
(b) Representation of a nonlinear photonic crystal in reciprocal space

A generalization of the quasi-phase matching technique to several dimensions was proposed in 1998 [BER 98]. The author talks about nonlinear photonic crystals. In this kind of photonic crystal, linear susceptibility $\chi^{(1)}$ is homogenous whereas nonlinear susceptibility $\chi^{(2)}$ is modulated at least in two dimensions of space (Figure 5.10a). This material can satisfy the phase matching condition simultaneously in different propagation directions for different wavelengths (Figure 5.10b).

5.3.1.4. Form birefringence

It is possible to obtain birefringence from isotropic materials when they are structured. It was proposed in [ZIE 75] to use the birefringence of a lamellar structure to achieve phase matching. This idea was recently used to achieve phase matching in an AlGaAs waveguide [FIO 98]. This waveguide is layered in one direction perpendicular to the propagation direction \mathbf{k} (Figure 5.11a). Using high index contrast materials such as AlGaAs and AlOx (aluminum oxide) it is possible to create sufficient artificial birefringence between TE and TM modes to achieve phase matching. In [FIO 98], the authors describe an experiment of phase matched difference frequencies ($\omega_3 = \omega_1 - \omega_2$). The wave at ω_2 frequency is TM polarized

whereas the waves at ω_1 and ω_3 frequencies are TE polarized. Consequently the phase matching condition reads:

$$n_{TM}(\omega_1)\omega_1 - n_{TE}(\omega_2)\omega_2 = n_{TE}(\omega_3)\omega_3 \quad (48)$$

The phase matching curve showing the generated field power as a function of the pump field wavelength is shown in Figure 5.11b. This method is very promising for implementing second order nonlinear optics in semiconductor guiding structures.

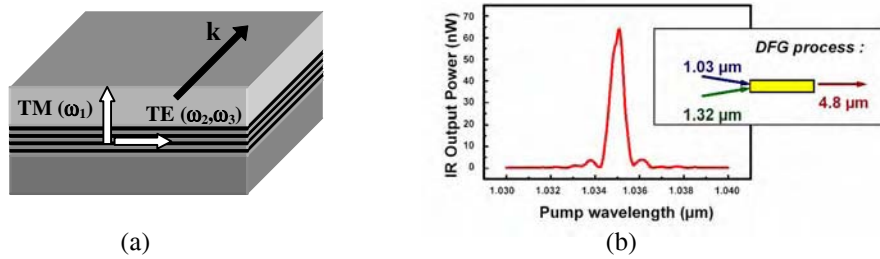


Figure 5.11. (a) A form birefringent layered waveguide optimized for frequency difference. (b) Phase matching curve for difference frequency generation in layered AlGaAs/AlOx waveguide

5.3.1.5. Phase matching in one-dimensional photonic crystals

The use of anomalous dispersion at the photonic band edges in lamellar structures to achieve phase matching was proposed in 1977 [YAR 77]. More recently, studies of periodical finite structures have succeeded in designing configurations where efficient second harmonic generation is expected [SCA 97; CEN 99]. Figure 5.12a shows a schematic view of an AlGaAs/AlOx 1D photonic crystal. The dispersion relation of a structure where the filling factor and the periodicity are chosen to satisfy the phase matching condition for an F wavelength at $1.55\mu\text{m}$ is represented in Figure 5.12b. Note that F and SH frequencies are both tuned at the edge of the Brillouin zone so that their wave vectors satisfy the vectorial phase matching condition (taking into account folding in the first Brillouin zone):

$$k_z(2\omega_0) = 2k_z(\omega_0) \quad (49)$$

On the other hand, near the band edges, F and SH fields experience low group velocity modes, which as a consequence enhances their intensity in the material and so increases conversion efficiency. In this condition efficiency η is proportional to the square of the propagation length and to the square of the inverse of the group velocity at F frequency [DAG 01]:

$$\eta \propto \left(L \times \frac{1}{v_g(\omega)} \right)^2 \quad (50)$$

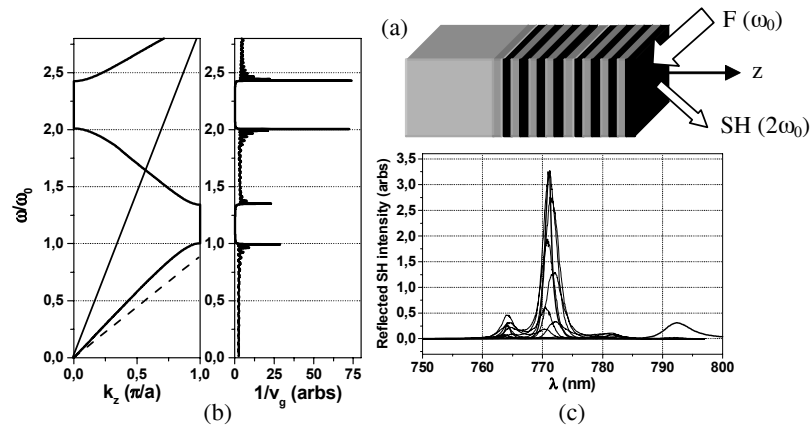


Figure 5.12. (a) An AlGaAs/AIOx 1D photonic crystal generating SH in reflection. (b) The dispersion relation of the z component of the wave vector and group velocity dispersion (z is the direction perpendicular to the layers). The AlGaAs layers are 151nm thick, periodicity is 270nm. (c) The spectra of the generated SH for different fundamental central wavelengths. The fundamental pulse duration τ is 150fs. The thick curve is deduced from a simulation obtained using nonlinear transfer matrices theory

For a lamellar structure, at the band edges, group velocity decreases with the square of the number of unit cells N [BEN 96]. This leads to a conversion efficiency which grows as the sixth power of the number of unit cells [DEA 01]. Figure 5.12c shows the superposition of the reflected SH spectra obtained in the femtosecond regime. The F field is tuned at the first resonance above the first stop-band and the SH field is tuned at the second resonance above the second stop-band. This configuration enables us to achieve phase matching and a good synchronization of group velocity. Comparing three structures of the same kind with different values of N , it is possible to verify relation (50) [DUM 02].

In order to take better advantage of the second order nonlinear tensor of AlGaAs and to obtain a better lateral confinement of the electric fields, it is possible to extend the method described above to the case of a deeply etched AlGaAs waveguide. Unfortunately the SH field is located above the light-lines of substrate (dash line) and air (full line) as it is represented in Figure 5.12b. This considerably affects the dependence of conversion efficiency on the number of periods. However, it has been shown that harmful diffraction losses can be limited by adapting the waveguide parameters [DUM 03].

5.3.1.6. Phase matching in two-dimensional photonic crystal waveguide

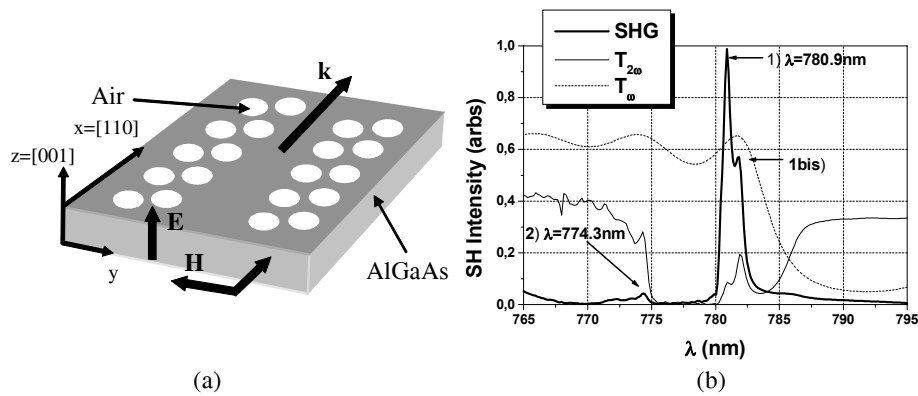


Figure 5.13. (a) A two-dimensional photonic crystal waveguide. The F field is H polarized and the SH field is E polarized. (b) The linear transmission of the F and SH fields, and the numerical calculations for the generated SH field

In two-dimensional photonic crystal W1 waveguides (see Chapter 1), several parameters can be adjusted to achieve simultaneous phase matching and group velocity synchronization. Moreover, these waveguides present a further advantage over the configuration shown in section 5.3.1.5: propagation with low diffraction losses is possible. It is, indeed, possible to obtain phase matching in a W1 waveguide fabricated in an AlGaAs planar waveguide. This waveguide consists of a single line defect in a triangular lattice of air holes. The air-filling factor of the structure is $f = 0.6$ [RAI 02]. Phase matching has been numerically demonstrated using on one hand the plane wave expansion program developed by the MIT [JOH] and, on the other, a finite difference time domain program. The results of the calculations are shown in Figure 5.13.

5.3.2. Third order nonlinear effects

5.3.2.1. Continuum generation in microstructured optical fibers

Microstructured optical fibers with silica cores (Figure 5.14a) guide the light like conventional optical fibers due to total internal reflection. However, these fibers have extra properties that cannot be obtained with conventional ones. For instance, it is possible to fabricate microstructured fibers having a zero-group velocity dispersion at lower wavelengths than in normal fibers. Moreover, because of the small dimension of the core of these fibers (diameter in the order of 1 micron), very small mode sizes are obtained and, as a consequence, enhanced efficiency of nonlinear processes is expected.

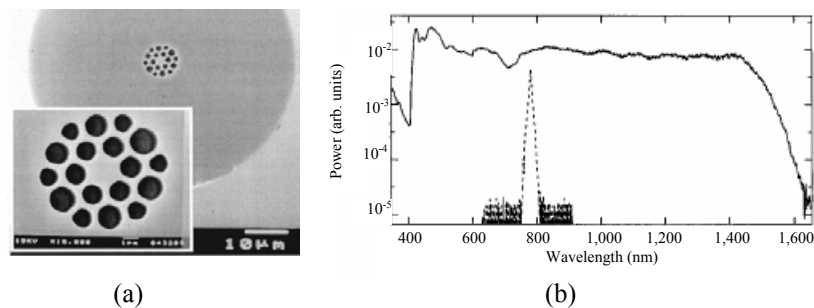


Figure 5.14. (a) A scanning electron micrograph of the cleaved face of a microstructured optical fiber with silica core. (b) The spectrum of the continuum generated in the fiber (full line). The spectrum of the incoming pulses is represented by a dotted line

These properties have been exploited to generate an ultra-broadband continuum of light going from ultraviolet to infrared (from 392nm to 1,600nm) [RAN 00]. 100fs-long pulses with energy per pulse of 890pJ and spectrally centered at the zero-group velocity dispersion (790nm) (dotted line in Figure 5.14b) are injected in the fiber. Because all the spectral components of the pulses are propagating at the same velocity, nonlinear interactions are efficient over the whole length of the fiber. Self-phase modulation and Raman scattering are at the origin of the generation of new spectral components that give the super continuum at the end of the fiber. The white light obtained can be used to simplify the measurement of optical frequencies from standard microwaves [DID 00].

5.3.2.2. Optical reconfiguration of two-dimensional photonic crystal slabs

Photonic crystals with their lattice dimensions in the order of the wavelength of the light offer an efficient way of controlling an electromagnetic field. By varying the opto-geometrical parameters of these structures (lattice, refractive indices contrast,

lattice constant ...), it is possible to engineer the dispersion properties of the matter or, in other words, to control phase and group velocities. For instance, structures can be designed such that light propagation is forbidden in every dimension of space in a wide range of frequencies, or such that light is considerably slowed down at a certain frequency in order to increase its interaction with matter (see Chapter 1 for more detail). Fabricating photonic crystals in a material that has a Kerr-type nonlinearity would make it possible to achieve systems where the propagation of light is controlled by the light itself through the nonlinear refractive index control. Devices such as ultrafast optical switches and all-optical routers could be fabricated and implemented in integrated optical circuits.

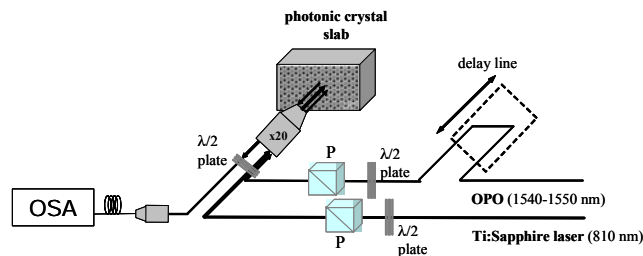


Figure 5.15. Set-up of a pump and probe experiment. Pulses obtained via an optical parametric oscillator (OPO) are used to probe photonic crystal reflectivity around $1.5\mu\text{m}$ as it is pumped by a pulsed Ti: Sapphire laser at 810nm . The incident power of each beam is controlled by rotating half-wave plates ($\lambda/2$ plate) behind polarizing beam splitters (P). Both beams are focussed on the sample due to an achromatic microscope objective. The reflected signal is injected in a single mode optical fiber connected to an optical spectrum analyzer (OSA)

Experiments have recently been carried out on two-dimensional semiconductor photonic crystals [RAI 05]. The investigated sample consists of an InP membrane incorporating four quantum wells transferred onto silicon where a graphite lattice of holes has been drilled. The idea is to change the semiconductor refractive index by varying the free carriers' population via optical excitation (pump). The experimental set-up is depicted in Figure 5.15. In the linear regime, a sharp resonance is observed in reflectivity in a direction parallel to the holes' axis ($\Delta\lambda = 0.4\text{nm}$ – $Q = 3,700$ – see Figure 5.16a), attesting to the presence at this wavelength of a low group velocity mode. When the pump is incident on the sample, resonance spectrally shifts towards the blue (towards lower wavelengths), the opposite way from that induced by thermal effects. The spectral shift increases as the pump intensity is increased up to free carriers' population saturation.

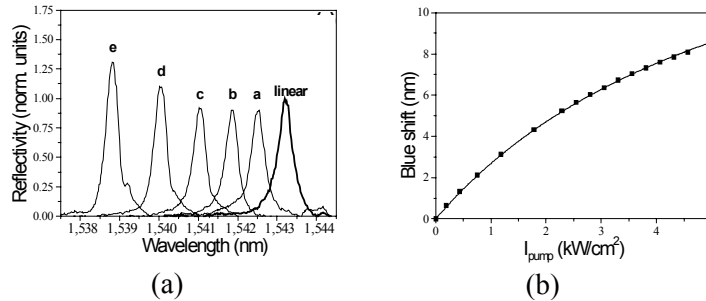


Figure 5.16. (a) Reflectivity spectrums measured for different values of pump intensity [0.19 kW/cm^2 (a), 0.43 kW/cm^2 (b), 0.74 kW/cm^2 (c), 1.13 kW/cm^2 (d) and 1.78 kW/cm^2 (e)].
(b) Blue shift in resonance as a function of pump intensity

This demonstrates that it is possible to spectrally shift the photonic bands of a photonic crystal efficiently. This constitutes the first step towards all-optical reconfigurable photonic crystals.

5.3.2.3. Spatial solitons in microcavities

The propagation of optical pulses in optical fibers is almost always accompanied by their spectral and temporal deformation because of chromatic dispersion and self-phase modulation. However, by choosing the fiber (normal or abnormal dispersion), the shape and the power of the pulses appropriately, it is possible that chromatic dispersion and nonlinear effects will compensate each other [AGR 95]. In this case, propagating pulses are called solitons, pulses that are not deformed during propagation.

By analogy, in optical microcavities, the compensation of phenomena that spread out beams (diffraction, scattering, self-defocussing) by phenomena that are focussing them (self-focussing, absorption saturation) can lead to spatial structuration in the opposite direction to the transmitted or reflected beams. In this case, we talk about spatial cavity solitons. This has recently been observed for the first time in VCSEL (Vertical Cavity Surface Emitting Lazer) used as an amplifier (electrical pumping under lazer threshold) [BAR 02] (see Figure 5.17a and 5.17b).

The control of transverse structuration of the electromagnetic field combined with the integration capacity of semiconductor-based technology opens the way to very important applications such as ultrafast optical memories.

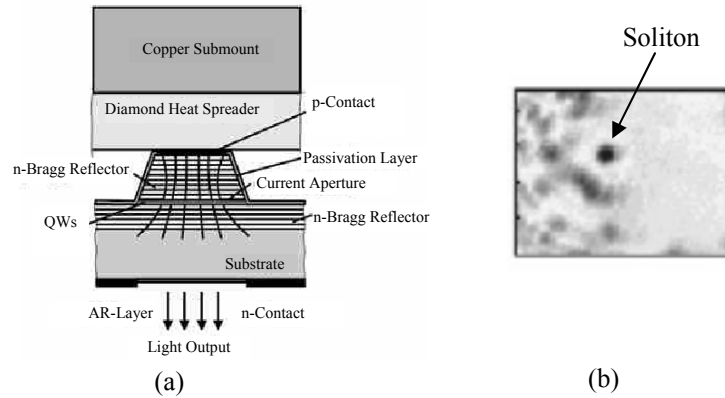


Figure 5.17. (a) The VCSEL used in [BAR 02]. (b) A picture obtained with a CCD where we can observe a spatial soliton

5.4. Conclusion

In this chapter, our goal was to give the reader a glimpse of the potential of the “marriage” between nonlinear optics and nano- or microstructures. We illustrated this with examples that second and third order nonlinear interactions could be enhanced in these materials. Engineering the nonlinear properties ($\chi^{(2)}$ domain inversion to achieve quasi-phase matching) and managing phase and group velocity is key to producing efficient nonlinear effects. In return, nonlinear optics offer to these nanotechnology jewels numerous new functionalities such as spectral tunability and ultrafast reconfiguration.

5.5. References

- [AGR 95] AGRAWAL G.P., *Nonlinear Fiber Optics*, Academic Press, San Diego, 1995.
- [ARM 62] ARMSTRONG J.A., BLOEMBERGEN N., DUCUING J., PERSHAN P.S., “Interactions between light waves in a nonlinear dielectric”, *Phys. Rev.*, 127, p. 1918, 1962.
- [BAL 99] BALAKIN A.V., BUSHUEV V.A., KOROTEEV N.I., MANTSYZOV B.I., OZHEREDOV I.A., SHKURINOV A.P., BOUCHER D., MASSELIN P., “Enhancement of second-harmonic generation with femtosecond laser pulses near the photonic band edge for different polarizations of incident light”, *Opt. Lett.*, 24, p. 793, 1999.

- [BAR 02] BARLAND S., TREDICCE J.R., BRAMBILLIA M., LUGIATO L.A., BALLE S., GIUDICI M., MAGGIPINTO T., SPINELLI L., TISSONI G., KNÖDL T., MILLER M., JÄGER R., “Cavity solitons as pixels in semiconductor microcavities”, *Nature*, 419, p. 699, 2002.
- [BEN 96] BENDICKSON J.M., DOWLING J.P., SCALORA M., “Analytic expression for the electromagnetic mode density in finite, one-dimensional, photonic band-gap structures”, *Phys. Rev.*, E 53, p. 4107, 1996.
- [BER 98] BERGER V., “Nonlinear photonic crystals”, *Phys. Rev. Lett.*, 81, p. 4136, 1998.
- [BLO 70] BLOEMBERGEN N., SIEVERS J., “Nonlinear optical properties of periodic laminar structures”, *Appl. Phys. Lett.*, 17, p. 483, 1970.
- [BUT 90] BUTCHER P.N., COTTER D., *The Elements of Nonlinear Optics*, Cambridge University Press, Cambridge, 1990.
- [CEN 99] CENTINI M., SIBILIA C., SCALORA M., D’AGUANNO G., BERTOLOTTI M., BLOEMER M.J., BOWDEN C.M., NEFEDOV I., “Dispersive properties of finite, one-dimensional photonic band gap structures: applications to nonlinear quadratic interactions”, *Phys. Rev. E* 60, p. 4891, 1999.
- [DAG 01] D’AGUANNO G., CENTINI M., SCALORA M., SIBILIA C., DUMEIGE Y., VIDAKOVIC P., LEVENSON J.A., BLOEMER M.J., BOWDEN C.M., HAUS J.W., BERTOLOTTI M., “Photonic band edge effects in finite structures and applications to X(2) interactions”, *Phys. Rev.*, E 64, p. 016609, 2001.
- [DEA 01] DE ANGELIS C., GRINGOLI F., MIDRIO M., MODOTTO C., AITCHISON J.S., NALESSO G.F., “Conversion efficiency for second-harmonic generation in photonic crystals”, *J. Opt. Soc. Am.*, B 18, p. 348, 2001.
- [DID 00] DIDDAMS S.A., JONES D.J., YE J., CUNDIFF S.T., HALL J.L., RANKA J.K., WINDELER R.S., HOLZWARTH R., UDEM T., HÄNSCH T.W., “Direct link between microwave and optical frequencies with a 300 THz femtosecond laser comb”, *Phys. Rev. Lett.*, 84, p. 5102, 2000.
- [DUM 02] DUMEIGE Y., SAGNES I., MONNIER P., VIDAKOVIC P., MÉRIADEC C., LEVENSON A., “Phase-matched frequency doubling at photonic band edges: efficiency scaling as the fifth power of the length”, *Phys. Rev. Lett.*, 89, p. 043901, 2002.
- [DUM 03] DUMEIGE Y., RAINERI F., LETARTRE X., LEVENSON A., “Second harmonic in one-dimensional photonic edge waveguides”, *Phys. Rev. E* 68, p. 066617, 2003.
- [FEJ 92] FEJER M.M., MAGEL G.A., JUNDT D.H., BYER R.L., “Quasi-phase-matched second harmonic generation: tuning and tolerances”, *IEEE J. Quantum Electron.*, 28, p. 2631, 1992.
- [FIO 98] FIORE A., BERGER V., ROSENCHER E., BRAVETTI P., NAGLE J., “Phase matching using an isotropic nonlinear optical material”, *Nature*, 391, p. 463, 1998.
- [FRA 61] FRANKEN P.A., HILL A.E., PETERS C.W., WEINRICH G., “Generation of optical harmonics”, *Phys. Rev. Lett.*, 7, p. 118, 1961.

- [GOL 99] GOLOVAN L.A., ZHELTIKOV A.M., KASHKAROV P.K., KOROTEEV N.I., LISACHENKO M.G., NAUMOV A.N., SIDOROV-BIRYUKOV D.A., YU TIMOSHENKO V., FEDOTOV A.B., "Generation of the second optical harmonic in porous-silicon-based structures with a photonic bandgap", *JETP Lett.*, 69, p. 300, 1999.
- [JAN 93] JANZ S., FERNANDO C., DAI H., CHATENOU D., DION M., NORMANDIN R., "Quasi-phase-matched second-harmonic generation in reflection from AlxGa1-xAs heterostructures", *Opt. Lett.*, 18, p. 589, 1993.
- [JOA 97] JOANNOPOULOS J.D., VILLENEUVE P.R., FAN S., "Photonic crystals: putting a new twist on light", *Nature*, 386, p. 143, 1997.
- [JOH] JOHNSON S.G., <http://ab-initio.mit.edu/mpb/>
- [MAI 60] MAIMAN T.H., "Stimulated optical radiation in ruby", *Nature*, 87, p. 493, 1960.
- [MAR 97] MARTORELL J., VILASECA R., CORBALAN R., "Second harmonic generation in a photonic crystal", *Appl. Phys. Lett.*, 70, 702, 1997.
- [RAI 02] RAINERI F., DUMEIGE Y., LETARTRE X., LEVENSON A., "Nonlinear decoupled FDTD code: phase-matching in 2D defective photonic crystal", *Electron. Lett.*, 38, p. 1704, 2002.
- [RAI 05] RAINERI F., COJOCARU C., RAJ R., MONNIER P., LEVENSON A., SEASSAL C., LETARTRE X., VIKTOROVITCH P., "Tuning a two-dimensional photonic crystal resonance via optical carrier injection", *Opt. Lett.*, 30, p. 64, 2005.
- [RAN 00] RANKA J.K., WINDELER R., STENTZ A.J., "Visible continuum generation in air-silica microstructure optical fibers with anomalous dispersion at 800nm", *Opt. Lett.*, 25, p. 25, 2000.
- [ROS 95] ROSENCHER E., VINTER B., BERGER V., "Second-harmonic generation in non birefringent semiconductor optical microcavities", *J. Appl. Phys.*, 78, p. 6042, 1995.
- [SCA 97] SCALORA M., BLOEMER M.J., MANKA A.S., DOWLING J.P., BOWDEN C.M., WISWANATHAN R., HAUS J.W., "Pulsed second-harmonic generation in nonlinear, one-dimensional, periodic structures", *Phys. Rev.*, A 56, p. 3166, 1997.
- [SIM 97] SIMONNEAU C., DEBRAY J.P., HARMAND J.C., VIDAKOVIC P., LOVERING D.J., LEVENSON J.A., "Second-harmonic generation in a doubly resonant semiconductor microcavity", *Opt. Lett.*, 22, p. 1775, 1997.
- [TRU 95] TRULL J., VILASECA R., MARTORELL J., CORBALÁN R., "Second-harmonic generation in local modes of a truncated periodic structure", *Opt. Lett.*, 20, p. 1746, 1995.
- [WAD 00] WADSWORTH W.J., KNIGHT J.C., ORTIGOSA-BLANCH A., ARRIAGA J., SILVESTRE E., RUSSELL P.S.T.J., "Soliton effects in photonic crystal fibers at 850nm", *Electron. Lett.*, 36, p. 53, 2000.
- [YAR 77] YARIV A., YEH P., "Electromagnetic propagation in periodic stratified media. II. Birefringence, phase matching, and x-ray lasers", *J. Opt. Soc. Am.*, 67, p. 438, 1977.
- [YOO 95] YOO S.J.B., BHAT R., CANEAU C., KOZA M.A., "Quasi-phase-matched second-harmonic generation in AlGaAs waveguides with periodic domain inversion achieved by wafer-bonding", *Appl. Phys. Lett.*, 66, p. 3410, 1995.

- [ZHL 00] ZHLETIKOV A.M., TARASISHIN A.V., MAGNITSKII S.A., “Phase and group synchronization in second-harmonic generation of ultrashort light pulses in one-dimensional photonic crystals”, *JETP Lett.*, 91, p. 298, 2000.
- [ZIE 75] VAN DER ZIEL J.P., “Phase-matched harmonic generation in a laminar structure with wave propagation in the plane of the layers”, *Appl. Phys. Lett.*, 26, p. 60, 1975.
- [ZIE 76] VAN DER ZIEL J.P., “Optical second harmonic generation in periodic multilayer GaAs-Al_{0.3}Ga_{0.7}As structures”, *Appl. Phys. Lett.*, 28, p. 437, 1976.

Chapter 6

Third Order Optical Nonlinearities in Photonic Crystals

6.1. Introduction

Since Yablonovitch's proposal regarding photonic band gap crystals [YAB 94], numerous studies have been performed throughout the world to realize and use such nanostructures in the optical domain [JOA 95a; JOA 95b; LOU 03]. These studies, whilst fascinating at a fundamental level, may also lead to applications concerning, for example, lasers without thresholds, guided propagation with very small curvature radii, or optically active elements for optical signal processing, all of which open the way to the optical information processing microcircuits of the future. To realize these optical information processing functions, the implementation of nonlinear optical interaction processes will be required, in which third order nonlinear effects will play an essential role.

Here we hit an important scientific stumbling block: how to obtain sufficient optical nonlinearities to realize, with sufficiently small laser energies, efficient control devices on optical microcircuits. As is well known, the use of one or many photon resonant, and possibly non-resonant, interactions in semiconductors produces high nonlinear effects on relatively small interaction lengths. However, for potential future information processing optical circuits, the interaction length will have to be on the micrometer range, leading to the necessity to further reinforce the optical nonlinearity of these materials. The nanostructuring of the material in the form of photonic band gap crystals, otherwise necessary for other linear elements of circuits,

may give us an elegant and efficient solution. This will particularly be the case for photonic crystals used at the edge of the photonic band gap, where the very high optical mode density may considerably increase nonlinear processes (in such cases the optical intensities inside the structures greatly exceed those injected in the devices).

Ignoring the already well reported study of second order nonlinear effects in photonic crystals [SI 02, BER 98, BRO 00, FIO 98, DUM 01], this chapter deals with the specificities of photonic crystals concerning third order optical nonlinearities. Its goal is to make the reader aware of the enormous potential of photonic crystals for the future realization of micrometer size nonlinear devices for optical information processing.

The chapter is organized into three sections. Section 6.2 presents a recall of the nonlinear optical processes of interest in photonic crystals, i.e. optical Kerr effect, two photon absorption and frequency degenerated four wave mixing, that will be at the origin of secondary effects which are promising for applications, such as optical bistability or instability, quantum noise reduction, soliton propagation and interaction, etc. Section 6.3 deals with the core of the problem, i.e. the influence of the local field inside the nanostructure. Finally, section 6.4 shows some results concerning the evaluation of local nonlinearity in the case of frequency degenerated four wave mixing.

6.2. Third order nonlinear optic reminder

When the intensity of light waves present in a material is intense, the electronic density of atoms' peripheral electrons is strongly disturbed so that the polarization induced in the material is no longer proportional to the electric field of the light wave. If the perturbation is not too large (i.e., for a field of the optical wave smaller than the ionization field of the atoms), one can express the induced polarization as a power series development of the optical field. In such a case, for a nonlinear process of the n th order, the corresponding nonlinear polarization depends on the n th power of the optical field and one can write nonlinear propagation equations for the waves intervening in the nonlinear interaction [SHE 84]. In this chapter we will limit ourselves to the third order nonlinearities that always exist whatever the optical material used.

6.2.1. Third order optical nonlinearities

In the most general case, third order optical nonlinearities occur when four waves of frequencies ω_1 , ω_2 , ω_3 , and ω_4 such as, for example, $\omega_4 = \omega_1 + \omega_2 + \omega_3$ are present in a material (see Figure 6.1). The total electric field is written:

$$\underline{E}(\underline{r}, t) = \sum_{j=1,4} \underline{E}_j(\underline{r}, \omega_j) \exp(-i\omega_j t) + C.C. \quad (1)$$

where the complex amplitude $\underline{E}_j(\underline{r}, \omega_j)$ of the plane and monochromatic optical wave of frequency ω_j is given by:

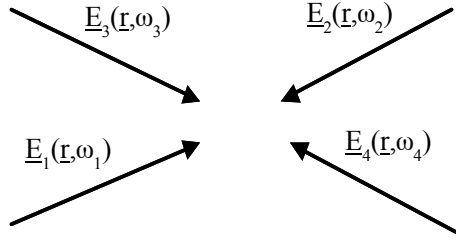


Figure 6.1. Schematic diagram of four wave mixing

$$\underline{E}_j(\underline{r}, \omega_j) = \hat{e}_j A_j(\underline{r}, \omega_j) \exp(i\mathbf{k}_j \cdot \underline{r}) \quad (2)$$

\hat{e}_j , $A_j(\underline{r}, \omega_j)$ and \mathbf{k}_j being respectively the polarization vector (taken linear in the following), the amplitude and the wave vector of the optical wave of frequency ω_j . The nonlinear propagation equation of the amplitude $A_4(\underline{r}, \omega_4)$ can then be written (in CGS units):

$$\hat{k}_4 \cdot \nabla A_4(\underline{r}, \omega_4) = i \frac{4\pi^2}{n_4 \lambda_4} \hat{e}_4 \cdot \underline{P}_{NL}^{(3)}(\omega_4) \exp[i(\mathbf{k}_\Sigma - \mathbf{k}_4) \cdot \underline{r}] \quad (3)$$

where \hat{k}_4 is the unitary wave vector in the direction of \mathbf{k}_4 and n_4 the index of refraction at the wavelength $\lambda_4 = 2\pi c / \omega_4$. In equation (3), the third order nonlinear polarization $\underline{P}_{NL}^{(3)}(\omega_4)$ of wave vector $\mathbf{k}_\Sigma = \mathbf{k}_1 + \mathbf{k}_2 + \mathbf{k}_3$ is expressed:

$$\underline{P}_{NL}^{(3)}(\omega_4) = D \underline{\chi}^{(3)}(\omega_1, \omega_2, \omega_3) \hat{e}_1 \hat{e}_2 \hat{e}_3 A_1(\underline{r}, \omega_1) A_2(\underline{r}, \omega_2) A_3(\underline{r}, \omega_3) \quad (4)$$

where D is the degeneracy factor of the three waves generating the nonlinear polarization ($D=3!=6$ for three different waves, $D=3$ when only two waves are different, and $D=1$ for three identical waves). Let us note that, taking into account the $\exp[i(\mathbf{k}_\Sigma - \mathbf{k}_4) \cdot \underline{r}]$ term of equation (3) that imposes a sinusoidal spatial

oscillation to $A_4(\underline{r}, \omega_4)$, the nonlinear process will be efficient only under phase matching conditions, i.e. if $\underline{k}_\Sigma = \underline{k}_4$.

6.2.2. Some third order nonlinear optical processes

In the following section, we will mention some third order nonlinear optical processes that are interesting for the study of optical information processing in photonic crystals.

Frequency degenerated four wave mixing

In this nonlinear process, two intense pump waves $\underline{E}_F(\underline{r}, \omega)$ and $\underline{E}_B(\underline{r}, \omega)$, of frequency ω and propagating in exactly opposite directions interact with a signal wave $\underline{E}_S(\underline{r}, \omega)$, at the same frequency, propagating in a different direction from that of $\underline{E}_F(\underline{r}, \omega)$ and $\underline{E}_B(\underline{r}, \omega)$.

If we consider the third order nonlinear polarization at frequency ω :

$$\underline{P}_{NL}^{(3)}(\omega) = 6\underline{\chi}^{(3)}(\omega, \omega, -\omega) \hat{e}_F \hat{e}_B \hat{e}_S A_F(\underline{r}, \omega) A_B(\underline{r}, \omega) A_S^*(\underline{r}, \omega) \quad (5)$$

which uses the same writing conventions for the electromagnetic field as equation (4), we note that the wave vector of this nonlinear polarization is $\underline{k}_\Sigma = -\underline{k}_S$. The wave radiated by this polarization is called the phase conjugate wave of $\underline{E}_S(\underline{r}, \omega)$. This wave propagates in a direction exactly opposite to the signal wave direction ($\underline{k}_C = -\underline{k}_S$): the four-wave mixing process is then phased matched and can thus be very efficient.

In the complete parametric regime of low energy transfer between the pump, signal and conjugate waves ($A_j(z', \omega) = A_{j0}, j = F, B$) and low amplification of the signal wave ($A_S(z, \omega) = A_{S0}$), it is easy, from the nonlinear propagation equation (3) written for the amplitude of the conjugate wave and the nonlinear polarization given by equation (5), to obtain the conjugate wave intensity $I_C = (cn/2\pi) |A_C(0, \omega)|^2$ for a nonlinear material of thickness L , that is:

$$I_C = \frac{64\pi^6}{c^2 n^4 \lambda^2} |6\underline{\chi}_{eff}^{(3)}|^2 I_F I_B I_S L^2 \quad (6)$$

The conjugate wave intensity appears then as proportional to the incident intensities of the “pump” and “signal” waves, to the square of the thickness of the nonlinear material and to the square of the modulus of the third order nonlinear susceptibility $\chi_{\text{eff}}^{(3)} = \hat{e}_C \cdot \underline{\underline{\chi}}^{(3)}(\omega, \omega, -\omega) \hat{e}_F \hat{e}_B \hat{e}_S$. For this automatically phase matched nonlinear process, one can directly obtain the effective nonlinear susceptibility value by a simple measurement of incident intensities. This is why frequency degenerated four wave mixing, otherwise very useful for optical information processing, is used in this chapter as a sign of the enormous progress of third order optical nonlinearities brought about by material nanostructuring.

Optical Kerr effect and two-photon absorption

Nonlinear effects not only exist when the interacting waves are different: they also exist in the propagation of a single intense optical wave in a nonlinear material. Those effects can also affect the intensity of the optical wave by the introduction of losses or the phase of this wave by a modification of the refractive index of the material. These effects are in fact described by the same nonlinear polarization:

$$\underline{P}_{\text{NL}}^{(3)}(\omega) = 3\underline{\underline{\chi}}^{(3)}(\omega, -\omega, \omega) \hat{e} \hat{e} \hat{e} |A(\underline{r}, \omega)|^2 A(\underline{r}, \omega) \quad (7)$$

Depending on the purely real or imaginary nature of the effective nonlinear susceptibility $\chi_{\text{eff}}^{(3)} = \hat{e} \cdot \underline{\underline{\chi}}^{(3)}(\omega, -\omega, \omega) \hat{e} \hat{e}$, we will speak of the optical Kerr effect or of two-photon absorption. Taking into account that the nonlinear polarization wave vector $\underline{k}_\Sigma = \underline{k}$ is exactly the same as that of the incident beam, these two automatically phase matched processes have a universal character: they occur in any material with any optical beam. Only the importance of the self-induced modification of the characteristics of the incident optical beam will depend on the beam intensity itself and on the value of the effective nonlinear susceptibility. The nonlinear propagation equation for the optical wave amplitude can then be written:

$$\frac{dA(z, \omega)}{dz} = i \frac{4\pi^2}{n\lambda} 3\underline{\underline{\chi}}_{\text{eff}}^{(3)} |A(z, \omega)|^2 A(z, \omega) \quad (8)$$

If $\chi_{\text{eff}}^{(3)}$ is purely imaginary, the intensity $I(L)$ transmitted by the material of length L for an incident intensity I_0 is given by:

$$I(L) = \frac{I_0}{1 + KI_0L} \quad (9)$$

where $K = (16\pi^3/cn^2\lambda)\text{Im}(3\chi_{\text{eff}}^{(3)})$ represents the two-photon transition strength. The beam intensity is then more attenuated at higher incident intensities.

If $\chi_{\text{eff}}^{(3)}$ is real, the optical beam intensity is unchanged; on the other hand its wave vector $\underline{k} = (n\omega/c)\hat{\mathbf{k}}$ is modified by a quantity $\underline{\Delta k} = (8\pi^3/cn^2\lambda)\text{Re}(3\chi_{\text{eff}}^{(3)})\mathbf{I}_0\hat{\mathbf{k}}$. For a monochromatic plane wave, the optical Kerr effect generates a phase variation that will have an incidence only when subject to light interferences. On the other hand, when associated to a spatial or temporal dependence of the incident optical intensity, the optical Kerr effect brings about spectacular effects such as self-focussing or self phase modulation and their derived products, spatial and temporal solitons.

6.2.3. Influence of the local field

In the nonlinear propagation equation (3) as well as in the expression of nonlinear polarization (equation (4)), the electric fields that represent optical waves are those that exist inside the material at point $\underline{\mathbf{r}}$. On the other hand, an evaluation of the efficiency of nonlinear effects is made from measurements realized outside the nonlinear material. It is thus useful to calibrate optical nonlinearities with the external fields. The local fields $\underline{E}_{\text{loc}}^{(j)}(\underline{\mathbf{r}}, \omega_j)$ actually present in the material must then be related to the external fields $\underline{E}_{\text{ext}}^{(j)}(\underline{\mathbf{r}}, \omega_j)$ actually measured. One notes then:

$$\underline{E}_{\text{loc}}^{(j)}(\underline{\mathbf{r}}, \omega_j) = f_j(\underline{\mathbf{r}}, \omega_j)\underline{E}_{\text{ext}}^{(j)}(\underline{\mathbf{r}}, \omega_j) \quad (10)$$

where $f_j(\underline{\mathbf{r}}, \omega_j)$ is the local field factor at the point $\underline{\mathbf{r}}$ for the frequency ω_j [FLY 75].

The local field appears in fact as a superposition of the external field and of the field radiated by polarization $\underline{P}_j(\underline{\mathbf{r}}, \omega_j)$ induced at point $\underline{\mathbf{r}}$ by the local field itself. One can then relate the two local and external fields by the relation:

$$\underline{E}_{\text{loc}}^{(j)}(\underline{\mathbf{r}}, \omega_j) = \underline{E}_{\text{ext}}^{(j)}(\underline{\mathbf{r}}, \omega_j) + \Lambda_j(\underline{\mathbf{r}}, \omega_j)\underline{P}_j(\underline{\mathbf{r}}, \omega_j) \quad (11)$$

where $\Lambda_j(\underline{\mathbf{r}}, \omega_j)$ is used as a measure of localization strength. In the linear regime polarization induced at the frequency ω_j is related to the local field through local linear susceptibility $\underline{\chi}_{\text{loc}}^{(j)}(\underline{\mathbf{r}}, \omega_j)$ by the relation:

$$\underline{P}_j(\underline{\mathbf{r}}, \omega_j) = \underline{\chi}_{\text{loc}}^{(j)}(\underline{\mathbf{r}}, \omega_j)\underline{E}_{\text{loc}}^{(j)}(\underline{\mathbf{r}}, \omega_j) \quad (12)$$

From equations (10) to (12), one easily finds the relation relating $f_j(\mathbf{r}, \omega_j)$ to $\Lambda_j(\mathbf{r}, \omega_j)$, that is:

$$f_j(\mathbf{r}, \omega_j) = \frac{1}{1 - \Lambda_j(\mathbf{r}, \omega_j) \underline{\chi}_{\text{loc}}^{(1)}(\mathbf{r}, \omega_j)} \quad (13)$$

In third order nonlinear optical processes, which we are interested in here, total polarization $\underline{P}(\mathbf{r}, \omega_4) = \underline{P}_L(\mathbf{r}, \omega_4) + \underline{P}_{\text{NL}}^{(3)}(\mathbf{r}, \omega_4)$ can be expressed as a function of the local fields using local nonlinearities of the material or as a function of the external fields using effective nonlinearities. Performing this operation, one finds the expressions relating the linear $\underline{\chi}_{\text{eff}}^{(1)}(\mathbf{r}, \omega_4)$ and nonlinear $\underline{\chi}_{\text{eff}}^{(3)}(\mathbf{r}, \omega_1, \omega_2, \omega_3)$ effective susceptibilities to the corresponding local susceptibilities $\underline{\chi}_{\text{loc}}^{(1)}(\mathbf{r}, \omega_4)$ and $\underline{\chi}_{\text{loc}}^{(3)}(\mathbf{r}, \omega_1, \omega_2, \omega_3)$:

$$\underline{\chi}_{\text{eff}}^{(1)}(\mathbf{r}, \omega_4) = f_4(\mathbf{r}, \omega_4) \underline{\chi}_{\text{loc}}^{(1)}(\mathbf{r}, \omega_4) \quad (14a)$$

$$\underline{\chi}_{\text{eff}}^{(3)}(\mathbf{r}, \omega_1, \omega_2, \omega_3) = f_4(\mathbf{r}, \omega_4) f_1(\mathbf{r}, \omega_1) f_2(\mathbf{r}, \omega_2) f_3(\mathbf{r}, \omega_3) \underline{\chi}_{\text{loc}}^{(3)}(\mathbf{r}, \omega_1, \omega_2, \omega_3) \quad (14b)$$

Equation (14a) shows that if $f_j(\mathbf{r}, \omega_j)$ is greater than 1, then the propagation speed of the optical wave related to the effective refractive index $n_{\text{eff}}(\mathbf{r}, \omega_j) = \sqrt{1 + 4\pi \underline{\chi}_{\text{eff}}^{(1)}(\mathbf{r}, \omega_j)}$ is smaller than for a material with the same refractive index but which does not present localization effects. Localization of light is then directly related to the slowing down of the optical wave in the material.

On the other hand, as shown by equation (14b), light localization plays an essential role in ensuring the efficiency of third order nonlinear processes since if we neglect dispersion in a first approximation, third order nonlinear susceptibility grows as the fourth power of the local field factor. This means that even for a moderate value $f_j(\mathbf{r}, \omega_j) = 3.3$, the effective nonlinearity of the considered material is 100 times greater than for a material that does not exhibit light localization effects. In a bulk material, the local field effect is due to the localization of electrons near the nucleus (the local field factor is then maximum for an ionic compound and zero for a metal). Below, we will ignore this effect, or more precisely we will suppose that the “bulk” local field effect is already incorporated in the value of local linear and

nonlinear susceptibilities. The following paragraph describes the effect of localization due to the nanostructure of the material.

6.3. Local field in photonic crystals

To show the physical origins of the huge enhancement in effective nonlinearities that can be obtained in photonic crystals, let us examine the value of the local field in a one-dimensional photonic crystal such as a Bragg mirror. Such a nanostructure (see Figure 6.2) is made of a stack of N periods of two layers of thickness e_1 and e_2 and refractive indices n_1 and n_2 , with the same optical thickness $\lambda_M/4=e_1n_1=e_2n_2$ where λ_M is the central wavelength of the forbidden band of the photonic crystal.

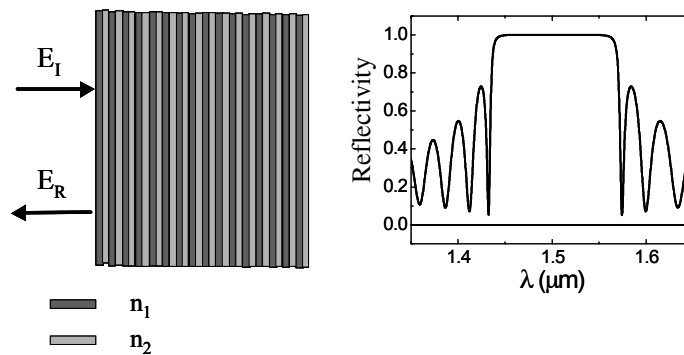


Figure 6.2. Structure and reflectivity spectrum of a one-dimensional photonic crystal

Such a device can be called a one-dimensional photonic band gap crystal, because of the existence of a frequency band for which propagation perpendicular to the periodicity is forbidden, light being totally reflected by the structure. The band structure of such an infinite crystal can be calculated relatively easily [JOA 95a, 95b]. The result is shown in Figure 6.3, with a particularly clear band gap in that case.

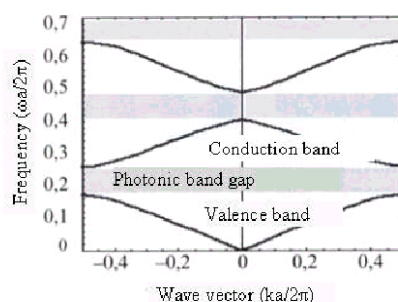


Figure 6.3. Band diagram of a one-dimensional photonic crystal

For any steady state optical device, the variation in volumic energy density per unit time is equal to the variation of optical intensity per unit length. Consequently, optical intensity at a given frequency is directly proportional to the density of modes contained by the device at the same frequency. Moreover, this density of modes $\rho = dk/d\omega$ defined from quantum electrodynamics [DOW 92] is the inverse of the group velocity $v_g = d\omega/dk$ defined from the propagation of the maximum rate of the pulse. The mean local field factor appears then as the square root of the ratio of the group velocity of the non-structured material to that of the photonic crystal. The local field factor will be then all the more important since the group velocity of light through the device will be small (this has been shown in a different manner in section 6.2.3). At the edge of the band gap (see Figure 6.3), the frequency varies only slightly with the wave vector, which means that group velocity will be small. Light remains in the structure for a very long time and can then interact at length with the nonlinear material. Another point of view says that the local amplitude of the field of the electromagnetic wave is increased by interferences due to multiple reflections on the interfaces separating the 1 and 2 media, as is the case in a Fabry-Perot etalon. The low value of group velocity is in fact obtained for a wavelength corresponding to a maximum of transmission of the photonic crystal, which means that in the absence of losses, the light stays in the nanostructure for a long time but exits it almost integrally, with only a small proportion being reflected. The local field factor in the one-dimensional photonic crystal is calculated for this wavelength.

As an example of an easy experiment, we consider a Bragg mirror centered at a wavelength of $1.5\mu\text{m}$ made of pairs of layers of CdMnTe ($n_1=2.937$) and CdMgTe ($n_2=2.547$) of optical thickness $\lambda/4$ grown on a CdMnTe substrate. The calculation is made using a matrix technique to determine the fields propagating forwards and backwards in the structure [DEL 05]. In order to fully show the importance of the nanostructuring of the material, the local field factor that we consider is the ratio

of the modulus of the field (forward or backward) at the point with ordinate z in the structure, to the one obtained in a bulk material of index n_1 .

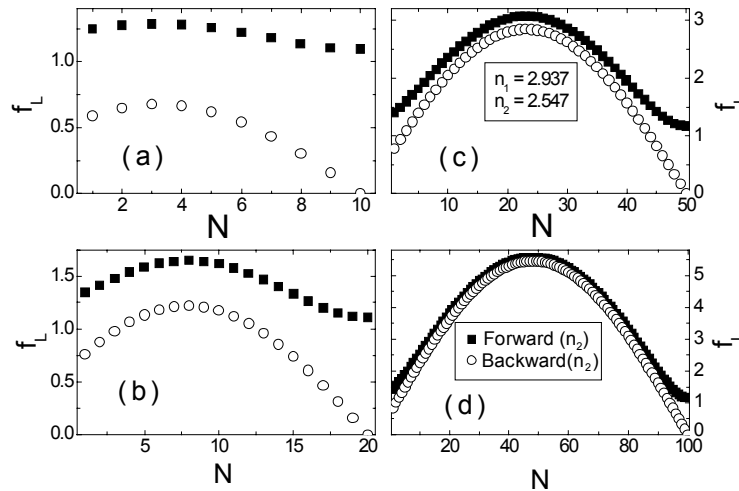


Figure 6.4. Distribution of the local field factor f_L in a photonic crystal of N periods ($N=10, 20, 50$ and 100 in (a), (b), (c) and (d) respectively)

Figure 6.4 shows the value of the local field factor inside the layers of index n_2 as a function of the number N of periods grown on the substrate for fields propagating forwards (full squares) and backwards (empty circles). The calculation is made for wavelengths chosen at the band edge ($\lambda=1.642, 1.598, 1.577$ and 1.573 for $N=10, 20, 50$ and 100 respectively) when the structure becomes transparent again. The local field factor f_L differs for the wave propagating forwards and backwards because of the dissymmetry introduced by the fact that only the forward propagating wave is incident on the structure. One may nevertheless note that the difference decreases when N increases because of the growing importance of multiple reflections that gives a maximum of the local field around the middle of the structure.

The slight dissymmetry of the curves is in fact due to that part of the structure itself that is exposed to open air on one side and to the substrate on the other side. Note also that because of the small value of the index mismatch ($\Delta n=n_1-n_2$), the local field factor in the layers of index n_1 is only slightly smaller than the one calculated in the layers of index n_2 . To show the effect of the resonance that occurs at the band edge, Figure 6.5 shows the spectra of the mean

local field factor $f_M = (1/2N) \sum_{j=1}^N \left(\sqrt{f_{\text{for}}(n_1, j) f_{\text{back}}(n_1, j)} + \sqrt{f_{\text{for}}(n_2, j) f_{\text{back}}(n_2, j)} \right)$

(averaged on the photonic crystal's length) for the structures of 10, 20, 50 and

100 layers considered previously. When the number of periods increases, the central wavelength of the mean local field factor peak comes closer to the theoretical band edge of an infinite photonic crystal. At the same time, the width of the peak decreases whereas the maximum of the curve increases, confirming resonance effect due to multiple interferences.

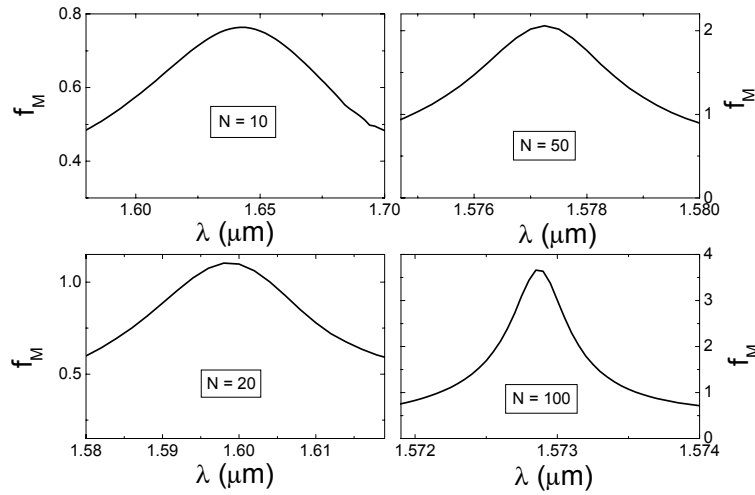


Figure 6.5. Mean local field factor spectra for a one-dimensional photonic crystal

Figure 6.6 shows the evolution of the maximum of the mean local field as a function of the number N of periods of the structure. The full squares correspond to the results of the previous numerical calculation. The full line curve corresponds to an evaluation of the local field factor made from the analytical formula giving the group velocity in the photonic crystal at the band edge [BEN 96]:

$$f_M = \sqrt{\frac{1 - T_{12} \cos^2(\pi/2N)}{T_{12} \sin^2(\pi/2N)}} \quad (15)$$

$T_{12} = 4n_1n_2/(n_1 + n_2)^2$ being the intensity transmission factor of the dioptr separating the two media of indices n_1 and n_2 .

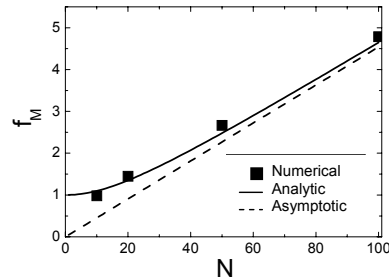


Figure 6.6. Mean local field factor variation versus the number of periods of the one-dimensional photonic crystal

For a sufficiently large value of N ($N > 20$), the local field is then directly proportional to the thickness of the nanostructure. Taking into account formula (14b), this means that effective third order nonlinear susceptibility grows as the fourth power of the thickness of the photonic crystal. Thus for 100 layers, effective nonlinear susceptibility is 400 times higher than in a bulk crystal, which indicates conceivable solutions for the realization of information processing functions with micrometer dimensions. In the case of the structure considered above, huge enhancements are made at the price of a large number of periods of the photonic crystal. This drawback can be eliminated if a higher index contrast between successive layers is used. Indeed, looking at equation (15) and the expression giving T_{12} shows that the local field factor increases in an important manner with the index contrast Δn . This is confirmed by the numerical calculation: in Figure 6.7 we see the spatial distribution of the forward local field factor in the high and low index layers of a structure with 20 periods, for a value of the refractive index of the low index layer $n_2 = 2.8, 2, 1.5$ and 1 , the high index layers maintaining an index $n_1 = 3$.

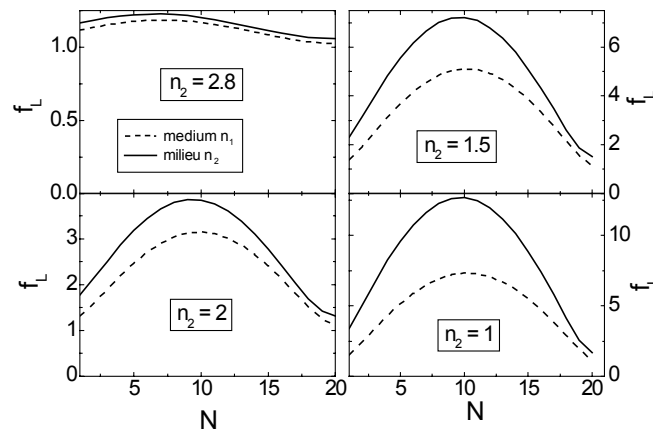


Figure 6.7. Local field factor distributions for photonic crystals with different index contrasts

As expected, the effect of the index contrast favoring the efficiency of the reflections on the different diopeters is spectacular on the enhancement of the local field factor with maximum values around 15, allowing nonlinear susceptibility to be raised by a factor $5 \cdot 10^4$. It is also important to note that, as the amplitude transmission factors differ for the crossing from low index to high index layers and vice versa, the local field factor is higher by a factor $\sqrt{n_1/n_2}$ in the low index layer. As the low index layer is also thicker by a factor n_1/n_2 , this point shows the importance of choosing a low index nonlinear material with the highest possible nonlinearity. This could be obtained, for example, by filling the interstices between high index layers with a gas having a resonance at the band edge frequency.

6.4. Nonlinearities in photonic crystals

The very strong influence of the local field factor on effective nonlinearities can easily be quantified using frequency degenerated four wave mixing. Indeed, as this process is automatically phase matched, a comparison of the measured or calculated conjugate intensities for a photonic crystal and for a bulk crystal made of the same material, and for identical pump and signal beam intensities makes it possible to obtain the nonlinearity gain $G = \chi_{PC}^{(3)} / \chi_{BC}^{(3)}$. Figure 6.8 shows the variation of the conjugate intensity as a function of the number of periods deposited on the substrate for the photonic crystal considered in Figures 6.4 and 6.5. The calculation is made using the same matrix technique as for the evaluation of the local field, the only difference being that nonlinear propagation in the different layers of the structure is taken into account.

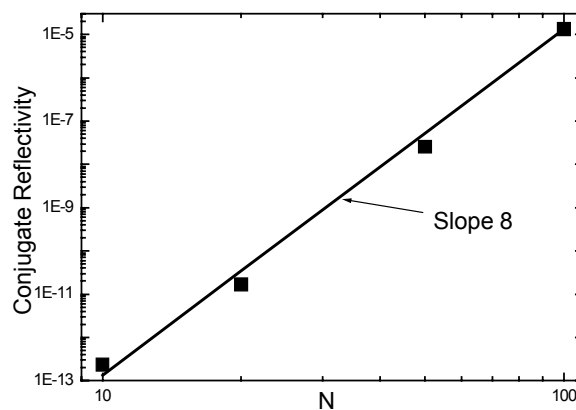


Figure 6.8. Phase conjugate reflectivity of a one-dimensional photonic crystal as a function of the number of periods in the structure

As expected, the growth of conjugate reflectivity is proportional to the eighth power of the structure's thickness, whereas growth is only proportional to the square of this thickness in the case of a bulk crystal. It brings about an improvement in performance of the device of several orders of magnitude, which means that we can expect the implementation of optical signal processing functions with micrometer-sized devices.

6.5. Conclusion

In this chapter, we have shown that the introduction of optical information processing functions in potential optical microcircuits made with photonic crystals necessitates an optimization of the nonlinear performance of the structures. After an introduction to third order nonlinear effects useful for optical information processing (mainly the optical Kerr effect, four wave mixing and derived processes), this chapter has shown the importance of light localization for nonlinear effects: an enhancement with the fourth power of the local field factor of third order nonlinear susceptibility has been shown. We have also indicated how the nanostructuring of materials with large intrinsic nonlinearities such as semiconductors considerably increases the efficiency of nonlinear processes occurring in these materials. The local field factor at the band edge increases with the number of periods, but at the expense of a decrease in the phenomenon spectral bandwidth. Furthermore, a large index contrast makes it possible to obtain a huge increase in the local field factor with a small number of periods. From this point of view, air-semiconductor structures have a lot of potential.

Of course, the results presented here for a one-dimensional structure give the general basis for optimization of two- or three-dimensional photonic crystals that have potential in various applications for optical information processing. Nevertheless, deeper studies incorporating in addition the influence of linear and nonlinear losses will have to be made in these much more complex, but also richer in terms of potential for of structuration, cases.

6.6. References

- [BEN 96] Bendickson J.M., Dowling J.P., Scalora M. (1996) Analytic expressions for the electromagnetic mode density in finite, one-dimensional, photonic band-gap structures. *Phys. Rev. E* 53: 4107
- [BER 98] Berger V. (1998) Nonlinear photonic crystals. *Phys. Rev. Lett.* 81: 4136
- [BRO 00] Broderick N.G.R., Ross G.W., Offerhaus H.L., Richardson D.J., Hanna D.C. (2000) Hexagonally poled lithium niobate: A two dimensional non linear photonic crystal. *Phys. Rev. Lett.* 84: 4345

- [DEL 05] Delaye Ph., Astic M., Frey R., Roosen G., (2005) Transfer-matrix modeling of four-wave mixing at the band edge of a one dimensional photonic crystal. *JOSA B*, 22: 2494
- [DOW 92] Dowling J.P., Bowden C.M. (1992) Atomic emission rates in inhomogeneous media with applications to photonic band structures. *Phys. Rev. A* 46: 612
- [DUM 01] Dumeige Y., Vidakovic P., Sauvage S., Sagnes I., Levenson J.A., Sibilica C., Centini M., D'Aguzzo G., Scalora M. (2001) Enhancement of second harmonic generation in a one dimensional semiconductor photonic band gap. *Appl. Phys. Lett.* 78: 3021
- [FIO 98] Fiore A., Berger V., Rosencher E., Bravetti P., Nagle J. (1998) Phase matching using isotropic nonlinear optical material. *Nature* 391: 463
- [FLY 75] Flytzanis C. (1975) Theory of nonlinear optical susceptibilities in Tang C.L. (ed) *Quantum Electronics*. Academic Press, New York, volume I, Part A
- [JOA 95a] Joannopoulos J.D. (1995) The magical world of photonic crystals in Soukoulis (ed) *Photonic Band Gap Materials*. Kluwer Academic Publishing, Dordrecht
- [JOA 95b] Joannopoulos J.D., Meade R.D., Winn J.N. (1995) *Photonic Crystals*. Princeton University Press, New Jersey
- [LOU 03] Lourtioz J.M., Benisty H., Berger V., Gérard J.M., Maystre D., Tchelmeikov A. (2003) *Les cristaux photoniques*. Hermès Sciences, Paris
- [SI 02] Special Issue (2002) NonLinear photonic crystals. *J. Opt. Soc. Am. B* 19
- [SHE 84] Shen Y.R. (1984) *The Principles of Nonlinear Optics*. John Wiley & Sons, New York
- [YAB 94] Yablonovitch E. (1994) Photonic crystals. *Journ. Mod. Phys.* 41: 17

Chapter 7

Controlling the Optical Near Field: Implications for Nanotechnology

7.1. Introduction

Until recently, the concept of near field has not been extensively exploited in optics. Indeed, since information contained in the signal could only be detected in far field, interest tended generally to be more focussed on the structure of the electromagnetic field in far field.

The advent of near field microscopies and integrated-optical devices first developed in the fields of microtechnology and nanotechnology is now changing this state of affairs. The control of the optical near field is now recognized as a key issue for the qualification of optical nanotechnology devices. The term “qualification” is used here to denote the control of specific properties of these devices, and the control of their local losses. In the medium term, the efficient development of active near field optical devices based on localized optical interactions will not be possible save through a thorough understanding of near field optics.

This chapter begins with a definition of the notion of near field in certain specific configurations. It then turns to a description of the methods used for detecting the near field, before providing the reader with some examples of applications. Since only a limited number of examples can be described in this chapter, we have chosen to restrict ourselves to a consideration of three: integrated waveguides, photonic

crystal cavities and metal perforated with sub-wavelength Hole Arrays. In our opinion, all three types of components are among the key optical devices that will be in used in nanotechnology in the future.

7.2. How is the near field defined?

The question of the definition of the near field is still debated. Here we will consider a few definitions, each of which might lead to a different conception of the near field. We shall first consider the case of the field radiated by a dipole, before turning our attention to the field scattered by an aperture with sub-wavelength dimension, and finally we will look at the evanescent field of a diopter illuminated under total internal reflection.

7.2.1. Dipolar emission

Let us consider a dipole oscillating along the z -axis, as represented in Figure 7.1. The electric polarization of the dipole follows the equation:

$$\vec{P}(\vec{r}, t) = p(t)\delta(\vec{r} - \vec{r}_0)\vec{n} \quad (1)$$

where $p(t)$ is the time-dependent polarizability.

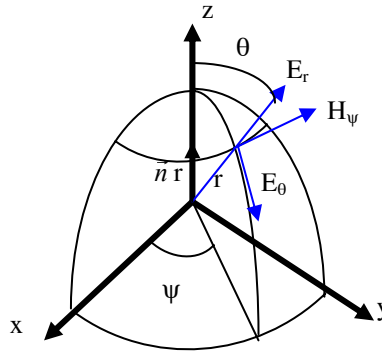


Figure 7.1. Schematic representation of a dipole with momentum parallel to Oz .

The components of the field generated by the dipole are given by the following equations [BOR 59]:

$$E_r = 2 \left(\frac{p}{r^3} + \frac{\dot{p}}{cr^2} \right) \cos \theta \quad (2)$$

$$E_\theta = \left(\frac{p}{r^3} + \frac{\dot{p}}{cr^2} + \frac{\ddot{p}}{c^2 r} \right) \sin \theta \quad (3)$$

$$H_\psi = \left(\frac{\dot{p}}{cr^2} + \frac{\ddot{p}}{c^2 r} \right) \sin \theta \quad (4)$$

where p , \dot{p} and \ddot{p} correspond to polarizability and its time derivatives.

The field emitted by the dipole can then be determined from these equations. By calculating the average flux of the Poynting vector through a sphere extending around the dipole, it can easily be demonstrated that only the $1/r$ terms have a non-null contribution. Therefore, the other terms represent the evanescent waves associated to the dipole.

In the case of a dipole, the near field region corresponds to the region of space where evanescent waves are in the majority. This region can therefore be determined using the previous relations. This leads to an estimation of the near field distance in the order of $\lambda/2\pi$.

Everything happens as if the energy associated with evanescent waves is periodically flowing out from and back to the source without ever being lost by the system.

For the purpose of demonstrating the existence of evanescent waves associated with the dipole, in 1913 Sélényi conducted the following experiment [SEL 13]. Having deposited fluorescent molecules on the plane surface of a semi-cylindrical prism, he then proceeded to measure their emitted power as a function of the emission angle. Since the signal detected in the prism above the critical angle was found to be non-null, Sélényi concluded that the signal was generated by the evanescent waves associated with the fluorescence emission.

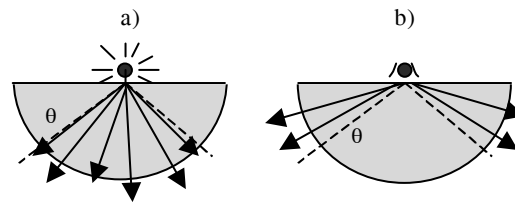


Figure 7.2. Sélényi's experiment, demonstrating the presence of evanescent waves in the vicinity of a dipole. The detected light comes from (a) waves associated with the dipole, (b) evanescent waves

The following figure presents the theoretical analysis underlying Sélényi's experiment.

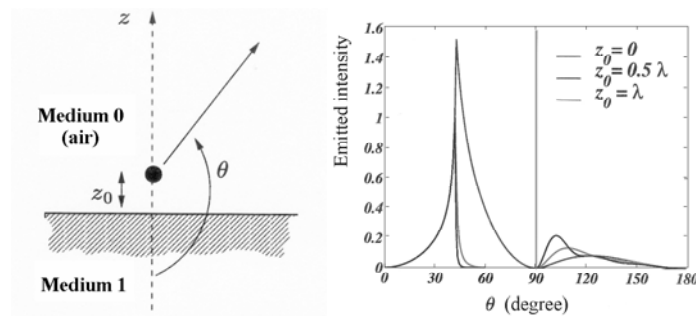


Figure 7.3. Emission diagram of a dipole located at different distances from a semi-infinite medium

If the near environment extending around a dipole can transform some of the evanescent waves into propagative waves, this means that the emission rate of the dipole increases. In other terms, the lifetime of the dipolar radiation/emission can be said to decrease. An alternative approach to coupling between the dipole and its environment consists of considering that the dipole acts as a probe in its near field. Thus, if for instance two metallic particles are located near the dipole, the lifetime associated with the dipole will be dependent on the distance separating it from the particles. The following figure shows that a loss in resolution occurs when the particles move outside the near field of the dipole. This demonstrates that sub-wavelength resolution is related to the interaction occurring with the evanescent waves associated to the dipole.

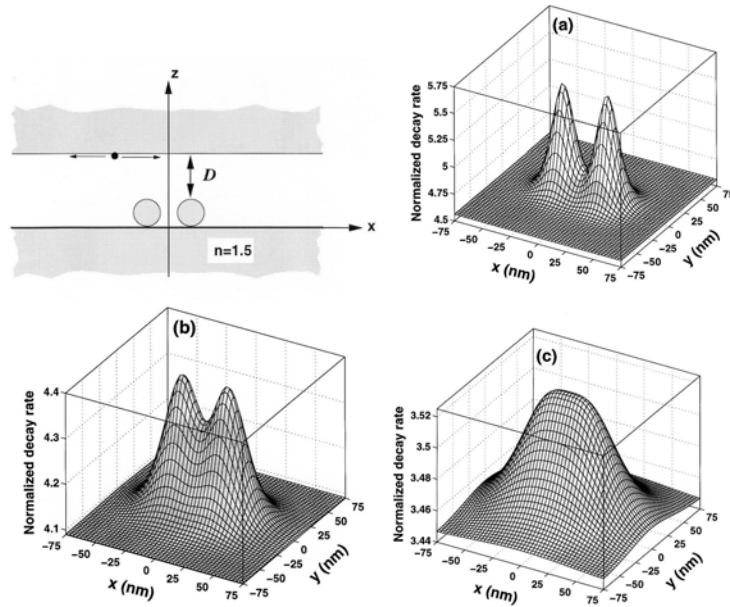


Figure 7.4. The dipole used as a probe moves in a plane parallel to the substrate upon which two metallic particles have been deposited. The image describes the variations of the emission rate as a function of the location of the probe with respect to the particles. The resolving power depends on the distance D , equal to (a) 10 nm, (b) 20 nm and (c) 40 nm respectively [RAH 97]

Let us now consider a second example of interaction in the near field of the dipole. It is known that, in order to optically excite a surface plasmon, it is necessary to resort to the so called Kretschmann configuration, where the evanescent wave generated by total internal reflection excites the plasmon [RAE 88]. A surface plasmon can also be excited from the evanescent wave of the dipole, as can be seen in the following figure, where a minimum appears when the dipole is near the surface ($\lambda \approx 320$ nm).

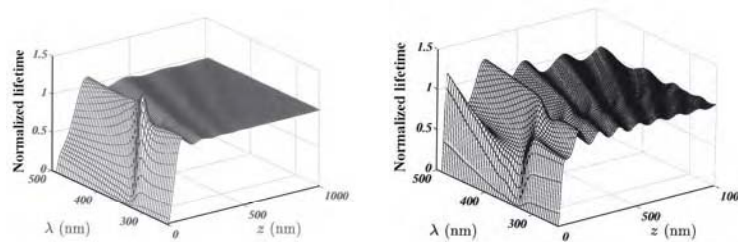


Figure 7.5. Excitation of plasmons by the field of a dipole: (a) dipole normal to the surface, (b) dipole parallel to the surface [RAH 01]

7.2.2. Diffraction by a sub-wavelength aperture

The following figure summarizes what happens when the size of an aperture illuminated by a plane wave is reduced. The parameter to be taken into consideration is the relative size of the aperture ($2a$) with respect to the wavelength of the incident wave (λ).

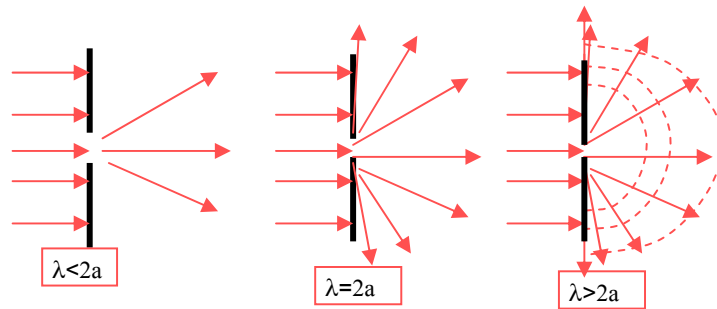


Figure 7.6. Schematic representation of the transmission of light through an aperture with variable size illuminated by a plane wave. The curves in dotted lines represent evanescent waves

As the size of the aperture decreases, the numerical aperture of the transmitted beam increases up to the point, at $\lambda = 2a$, where it completely fills the half-space. From this value onwards, evanescent waves appear.

The equation for the evanescent field when $\lambda > 2a$ is:

$$E = E_0 \exp(-z / d_p) \exp(j\omega t - k_x x - k_y y) \quad (5)$$

where d_p is the penetration depth of the evanescent waves, as given by the following equation:

$$d_p = \left(k_x^2 + k_y^2 - \frac{\omega^2}{c^2} \right)^{-1/2} \quad (6)$$

The idea of using the field generated by a sub-wavelength aperture for enhancing the resolution power of microscopes was first suggested by Synge in a letter written to Einstein at the beginning of the twentieth century [SYN 28]. However, it was only much later that these ideas were actually implemented in optics [LEV 86]. Applications to near field microscopy were developed on the basis of the studies conducted on diffraction by a sub-wavelength aperture [BET 44; BOU 50; LEV 86]. The following figure shows the average flux of the Poynting vector, represented as a

function of the distance from the aperture. The rapid decay of the transmitted intensity is apparent on these curves. The determination of the electromagnetic field shows that, at a great distance from the aperture, the latter acts as a dipole.

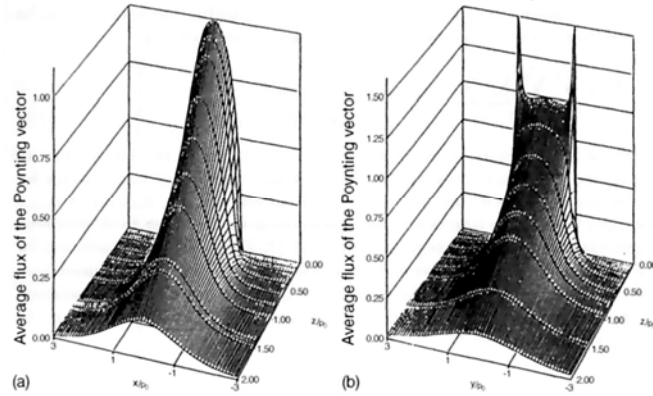


Figure 7.7. Evolution of the average flux of Poynting's vector transmitted through a sub-wavelength aperture, plotted against the distance from the aperture. The electric field in the plane of the aperture extends (a) along Ox , (b) along Oy [LEV 86]

As has been seen, the near field region can be defined as the region of space where evanescent waves predominate. The final example that we consider here is that of total internal reflection.

7.2.3. Total internal reflection

Let us consider an ensemble consisting of two semi-infinite media, with refractive indices n_1 and n_2 , where $n_1 > n_2$. Depending on the illumination conditions, either refraction (if $\theta < \theta_c$) or total internal reflection (if $\theta > \theta_c$) will occur. Here θ_c is the critical angle of refraction, as given by the equation:

$$\theta_c = \text{Arcsin}(n_2 / n_1) \quad (7)$$

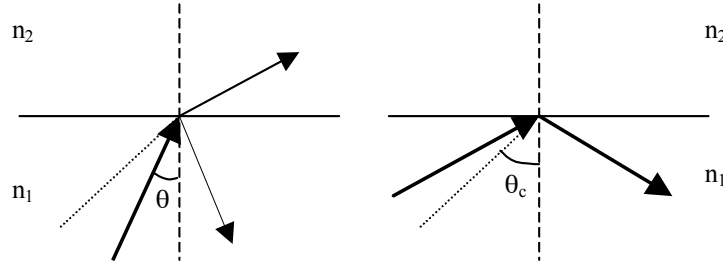


Figure 7.8. Schematic representation of the refraction phenomenon for $\theta < \theta_c$ and $\theta > \theta_c$.

Assuming Oz to be the normal axis with respect to the interface between the two media, and the incidence plane to be defined Ox, Oz, then the field in the second medium obeys the following equation:

– in *p*-polarization:

$$\vec{E}_p(z) = E_p^i \frac{(2 \cos \theta) \exp(-z/d_p)}{n^2 \cos \theta + j(\sin^2 \theta - n^2)^{1/2}} \left[-j(\sin^2 \theta - n^2)^{1/2} \vec{e}_x + \sin \theta \vec{e}_z \right] \quad (7a)$$

– in *s*-polarization:

$$\vec{E}_s(z) = E_s^i \frac{(2 \cos \theta) \exp(-z/d_p)}{\cos \theta + j(\sin^2 \theta - n^2)^{1/2}} \vec{e}_y \quad (8)$$

The d_p term is the penetration depth of the evanescent field in the second medium.

$$d_p = \frac{\lambda}{2\pi \sqrt{n_1^2 \sin^2 \theta - n_2^2}} \quad (9)$$

d_p depends on the incidence angle, on the refractive indices of the two media, and on the wavelength. It is not polarization-dependent.

For a better insight into the order of magnitude of this parameter, the following table provides a few values for d_p in different configurations.

λ (nm)	n_1	n_2	θ_c	θ	d_p (nm)
1,300	Glass	Air	43.3	45	825
1,300	Silicon	Air	16.9	45	94
633	Glass	Air	43.3	45	402
633	Glass	Air	43.3	85	96
633	Glass	Water	65.8	85	173
414	Glass	Air	43.3	85	63

Table 7.1. Value of the penetration depth of the evanescent wave for different values of refractive indices of the media, different incidence angles and different wavelengths

Let us now return to the criterion that we previously determined for the near field. In the case of a plane surface illuminated under total internal reflection, we can no longer use the same definition of the near field as for a dipole or an aperture. Indeed, the possibility may now exist that θ is close to θ_c and that the evanescent wave has such a great spatial extension (with d_p assuming a high value) that only this evanescent wave exists. In such a case, the value for d_p is to be considered as given and defines the spatial extension of the near field.

Another property to be pointed out is the dependence of the value of the field at the interface between the two media on the incidence angle. It can be seen from the following figure that the maximal value for the field has reached near total internal reflection, and that when the surface is illuminated at an angle above θ_c the field decreases relatively rapidly. A slight difference in the behavior of the curve can be observed depending on the polarization.

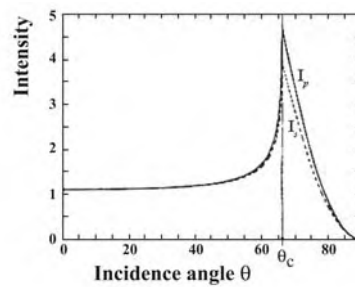


Figure 7.9. Variation of the intensity of the electric field at the interface between the two media in *s* and *p* polarizations as a function of the incidence angle. $n_1=1.46$ and $n_2=1.33$

The existence of the evanescent field in total internal reflection was first experimentally demonstrated by Newton. He brought near the hypotenuse face of a right-angle prism a second optical element consisting of a modified prism whose hypotenuse face had a large radius of curvature. Observation of the transmitted signal reveals that transmission between the two prisms takes place not only at the contact point, but also in regions where the distance between the two surfaces, while non-null, remains small with respect to the wavelength. In such a case, total internal reflection is said to be frustrated. This result was interpreted by Newton as demonstrating the penetration of light in the second medium at total internal reflection.

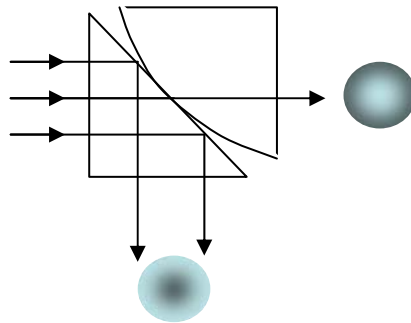


Figure 7.10. Experiment demonstrating the existence and the frustration of the evanescent wave

A more local method for demonstrating the penetration of the field in the second medium consists of moving a thinned/sharpened optical fiber close to the interface where total internal reflection occurs, in order to measure the signal thus transmitted.

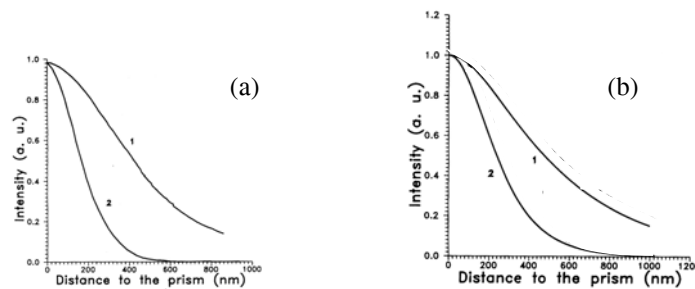


Figure 7.11. Detection of the near field with a sub-wavelength probe consisting of a sharpened fiber, $\theta = 50^\circ$ and 60° , $\lambda = 1.3 \mu\text{m}$. (a) Experimental measurement; (b) Numerical model [FOR 93]

When the probe is at a distance larger than 200nm, the curve is exponential and follows the relation given by the previous equations. By contrast, when the probe is very close to the surface, this exponential variation no longer exists. At a great distance from the surface, the field extending in this region takes into account the presence of the probe. The latter therefore causes only a slight perturbation. Thus, in order to simulate such systems, it is necessary to take into account the presence of the probe, as in the curve shown in Figure 7.11b.

7.3. Optical near field microscopies

7.3.1. Introduction

The properties of the near field can be exploited in a variety of fields, including waveguides, sensors and antennas. In this chapter we shall restrict ourselves to the field of nanosciences, and in particular to so called optical near field microscopies.

7.3.2. Fundamental principles

The principle of near field microscopies can be summarized in the following simple fashion. Since far field detection does not give access to sub-wavelength information contained in evanescent waves, an alternative way of overcoming the Rayleigh criterion would be the detection of these waves. At the risk of oversimplification, near field microscopy can thus be described as a method for collecting local information in the near field of the object under study. These microscopes are described in more detail in the book by D. Courjon and C. Bainier, and only a few specific examples will be presented here [COU 01]. The following figure shows the main configurations which are currently used in near field microscopy. Near field optical microscopes are generally referred to as scanning near field optical microscopes (SNOM) [FOR 01].

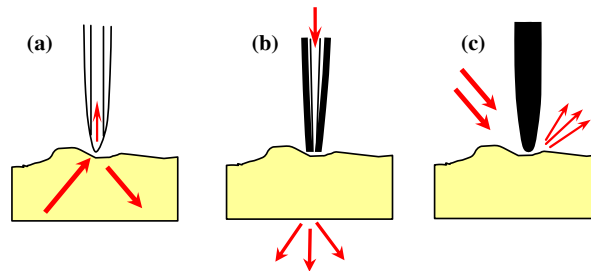


Figure 7.12. Main configurations for near field microscopes (SNOM):
 (a) Photon Scanning Tunneling Microscopy (PSTM), (b) Scanning Near field Optical Microscopy (SNOM), (c) Apertureless microscope

With the PSTM, the object to be studied is illuminated under total internal reflection, while the probe, which usually consists of an optical fiber, detects the field in the vicinity of the object. It collects part of the radiative waves and transforms part of the evanescent field into a propagative field. For near field optical microscopes with an aperture, a first possibility consists of using the metallized fiber as a sub-wavelength probe: in this case, the evanescent field localized in the vicinity of the aperture is transformed into a propagative field either through scattering by the sub-wavelength features of the sample or through other types of interaction, for instance fluorescence phenomena. This configuration is referred to as scanning near field microscopy in emission mode. Note that the signal can be detected either after its propagation through the sample or by means of the fiber used for the illumination. Near field optical microscopes can also be operated in collection mode, as is the case for PSTM: the probe here is used for detecting a part of the field. Detection depends on the size of the aperture, on the refractive index of the probe, and on the material from which the aperture is realized.

In apertureless mode, an opaque probe with sub-wavelength size is brought inside the near field of the object under investigation, the latter generally being illuminated under external reflection. The detected signal results from the diffraction of the incident beam by the extremity of the probe. This generates a strong evanescent field which interacts with the surface. Likewise, the sub-wavelength features of the surface generate an evanescent field, which is transformed into a propagative field by the probe. The signal is detected in far field with a high numerical aperture.

For all these microscopes, the theoretical analysis of the detected signal requires, when the probe is extremely close to the surface, that the system formed by the probe and the surface be considered as a whole. For near field measurements, the distance between the probe and the object goes from a few nanometers to a few tens to nanometers. In the following figure an example of near field detection is given.

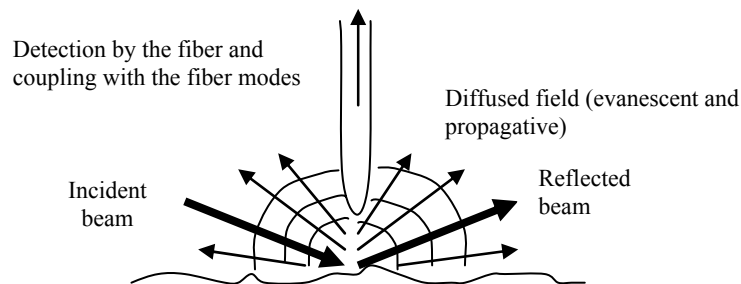


Figure 7.13. Schematic representation of the near field detection by a sharpened fiber

In collection mode, it is necessary to take into account not only the interaction in near field between the extremity of the probe and the object, but also the coupling between the detected signal and the guided modes of the probe. The latter typically consists of an optical fiber, which can be either multimode or single-mode [ADA 82; GOU 05].

7.3.3. Realization of near field probes

Depending on the type of microscope where they are to be used, near field probes need to satisfy different criteria. For the PSTM, the probe must be small if it is to locally transform part of the evanescent waves into propagative waves and to detect a part of the propagative waves existing in the vicinity of the structure under investigation. Thus far, the existence of a direct relation between the resolving power of this type of microscope and the optogeometrical properties of the probe has not been demonstrated, either experimentally or theoretically.

With the exception of the apertureless microscope, probes used in near field microscopy are generally realized from optical fibers. Their structure is described in the following figure.

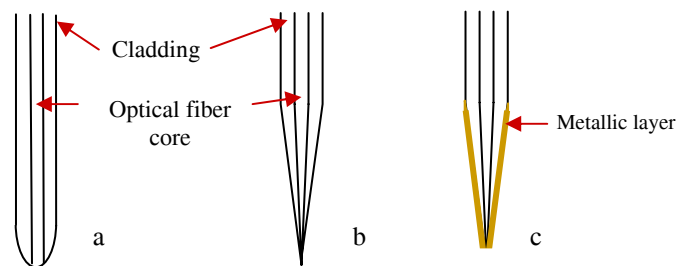


Figure 7.14. *Different types of probes used for microscopes operating in collection or emission mode*

The difficulty of realizing these probes lies in the problem of their reproducibility and of controlling the shape of the extremity, the quality of the metallic layer and the size of nano-aperture, which is typically between 50 and 200nm.

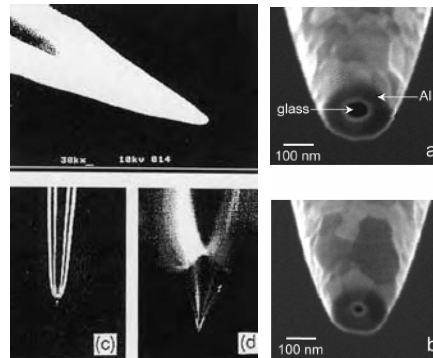


Figure 7.15. Photographs of some near field probes. On the left-hand side of the figure are three chemically etched probes (the first without pulling), and on the right-hand side are two metallized probes

Probes used for apertureless microscopy can be realized from AFM or tungsten probes. Techniques originally developed for scanning tunneling microscopy can be used for the realization of these probes [COU 01].

7.3.4. Imaging methods in near field optical microscopes

Images are obtained by having the surface scanned “line by line” by the probe. Different scanning modes exist, which are as follows.

Constant height mode (CHM) (Figure 7.16a)

- The analysis of the optical images is relatively straightforward.
- Mechanical shift problems may arise during scanning.
- Controlling the displacement plane of the probe with respect to the average plane of the sample can be difficult.

Constant distance mode (CDM) (Figure 7.16b)

- The distance between the probe and the surface is kept constant through the use of an AFM or shear-force regulation. The distance between the probe and the surface is then in the order of a few nanometers.
- Analysis of the images is more difficult, due to the possibility that the displacement of the probe may directly induce intensity variations.

Constant (optical) intensity mode (CIM) (Figure 7.16c)

- If the detected intensity is a monotonous function of the distance between the end of the probe and the surface, the position of the probe can be controlled by keeping the optical signal constant.

- This mode is used for the PSTM, with the probe at a 50 to 250nm distance from the surface.
- The image gives “isointensity” curves of the optical signal.

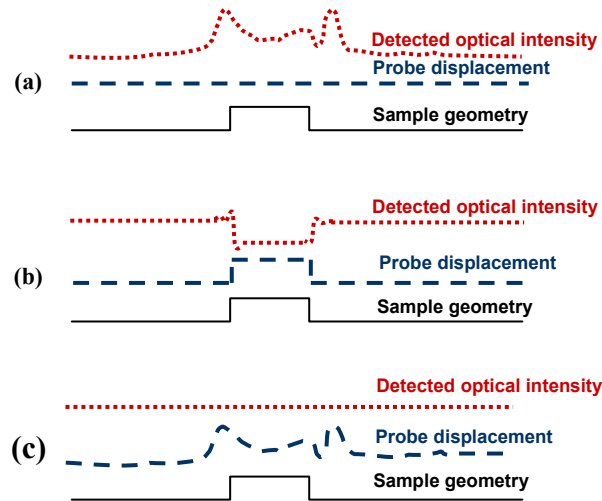


Figure 7.16. Different scanning modes used in near field microscopy: (a) constant height mode, (b) constant distance mode, (c) constant (optical) intensity mode

For each of these configurations, a variety of different arrangements exist. The two following figures show an apertureless microscope with an AFM regulation and a microscope operating in collection mode with a shear-force feedback.

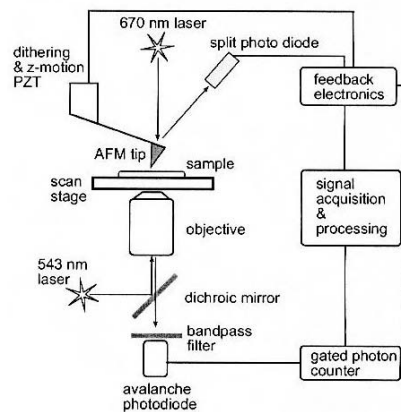


Figure 7.17. Schematic representation of an apertureless microscope with AFM regulation

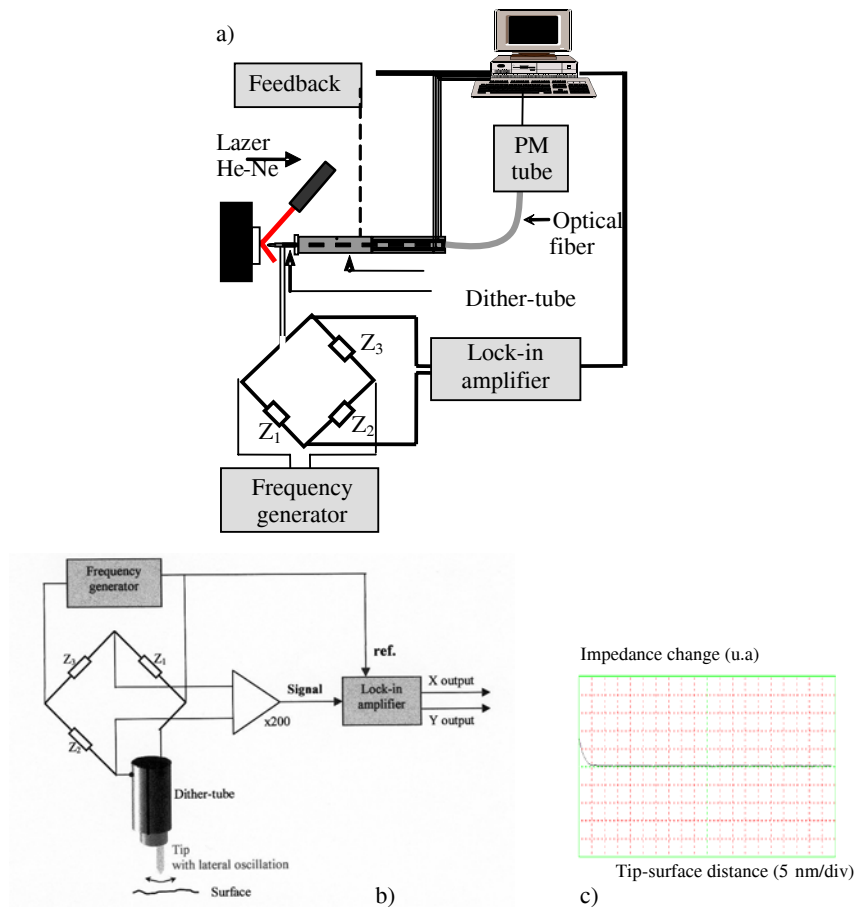


Figure 7.18. (a) SNOM operating in collection mode with shear-force regulation, (b) detailed view of the shear-force regulation mechanism, (c) variation of the impedance of the dither-tube at the resonance, represented as a function of the distance between the probe and the surface. The interaction occurs for distances less than 12nm

7.3.5. Feedback

In order to control the position of the probe with respect to the detected signal, it is necessary that the signal should be varying monotonously as a function of the distance between the probe and the surface of the sample. As far as the optical signal is concerned, only the configuration where the sample is illuminated under total internal reflection may satisfy this criterion. For the regulation to be as efficient as possible, it is preferable that the variation curve be as steep as possible. This leads to envisioning the highest possible angle, as

well as materials with high dielectric contrasts (see the values for d_p given in Table 7.1). Operating scanning near field optical microscopes in illumination mode is more complicated, due to the multiple reflections which may arise between the probe and the surface.

In cases where it is not possible to keep the optical signal constant, complementary regulation methods include AFM regulation and shear-force feedback. The latter relies on the shear-force type interactions occurring between the surface and the probe which oscillates laterally with an amplitude of a few nanometers. Finally, when both the probe and the sample are metallic or metallized, the electronic tunneling effect can be used for controlling the position of the probe. By keeping the signal constant, the distance between the probe and the surface of the sample can be controlled from a few tens of nanometers to λ , i.e. in the visible range up to 600nm. The utilization of tunnel current or mechanical forces makes it possible to keep the probe at a distance of a few nanometers from the surface.

7.3.6. What is actually measured in near field?

Answering this seemingly simple question is far from simple. This is because determining the signal, whether it be detected through the probe operating in collection mode, collected in far field in illumination mode, or generated by the interaction between the surface and the field scattered by the metallic probe, is not an easy task, which varies depending upon which configuration is used. However, certain configurations exist where a relatively clear-cut answer can be given to this question.

7.3.7. PSTM configuration

Let us return to the example described by L. Salomon, where gold pads were deposited on a silicon substrate illuminated under total internal reflection [SAL 01]. The following figure describes this experiment, and provides a comparison between the images thus obtained and the distribution of the square of the electric field. A very good agreement can be noted between these two series of results. This can be explained either by the fact that the probe does not significantly perturb the field in the vicinity of the structure, or by the fact that the perturbation thus induced is the same at any point. It should be noted that the fiber used here is a multimode fiber, which causes the angular filtering during detection of the near field to be limited. In this case, what is recorded is the distribution of the electric field. Had a single-mode probe been used instead, the results obtained for the square of the electric field would have been markedly different.

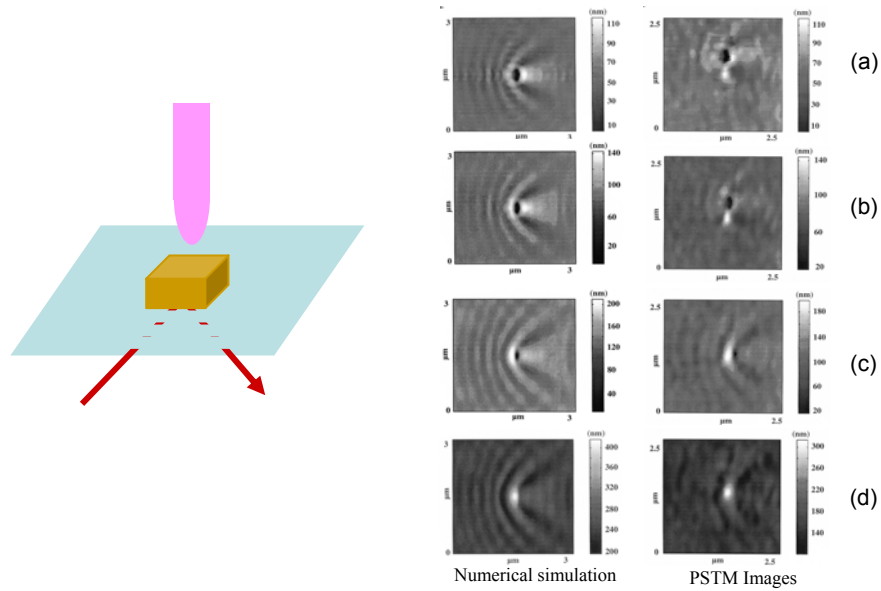


Figure 7.19. Comparison between the iso-intensity images obtained in PSTM and the iso-intensity surfaces of the square of the electric field, for different reference values of the intensity. Image (a) corresponds to the contact between the probe and the gold pads, while image (d) corresponds to an average distance value equal to 400nm [SAL 02]

Devaud *et al.* have demonstrated that, in the case where the probe is covered with some specific metallic layer, the image obtained in PSTM in constant height mode is close to the magnetic field distribution [DEV 00]. This occurs only under specific conditions as regards both the nature and the thickness of the metallic layer, such that a surface plasmon can be excited. In this case, the optical signal detected by the probe is close to the magnetic field.

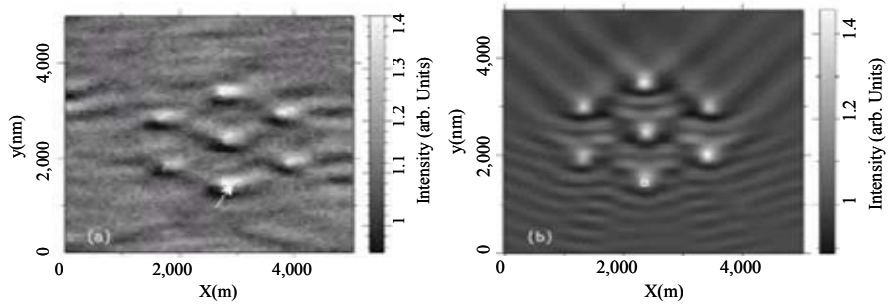


Figure 7.20. (a) PSTM image obtained in constant intensity mode with a fiber coated with 20nm gold layer; (b) Distribution of the magnetic field $|B|^2$; for $\lambda = 633\text{nm}$, in TE polarization

7.3.8. Apertureless microscope

The PSTM mode can be easily (!) simulated. Indeed, provided that the probe can be assumed to be passive, the formation of the images is a relatively straightforward process. For other types of microscopes, however, relatively few studies comparing experimental results and theoretical simulations have been conducted. We mention here the first works carried out at ESPCI (Paris), which provide a comparison between the intensity of the flux of the Poynting vector and the images obtained in apertureless mode.

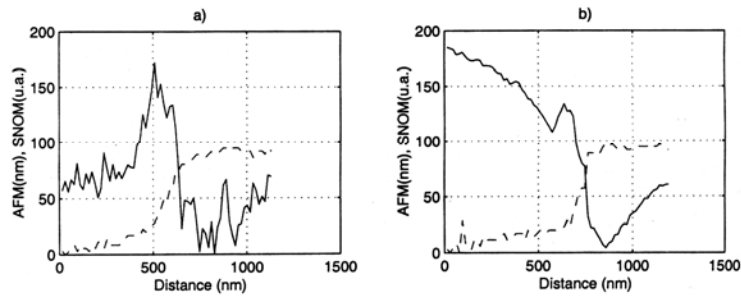


Figure 7.21. Optical images of a step obtained in apertureless mode, in *s* (a) and *p* (b) polarization respectively. The topography of the sample is represented by the dotted curves [GRE 99]

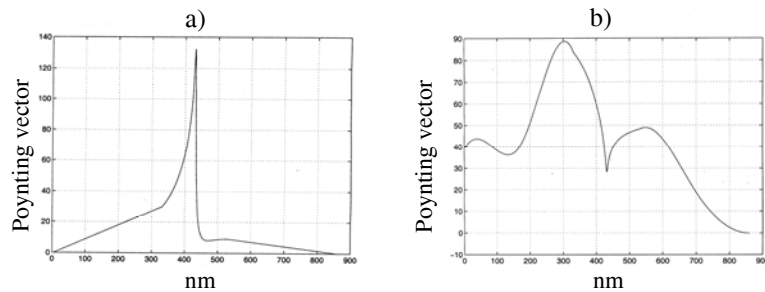


Figure 7.22. Calculation of the Poynting vector for a conductive half-plane whose edge is placed at the 430nm abscissa. The field is *s* (a) and *p* (b) polarized respectively [GRE 99]

More recent approaches take into account in the analysis of the signal the fact that the probe oscillates periodically and orthogonally to the surface of the sample. Using numerical methods allowing for interaction between the probe and the sample, images in agreement with experimental optical images can be retrieved [FIK 03].

7.3.9. Effect of coherence on the structure of near field images

As in classical microscopy, interference phenomena induced by the coherence of light waves may appear. The following figure shows the image obtained with a PSTM of a topographic step. The fringes that can be observed on this figure are caused by interferences between the transmitted evanescent field and the field scattered by the edge of the step, which propagates parallel to the surface from the edge.

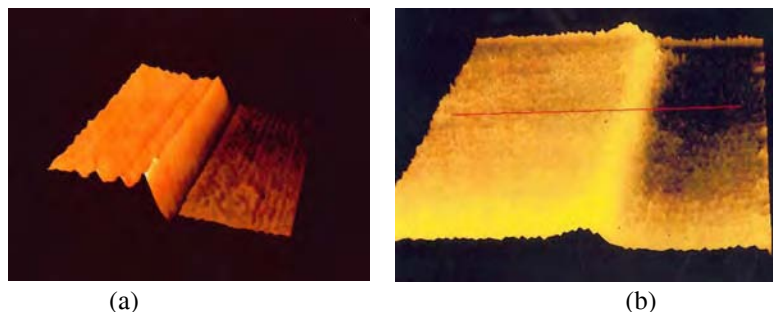


Figure 7.23. PSTM image of (a) coherent illumination, (b) incoherent illumination [FOR 01]

Spectrally incoherent illumination can be considered as being equivalent to illumination by an ensemble of coherent sources with different wavelengths. Therefore, the oscillations that were present under incoherent illumination now disappear under coherent illumination. This phenomenon can also be observed in classical microscopy. More surprisingly, it also occurs in illumination mode. Indeed, the signal detected by the probe may actually be the sum of different signals coming from different points of the surface and propagating along different paths. If the source is coherent enough, these signals may interfere. This phenomenon, first demonstrated by E. Betzig, is shown here in Figure 7.24.

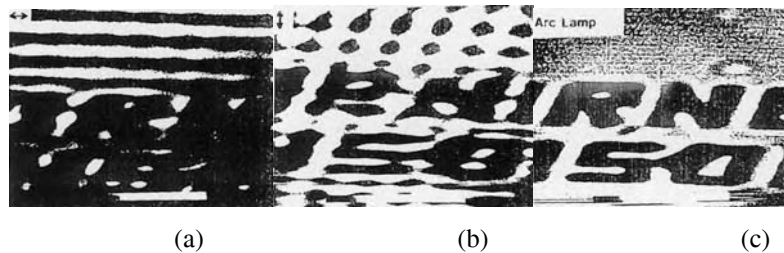


Figure 7.24. Effects of coherence and polarization on an SNOM image in transmission mode: (a) and (b) coherent illumination, with the electric field being horizontally and vertically polarized respectively; (c) incoherent illumination [BET 88]

The effect of coherence for the analysis of near field images is of importance, not only for simple structures of the kind described above, but for random surfaces as well. In practice, numerous surfaces actually exhibit a random structure with a very large roughness spectrum. In such cases, it is necessary, when analyzing optical near field measurements, to take into account the coherence phenomena occurring in near field [APO 03].

7.4. Characterization of integrated-optical components

Since near field microscopies offer a method for probing the electromagnetic field, they can be used for the characterization of different integrated-optical components, including such devices as [COU 01; FOR 01]:

- 1) optical waveguides,
- 2) photonic crystals,
- 3) microcavities,
- 4) periodical structures with certain specific properties.

This shows the implications that these characterization methods have in the field of nanotechnology.

7.4.1. Characterization of guided modes

In light of the importance of waveguides in integrated optics, their characterization has important implications. Guided modes are modes whose field is partly confined in the core of the waveguide (i.e. in the region with a higher refractive index) and partly extends outside the waveguide. When the probe is brought near the waveguide, it detects this evanescent part of the field of guided modes. Thus, by moving the probe along the waveguide, the field distribution of the mode(s) can be mapped. Methods for measuring losses or the effective refractive index of guided modes have been developed on this principle, and are now widely used [TSA 90; FOR 01]. Here we describe some of the results obtained at the University of Twente concerning the observation of phase singularities in waveguides [BAL 02]. A part of the laser beam is coupled to the waveguide, while the other part is used as a reference. The two intensities are then summed up using a coupler, which makes it possible to determine the relative phase and amplitude of the guided signal. The following figure shows the variations in amplitude and phase occurring for a single-mode excitation (TM_{00}).

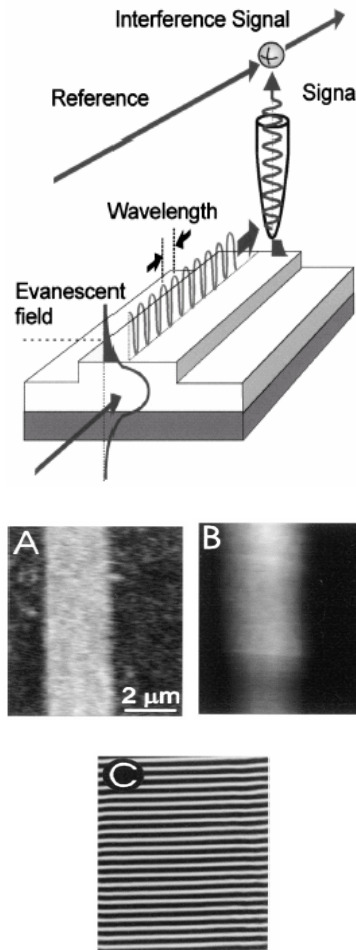


Figure 7.25. (a) Interferometric arrangement for the PSTM; (b) topography of the ruban waveguide, amplitude of TM_{00} mode excited in the waveguide and variation of the phase recorded along the waveguide. The effective index of the waveguide can be determined for this mode from the interfering value

As modal excitation ceases to be single-mode, phase singularities can be observed in near field. At the points where the amplitude of the field is null, the phase is no longer determined, and it may exhibit discontinuities, such as can be seen in the bordered areas in the next figure. These singularities are caused by the fact that the probe sums up the signals detected in near field. However, the summation of the TE and TM modes cannot take place in the waveguide, since these modes are of a different order.

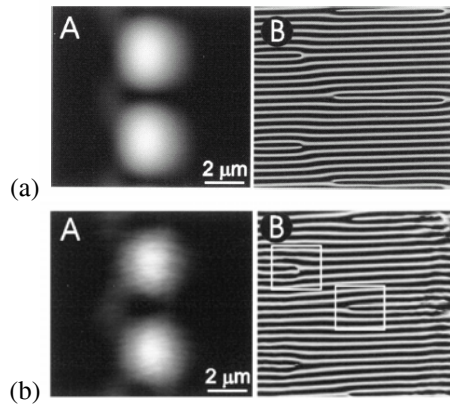


Figure 7.26. (a) Interferometric measurement of the amplitude (A) and phase variation (B) of the combination of excited TE_{00} , TE_{01} and TM_{00} modes; (b) corresponding numerical simulation

7.4.2. Photonic crystal waveguides

Waveguides realized from a photonic crystal by removing a row of holes should theoretically exhibit a higher degree of robustness in the presence of bends. These waveguides are generally characterized by means of the measurement of their transmission loss ratio [LOU 05b]. In this respect, near field microscopy provides a complementary method, which turns out to be perfectly well suited to the local characterization of these particular waveguides.

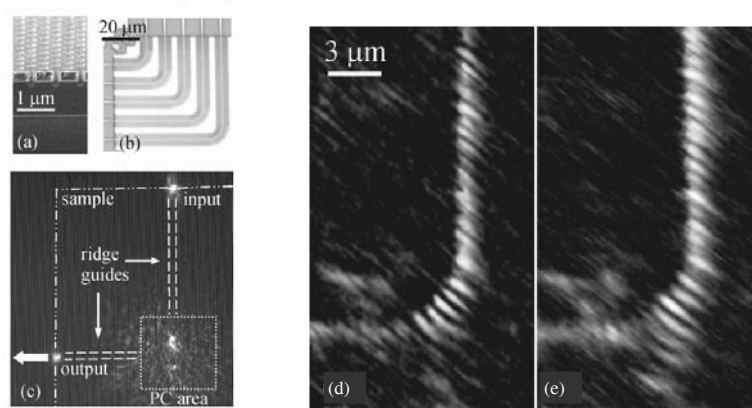


Figure 7.27. (a) SEM image of the structure; (b) overall view of the different waveguides; (c) image obtained using a CCD camera; (d) and (e) images obtained in near field, showing the localization of the losses and the guiding as a function of the wavelength [BOZ 02]

Interferences can be observed on the near field image of the waveguide. These interferences are due to the field reflected by the exit side of the waveguide, but also to the waveguide itself. This measurement technique can be used for drawing effective comparisons between the effects induced by a bend on the propagation of the mode at different wavelengths [BOZ 02]. Recent research has made it possible to determine the group velocity of modes propagating along a W3 waveguide [GER 05].

7.4.3. Excitation of cavity modes

The first cavity that we shall consider here is a hexagonal ring-shaped cavity, whose structure is schematically represented in the following figure. The excitation of the cavity modes is achieved through the external illumination of the structure. This causes excitation of the luminescence of both the structure and the guided mode.

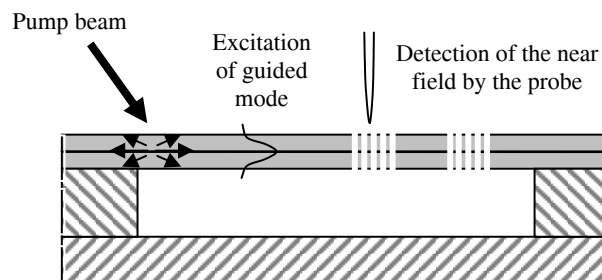


Figure 7.28. Schematic representation of the excitation of guided modes in a suspended membrane and detection of the near field. A is the InP membrane with InAsP quantum well, B is the InGaAs sacrifice layer, and C is the InP substrate

The probe, whose displacements are shear-force controlled, penetrates the holes with a 100nm depth. The membrane has a 200nm thickness and its extremity is located at the center of the waveguide. Three different regions can be distinguished on the optical image, represented here in Figure 7.29. In the A region, where the sacrifice layer is still present, index guiding does not occur, leading to the presence of detected losses.

The B region corresponds to the photonic crystal: it can be noted that, with the exception of the first series of holes, the signal is of the same order of magnitude as the noise occurring during the experiment. This results from the fact that the photonic crystal inhibits luminescence, thereby preventing the guided mode of the membrane from propagating in the crystal. Thus, as might be expected, only in the first row of holes do out-of-plane losses occur. The analysis of the optical image

compared to the topography of the sample clearly shows that if the period is not adequately chosen, then the photonic band gap effect of the crystal disappears (see the arrow and bordered area).

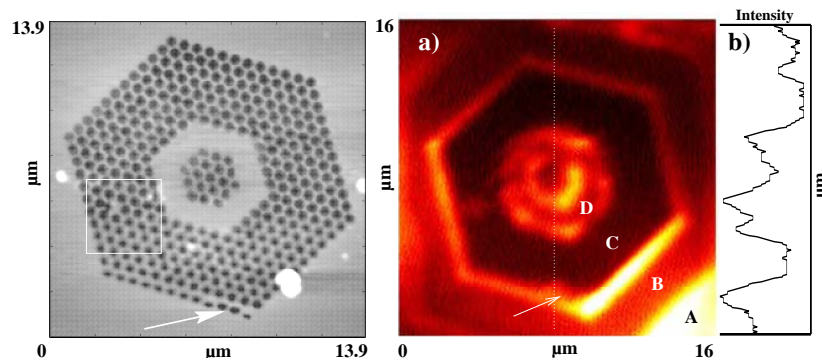


Figure 7.29. Topographical image and optical near field image of a cavity realized in a two-dimensional photonic crystal [GER 02]

In this example, cavity modes could not be detected, owing to the fact that the detection was conducted without spatial resolution. Single-mode as well as multimode cavity modes have recently been imaged and studied [KRA 04; GER 04; LOU 05].

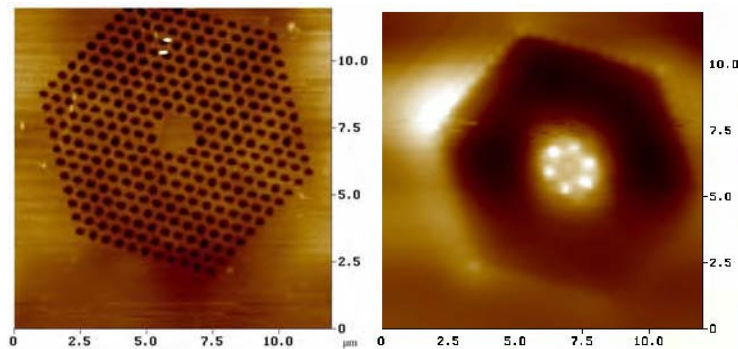


Figure 7.30. Topography of a hexagonal cavity and imaging of the modal structure of the cavity [GER 04]

Figure 7.30 shows a mode of an H2 cavity. Had the cavity exhibited a lack of symmetry, the modal structure would have presented an asymmetry as well. Only through such a near field observation can the cavity be locally controlled. This makes it possible to correlate the measurements thus realized and the quality factor of the cavity.

7.4.4. Localized generation of surface plasmons

The last section of this chapter is devoted to the study of locally excited plasmons. Two of the essential properties of surface plasmons are their strong confinement near the interface which has generated them, and the strong amplification of their evanescent field compared to the incident field [RAT 88]. These properties have been extensively exploited for the realization of sensors. Numerous studies have been conducted on plasmons and on their spontaneous generation [PIN 94]. We shall describe here an extremely simple example, that of a gold strip deposited on a dielectric substrate, as represented in Figure 7.31.

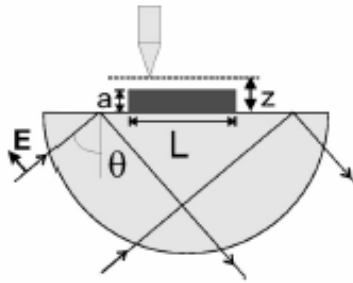


Figure 7.31. Schematic representation of the structure under consideration

The sample consists of 40 μm large gold strips deposited on a silicon substrate. The following curves present the variation of the intensity of the electric field, calculated at a 50nm distance from the surface of the sample. Two incident angles were selected, the first near the resonance of the plasmon of the metal/air interface, the second far from the resonance. The following figure presents the values of the electric field in the near field of the structure.

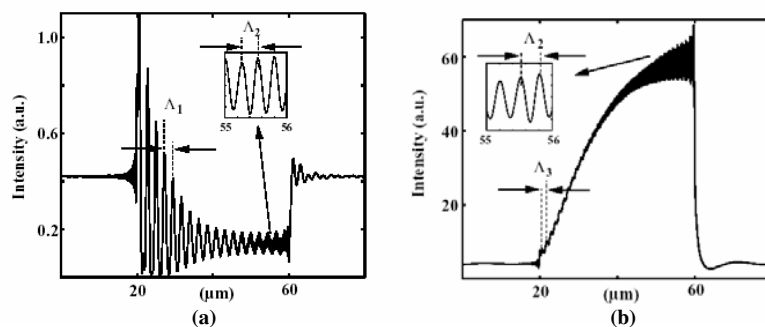


Figure 7.32. Intensity of the electric field at a 50nm distance from the gold strip: (a) outside the plasmon resonance associated with the air/gold interface, $\theta=60^\circ$; (b) near the resonance, $\theta=45.7^\circ$ [SAL 02]

It can be seen, by considering the field above the gold area, that this field is, on average, weaker than above the silicon substrate. This simply results from the fact that gold absorbs part of the light. Two series of exponentially decreasing oscillations can also be observed, starting from each edge of the strip. The period of these oscillations corresponds to the interfringe distance between the interferences created between the field transmitted through the metal (evanescent field) and the surface plasmon excited at each edge. Thus:

$$2\pi / \Lambda_{1,2} = (\omega / c)n \sin \theta \mp \text{Re}(k_{SP}^{am}) \quad (10)$$

It can be seen that the intensity of the field is multiplied more than a hundred times at the resonance. Of course, it can be noted that the oscillations with period Λ_1 disappear at the resonance, whereas those with period Λ_2 are still present. On the other hand, new oscillations with a Λ_3 period now appear from the left edge. These oscillations correspond to interferences occurring between the transmitted field and the metal/glass interface plasmon.

$$2\pi / \Lambda_3 = (\omega / c)n \sin \theta - \text{Re}(k_{SP}^{sm}) \quad (11)$$

These different interfringes, as well as the lateral attenuation, were experimentally measured in near field microscopy [SAL 02]. Further, such measurements can also enable the local determination of the dielectric constant of the metal.

The generation of plasmons can be due to either an edge effect or a periodical perturbation of a metallic film. Both of these effects are at work in the enhancement of the transmission through a silver film drilled with periodically distributed holes [EBB 98]. We shall concentrate instead on near field issues, and more specifically on the problem of determining the structure of the electromagnetic field inside the apertures and in their close vicinity. The field is calculated using the differential method. The following figure presents the distribution of the intensity of the electric field for different distances from the aperture.

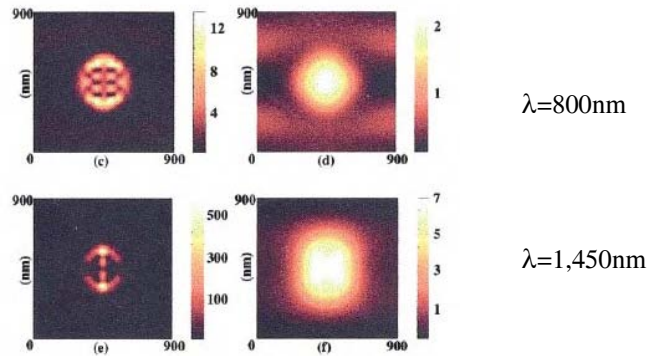


Figure 7.33. Distribution of the intensity of the transmitted field at two different wavelengths exhibiting field exaltations. The diameter d of the apertures and their period D are equal to 300nm and 900nm respectively. The field is calculated at a 15nm distance (c) and (e) and at a 100nm distance (d) and (f) from the surface respectively [SAL 01]

It can be noted that intensity is strongly amplified in the immediate vicinity of the apertures, this being due to the weight of the evanescent waves localized at the center of the apertures. Besides the exaltation of the intensity, which can reach several orders of magnitude in the immediate vicinity of the aperture, attention should be given to the particular structure of the lateral field distribution. This stems from the fact that excitation of plasmons can be partly induced by the periodical structuring of the metallic film. This phenomenon is described by the following equation:

$$k_{sp} = k_0 \sin \theta_0 \pm p \frac{2\pi}{D} u_x \pm q \frac{2\pi}{D} u_y \tag{12}$$

A schematic representation of this relation is given in the following figure, indicating the directions of propagation of the plasmons for the different values for p and q .

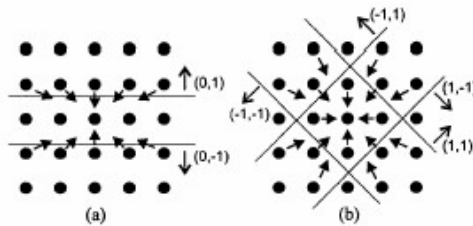


Figure 7.34. Description of plasmon excitation associated with the periodicity of the system of apertures, and inducing a structuring of the field in the apertures

This type of periodical structure has given rise to numerous publications, most of which have been of a theoretical nature [LAL 03; BAR 04]. Thus far, no measurement of the field in the apertures has been realized. It would be interesting to determine the conditions making the measurement of field distribution possible without perturbing it, or conversely the effect of a local perturbation on transmission in these structures.

7.5. Conclusion

In optics, but also in acoustics and hyperfrequency, the near field of an object contains both evanescent and propagative waves generated by this object. More precisely, the near field is the region where evanescent waves exert a strong influence. Conversely, at a great distance from the object, i.e. in far field, these waves play a negligible role.

The specific properties of the near field derive from those of the evanescent waves with which it is intimately associated. Thus, in near field, localization as well as amplification phenomena may for instance occur. Surface plasmons are an example of a phenomenon where amplification and local confining of the field occur simultaneously. Phenomena associated with properties of the far field, such as interference or coherence phenomena, are also to be found in near field.

In the field of nanotechnology, the development of optical nanodevices necessarily requires that control of the field distribution be achieved, both in the devices themselves and in their immediate vicinity. This is necessary not only for the realization of devices with certain specific properties (waveguides or loss-less cavities), but also for their characterization (localization of losses in order to control the design and fabrication processes). To this end, an exhaustive and complete analysis of the field must be undertaken, which can be complemented by its characterization in near field microscopy.

The sensitivity of certain structures to their near environment has been exploited for the realization of sensors and nanosensors. The confinement of the field for cavity modes or plasmons can be compared to resonance or modal excitation phenomena. Since modifying the environment of the device where these resonances take place causes a modification in its response, nanodevices can thus be created by actively modifying the near environment of such structures. This leads to the possibility of envisioning the realization of active near field functions.

7.6. References

- [ADA 81] Adams M. J.: *An introduction to optical waveguide*, New York, Wiley, 1981.
- [APO 03] Apostol A. *et al.*: “Coherence properties near interfaces of random media”, *Phys. Rev. E* 67, 055601, 2003.
- [BAL 00] Balistreri *et al.*: “Local observations of phase singularities in optical fields in waveguide structure” *PRL*, 18, 2, 294–297, 2000.
- [BAT 04] Barnes W. L. *et al.*: “Surface plasmon polaritons and their role in the enhanced transmission of light through periodic arrays of sub-wavelength holes in a metal film” *Phys. Rev. Lett.* 92, pp 107401, 2004.
- [BET 44] Bethe H. A.: “Theory of diffraction by small holes”, *Phys. Rev.*, 66–8, 163–182, 1944.
- [BET 88] Betzig E.: PhD Thesis, Cornell University, 1988.
- [BOR 59] Born M. and Wolf E.: *Principles of Optics*, Pergamon Press, London, 1959.
- [BOU 50] Bouwkamp C. J.: “On the diffraction of electromagnetic waves by small circular disks and holes”, *Philips Recs. Rep.*, 5, 401–22, 1950.
- [BOZ 02] Bozhevolnyi S. *et al.*: “Direct mapping of light propagation in photonic crystal waveguides”, *Optics Communications* 212, 51–55, 2002.
- [COU 01] Courjon D. and Bainier C.: “Le champ proche optique, théorie et applications” *Collection Technique et Scientifiques des Télécommunications*, Springer, Paris, 2001.
- [DEV 00] Devaud E. *et al.*: “Local detection of the optical magnetic field in the near zone of dielectric samples” *PR B* 62, 15, 2000.
- [EBB 98] Ebbesen T. W. *et al.*: “Extraordinary optical transmission through sub-wavelength hole arrays”, *Nature* 391, 667–69, 1998.
- [FIK 02] Fikri R. *et al.*: “Apertureless scanning near field optical microscopy: on the need of the probe vibration modelling”, *Optics Letters* Vol. 28, No 22, 2147–2149, 2003.
- [FOR 93] de Fornel F. *et al.* “First images obtained in the near infrared spectrum with the photon scanning tunneling microscope”, *Optics Comm.*, 102, 1–5, 1993.
- [FOR 01] de Fornel F.: *Evanescence Waves: From Newtonian Optics to Atomic Optics*, Springer Verlag GmbH (Heidelberg), in the Optical Sciences series, 2001.
- [GER 02] Gérard D. *et al.*: “Near field probing of active photonic-crystal structures” *Optics Letters*, 27, 3, 173, 2002.
- [GER 04] Gérard D.: “Etude en champ proche et en champ lointain de composants périodiquement nanostructurés: cristaux photoniques et tamis à photons”, Thesis, 2004.
- [GER 05] Gersen H. *et al.*: “Real-space observation of ultraslow light in photonic crystal waveguides”, *PRL*, 94, 073903, 2005.
- [GOU 05] Goumri-Said S., Salomon L, Dufour J.P., de Fornel F. and Zayats A.: “Numerical simulations of photon scanning tunneling microscopy: role of a probe tip geometry in image formation”, *Optics Comm.*, 244, 245–258, 2005.

- [GRE 99] Grésillon S.: “Microscopie optique en champs proche en transmission avec une sonde métallique: exaltation de champ et spectroscopie de nanoparticules”, Thesis, Paris VI, 1999.
- [KRA 04] Kramper P. *et al.*: “Near field visualization of light confinement in a photonic crystal microresonator”, *Opt. Lett.* 29, 174, 2004.
- [LAL 03] Lalanne P. *et al.*: “Perturbative approach for surface plasmon effects on flat interfaces periodically corrugated by subwavelength apertures”, *PRB*, 68, 125404, 2003
- [LEV 86] Leviatan Y.: “Study of near-zone fields of a small aperture”, *J. Appl. Phys.*, 60, 5, 1986
- [LOU 05a] Louvion N. *et al.*: “Local observation and spectroscopy of Optical Modes in Active Photonic Crystal Microcavity” 94, 113907, 2005.
- [LOU 05b] Lourtioz J.M., Benisty H., Berger V., Gérard J.M., Maystre D. and Chelnokov A. (2005), *Photonic Crystals: Towards Nanoscale Photonic Devices*, Springer, Berlin-Heidelberg-New York.
- [RAH 97] Rahmani A. *et al.*: “Field propagator of a dressed junction: fluorescence lifetime calculations in a confined geometry” *Phys. Rev. A*, 56, 3245–3254, 1997.
- [RAH 01] Rahmani A. *et al.*: “Environment-induced modification of spontaneous emission: Single-molecule near field probe” *Phys. Rev. A* 63, 23819-23830, 2001.
- [SAL 00] Salomon L. *et al.*: “Near field study of mesoscopic Au periodic samples. Effect of the polarisation and comparison between different imaging modes”, *PRB*, 6, 2000.
- [SAL 01] Salomon L. *et al.*: “Near field distribution of optical transmission of periodic subwavelength holes in a metal film”, *Phys. Rev. Lett.*, Vol. 86, no 6, 1110-1113, 2001.
- [SAL 02] Salomon L. *et al.*: “Local excitation of surface plasmon polaritons at discontinuities of a metal film: theoretical analysis and optical near field measurements”, *Phys. Rev. B*, 65, 2002.
- [SEL 13] Sélényi P.: “Sur l’existence et l’observation des ondes lumineuses inhomogènes”, *Comp. Rend.*, 157, 1408, 1913.

Chapter 8

Sub-Wavelength Optics: Towards Plasmonics

8.1. Technological context

Today's performances of optical devices are limited by the restricted framework of the underlying fundamental concepts. These concepts rely exclusively on the notion of radiative electromagnetic eigenmodes sustained by large scale dielectric structures. The mathematical description of these modes includes at least an exponential of imaginary argument to account for propagation over distances much longer than the incident wavelength. Practically, such standard waveguides are rectilinear and feature transverse sections of several square micrometers.

Recently, researches on optical waveguides addressed the question of keeping a reasonable transmission level through a constriction whose width is smaller than the incident wavelength. Up to now, two research areas arise as being pertinent for the purpose of miniaturizing optical connections, namely: photonic crystals research and interface polaritons research.

At visible frequencies, interface polaritons are easily obtained at metal-dielectric interfaces: one speaks then of surface plasmon polaritons (SPP). This chapter will ignore all aspects dealing with photonic crystals (which is covered by other authors in this book) in order to bring to the fore the potential of sub-wavelength plasmonics devices as compared to high refraction index devices.

Whichever road map is followed, miniaturizing optical connections raises fundamental physical questions. A first set of questions deals with the basic concepts of non-radiative photonic transport through solid state mesoscopic and nanoscopic structures, including the practical problems of injection and detection in sub-wavelength structures. Characterizing the optical functionalities of such devices requires a coherent point of view on the issues related to detecting optical fields with a sub-wavelength resolution. The next section will show that exciting surface plasmons featuring a magnetic dipolar moment is essential for this purpose.

8.2. Detecting optical fields at the sub-wavelength scale

8.2.1. Principle of sub-wavelength measurement

Optical measurements with a sub-wavelength resolution has been actively investigated since the 1980s by a generation of surface physicists who worked on the development of a new class of instruments known today as near-field optical microscopes. Various configurations of near-field optical microscopes have been developed around two generic experimental configurations: the *Scanning Near-Field Optical Microscope* (SNOM) and the *Photon Scanning Tunneling Microscope* (PSTM).

As introduced in the preceding chapter, the SNOM exploits the analogy to the electron *Scanning Tunneling Microscope* (STM): a nanometer size source of light scans the sample surface. According to the nature of the sample, the outgoing light is detected in transmission or in reflection. Although reflection SNOM devices use their tips both as local emitter and local probe, the discussion below will make clear that the SNOM is a fundamentally *illuminating* probe device.

The PSTM operates differently. The sample lies on a glass prism which makes it possible to shine light in total internal reflection. The nanometer sized tip scanning the surface then frustrates the total reflection. The PSTM probe tip is thus used as a detector of the optical field close to the surface. This is referred as the *collection* mode.

Both configurations mainly use tips obtained by pulling optical fibers which may eventually be coated with a metal. The structure of the metallization at the tip apex is not trivial. A simplifying assumption models this structure by a sub-wavelength aperture. During the 1990s, the development of near-field optical microscopy was hindered by the absence of a criterion defining rigorously this sub- λ nature. This lack of any reliable criterion led to controversies about the interpretation of near-field optical images [Hecht *et al.*, 1997].

In order to interpret the images obtained by one or other of the generic setups, we propose a practical point of view relying on the Heisenberg uncertainty principle,

which deals with the measurement in a volume δl^3 such that δl is of sub-wavelength (sub- λ) size.

By going through a sub- λ structure, the incident wave faces the consequence of the Heisenberg uncertainty principle ($i = x, y, z$):

$$\Delta x_i \Delta p_i \geq \frac{\hbar}{2} \quad (1)$$

For an electromagnetic wave, this leads to an uncertainty principle which, through the cyclic permutation of the indexes ($i, j = x, y, z$), binds the components of the electric E_i and magnetic H_j fields of the optical wave and the typical size δl (SI units) [Heisenberg, 1930]:

$$\Delta E_i \Delta H_j \geq \frac{\hbar}{2} \frac{c^2}{(\delta l)^4} \quad (2)$$

If $\delta l \leq 0.1 \mu\text{m}$, the right hand side of this formula becomes large (Figure 8.1). This uncertainty principle means that a simultaneous (in the sense of quantum theory, i.e. without any reciprocal influence) measurement of the electric field and of the magnetic field is not possible if the detection occurs in a volume δl^3 such that δl is sub- λ . Consequently, measuring the energy of an electromagnetic wave, the sum of the electric and magnetic contributions, also becomes uncertain (in the sense of quantum theory) in a sub- λ volume. Therefore, one cannot conceive any sub- λ measurement by a near-field optical microscope which could be interpreted like the far-field measurement of the reflected or the transmitted energy which occurs in a standard microscope.

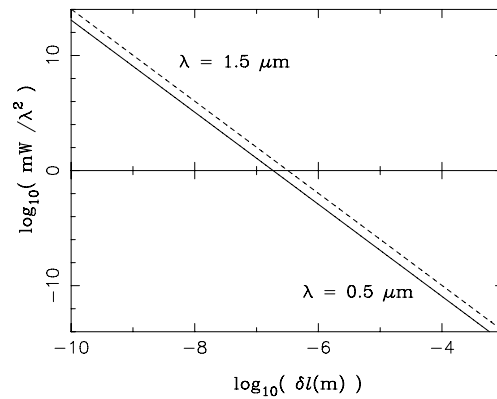


Figure 8.1: Evaluation of the right hand side of equation 2 for two typical wavelengths λ in vacuum

Moreover, the essential feature of any measuring instrument is to enable recording data about a physical system in such a way that these data are, to a reasonable degree of accuracy, still relevant to describe the system which is not interacting with the said measuring instrument. In the context of near-field optical microscopy, this feature means that the data recorded using the scanning local probe have a practical value if they still represent the physical system not interacting with the local probe, i.e. *in the absence of any tip*.

The practical point of view that we propose *defines* the sub- λ resolution by the detection of the spatial distribution of intensity either of the electric field or (exclusive) of the magnetic field close to the sample surface, as it exists when no tip is present. Justifying this criterion to the case of SNOM setups is somewhat less intuitive. Indeed, since the local probe is then the source of light, how can the field be identified in the absence of the tip which the practical point of view aims at detecting? To answer this question, one needs to remember that the field in the absence of external excitation is the fundamental state of the electromagnetic field. This fundamental state is described by the electromagnetic (*Local Density Of States*, LDOS) at the frequency of the laser. The practical point of view thus leads to consider that the criterion of sub-wavelength resolution is met by SNOM configurations when a signal proportional to the electromagnetic LDOS is detected.

Practically, we suggest that the sub- λ resolution is achieved if [Dereux *et al.*, 2000], [Dereux *et al.*, 2001]:

- *in collection mode*, the experimental images agree with the theoretical distribution of the electric *or* the magnetic field scattered by the sample surface, as computed without including any tip;
- *in illumination mode*, the experimental images agree with the theoretical distribution of the electromagnetic *Local Density of States* (LDOS) at optical frequencies, as computed without including any tip.

This criterion makes it possible to determine rigorously not only the quality of the probe tip, but also the quality of the whole experimental setup. It requires the capacity to compute the electromagnetic field and the electromagnetic LDOS in the near-field zone. The scattering theory explained in the next chapter makes it possible to compute both within a single framework.

8.2.2. Scattering theory of electromagnetic waves

From the mathematical point of view, scattering theory casts the most general analytical solution of the inhomogeneous wave equation as an integral equation where

the kernel is a Green's function [Newton, 1966]. Several variants of electromagnetic scattering theory were applied successfully to the modelization of near-field optical phenomena. Although Green's function may be expanded in Fourier or multipoles series, most variants preferred a discretization in the direct space since near-field optical phenomena occur on a sub-wavelength scale. Here, we restrict the presentation to the steps needed to establish the link with the measured quantities discussed in the next sections. For more details, the reader may consult [Girard & Dereux, 1996, Dereux *et al.*, 2000] and the references therein.

With the $\exp(-i\omega t)$ time dependence, the Maxwell's equations in the absence of any external source lead to the following vector wave equation for the electric field $\mathbf{E}(\mathbf{r})$ (SI units, c is the speed of light in vacuum):

$$-\nabla \times \nabla \times \mathbf{E}(\mathbf{r}) + \frac{\omega^2}{c^2} \varepsilon(\mathbf{r}) \mathbf{E}(\mathbf{r}) = 0 \quad (3)$$

may be cast as:

$$-\nabla \times \nabla \times \mathbf{E}(\mathbf{r}) + q^2 \mathbf{E}(\mathbf{r}) = V(\mathbf{r}) \mathbf{E}(\mathbf{r}) \quad (4)$$

with:

$$q^2 = \frac{\omega^2}{c^2} \varepsilon_{ref}. \quad (5)$$

Any complicated behavior due to the anisotropy or to the low-symmetry of the geometrical shape of the original dielectric tensor profile $\varepsilon(\mathbf{r})$ is described as a difference relatively to the reference system ε_{ref} (I is the unit dyadic):

$$V(\mathbf{r}) = \frac{\omega^2}{c^2} I (\varepsilon_{ref} - \varepsilon(\mathbf{r})). \quad (6)$$

Through the dielectric function $\varepsilon(\mathbf{r})$ (depending also on the pulsation ω), this equation includes a macroscopic description of the linear response of matter to electromagnetic excitations. This dielectric function (equal to the square of the complex index of refraction) is built from the response of a large number of atoms and is thus valid if the size of the scatterers is sufficiently larger than the wavelength. At visible frequencies, it is generally accepted that $\varepsilon(\mathbf{r})$ is valid to model scatterers typically larger than 10 nm.

The solution of (4) is obtained from the implicit Lippmann-Schwinger equation:

$$\mathbf{E}(\mathbf{r}) = \mathbf{E}_o(\mathbf{r}) + \int_D d\mathbf{r}' G_o(\mathbf{r}, \mathbf{r}') V(\mathbf{r}') \mathbf{E}(\mathbf{r}'). \quad (7)$$

In scattering theory, the first term $\mathbf{E}_o(\mathbf{r})$ is referred to as the incident field while the second term is called the scattered field obtained from the integration over the domain D where $V(\mathbf{r}')$ is non-zero.

To solve the Lippmann–Schwinger equation, we need to know the analytical solution $\mathbf{E}_o(\mathbf{r})$ satisfying:

$$-\nabla \times \nabla \times \mathbf{E}_o(\mathbf{r}) + q^2 \mathbf{E}_o(\mathbf{r}) = 0 \quad (8)$$

and the associated Green's dyadic defined by:

$$-\nabla \times \nabla \times G_o(\mathbf{r}, \mathbf{r}') + q^2 G_o(\mathbf{r}, \mathbf{r}') = I \delta(\mathbf{r} - \mathbf{r}'). \quad (9)$$

The reference structure ε_{ref} is usually a homogeneous background material or a semi-infinite surface system. For homogeneous media, the analytical form of $G_o(\mathbf{r}, \mathbf{r}')$ is known from ancient works [Morse & Feshbach, 1953, Levine & Schwinger, 1950] to be:

$$G_o(\mathbf{r}, \mathbf{r}') = \left[I - \frac{1}{q^2} \nabla \nabla \right] g(\mathbf{r}, \mathbf{r}') \quad (10)$$

where $g(\mathbf{r}, \mathbf{r}')$ is the Green function associated to a scalar Helmholtz equation, i.e. a spherical wave emitted at \mathbf{r}' :

$$g(\mathbf{r}, \mathbf{r}') = -\frac{\exp(iq |\mathbf{r} - \mathbf{r}'|)}{4\pi |\mathbf{r} - \mathbf{r}'|}. \quad (11)$$

For a surface system, the expression of the propagator is somewhat more elaborated [Agarwal, 1975, Metiu, 1984, Girard & Bouju, 1992].

8.2.3. Electromagnetic LDOS

The electromagnetic *Local Density of States* (LDOS) of vacuum $\rho_o(\mathbf{r}, \omega)$ is well-known as the factor multiplying the Bose–Einstein distribution in the Planck's law describing the black–body radiation (k_B is the Boltzmann constant and \hbar is the Planck constant):

$$U(\omega) d\omega = \rho_o(\mathbf{r}, \omega) \frac{\hbar\omega}{e^{\frac{\hbar\omega}{k_B T}} - 1} d\omega \quad (12)$$

It is also underlying the *Fermi Golden Rule* which casts the decay rate in the problem of coupling of a discrete system with a continuum. Indeed, from (\mathbf{p} being the dipolar moment operator while $|i\rangle$ and $|f\rangle$ respectively stand for the initial and final states of the discrete system):

$$\Gamma = \frac{2\pi}{\hbar} |\langle f | \mathbf{p} \cdot \mathbf{E}(\mathbf{r}) | i \rangle|^2 \delta(\omega = \omega_f - \omega_i) \quad (13)$$

one can prove that:

$$\Gamma = \frac{2\pi}{\hbar} |\langle f | \mathbf{p} | i \rangle|^2 \rho_o(\mathbf{r}, \omega). \quad (14)$$

Applying the standard calculus of distributions makes it possible to show that the factor $\rho_o(\mathbf{r}, \omega)$ is deduced from the electric Green dyadic G_o of vacuum ($\epsilon_{ref} = 1$):

$$\rho_o(\mathbf{r}, \omega) = -\frac{1}{\pi} \Im \text{Trace } G_o(\mathbf{r}, \mathbf{r}', \omega) = \sum_{j=x,y,z} \rho_{o;j}(\mathbf{r}, \omega) = \frac{1}{\pi^2} \frac{\omega^2}{c^3} \quad (15)$$

where, to account for the vector nature of electromagnetic fields, we have defined the “partial” LDOS by:

$$\rho_{o;j}(\mathbf{r}, \omega) = -\frac{1}{\pi} \Im G_{o;jj}(\mathbf{r}, \mathbf{r}, \omega) \quad (16)$$

Close to sub- λ structures deposited on surfaces, this LDOS may vary from place to place and may depend on the polarization of the exciting dipole. In the case of a system described by its dielectric function $\epsilon(\mathbf{r})$, the LDOS is related to (but not equal to) the dipolar point source corresponding to the Dirac δ function which arises in the wave equation defining the Green dyadic of the system:

$$-\nabla \times \nabla \times G(\mathbf{r}, \mathbf{r}', \omega) + \frac{\omega^2}{c} \epsilon(\mathbf{r}, \omega) G(\mathbf{r}, \mathbf{r}', \omega) = I \delta(\mathbf{r} - \mathbf{r}') \quad (17)$$

The Green dyadic $G(\mathbf{r}, \mathbf{r}', \omega)$ of the actual system $\epsilon(\mathbf{r})$ may be deduced numerically from the one of a reference system after casting a Dyson equation:

$$G(\mathbf{r}, \mathbf{r}') = G_o(\mathbf{r}, \mathbf{r}') + \int_V G_o(\mathbf{r}, \mathbf{r}'') V(\mathbf{r}'') G(\mathbf{r}'', \mathbf{r}') d\mathbf{r}'' \quad (18)$$

Let us note that, at least in principle, the Green dyadic of the reference system may be computed using a similar Dyson equation on the basis of the knowledge of the Green dyadic pertaining to vacuum.

The LDOS is then deduced from G :

$$\rho(\mathbf{r}, \omega) = -\frac{1}{\pi} \Im \text{Trace } G(\mathbf{r}, \mathbf{r}', \omega) = \sum_{j=x,y,z} \rho_j(\mathbf{r}, \omega) \quad (19)$$

where, again, we have to define the “partial” LDOS by:

$$\rho_j(\mathbf{r}, \omega) = -\frac{1}{\pi} \Im G_{jj}(\mathbf{r}, \mathbf{r}, \omega) \quad (20)$$

Through the unit dyadic I , each partial LDOS is related to a given orientation x, y , or z of the point-like source. The above summary aims at pointing out that, to detect a signal proportional to the LDOS, the adopted point of view aims at finding the experimental conditions such that, *in practice*, one can consider the probe tip as a point-like dipole oscillating at the angular frequency ω .

8.2.4. PSTM detection of the electric or magnetic components of optical waves

In the context of the interpretation of PSTM images, the tip design is of primary importance. It turned out that dielectric tips obtained by pulling optical fibers provide a signal proportional to the electric field associated to the optical wave [Weeber *et al.*, 1996]. These tips coated with a thin film of gold (10 nm to 50 nm) provide a signal proportional to the magnetic field associated to the optical wave [Devaux *et al.*, 2000]. Theoretical studies have confirmed that the observed signal is indeed proportional to the distribution of the optical magnetic field such as found by solving Maxwell equations.

The experiments reproduced the phenomenon of detection of the magnetic component of the optical wave at several incident wavelengths. However, to observe this phenomenon at a given wavelength, the thickness of the gold coating surrounding the dielectric core of the tip has to be adjusted precisely in order to excite a circular symmetry plasmon in the said coating.

Figures 8.2, 8.3 and 8.4 illustrate the detection of the optical magnetic field close to nanostructures observed by PSTM. Figure 8.2 shows an AFM image of the topography of the reference nanostructure. Figure 8.3 displays the theoretical distributions of the intensities of the electric (a) and magnetic (b) fields. For this specific sample, the distributions keep the same features if $\lambda = 543$ nm. The calculations assume that the nanostructures are deposited on a perfectly plane surface. This leads to strong interferences in the vicinity of the pads. In the experiments, realistic surfaces downgrade these interferences into a speckle, so that the comparison between theory and experiment must be limited to the contrast on top of each pad.

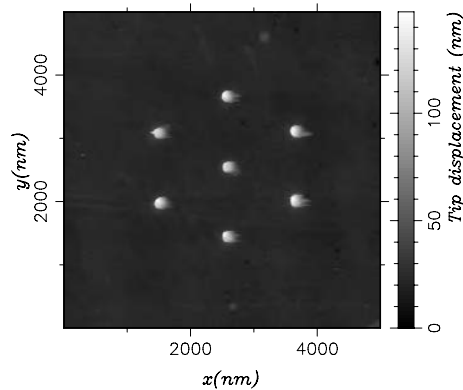


Figure 8.2: AFM image of the topography of the reference nanostructure: seven gold glass pads ($130 \text{ nm} \times 130 \text{ nm} \times 100 \text{ nm}$) are deposited on a plane surface of glass

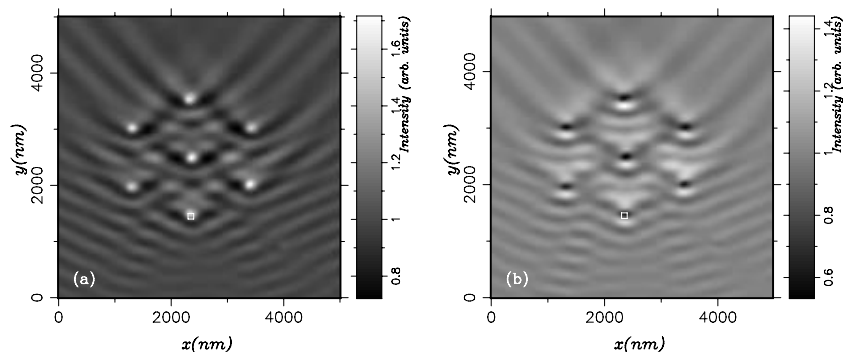


Figure 8.3: Theoretical distributions (angle of incidence = 60 degrees, TM polarization, $\lambda = 633$ nm) of the intensity of the electric (a) and magnetic (b) fields scattered in the near-field zone close to the surface of the sample of Figure 8.2

Figure 8.4 gathers PSTM images recorded above the sample of Figure 8.2 using optical fiber tips coated with different thicknesses d of gold. In Figure 8.4(a) and (c), the thicknesses have been selected in order to excite a circular symmetry plasmon. The images (a) and (c) agree with the distribution of the optical magnetic field (Figure 8.3(b)) while the images (b) and (d) agree with the distribution of the electric field (Figure 8.3(a)). At both wavelengths $\lambda = 543$ nm and $\lambda = 633$ nm, dielectric (uncoated) tips provide images similar to (b) and (d).

Using another incident polarization or observing a different kind of sample, such as gold pads sustaining plasmon resonances, leads to similar conclusions.

The unprecedented agreement of experimental PSTM results with the relevant theoretical distributions validates the practical point of view proposed in section 8.2 for collection mode near-field optical microscopes. In this context, exciting a circular symmetry plasmon in the probe tip turns out to be of great importance in order to establish the coherence of the proposed point of view.

8.2.5. SNOM detection of the electromagnetic LDOS

The experimental test of the hypothesis of detection of the electromagnetic LDOS by SNOM configurations makes it necessary to realize specific nanostructures. Numerical simulations [Colas des Francs *et al.*, 2001a, Colas des Francs *et al.*, 2001b] of the spatial distribution of the variation of the LDOS $\Delta\rho_x(\mathbf{r}, \omega)$ and $\Delta\rho_y(\mathbf{r}, \omega)$ relatively to the constant value in vacuum (see Figure 8.5(b) and (c)) have established that the “stadium” geometry (Figure 8.5(a)) makes it possible to easily study the effects related both to the polarization and to the sub- λ tailoring of the LDOS. Inside the

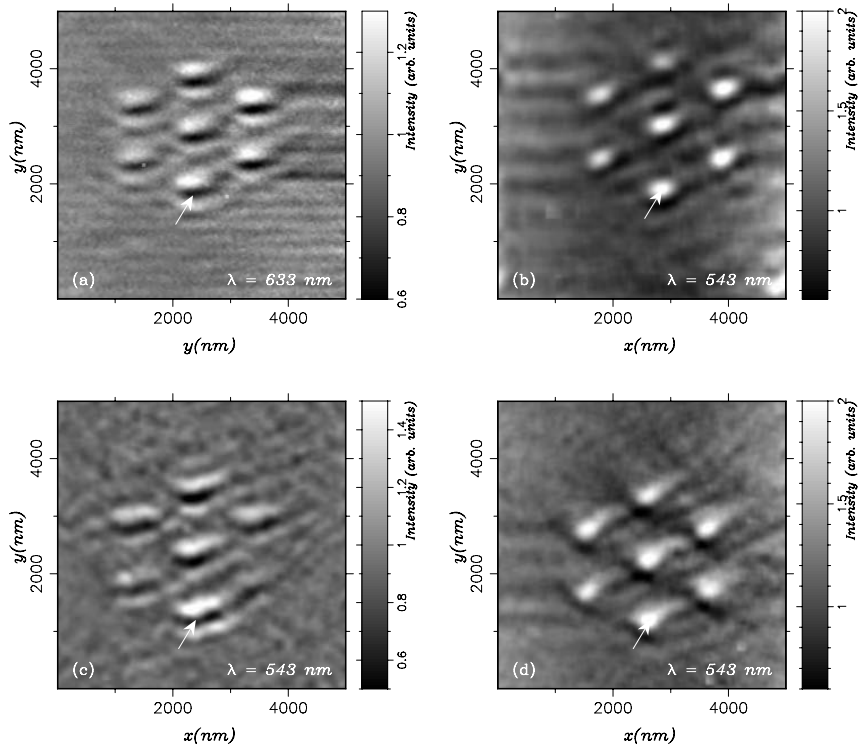


Figure 8.4: PSTM images (TM polarization, angle of incidence = 60 degrees): (a) $d = 20$ nm, $\lambda = 633$ nm; (b) $d = 20$ nm, $\lambda = 543$ nm; (c) $d = 30$ nm, $\lambda = 543$ nm; (d) $d = 35$ nm, $\lambda = 543$ nm

stadium, $\Delta\rho_x(\mathbf{r}, \omega)$ displays a pattern of concentric replica of the stadium shape, while $\Delta\rho_y(\mathbf{r}, \omega)$ features two “focal” zones.

The experiments (Figure 8.6) lead to the following conclusions about the necessary conditions to detect the LDOS [Chicanne *et al.*, 2002]:

- including a device to detect the scattered light at angles larger than the critical angle for total reflexion in the substrate;
- using a specific tip whose emission features can be considered as a point-like dipole. Bare (uncoated) optical fiber tips turned out to be inefficient for this purpose. The same optical fiber tip coated with gold provide a signal proportional to the LDOS. Contrary to an assumption commonly spread in the literature, it was not found necessary to form a small hole in the coating at the apex of the tip.

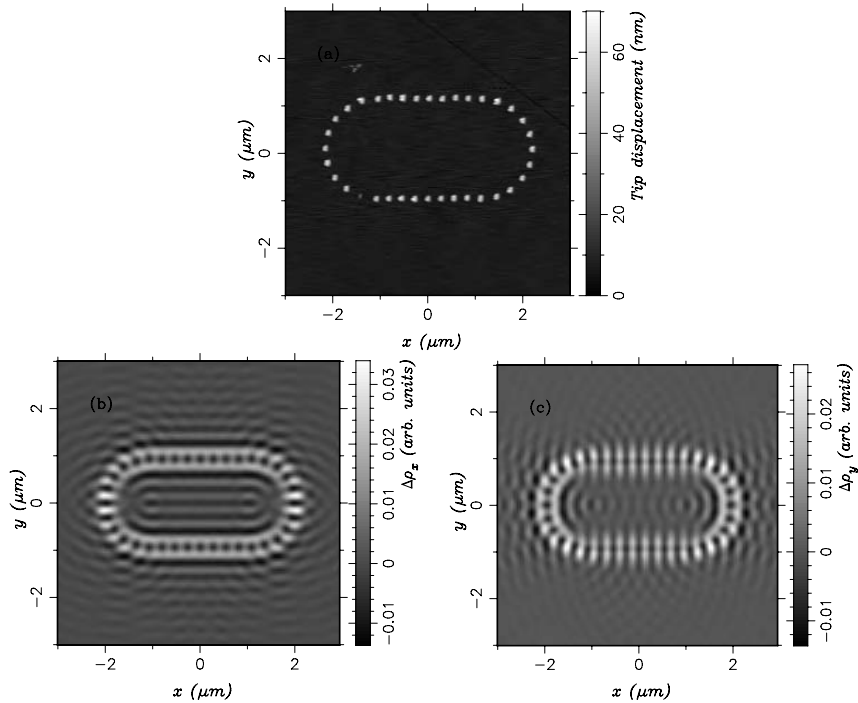


Figure 8.5: (a) AFM images of the reference sample. Gold particles ($100 \text{ Nm} \times 100 \text{ nm} \times 50 \text{ nm}$) are deposited on a flat surface of glass. Relatively to the constant value of vacuum, theoretical distributions of partial LDOS changes close to the sample (height of calculation plane: $z = 160 \text{ nm}$ above the substrate): (b) $\Delta\rho_x(\mathbf{r}, \omega)$, (c) $\Delta\rho_y(\mathbf{r}, \omega)$

The agreement between the experimental results of Figure 8.5 with the theoretical distributions (Figure 8.4(a) and (b)) is unprecedented in the context of SNOM research and confirms the possibility to detect a signal proportional to the electromagnetic LDOS. The practical point of view suggested in section 8.2 is thus also validated for illumination mode near-field optical microscopes [Colas des Francs *et al.*, 2002], [Dereux *et al.*, 2003].

8.3. Localized plasmons

This section provides various illustrations of the observation of plasmonic phenomena at the sub-wavelength scale by operating a PSTM equipped with probe tips detecting the intensity of the electric field.

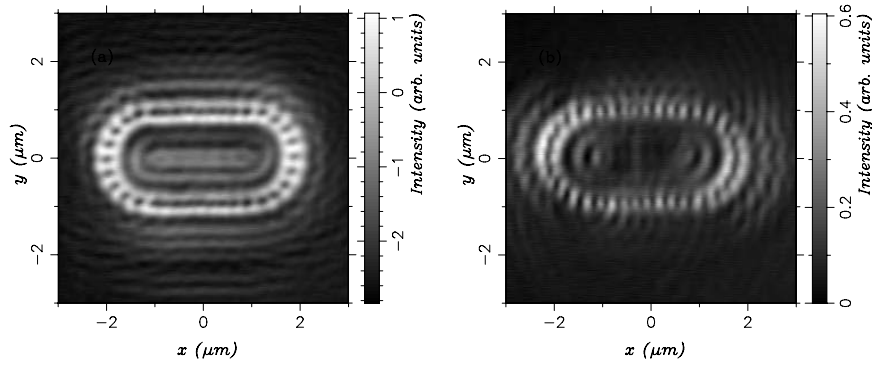


Figure 8.6: SNOM images recorded above the sample of Figure 8.4(a) for two polarization states giving rise to an effective dipole oriented along x (a) and y (b) at the tip apex

8.3.1. Squeezing of the near-field by localized plasmons coupling

Metal nanostructures were fabricated on glass surfaces. Very sensitive measurements were realized with a PSTM operated at constant height above single gold particles ($100 \text{ nm} \times 10 \text{ nm} \times 40 \text{ nm}$) (Figure 8.7) [Krenn *et al.*, 1999b]. In the computation (Figure 8.7(a)), such a particle is centered at the origin of the coordinate system while it is slightly translated to the right in the experimental image (Figure 8.7(b)). The agreement between the patterns of the calculated and the experimental images is excellent. Since the simulation has not included the tip, the experimental image exhibits a broader and less contrasted pattern. The simulation successfully recovers the inter-

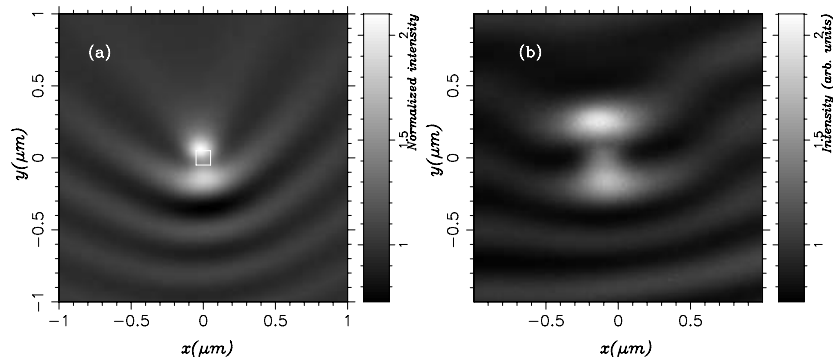


Figure 8.7: At 40 nm above a gold particle ($100 \times 100 \times 40 \text{ nm}^3$) deposited on a ITO glass substrate: theoretical distribution of the electric associated to the optical near-field (a) and PSTM image (b)

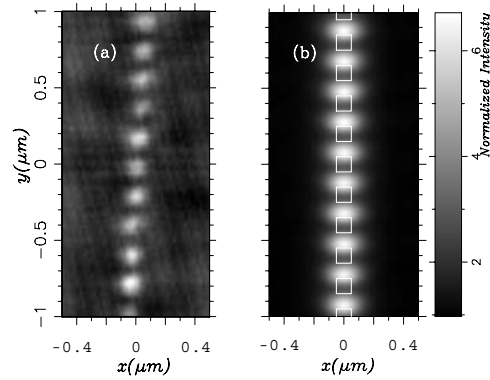


Figure 8.8: Constant height PSTM image PSTM (a) recorded above a section of a chain made of 10,000 gold particles deposited on ITO glass substrate compared to a numerical simulation (b) taking into account only a few tens of particles

ference between the incident surface optical wave and the wave scattered by the gold particle. This confirms the relatively passive role of the probe tips even when scanning samples sustaining plasmons resonances.

In order to test the hypothesis of non-radiative coupling, small gold particles ($100 \text{ nm} \times 100 \text{ nm} \times 40 \text{ nm}$) were aligned in a row with a spacing of 100 nm. The experimental result makes it possible to observe that the plasmon coupling between the particles confines the electromagnetic field within the width of the chain (Figure 8.8(a)) [Krenn *et al.*, 1999b]. Indeed, the tip has integrated the detection of the optical field over its own volume at least (as in Figure 8.7). Consequently, the field distribution in the absence of the tip is probably narrower.

The squeezing effect is related to the mutual coupling of the localized plasmons of each individual nanoparticle setting a hybrid plasmon mode. The model calculation (Figure 8.8(b)) confirms that the spots are narrower than in the case of the single gold particle and that they are not centered on top of the particles. The effect observed in Figure 8.8(a) is thus the plasmon coupling and not the underlying topography. However, the calculated squeezing is not so narrow as in the experiment since the modeling involved only 30 particles instead of the 10,000 present in the experiment. The squeezing probably increases as the chain length grows.

8.3.2. Controlling the coupling of localized plasmons

Subsequently, it was possible to control the plasmon coupling between two gold nanostructures of different shapes [Krenn *et al.*, 1999a]. In the sample of Figure 8.9,

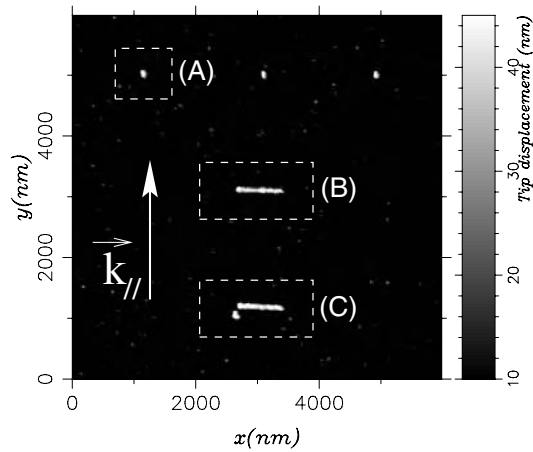


Figure 8.9: AFM image of the test sample used to demonstrate the control of plasmon coupling between nanostructures. The white arrow shows the direction of propagation of the surface wave obtained by total internal reflexion

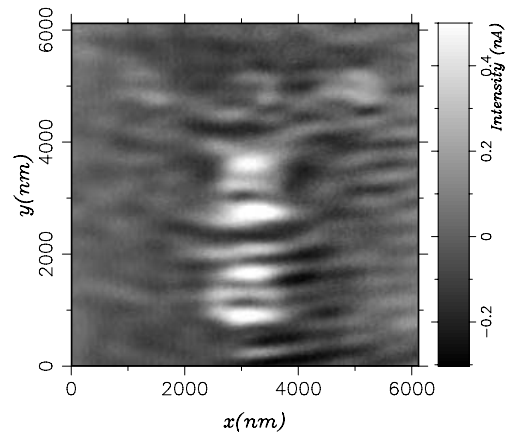


Figure 8.10: PSTM image above the sample of Figure 8.9 obtained by shining a TM polarized laser beam TM (wavelength 633 nm). The angle of incidence is 60° . At this wavelength, the particles and the nanowires are not resonant

all particles have a volume $120 \times 60 \times 40 \text{ nm}^3$ and all nanowires have a volume of $660 \times 60 \times 40 \text{ nm}^3$. We demonstrated that it is possible to switch on (Figure 8.11) or off (Figure 8.10) the excitation of the resonant mode of a gold nanowire by changing

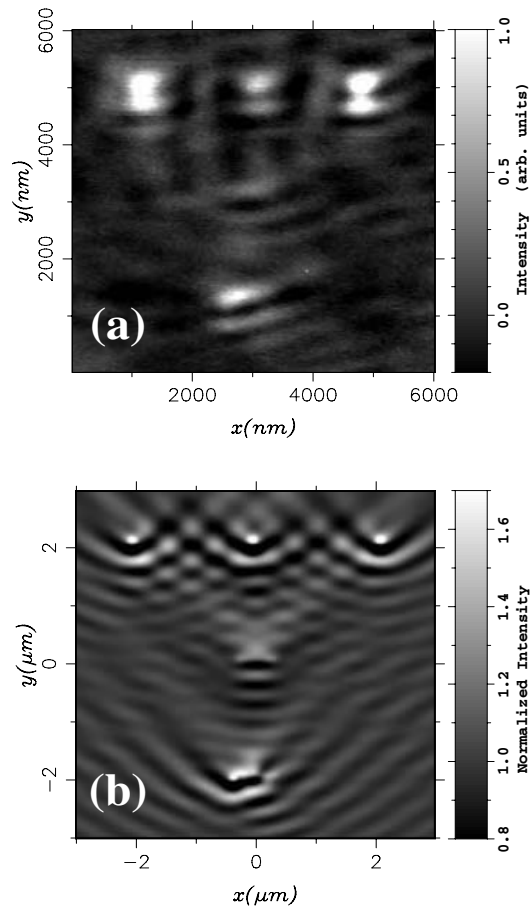


Figure 8.11: (a) PSTM image of the sample of Figure 8.9 obtained by shining a TM polarized laser beam (wavelength 740 nm). (b) Theoretical distribution of the intensity of the electric field associated to the optical near-field (normalized relatively to the intensity of the incident field, same illumination conditions as in the experiment)

the position of a gold particle located at a sub-wavelength distance of the wire. In Figure 8.10, the isolated particles (zone A) do not give rise to any significant signal while the nanowires produce a signal proportional to their volumes. This explains the minor difference between the zone B (isolated nanowire) and the zone C (nanowire close to a particle).

In Figure 8.11(a), the isolated particles (zone A) are excited resonantly while the nanowire in zone B is not because of a selection rule involving the incident polarization.

However, the nanowire in zone C is excited because it lies close to a resonant gold nanoparticle. This resonant nanoparticle scatters all kinds of possible polarizations, among which the polarization leading to the resonant excitation of the nanowire C. Let us note that, to design the sample which made this demonstration possible, the numerical simulations (Figure 8.11(b)) were realized *before* the experiment.

8.4. Sub- λ optical devices

8.4.1. Coupling in

An efficient (i.e. minimizing losses) coupling of light into a sub- λ optical device is a difficult problem. We developed successfully an original injection technique exploiting the Goos-Hänchen effect (Figure 8.12). We can therefore deal with the transition of optical signals coming out of macroscopic optical devices (lenses, etc.) towards nanostructures. Resulting from a nanofabrication process, a sub- λ devices lying on the surface of a glass substrate (dielectric function ϵ_1) is illuminated by a Gaussian beam reflected at the interface between the substrate and the external medium (air, dielectric function ϵ_3). The PSTM probe tip detects the optical near-field in an observation plane parallel to the surface of the substrate.

8.4.2. Sub- λ waveguides

The coupling technique of Figure 8.12 was tested using a sample obtained by electron beam lithography: on a plane surface of BK7 glass lies a 200 nm wide, 150 nm high and 40 μm long TiO_2 sub- λ waveguide [Quidant *et al.*, 2001, Weeber *et al.*, 2000].

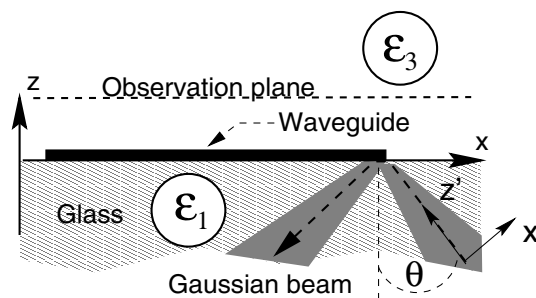


Figure 8.12: Geometry of the technique used to couple an incident field to a sub- λ device. In the example of the figure, the device is a sub- λ waveguide

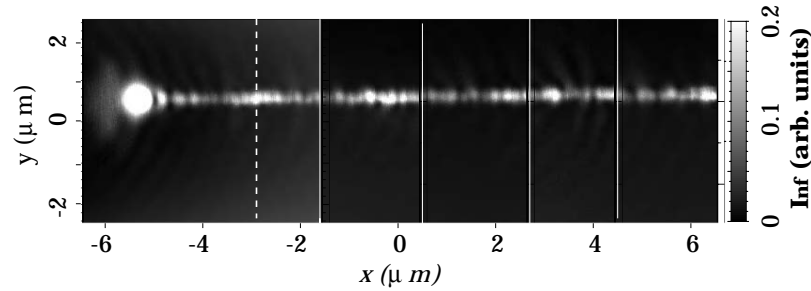


Figure 8.13: Assembling of five $5 \mu\text{m} \times 5 \mu\text{m}$ PSTM images recorded above the last quarter of a TiO_2 sub- λ waveguide excited using the technique of Figure 8.12. The vertical lines locate the boundaries of the superimposed images. The leftmost image, where a bright spot shows up (here the intensity has been saturated), corresponds to the area at the exit of the sub- λ waveguide

The wavelength in vacuum of the incident light being fixed to 633 nm, the coupling into the guided is observed with the PSTM (Figure 8.13). The sub- λ waveguide sustains a mode featuring a very narrow spatial width ($\simeq 300 \text{ nm}$). A bright spot shows up at the exit end of the guide. This experiment confirms not only the efficiency of the injection method, but also the ability of the PSTM to map, in direct space, the optical phenomena associated to sub- λ waveguides, thereby demonstrating the pertinence of performing a measurement, *in the near-field zone at the exit of the device*, in a sub- λ volume (in this case, the PSTM tip), of a signal not proportional to the Poynting vector, but proportional to the intensity of the optical electric field.

8.4.3. Towards plasmonics: plasmons on metal stripes

Another coupling technique has been tested on a silver sample deposited on glass, also designed by electron beam lithography (Figure 8.14). Several stripes of various width are connected to a large $250 \times 250 \mu\text{m}^2$ thin film. The thickness (60 nm) of this area makes it possible to launch a surface plasmon by total internal reflection through the glass substrate. The PSTM maps in direct space the coupling of plasmons launched on the large square area to the finite widths stripes [Weeber *et al.*, 2001].

Figure 8.15 confirms that only surface plasmons play a role in this experiment. The asymmetrical shape of the incident spot proves that surface plasmons are launched from the right to the left. When the incident spot is aligned along the axis of the stripe, a smaller spot shows up at the exit end of the stripe (Figure 8.15(a)). If the incident spot is misaligned, the coupling is inhibited and the glass surface acts as a barrier (Figure 8.15(b)).

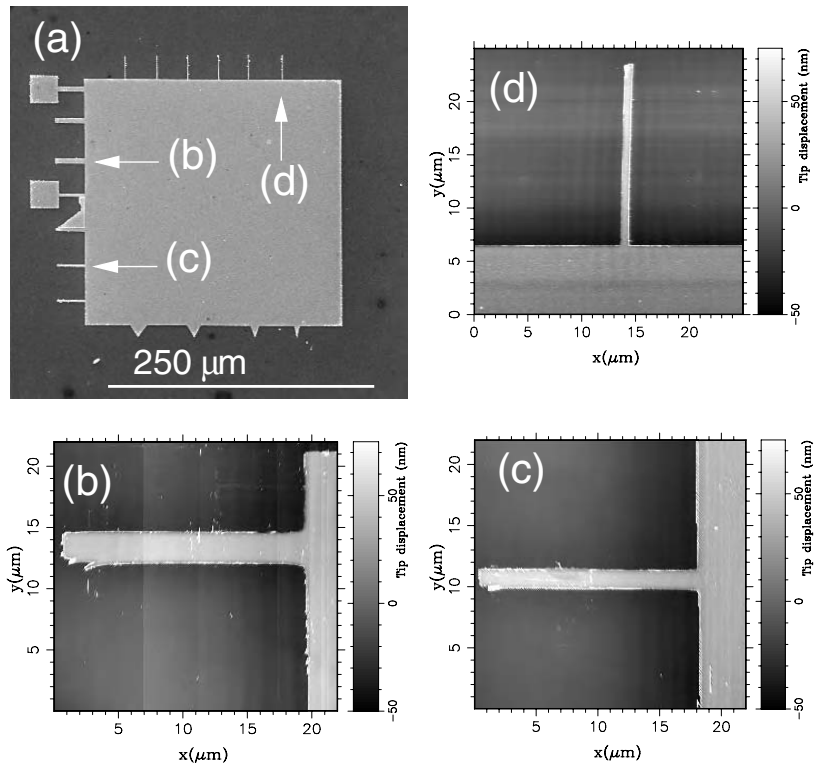


Figure 8.14: (a) Electron microscope image of the silver sample (60 nm thick) deposited on glass and designed to study the coupling between surface plasmons and the modes of the silver stripes. AFM images of various stripes which can be addressed by the surface plasmons launched on the large square area; (b) width = 2.5 μm; (c) width = 1.6 μm; (d) width = 1.0 μm

Successive zooms (corresponding to decreasing heights of the observation plane) above the exit end of the strip (Figure 8.16) reveal the intensity of the field of the plasmons which couple to the finite width stripe. The interference pattern is built by the plasmons which reach the end of the $\approx 20 \mu\text{m}$ long stripe where they are reflected back. Let us notice that the plasmon field is strictly confined to the width of the stripe.

8.4.4. Prototypes of submicron optical devices

Fundamental research make the control transfer of electromagnetic signals, at infra-red and visible wavelengths, plausible in the submicron range, thus breaking

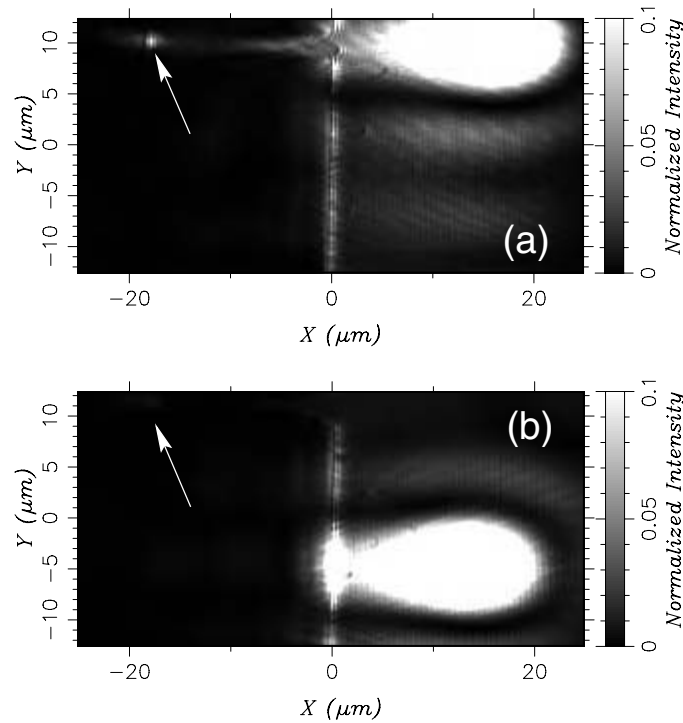


Figure 8.15: PSTM image of the $2.5 \mu\text{m}$ wide stripe excited by a surface plasmon launched on the large square area visible in the middle of Figure 8.14. (a) The incident spot is aligned along the axis of the stripe. At the exit end of the stripe, a spot shows up (white arrow). (b) The incident spot is shifted $15 \mu\text{m}$ in the y direction while keeping the same scanning area as in (a)

the diffraction limit [Quidant *et al.*, 2002], [Quidant *et al.*, 2004]. The main features of the new kind of devices we propose are:

1. sub- λ cross-sections;
2. introduction of heterostructures in the direction of propagation;
3. excitation by non-radiatives waves;
4. transmission efficiency defined in the near-field zone (submicron distance) close to the exit end of the device.

The rest of this section provides some examples of recent achievements pertaining to high index dielectric waveguides and to plasmonics. Both technologies are relatively

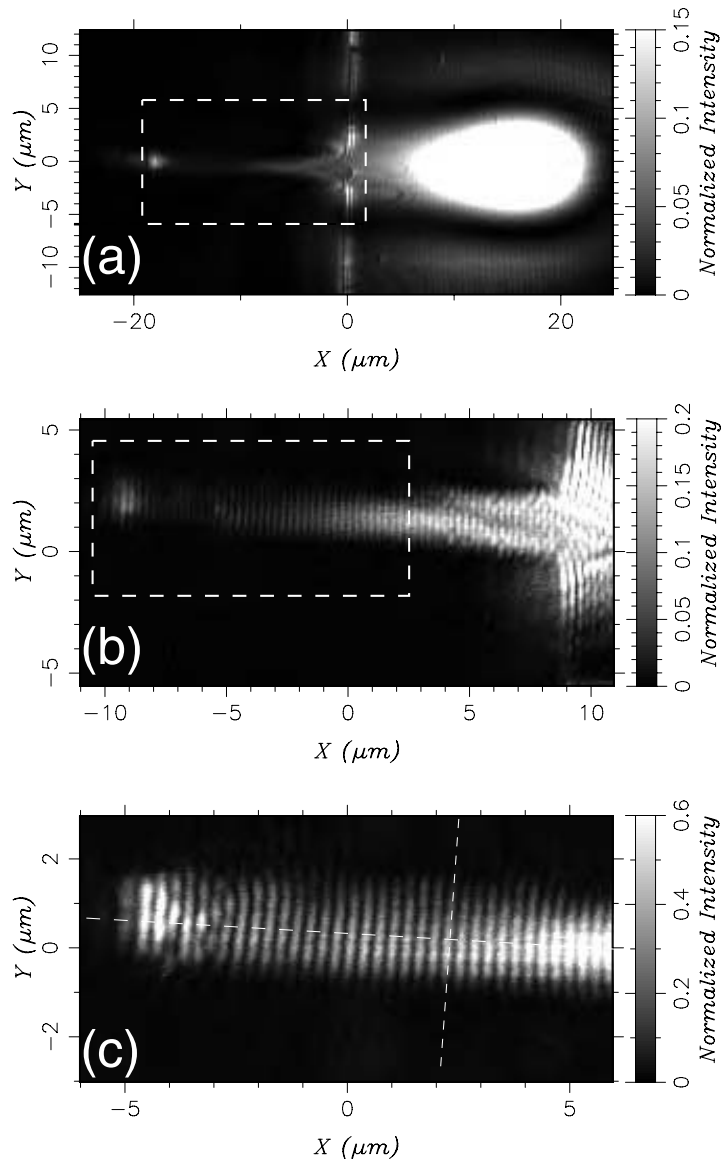


Figure 8.16: PSTM image of the 2.5 μm wide stripe of Figure 8.14 excited by a surface plasmon launched on the large square area visible in the middle of Figure 8.14. (a) The tip to sample d is about 350 nm; (b) $d \simeq 100$ nm; (c) $d < 50$ nm. The dimensions of the images (b) and (c) correspond to the areas inside the rectangles visible in (a) and (b) respectively

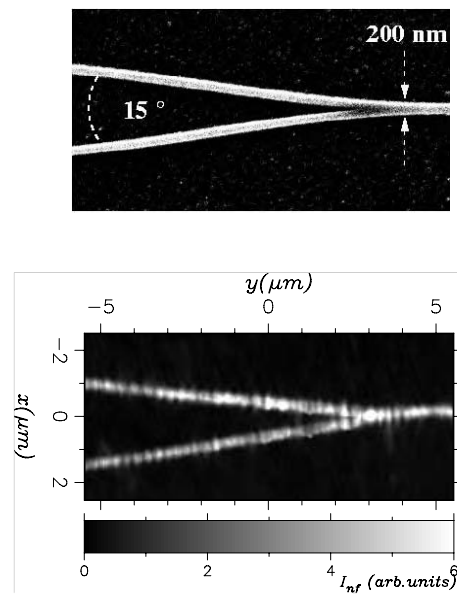


Figure 8.17: *Top: Electron microscope image of a Y junction made of TiO_2 featuring a sub- λ cross-section and deposited on a glass substrate. Bottom: PSTM image of the Y junction excited from the right using the technique of Figure 8.12*

easy to combine with each other. Therefore, optical devices relying on a combined use of metals and high index materials are expected in the near future.

Splitter

Figure 8.17 demonstrates the feasibility of TiO_2 Y junctions featuring sub- λ (≈ 200 nm) cross-sections. This junction splits the mode coming from a sub- λ waveguide similar to the one of Figure 8.13. The PSTM makes it possible to observe that the separation of the mode occurs over a distance of a few μm with minimal losses and minimal cross-talk between the branches. To appreciate this result, one should remember that today's technology obtains such splitting using waveguides with transverse sizes larger than several μm and over a range of several *hundredths* of μm .

Coupling a sub- λ waveguide to an annular microstructure

Figure 8.18 shows the addressing of an TiO_2 annular microstructure featuring sub- λ (≈ 200 nm) cross-sections by a sub- λ waveguide similar to the one of Figure 8.13

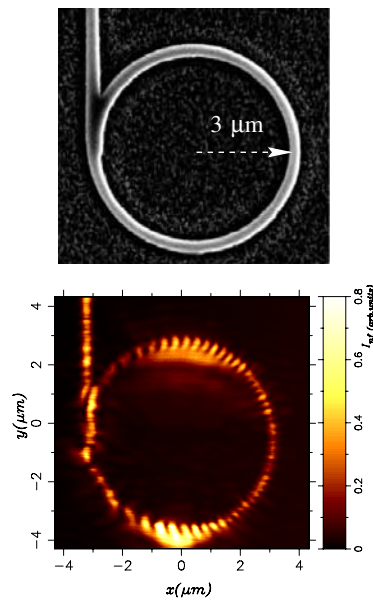


Figure 8.18: *Top: Electron microscope image of an annular microstructure made of TiO_2 featuring a sub- λ cross-section and deposited on a glass substrate. Bottom: PSTM image of this annular microstructure excited by a mode going out a sub- λ waveguide (from the upper left part of the image)*

which is in turn excited according to the principle of Figure 8.12. Such geometry provides the basic of the so-called add-drop filters. As in the case of the Y junction, the PSTM images makes it possible to observe that the coupling occurs with minimal radiative losses. The diameter of the ring is among the smallest diameters reported in the literature until now

Optical tunnel effect through heterostructures with sub- λ cross-sections

PSTM imaging also led to the mapping in direct space of the light propagation through heterostructures obtained by aligning rows of mesoscopic particles which have a high index of refraction (shortened as “heterowires”). Numerical simulations first determined the geometrical parameters of two heterowires featuring respectively either a high (passing) or low (stopping) transmission efficiency at an incident frequency corresponding to a wavelength in vacuum of 633 nm. The heterowires were microfabricated following the calculated parameters (Figure 8.19) and were optically excited by a sub- λ waveguide similar to the one of Figure 8.13. The constant height PSTM images of Figure 8.20 makes it possible to observe the details of the optical tunnel effect across

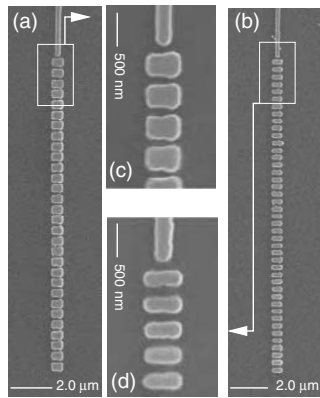


Figure 8.19: Electron microscope image of two TiO₂ samples deposited on a glass substrate. The particles width is $W=(350\pm 20)$ nm in sample (a) and $W=(210\pm 20)$ nm in sample (b). (c) (resp. (d)) Electron microscope image of the junction between the sub- λ waveguide used to address optically the heterowires (a) (resp. (b))

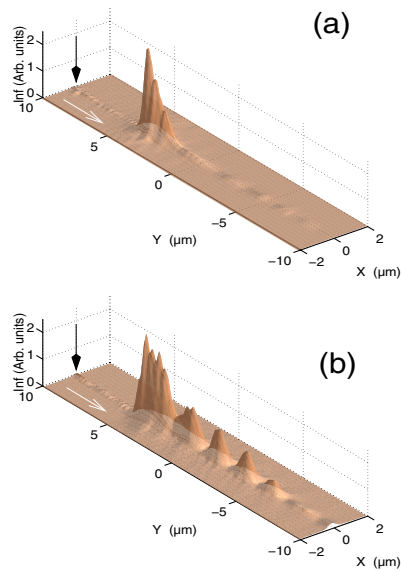


Figure 8.20: PSTM images recorded above the two heterowires described in Figure 8.19 and excited by a frequency corresponding to the wavelength $\lambda = 633$ nm in vacuum. (a) “Stopping” heterowire ($W = 350$ nm). (b) “Passing” heterowire ($W = 210$ nm)

the heterowires. The black arrows point to the position of the sub- λ waveguides used to excite the heterowires. The white arrows show the direction of the incident light. The near-field intensity is spread along more than $10\ \mu\text{m}$ over the passing heterowire while it is drastically damped above the stopping heterowire. Such heterowires may turn out to be of practical use in designing reduced sizes optical devices.

Plasmonic devices

Fundamental researches about the confinement of the electromagnetic field by localized plasmon coupling (see section 8.3.1) and about the thin metal stripes plasmons (see section 8.4.3) are among the pioneering works which triggered the international trend towards the development of miniaturized optical devices exploiting surface plasmon effects, also called “plasmonics” [Barnes *et al.*, 2003]. An appealing feature of plasmonics is that the same thin metal circuitry can carry electric charges and electromagnetic waves at infra-red and visible frequencies [Weeber *et al.*, 2003]. An example of the rapid evolution towards applications appears in Figure 8.21 [Devaux *et al.*, 2003].

Results presented in this chapter are due to various collaborations which are gratefully acknowledged, namely: Ch. Girard, J.R. Krenn, T.W. Ebbesen, J.P. Goudonnet,

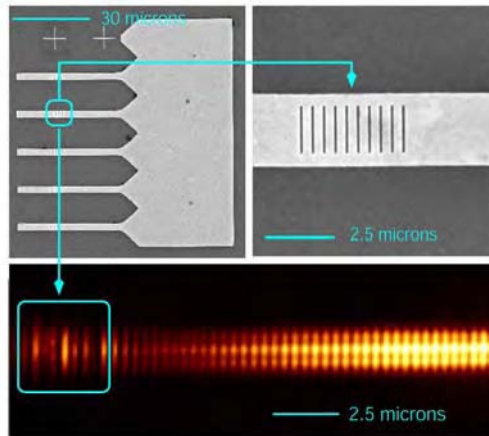


Figure 8.21: Top: SEM images of a the result of nanofabrication process aimed at designing a Bragg mirror for stripe plasmons. A Focused Ion Beam carved a series of nanoslots in a 40 nm thin gold stripe deposited on glass obtained by e-beam lithography (LPUB–Dijon). Bottom: PSTM image of the stripe plasmon (incident from right to left, launched using a wavelength in vacuum equal to 800 nm according to a procedure explained in section 8.4.3) reflected by the Bragg mirror. The quality of the nanoslots mirror is such that, to the left of the mirror zone, the intensity falls dramatically down to a value not detectable by the PSTM tip

E. Bourillot, T. David, Y. Lacroute, L. Markey, J.C. Weeber, E. Devaux, R. Quidant, U. Schröter, C. Chicanne and G. Colas des Francs. This work was supported by the Conseil Régional de Bourgogne (ARCEN project) and the European Commission (Contracts NoE FP6-IST-2002-1-507879 and STRP FP6-NMP-2002-1-001601).

8.5. References

- [Agarwal, 1975] Agarwal, G. S. 1975. Quantum electrodynamics in the presence of dielectrics and conductors. I. Electromagnetic-field response functions and black-body fluctuations in finite geometries. *Phys. Rev. A*, **11**, 230–242.
- [Barnes *et al.*, 2003] Barnes, W.L., Dereux, A., & Ebbesen, T.W. 2003. Surface plasmon sub-wavelength optics. *Nature*, **424**, 824–830.
- [Chicanne *et al.*, 2002] Chicanne, C., David, T., Quidant, R., Weeber, J. C., Lacroute, Y., Bourillot, E., Dereux, A., Colas des Francs, G., & Girard, C. 2002. Imaging the local density of states of optical corrals. *Phys. Rev. Lett.*, **88**, 097402 (4 pages).
- [Colas des Francs *et al.*, 2001a] Colas des Francs, G., Girard, C., Weeber, J.C., Chicanne, C., David, T., Dereux, A., & Peyrade, D. 2001a. Optical analogy to electronic quantum corrals. *Phys. Rev. Lett.*, **86**, 4950–4953.
- [Colas des Francs *et al.*, 2001b] Colas des Francs, G., Girard, C., Weeber, J. C., & Dereux, A. 2001b. Relationship between scanning near-field optical images and local density of states. *Chem. Phys. Lett.*, **345**, 512–516.
- [Colas des Francs *et al.*, 2002] Colas des Francs, G., Girard, C., & Dereux, A. 2002. Theory of near-field optical imaging with a single molecule as light source. *Single Molecules*, **3**, 311–312.
- [Dereux *et al.*, 2000] Dereux, A., Girard, C., & Weeber, J.C. 2000. Theoretical principles of near-field optical microscopies and spectroscopies. *J. Chem. Phys.*, **112**, 7775–7790.
- [Dereux *et al.*, 2001] Dereux, A., Devaux, E., Weeber, J.C., Goudonnet, J.P., & Girard, C. 2001. Direct interpretation of near-field optical images. *J. Microscopy*, **202**, 320–331.
- [Dereux *et al.*, 2003] Dereux, A., Girard, C., Chicanne, C., Colas des Francs, G., David, T., Bourillot, E., Lacroute, Y., & Weeber, J. C. 2003. Subwavelength mapping of surface photonic states. *Nanotechnology*, **14**, 935–938.
- [Devaux, 2000] Devaux, E., Détection de champs magnétiques associés aux champs optiques, 2000 (October). PhD Thesis, University of Bourgogne, Dijon.
- [Devaux *et al.*, 2000] Devaux, E., Dereux, A., Bourillot, E., Weeber, J. C., Lacroute, Y., Goudonnet, J. P., & Girard, C. 2000. Local detection of the optical magnetic field in the near zone of dielectric samples. *Phys. Rev. B*, **62**, 10504–10514.
- [Devaux *et al.*, 2003] Devaux, E., Ebbesen, T.W., Weeber, J.C., & Dereux, A. 2003. Launching and decoupling surface plasmons via micro-gratings. *Appl. Phys. Lett.*, **83**, 4936–4938.
- [Girard & Bouju, 1992] Girard, C., & Bouju, X. 1992. Self-consistent study of dynamical and polarization effects in near-field optical microscopy. *J. Opt. Soc. Am. B*, **9**, 298–305.
- [Girard & Dereux, 1996] Girard, C., & Dereux, A. 1996. Near-field optics theories. *Rep. Prog. Phys.*, **59**, 657–699.

- [Hecht *et al.*, 1997] Hecht, B., Bielefeldt, H., Novotny, L., Inoue, Y., & Pohl, D.W. 1997. Facts and artifacts in near-field microscopy. *J. Appl. Phys.*, **81**, 2492–2498.
- [Heisenberg, 1930] Heisenberg, W. 1930. *Physical Principles of Quantum Theory*. New York: Dover.
- [Krenn *et al.*, 1999a] Krenn, J.R., Dereux, A., Weeber, J.-C., Bourillot, E., Lacroute, Y., Goudonnet, J.-P., Schider, G., Leitner, A., Aussenegg, F.R. & Girard, C. 1999a. Direct observation of localized surface plasmon coupling. *Phys. Rev. B*, **60**, 5029.
- [Krenn *et al.*, 1999b] Krenn, J.R., Dereux, A., Weeber, J.-C., Bourillot, E., Lacroute, Y., Goudonnet, J.-P., Schider, G., Gotschy, W., Leitner, A., Aussenegg, F.R., & Girard, C. 1999b. Squeezing the optical near-field zone by plasmon coupling of metallic nanoparticles. *Phys. Rev. Lett.*, **82**, 2590.
- [Levine & Schwinger, 1950] Levine, H. & Schwinger, J. 1950. On the theory of electromagnetic wave diffraction by an aperture in an infinite plane conducting screen. *Comm. Pure App. Math.*, **3**, 355–391.
- [Metiu, 1984] Metiu, H., Surface enhanced spectroscopy. *Prog. Surf. Sci.*, **17**, 153.
- [Morse & Feshbach, 1953] Morse, P.M., & Feshbach, H. 1953. *Methods of Theoretical Physics*. New York: McGraw-Hill. Ch. 13.
- [Newton, 1966] Newton, R. G. 1966. *Scattering Theory of Waves and Particles*. New York: McGraw-Hill. Ch. 4.
- [Quidant *et al.*, 2001] Quidant, R., Weeber, J.C., Dereux, A., Peyrade, D., Colas des Francs, G., Girard, C. & Chen, Y. 2001. Addressing and imaging high optical index dielectric ridges in the optical near-field. *Phys. Rev. E*, **64**, 066607 (6 pages).
- [Quidant *et al.*, 2002] Quidant, R., Weeber, J.C., Dereux, A., Peyrade, D., Girard, C. & Chen, Y. 2002. Spatially resolved photonic transfer through mesoscopic heterowires. *Phys. Rev. E*, **65**, 036616 (4 pages).
- [Quidant *et al.*, 2004] Quidant, R., Girard, C., Weeber, J.C. & Dereux, A. 2004. Tailoring the transmittance of integrated optical waveguides with short metallic nanoparticles chains. *Phys. Rev. B*, **69**, 085407 (7 pages).
- [Schröter & Dereux, 2001] Schröter, U. & Dereux, A. 2001. Surface plasmon polaritons on metal cylinders with dielectric core. *Phys. Rev. B*, **64**, 125420 (10 pages).
- [Weeber *et al.*, 1996] Weeber, J.C., Bourillot, E., Dereux, A., Goudonnet, J.P., Chen, Y. & Girard, C. 1996. Observation of light confinement effects with a near-field optical microscope. *Phys. Rev. Lett.*, **77**(27), 5332–5335.
- [Weeber *et al.*, 2000] Weeber, J.C., Dereux, A., Girard, C., Colas des Francs, G., Krenn, J.R., & Goudonnet, J. P. 2000. Optical addressing at the subwavelength scale. *Phys. Rev. E*, **62**, 7381–7388.
- [Weeber *et al.*, 2001] Weeber, J.C., Krenn, J.R., Dereux, A., Lamprecht, B., Lacroute, Y. & Goudonnet, J.P. 2001. Near-field observation of surface plasmon polariton propagation on thin metal stripes. *Phys. Rev. B*, **64**, 045411 (9 pages).
- [Weeber *et al.*, 2003] Weeber, J. C., Lacroute, Y. & Dereux, A. 2003. Optical near-field distributions of surface plasmon waveguide modes. *Phys. Rev. B*, **68**, 115401 (10 pages).

Chapter 9

The Confined Universe of Electrons in Semiconductor Nanocrystals

9.1. Introduction

Semiconductor nanocrystals are clusters of nanometric size that contain hundreds to thousands of atoms. Their chemical composition is that of a semiconductor and they are usually embedded in a transparent matrix, which makes their optical study possible (polymer, solution, gel, glass, etc.).

The main characteristic of these materials is the presence of electronic confinement effects. These effects appear when the size of nanocrystals is as large as the electron wavelength in the material and when energy barriers surround electrons. For electrons, semiconductor nanocrystals represent real three-dimensional potential quantum wells, and then they are veritable quantum dots. The restriction of available space for the movement of electrons in the three dimensions is at the origin of its energy level quantification. That is why semiconductor nanocrystals are often called solid-state atoms. Quantum confinement effects are, then, at the origin of the specific electronic and optical properties of these nano-objects. The study of these new properties constitutes a huge domain for basic and applied research.

In this chapter, we will describe the fundamental characteristics of the electronic structure of these nano-objects. We will underline the connection between this structure and the new properties of nanocrystals. We will also discuss in more detail the latest knowledge concerning applications in nanophotonics of semiconductor nanocrystals. Three different fields will be considered: the obtaining of single

Chapter written by Maria CHAMARRO.

photon sources, biological labeling, and the obtaining of wavelength tunable laser nano-sources.

9.2. Electronic structure

Optical properties of semiconductor nanocrystals depend on the structure of valence and conduction electronic states. For their definition it is possible to use the same approach as in bulk crystal, i.e., effective mass approximation. In this framework, the effect of all the atoms in the crystal on electronic movement is taken into account by giving an effective mass to the electron which is different to the free electron mass. This approach could be borne out, for nanocrystals which are not very small, by the fact that, typically, a nanocrystal of CdSe with a radius of 3.5nm contains about 7,700 atoms: this observation should give the area meaning.

9.2.1. “Naïf” model

The simplest model takes as its starting point a semiconductor with only one parabolic band for electrons and for holes. The wavefunction of one particle in the bulk material can be expressed as a linear combination of Bloch wavefunctions. However, if the particle is in a nanocrystal the wavefunction will be written as a product of wavefunctions: one which contains the periodic part of the Bloch function and another which is called the envelope function and takes into account symmetries of the confinement potential. We will discuss the determination of this latter part of wavefunction below.

Usually, in effective mass approximation, the matrix is described as infinite potential out of a nanocrystal. That is well justified when the nanocrystal is immersed in a glass matrix with a gap energy of about 5 eV because this value is larger than the same value in a semiconductor, for example 1.7 eV for CdSe at room temperature. The following hypotheses simplify the problem further: nanocrystals have a spherical shape and there is no interaction between them. In the simplest model, the Hamiltonian of the electron-hole system contains kinetic energy of electron and hole, their Coulomb interaction energy and the confinement potential for electron and hole. It is written as follows [EFR 82]:

$$H = -\frac{\hbar^2}{2m_e} \nabla_{r_e}^2 - \frac{\hbar^2}{2m_t} \nabla_{r_t}^2 - \frac{e^2}{\epsilon|r_e - r_t|} + V_e(r_e) + V_t(r_t) \quad (1)$$

where $m_{e,t}$ denotes the electron or hole effective mass, $r_{e,t}$ is the electron or hole position respectively, ϵ is the relative dielectric constant of the nanocrystal taken with respect to the matrix, $V_{e,t}$ is zero if $r_{e,t}$ is smaller than the nanocrystal radius, R ,

and infinite otherwise. Charged particles, electrons and holes, then, have two potentials: the interaction Coulomb potential and the spherical well potential of radius R that quantifies the kinetic energies of the electron and hole. The Coulomb energy scales as $e^2/\epsilon R$; meanwhile electron-hole pair kinetic energy in the well of radius R scales as $\hbar^2/2\mu R^2$ where $\frac{1}{\mu} = \frac{1}{m_e} + \frac{1}{m_t}$. The relative importance of these two potentials enables us to distinguish three different confinement regimes.

When the Coulomb energy is much larger than the confinement energy, the regime is called “weak confinement”. If we define the Bohr radius of the electron-hole pair, a_B , as $a_B = \frac{\hbar^2 \epsilon}{2\mu e^2}$, this regime appears when R is much larger than a_B .

That is the case, for example, for CuCl nanocrystals of average sizes (about 4nm). Indeed, the binding energy of the electron-hole (e-h) pair is large $\epsilon_{exc} = 213$ meV and its Bohr radius is very small, $a_B = 7$ Å. In this situation the e-h pair is confined as a whole and then the quantification of the movement of the center of mass is accomplished. The envelope wavefunction of the e-h pair is then given by the product of two wavefunctions, the first one describing the movement of the e-h pair with respect to its center of mass, and the second one describing the movement of the center of mass confined in the infinite spherical well. After resolution of the Schrödinger equation, the energies of possible optical transitions are:

$$E_n = E_g - \epsilon_{exc} + \frac{\hbar^2 \pi^2 n^2}{2MR^2} \quad (2)$$

where $M = m_e + m_t$ is the total mass of the electron and hole together, $R = \frac{m_e r_e + m_t r_t}{m_e + m_t}$ is the position of the center of mass, E_g denotes the gap of bulk crystal and n is an integer number that we have taken ($l=m=0$). n, l, m are quantum numbers with the same meaning as in atomic physics.

The second regime, the opposite of the one already described, is called “strong confinement”. Here the Coulomb energy is negligible with respect to confinement energy. This regime appears when R is much smaller than the a_B . In this case, both the electron and the hole are confined separately. The movement of both carriers is independent and they are considered separately confined in the infinite spherical potential. Confinement energies of the electron and hole depend only on n and l quantum numbers and are written as follows:

$$E_{n,l}^{(e,t)} = \frac{\hbar^2 \alpha_{n,l}^2}{2m_{(e,t)} R^2} \quad (3)$$

$$\text{with } \alpha_{1,0} = \pi, \alpha_{1,1} \approx 1.43\pi, \alpha_{2,1} \approx 1.83\pi, \text{ etc...} \quad (4)$$

In general, the electronic state is denoted $n\ell$ where ℓ is the usual atomic symbol (S,P,D ...) which corresponds to a given value l ($l=0,1,2 \dots$). Each state is $2(2l+1)$ fold degenerated when electronic spin is considered. Optical transitions are accomplished between two quantum states: one for the electron and the other for the hole. Calculation of selection rules for dipolar transitions shows that in the optically allowed possible transitions the quantum numbers n and l are preserved. Then, if Coulomb energy is calculated with a perturbation approach, the total energy of the first optical transition, $1S-1S$ ($n_e=n_i=1, l_e=l_i=0, m_e=m_i=0$), is written as follows [BRU 83, 84]:

$$E_{1S-1S} = E_g + \frac{\hbar^2 \pi^2}{2\mu R^2} - \frac{1.8e^2}{\epsilon R} \quad (5)$$

GaAs or PbS nanocrystals are good examples of a strong confinement regime: electron-hole binding energy is equal to 4 meV for GaAs and 2 meV for PbS, and their Bohr radii are respectively equal to 100\AA and 180\AA .

The third regime is called “intermediate”, and Coulomb energy is no longer negligible with respect to confinement energy. In general, the electron and hole have very different effective masses. The electron is the lightest particle, and only its movement is confined. Exact calculations for the electronic structure are more complicated because the two terms of interaction have to be considered at the same level in the Hamiltonian. To solve the problem in this situation, the results of “strong confinement” are taken as a departure point to diagonalize the Hamiltonian and to use a variational calculation or a perturbative calculation to take into account Coulomb interaction. CdS and CdSe nanocrystals having a radius of about of 4–5nm are good examples of an intermediate confinement regime (the Bohr radius is equal to 3nm for CdS and 5nm for CdSe). In any case, the boundaries of the different regimes are not really strict. For example, in the literature, it is common for these nanocrystals to take expressions usually given to strong confinement to describe transitions near the threshold of optical absorption.

9.2.1.1. Absorption and luminescence spectra

The main results in the effective mass approximation which are summarized in equations (2) and (5) are: first, the transformation of a band structure in a series of discrete levels for which their energy depends on nanocrystal size; second, the increase of the first optical transition energy with respect to the bulk gap energy E_g .

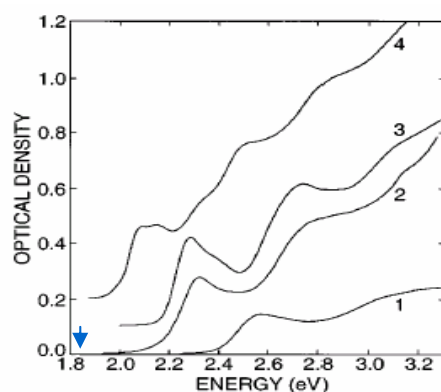


Figure 9.1. Absorption spectra, at 5K, of CdSe nanocrystals in silicate glasses, from the reference [CHA 96b]. Average radii are 25, 19.7, 18.3 and 11.4 Å for samples from 4 to 1, respectively. The arrow gives the energy band gap of bulk CdSe

Optical absorption spectra clearly show the existence of confinement effects for charged carriers [EKI 85]. For PbS, for example, a very important blue shift of absorption threshold (>1.5 eV at room temperature) has been observed [GAC 94]. Figure 9.1 represents absorption spectra in the case of CdSe nanocrystals. This figure shows the blue shift of the absorption threshold and also the presence of different bands, which are related to different optical transitions between discrete levels. Moreover, their maximal energy position depends on nanoparticle size. A comparison between theoretical and experimental results for the lowest energy transition is represented in Figure 9.2 for CdSe nanocrystals. The plain line gives the energy of the first electronic transition E_{1S-1S} as a function of the average radius of nanocrystals. This line was obtained using effective mass approximation (equation (5)). Circles represent the energy of the first absorption band maximum, measured by Wang and N. Herron for CdS nanocrystals of average size [WAN 90]. Theoretical values given by effective mass approximation and experimental values are in agreement when nanocrystal radii are larger than 2nm, but there is less agreement for nanocrystals having radii of less than 2nm. In fact, equation (5) is obtained in a very simple model: only one parabolic band is considered for electrons and holes. This approximation can only be justified when the confinement effect is

not very important. A theoretical model taking into account the complexity of the electronic structure of conduction and valence bands has been proposed in the strong confinement regime and gives a better result [XIA 89; GRI 90; VAH 90; EKI 93; RIC 96]. Meanwhile, for very small nanocrystals, from a purely intellectual point of view, other approaches seem more reasonable, such as tight-binding approximation [LIP 89; RAM 93; ALB 98; PER 01] or pseudo-potential calculations [ZUN 98]. These two approaches have a more microscopic approach that consists of building nanocrystals from isolated atoms. Tight binding is used to calculate the size dependence of the energy shift of the optical absorption threshold and the results are given in Figure 9.2 (dashed line). We can see that this latter method gives a better agreement for smallest sizes.

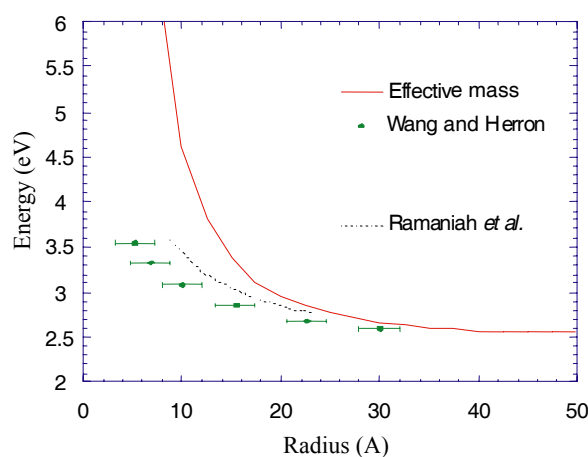


Figure 9.2. Size dependence of energy of the lowest optical transition of CdS nanocrystals. The plain line represents a theoretical calculation in the effective mass approximation equation (5). The dashed line represents a theoretical calculation using tight binding [RAM 93]. Experimental points are taken from WAN 90

Luminescence experiments give complementary information, but they need a more complicated interpretation than optical absorption spectra. Luminescence spectra show in general broader bands and luminescence maxima are shifted to lower energies with respect to absorption spectra, as shown in Figure 9.3 (see bands denoted a and b). Moreover, this red shift is a function of average size and increases when size decreases. Figure 9.3 also shows a very broad band at lower energy, denoted c). Impurities are certainly at the origin of this band. Some authors also discuss this band in terms of surface states [SPA 87].

9.2.2. Fine electronic structure

Absorption and luminescence spectra show broad bands even at low temperatures. Two mechanisms are mainly responsible of this broadening. First, an intrinsic mechanism which is responsible for a homogeneous broadening due to phonon-electron coupling (phonons are the vibration quanta of the crystal structure); second, an extrinsic mechanism which is the dominant mechanism in these materials. This latter point is due to a size dispersion of the nanocrystal and induces an inhomogeneous broadening, which is not temperature dependent. Size dispersion is related to the fabrication procedure. Despite the high quality of samples that are currently fabricated, residual sample homogeneous still remain and size dispersion is at best in the order of 5% r.m.s. [MUR 93]. Each nanocrystal absorbs and emits at a given energy which is characteristic of its size. That is why absorption and luminescence spectra give information not about a given nanocrystal size but about an average nanocrystal size. Contributions of different sizes are mixed together in a broad inhomogeneous band.

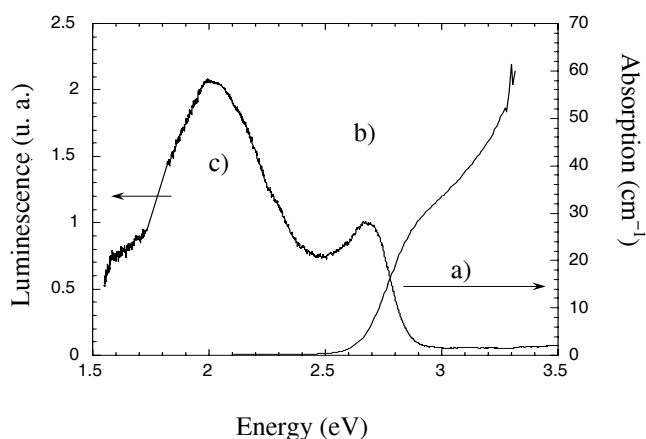


Figure 9.3. Absorption and luminescence spectra at room temperature of a sample containing CdS nanocrystals with average radius 15 Å

9.2.2.1. Size-selective excitation

Several spectroscopic techniques are used in order to avoid this difficulty and to obtain more precise information on the electronic structure of nanocrystals. A very important example of these techniques is based on the selection of a small number of

nanocrystals among those contained in the sample. That is done by reducing spatially the excitation area through *micro-luminescence* experiments (we will discuss these experiments in more detail in section 9.3), or by using spectral selection that gives information about an isolated nanocrystal's size in the distribution: the *size-selective technique*. Hole-burning is one example of the latter technique, and luminescence size-selective excitation or detection is another example. In the following paragraphs we will describe the principle of luminescence size-selective excitation and the main parameters obtained when this technique is used.

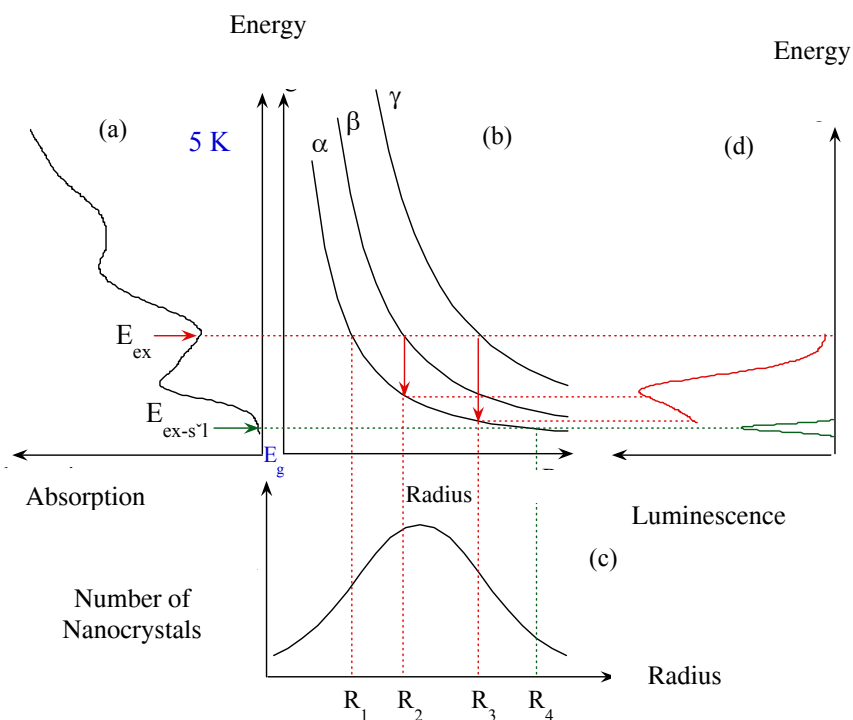


Figure 9.4. The principle of size-selective excitation of the luminescence (scheme). (a) Two arrows indicate energies discussed in the text. (b) Scheme of three first optical transitions energies as a function of nanocrystal size. The scale has been exaggerated for clarity. (c) Nanocrystal size distribution in the sample (scheme). (d) Luminescence spectra of excited nanocrystals at high energy and under selective size excitation

The objective of size-selective excitation is to isolate in the luminescence spectrum the contribution of a given nanocrystal size which is contained in the size distribution of the sample. This principle is represented in the scheme of Figure 9.4. Part (a) gives the absorption of the sample. Part (b) schematically represents the correspondence of nanocrystal radius to energy for the first three optical transitions which have been arbitrarily denoted α , β and γ . Part (c) represents the size distribution of the nanocrystal which is at the origin of the spectral broadening of absorption and luminescence spectra. If we assume that the excitation energy is equal to E_{exc} , several optical transitions of different nanocrystal sizes are excited. In Figure 9.4b we give the size dependence of the energy of three first optical transitions: the lowest transition corresponds to nanocrystals having a radius equal to R_1 , the second electronic transition corresponds to nanocrystals having a radius equal to R_2 , and the third one corresponds to a radius equal to R_3 . Whatever the optical transition excited in the nanocrystal after a very quick relaxation to the lowest electronic state, α , nanocrystals give luminescence at an energy corresponding to their lowest optical transition, α . Each nanocrystal size contributes to the luminescence spectrum at a characteristic energy. Thus a broad luminescence spectrum that contains contributions of different sizes is obtained in Figure 9.4d. When excitation energy decreases to get a value at the threshold of the optical absorption spectrum, denoted $E_{\text{exc-sel}}$ in the figure, there are very few electronic levels available to be excited. In Figure 9.4b, there is only one optical transition denoted α which corresponds to the nanocrystals having a radius equal to R_4 , i.e., among the biggest radius in the sample. Under these excitation conditions, the luminescence spectrum is much more narrow than for non-selective excitation and gives information about the luminescence of one set of nanocrystals, in this case nanocrystals of size equal to R_4 .

In summary, with selective excitation, there is only one excited optical transition: the lowest optical transition for the biggest size in the distribution.

When the size-selective luminescence of nanocrystals in the strong confinement regime is studied, a universal phenomenon is observed: the presence of red energy shift between luminescence and absorption. More precisely, the luminescence peak which is observed at a lower energy than the excitation energy is accompanied by one or two phonon replicas, i.e. emission composed of photons and phonons [CAL 93; NIR 95; CHA 95; BAN 97; MIC 97; CHA 98; LAV 02]. Figure 9.5 shows the absorption and luminescence spectrum for CdSe nanocrystals with an average radius of 18 Å. Indeed, for a size-selective excitation (excitation energy equal to 2.14 eV), near the laser line we observe three very well resolved peaks. Moreover, in the low energy side of this size-selective luminescence spectrum we also observe a broader band related to the presence of some defects in the sample. Temporal behavior of the three luminescence peaks reveals a non-exponential decay with a very fast component in the order of a hundred of picoseconds and a slower component with a

time constant in the order of several tenths of nanoseconds. The authors who originally observed this size-selective luminescence attributed it to the presence of surface states [BAW 90; BAW 92]. However, the polarization properties of size-selective luminescence show clearly that this luminescence has an intrinsic character [CHA 96a]. In the next section we will briefly describe this intrinsic origin.

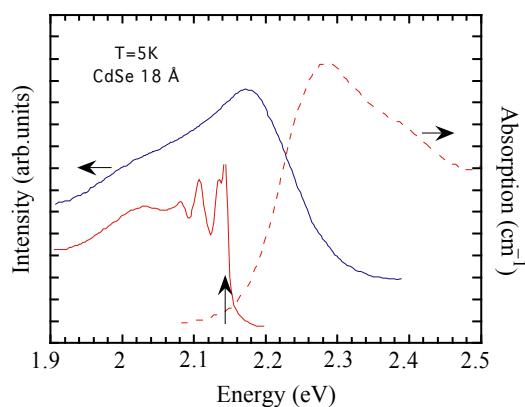


Figure 9.5. Absorption (dashed line) and luminescence (blue plain line) spectra of CdSe nanocrystals embedded in a glass matrix. The size-selective luminescence spectrum is also represented in this figure with a full red line. A vertical arrow gives the used excitation energy

9.2.2.2. “Dark” electron-hole pair

When nanocrystal size decreases, the overlap of the electron and hole wavefunctions increase and the Coulomb interaction between particles also increases. In the framework of the strong confinement regime Coulomb interaction is introduced in a perturbative scheme. In Coulomb interaction two parts can be distinguished: first, a direct term which is responsible for electron-hole pair binding, and second, an electron-hole exchange term usually weaker than the direct term. The direct term gives a red shift of the optical transition associated to the electron-hole pair. This term scales as $1/R$ (see equation (5)).

When a more sophisticated model than that described in section 9.2.1 is used, the electron-hole pair state is in fact constituted of an electron having a $1/2$ spin and a hole characterized by a $3/2$ angular momentum [EKI 93]. The electron-hole exchange term is, then, at the origin of the splitting of the electron-hole pair state into two groups of states: one characterized by an angular momentum $J_{\text{pair}}=1$ and another characterized by a momentum $J_{\text{pair}}=2$. The first group is connected to the fundamental state via the absorption or emission of photons; this is why it is usually said that this level is optically allowed. The second group is not connected with the fundamental one via the absorption

or emission of photons. The latter states are optically forbidden states or dark states. Several authors have calculated the splitting energy of these two groups of states in the effective mass approximation [TAK 93; ROM 94; GOU 98] or by using a tight binding method [PER 01] or in the pseudo-potential formalism [FRA 98]. In the effective mass approximation this splitting, called electron-hole exchange interaction energy, scales as the inverse of the nanocrystal volume.

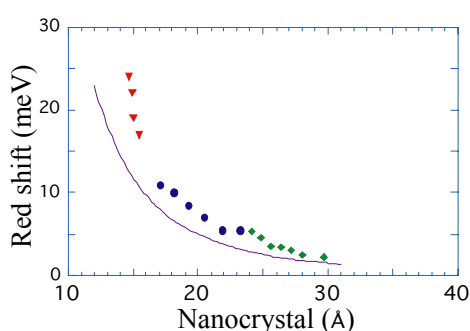


Figure 9.6. Size dependence of the red shift of the size-selective excited luminescence obtained in CdSe nanocrystals. The continuous line represents the result of the electron-hole exchange interaction calculation in the effective mass approximation. Results taken from [TAK 93]

Now we are able to better understand the results of a size-selective luminescence technique. Indeed, in these experiments, the optically active states, which are associated with important oscillator strength, are populated, and then a relaxation to the optically forbidden states occurs. Emission from the optically forbidden states at a low temperature is possible due to electron-phonon interaction in nanocrystals [EFR 91]. Then, the red shift between the excitation energy and the emission energy is in fact the energy splitting between allowed and forbidden states. This splitting is very weak in the bulk material, in the order of 0.12 meV or 0.24 meV for CdSe and CdS, respectively. For nanocrystals it is a function of excitation energy, i.e. of the excited nanocrystal size. Figure 9.6 shows that for CdSe nanocrystals with radii values from 30 Å to 15 Å the red shift between emission and excitation increases with decreasing nanocrystal size and is several orders of magnitude larger than in the bulk material.

9.3. Micro-luminescence

Micro-luminescence experiments are essentially experiments in luminescence with a spatial resolution near to the diffraction limit. This resolution is usually obtained by using a microscope objective with a big numerical aperture ≈ 0.7 or by using an immersion lens with numerical aperture ≈ 1.25 . Under these excitation conditions and if the sample contains very few nanocrystals, it is possible to study a few nanocrystals (or one isolated nanocrystal) which are in the excitation spot area. The first experiments of this kind were carried out in 1996 by the M. G. Bawendi group at the Massachusetts Institute of Technology, United States [EMP 96]. They showed a very characteristic behavior for CdSe nanocrystals at a low temperature (10K). First, micro-luminescence spectra show essentially the same basic structure as luminescence spectra obtained by the size-selective excitation technique, described in the last section, but they are spectrally narrower. A narrow peak and one or two more peaks at lower energy (phonon replica) constitute the spectrum of an isolated CdSe nanocrystal, as shown in Figure 9.7. Moreover, we have to underline that the dynamics of luminescence of a single nanocrystal is a function of temperature [LAB 03] and the results confirm the results obtained in size-selective experiments [CHA 96b].

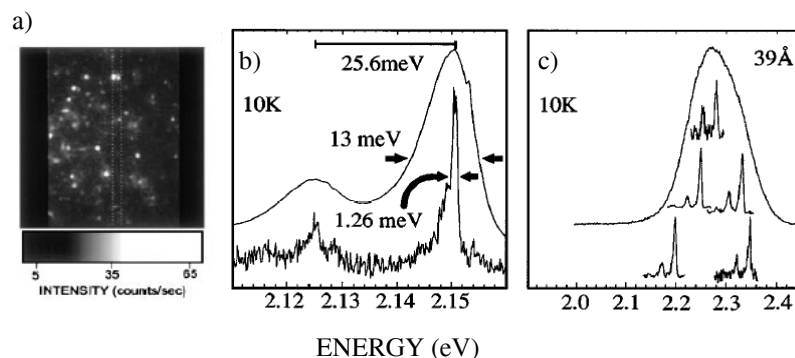


Figure 9.7. Figures from [EMP 96]. (a): Typical image of the micro-luminescence of CdSe nanocrystals obtained at 10K with an integration time of 0.5 s and an excitation density of about 150 W/cm^2 . The white points represent places from which the luminescence of an isolated nanocrystal is collected. (b) Comparison of standard luminescence spectra of CdSe nanocrystals with an average size of 45 \AA (bandwidth of 13 meV) and the luminescence spectrum of an isolated nanocrystal excited with a power of 2.5 KW/cm^2 (bandwidth of 1.26 meV). (c) Comparison of standard luminescence spectra, from all excited CdSe nanocrystals in the sample, and from different isolated CdSe nanocrystals contained in the studied sample. Micro-luminescence spectra were obtained for an integration time of 60 s

Second, micro-luminescence spectra show a reversible red shift, which depends on the excitation density. For an excitation density of 2.5 KW/cm^2 at the energy of

the Ar green laser line, it is possible to measure a spectral shift of about 60 meV after several minutes. Moreover, a decrease in the intensity of the luminescence band and an increase in phonon replica intensity is observed: see Figure 9.8. That has been interpreted as a Stark effect induced by the existence of a local electric field, which fluctuates as a function of trapping and detrapping of charges in the nearest environment of the nanocrystal. The presence of the already described behavior makes it difficult to measure the homogeneous bandwidth. Indeed, to obtain a spectrum it is necessary to average for several minutes and then the obtained luminescence spectrum is, in fact, an average luminescence spectrum, which contain several luminescence spectra shifted in energy. M. G. Bawendi's group has obtained at low excitation density a bandwidth of the main micro-luminescence line of 120 μeV ($25\text{W}/\text{cm}^2$) [EMP 96]. This value is in reality a higher limit for the real value because it is forced by the resolution of the detection system that was used.

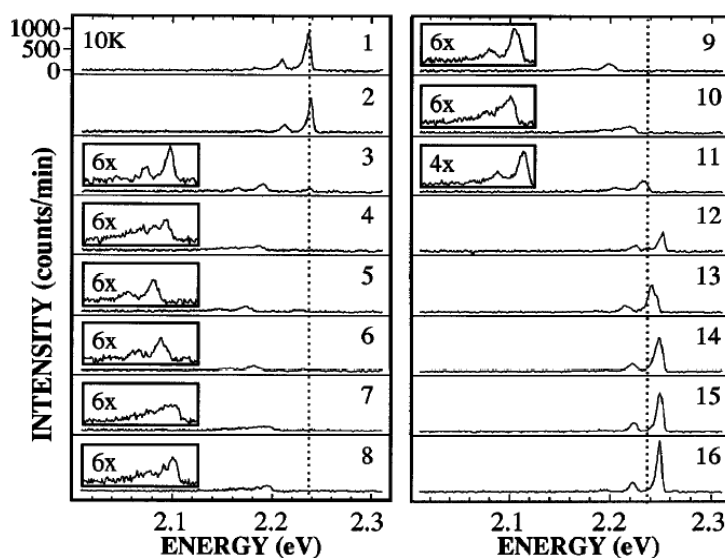


Figure 9.8. Figure from [EMP 96]. Sixteen consecutive luminescence spectra of an isolated CdSe nanocrystal taken minute by minute. Spectra were obtained using an excitation density of $2.5\text{ KW}/\text{cm}^2$. Insets show magnifications of the same spectra

Third, from the first measurements of micro-luminescence, its telegraphic behavior has been observed. Indeed, nanocrystal fluorescence under continuous excitation turns on and off intermittently with a characteristic time scale of several

seconds. This intermittency is not apparent from ensemble measurements on many nanocrystals. Figure 9.9 shows, over a range of several minutes, the temporal behavior of the intensity of emitted light, integrated with the whole spectrum. This figure evidences the presence of bright intervals (for which luminescence is active, “on” intervals) and dark intervals (for which the luminescence is absent, “off” intervals). The duration of “off” intervals is independent of the excitation density, but the duration of “on” intervals is proportional to the inverse of the excitation density. Moreover, as is shown in Figure 9.9, the stability of “on” intervals becomes better when nanocrystals are encapsulated by a layer of another semiconductor having a higher gap energy.

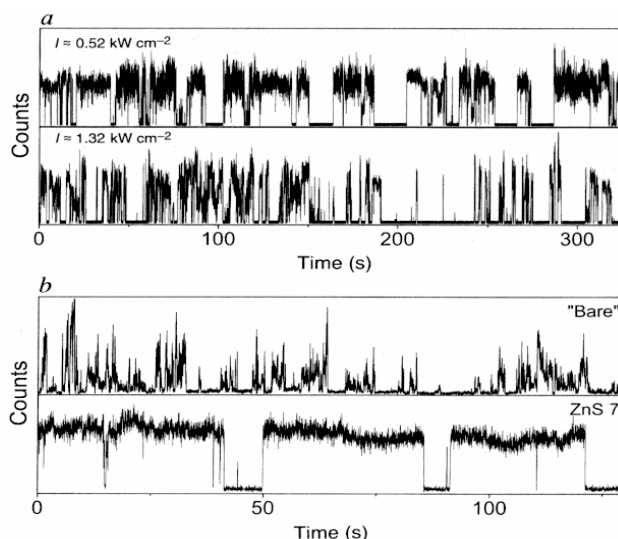


Figure 9.9. Figures from [NIR 96]. (a) Comparison of micro-luminescence intensity as a function of the observation time measured for two excitation densities for a CdSe nanocrystal encapsulated by four monolayers of ZnS. (b) Comparison of the intensity of micro-luminescence as a function of the observation time obtained for a “bare” nanocrystal (which is not encapsulated by another semiconductor) and for a nanocrystal encapsulated by 7 monolayers of ZnS. Excitation density is equal to 0.7 KW/cm^2

Efros *et al.* [EFR 97] give the following explanation for all these experimental observations:

Bright intervals correspond to the radiative recombination of an electron-hole pair photo-created in the nanocrystal. Dark intervals appear because the probability

of creating two electron-hole pairs in a nanocrystal is not negligible. When two electron-hole pairs are in the nanocrystal a phenomenon known as Auger ionization becomes important. Moreover this phenomenon is increased by a confinement effect, which we will discuss later in this chapter. Auger ionization consists of an energy transfer from one electron-hole pair, which relaxes non-radiatively, to the other pair in the nanocrystal. Then the ejection of an electron or a hole belonging to the second pair to the surrounding matrix occurs. In this way, as long as the nanocrystal is charged, electron-hole pairs recombine non-radiatively preferentially via an Auger effect. Detrapping of the electron or the hole and its return in the nanocrystal neutralizes the nanoparticle and makes the reactivation of the luminescence possible. This model is not completely satisfactory but gives a global description of the main experimental facts. Indeed, the telegraphic behavior of luminescence in this model is a function of the excitation density. Moreover, this model explains the red shift of the micro-luminescence spectrum and its less important intensity as a result of the trapping and detrapping of charges in the near surroundings of the nanocrystal which creates a fluctuating electric field at the origins of the Stark effect in luminescence [EMP 97].

9.4. Auger effect

Auger effect efficiency is related to electron-hole Coulomb interaction. This efficiency is less important in bulk semiconductors than it is in atoms because of the reduction in electron-electron interaction and because of kinetic restrictions imposed by energy and momentum conservation. In the case of semiconductor nanocrystals, electronic confinement increases Coulomb interactions and relaxes conservation rules of quantity of movement and in this manner should increase the Auger effect, whereas a discrete electronic structure imposes restrictions on the accessible electronic states, which make energy conservation possible in the overall process. That leads to an Auger recombination that is efficient only when it is assisted by phonons or when the final state is the continuum, i.e. states outside of the nanocrystal. That is known as Auger ionization. Theoretical treatment of this process is complex [CHE 90]. In this section we have chosen to summarize the main results of experiments concerning the phenomenological study of Auger ionization [KLI 00a].

In the case of CdSe nanocrystals, a lifetime study of several electron-hole pair states as a function of number of pairs is summarized in Figure 9.10a. We underline that for a given size, the lifetime of several electron-hole pairs becomes shorter and shorter as the number of pairs increases. Moreover, if the number of electron-hole pairs, N , is fixed, the lifetime of a state containing several pairs, τ_N , decreases when nanocrystal size decreases. Indeed, in Figure 9.10b we can see that the lifetime of a two electron-hole pairs state τ_2 decreases from 363 ps to 6 ps when its radius varies

from 4.1 to 1.2 nm. This means that τ_2 is proportional to the volume of the nanocrystal. This experimental rule has been also obtained for τ_3 and τ_4 respectively. In the lower part of Figure 9.10 we show the value of the Auger constant, C_A , as a function of nanocrystal radius. This constant is defined in the following way for $N \geq 2$:

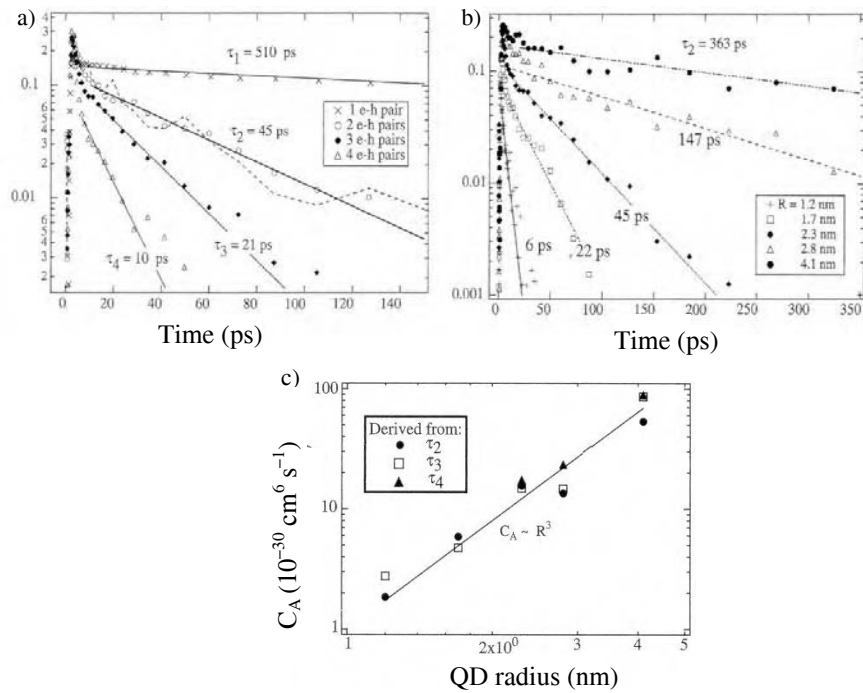


Figure 9.10. Figures from [KLI 00a]. (a) Dynamics of two, three or four electron-hole pair states in CdSe nanocrystals with an average size of 23 Å. Curves were obtained after an analysis of differential transmission measurements as a function of excitation density. (b) Dynamics of two electron-hole pair state for samples containing CdSe nanocrystals with different average sizes. (c) Size dependence of Auger constant C_A . The line represents a fit of experimental data

$$C_A = \tau_N^{-1} \frac{V^2}{N^2} \propto R^3 \quad (6)$$

where V is the nanocrystal volume. Experimental results show that the Auger constant is proportional to the volume of the nanocrystal. When size decreases, Auger recombination becomes very important and consequently the lifetime of four, three or two electron-hole pairs decreases significantly.

9.5. Applications in nanophotonics

We have summarized the specific electronic properties of semiconductor nanocrystals. Absorption and emission energy is a function of nanocrystal size. Absorption and emission spectra evidence the discretization of their electronic structure. Coulomb effects are greatly enhanced with respect to the same effects in bulk material. This leads to two main consequences when nanocrystals are in the strong confinement regime: first, low temperature emission which comes from a “dark” state and, second, the enhancement of Auger recombination which is responsible for the shortening of lifetimes of states containing several electron-hole pairs. Moreover, micro-luminescence experiments evidence sensitivity to the nearest nanocrystal surrounding.

The combination of these electronic properties added to the versatility of chemical methods used for their fabrication makes these materials very interesting for a huge number of potential applications: saturable filters [BRE 64], bistables [YUM 87], electroluminescent diodes [COL 94], one electron transistor [KLE 97], lasers [PAV 00], “qubits” in quantum computers [BRU 00], photovoltaic cells [HUY 02], etc.

In the next section we will describe the main advantages of nanocrystals in three kinds of application in the domain of nanophotonics.

9.5.1. *Semiconductor nanocrystals: single photon sources*

Conventional light sources, i.e. laser diodes or lasers, generate radiation which is well described by the classic Maxwell equations. On the other hand, there are applications in the very new domain of quantum information which require optical sources with very weak intensity but emitting a controlled number of photons [BOU 00]. Among these sources, these emitting pulses containing only one photon are of prime importance. That is particularly true for quantum cryptography, where the main objective is communications security through the intelligent use of the concept of quantum measure. One essential element in secure distribution is the use of an optical source, which has to emit a series of impulsions containing one, and only one, photon; each photon codes an information bit. In this manner any spy that taps information, by measuring the

state of the single photon, perturbs the state of the photon and makes it possible to detect the tap on the transmission line.

A prerequisite for obtaining single photon sources is the existence of isolated single photons emitting materials exhibiting the phenomenon known as “photon antibunching”: a dark time between two successive photon emissions. This phenomenon has so far been observed in several materials: atoms [KIM 97], molecules [BAS 92], nitrogen vacancies in diamond [KUR 00; BRO 00], quantum dots obtained by molecular beam epitaxy [MIC 00a; MOR 01]. Semiconductor nanocrystals are very good candidates for producing single photon sources. They have several advantages over other materials. Radiation stability is higher than the stability of dye molecules. Moreover, contrary to quantum dots obtained by epitaxy, they can be used at room temperature.

Recently, photon antibunching has also been observed for semiconductor nanocrystals [MIC 00b; LOU 00]. Experimental set-up is essentially a micro-luminescence set-up added to a Hanbury Brown and Twiss interferometer joined to a photon correlation time detection system. This experimental set-up measures the second order auto-correlation function of nanocrystal emitted light, which is given by the following expression:

$$g^2(\tau) = \langle I(t)I(t + \tau) \rangle / \langle I(t) \rangle^2 \quad (7)$$

where τ is the time between two successive detections of photons, the first arriving at the detection system of one of the interferometric arms and the second at the other detection system at the end of the second interferometric arm. $\langle \rangle$ denotes a temporal average of $I(t)$, the measured intensity at time t .

In Figure 9.11, we can see the histogram for τ values of emitted photons of an isolated CdSe nanocrystal encapsulated by several monolayers of ZnS. The histogram is proportional to the second order correlation function. The signature of photon antibunching is given by the observation of no signal at $\tau=0$ and a signal which increases as the absolute value of time delay τ values increases. These experiments also give a measurement of the lifetime of the emitting state [MIC 00b].

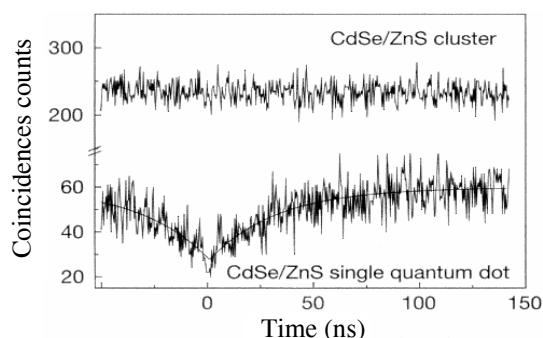


Figure 9.11. Figure from [MIC 00b]. Histogram of time delay between two consecutive emitted photons of an isolated CdSe nanocrystal encapsulated by several monolayers of ZnS

In quantum dots, the probability of the creation of several electron-hole pairs after excitation is negligible. When epitaxial quantum dots are used, it is necessary to select the detected signal spectrally in order to observe no signal at $\tau=0$ and isolate the emission of single photons from other kinds of emissions: wetting layer and several pair states. On the other hand, when semiconductor nanocrystals are used in the Auger process, which is more efficient in the case of nano-objects than for epitaxial quantum dots, the radiative recombination of states containing several pairs is inhibited.

These first experiments showing the existence of strong photon antibunching are very promising. Several groups are now working on the characterization of single photon sources based in semiconductor nanocrystals.

9.5.2. Semiconductor nanocrystals: new fluorescent labels for biology

A connection between biology and optics has long existed within the very active domain of microscopy. This synergy has increased because of increasing interest in biotechnologies. In this respect, biophotonics is a very dynamic branch, which has improved and renewed detection procedures. One possibility, explored below, is to use semiconductor nanocrystals as labels of biological molecules [BRU 98; CHAN 98; DAH 03]. In this section, we will underline the main advantages of nanocrystals in this domain.

A method widely used in biology to analyze different entities is to attach a fluorescent compound to the entity under study. This compound is usually a dye molecule.

Dye molecules have relatively narrow absorption and luminescence spectra with maxima slightly shifted in energy. Luminescence spectra are slightly asymmetric and showing shoulders at low energy. These characteristics make them very interesting as biological labels but they are also the cause of several of their limitations, in particular when we are interested in the multidetection of molecules with a discrimination based on the color of the scratched molecule. Indeed, the experiment consists of attaching different molecules to different biological entities and following this combination via the detection of the luminescence of dye molecules. The first difficulty in this situation arises from the fact that in order to excite all the dye molecules it is necessary to use a tunable source or several sources delivering all wavelengths, which can be absorbed by dye molecules. The second difficulty comes about because detection could be less selective than expected due to the presence of long queues of luminescence which could give conflicting information. Meanwhile, the main difficulty is, in general, degradation of luminescence of dye molecules under irradiation, a phenomenon that is called photodarkening.

Spectroscopic characteristics of semiconductor nanocrystals are well adapted to give a more satisfactory answer to the constraint of experiences in biology. Semiconductor nanocrystals show, as already discussed, relatively narrow luminescence spectra and the associated absorption spectra are larger than the spectra of dye molecules. Then, it is possible to excite a group of nanocrystals of different sizes using only one source and to obtain the luminescence of all of the nanocrystals. Concerning the degradation of luminescence under illumination, it has been shown that the luminescence photostability of a set of nanocrystals is much more satisfactory than that of a set of dye molecules typically used as probes in biology [BRU 98]. Only telegraphic emission (see section 9.3) may introduce limitations for using nanocrystals in this domain.

We would like to add that when nanocrystals are used as biological label, they must be soluble in water and bio-compatible. In this respect, researchers have found an intelligent solution which consists of encapsulating nanocrystals in several layers which makes them more stable and also increases their solubility in water. Then a CdSe nanocrystal is encapsulated by another semiconductor with higher gap energy, for example the ZnS, in order to improve their luminescence stability. Finally, a silica layer encapsulates this ensemble core-shell which makes it soluble in water [BRU 98].

These kinds of studies are in their infancy, but early results are very promising. In this book the reader can find more information in Chapter 10 on nanobiophotonics.

9.5.3. Semiconductor nanocrystals: a new active material for tunable lasers

Quantum dots, auto-assembled or semiconductor nanocrystals, have two main advantages as the active material in lasers sources. First, due to the fact that emission wavelength is a function of quantum dot size, it is possible to obtain tunable lasers in a very large domain by choosing the size of emitting quantum dots. Second, because the energy difference between two electronic states is also a size function, it is possible to fabricate laser sources for which the threshold of laser emission will not depend on temperature. Indeed, in the strong confinement regime, this energy difference is very high as compared with thermal energy, in such a way that electronic levels, which are near the band gap, are nearly always populated.

Laser effect was also shown in quantum dots obtained by molecular beam epitaxy (auto-assembled dots). However, for this application, semiconductor nanocrystals have several advantages with respect to assembled dots. First, it is possible to obtain very narrow size distribution (5%). Second, its fabrication using chemical methods gives rise to very new possibilities for integration. Moreover, sizes are an order of magnitude smaller than sizes of quantum dots obtained by molecular beam epitaxy and potential barriers, which are fixed by the matrix in which dots are immersed, are greater in semiconductor nanocrystals. These two last characteristics of nanocrystals means that the strong confinement regime is easily achieved, which is a more promising departure point for obtaining temperature independent lasers sources. In spite of this, very few works investigate stimulated emission in nanocrystals. In the strong confinement regime, semiconductor nanocrystals also show an enhanced Auger recombination, which is a very important disadvantage.

Klimov *et al.* [KLI 00b] recently observed optical gain in films containing a compact arrangement of nanocrystals [MUR 95] and for encapsulated nanocrystals [DAB 97]. The maximum gain obtained for nanocrystals having radii from 10 to 30 Å was 510cm⁻¹. When nanocrystals are excited at very high energy the necessary condition for the gain is that the relaxation time for electrons and for holes to the emitting state will be very short as compared with the non-radiative time, Auger recombination of a two-particle state τ_2 . This condition is generally satisfied, as shown by several experimental studies [KLI 87; KLI 99]. Meanwhile, the existence of an optical gain is not a guarantee of the existence of stimulated emission. This emission is observed if the time necessary for stimulated emission, τ_s , is faster than the gain relaxation time which is supposed to be of the same order of magnitude as the two pairs recombination τ_2 .

$$\tau_s = \frac{4\pi R^3}{3} \frac{1}{\xi} \frac{n_r}{\sigma_g c} < \tau_2 \equiv \beta R^3 \quad (8)$$

where n_r is the refraction index of the sample, c is the light speed, and σ_g is the gain transversal section. If we use the value measured by Klimov [KLI 00a] for nanocrystals having a radius equal to 13 Å we will obtain $\xi = 4\pi\bar{n}R^3/3 > 0.002$ where \bar{n} is nanocrystal concentration in the sample. This value of volume concentration is very difficult to obtain for the usual fabrication methods which use the precipitation of nanocrystals in a glass matrix. That is why very few works deal with the observation of stimulated emission of nanocrystals in glass matrices [DNE 92]. Stimulated emission has been observed recently in samples containing compact arrangements of nanocrystals [KLI 00b] and in titanium oxide sol-gel in which a very high concentration of nanocrystals was achieved [EIS 02]. For this latter kind of sample Eisler *et al.* show that is possible to tune the emission energy from 2 eV to 2.2 eV using nanocrystals 27 to 17 Å in size, respectively. Moreover, these authors show the feasibility of stimulated emission at room temperature.

9.6. Conclusions

Studies completed in the 1980s and 1990s on the determination of the electronic structure of semiconductor nanocrystals have revealed their main characteristics. We have given a short description of the electronic properties of semiconductor nanocrystals and we have also underlined two main characteristics of these materials: on the one hand, the discretization of their electronic structure and its size dependence and, on the other hand, the enhancement of Coulomb effects. We have also shown that their properties could play a very different role as a function of the application considered. Indeed, the enhancement of Coulomb effects becomes more favorable to the photon antibunching of luminescence of an isolated nanocrystal, but also makes the observation of a stimulated emission more difficult.

Nowadays, the main questions are articulated around the role that surface states have in the telegraphic behavior of micro-luminescence and also the microscopic origins of this behavior. But, in addition, new perspectives for applied and fundamental research in nanophotonics are being considered due to the versatility of chemical methods of fabrication. New materials are in production: nanocrystals containing only one impurity, or an isolated magnetic ion [NOR 01], molecules of nanocrystals, microcavities containing nanocrystals [POI 03], and also controlled negatively charged nanocrystals [CON 01].

9.7. References

- [ALB 98] Albe V, Jouanin C, and Bertho D (1998) Confinement and shape effects on the optical spectra of small CdSe nanocrystals. *Phys. Rev. B* 58: 4713–4720
- [BAN 97] Banin U, Lee JC, Guzelian AA, Kadavanich AV and Alivisatos AP (1997) Exchange interaction in InAs nanocrystal quantum dots. *Superlattices and Microstructures* 22: 559–567
- [BAS 92] Basché Th and Moerner WE (1992) Photon antibunching in the fluorescence of a single dye molecule trapped in a solid. *Phys. Rev. Lett.* 69: 1516–1519
- [BAW 90] Bawendi MG, Wilson WL, Rothberg L, Carroll PJ, Jedju TM, Steigerwald ML and Brus LE (1990) Electronic structure and photoexcited-carrier dynamics in nanometer-size CdSe clusters. *Phys. Rev. Lett.* 65: 1623–1626
- [BAW 92] Bawendi MG, Carroll PJ, Wilson and Brus LE (1992) Luminescence properties of CdSe quantum crystallites: resonance between interior and surface localized states. *J. Chem. Phys.* 96: 946–954
- [BRE 64] Bret G and Gires F (1964) Giant-pulse laser and light amplifier using variable transmission coefficient glasses as light switches. *Appl. Phys. Lett.* 4: 175–176
- [BRO 00] Brouri R, Beveratos A, Poizat JP and Grangier P (2000) Photon antibunching in the fluorescence of individual color centers in diamond. *Opt. Lett.* 25: 1294–1296
- [BRU 98] Bruchez Jr M, Moronne M, Gin P, Weiss S, and Alivisatos AP (1998) Semiconductor nanocrystals as fluorescent biological labels. *Science* 281: 2013–2016
- [BRU 00] Brun TA and Wang H (2000) Coupling nanocrystals to a high-Q silica microsphere: Entanglement in quantum dots via photon exchange. *Phys. Rev. A*, 61: 032307–1,5
- [BRU 83] Brus LE (1983) A simple model for the ionization potential, electron affinity, and aqueous redox potentials of small semiconductor crystallites. *J. Chem. Phys.* 79: 5566–5571
- [BRU 84] Brus LE (1984) Electron-electron and electron-hole interactions in small semiconductor crystallites: the size dependence of the lowest excited electronic state. *J. Chem. Phys.* 80: 4403–4409
- [CAL 93] Calcott PDJ, Nash KJ, Canham LT, Kane MJ and Brumhead D (1993) Identification of radiative transitions in highly porous silicon. *J. Phys.: Condens. Matter* 5: L91–L98
- [CHAN 98] Chan WCW and Nie S (1998) Quantum dot bioconjugates for ultrasensitive nonisotopic detection. *Science* 281: 2016–2018
- [CHA 95] Chamarro M, Gourdon C, Lavallard Ph and Ekimov AI (1995) Enhancement of exciton exchange interaction by quantum confinement in CdSe nanocrystals. *Jpn. J. Appl. Phys.* 34: 12–14
- [CHA 96a] Chamarro M, Gourdon C and Lavallard P (1996) Photoluminescence polarization of semiconductor nanocrystals. *J. of Lum.* 70: 222–237
- [CHA 96b] Chamarro M, Gourdon C, Lavallard Ph, Lublinskaya O and Ekimov AI (1996) Enhancement of electron-hole interaction in CdSe nanocrystals: a quantum confinement effect. *Phys. Rev. B* 53: 1336–1342

- [CHA 98] Chamarro M, Dib M, Voliotis V, Filoramo A, Roussignol P, Delerue C, Allan G and Lannoo M (1998) Interplay of Coulomb, exchange and spin-orbit effects in semiconductor nanocrystals. *Phys. Rev. B* 57: 3729–3732
- [CHE 90] Chepic DI, Efros AL, Ekimov AI, Ivanov MG, Kharchenko VA, Kudriavtsev IA and Yazeva TV (1990) Auger ionization of semiconductor quantum drops in a glass matrix. *J. of Lum.* 47: 113–127
- [COL 94] Colvin VL, Schlamp MC and Alivisatos AP (1994) Light-emitting diodes made from cadmium selenide nanocrystals and a semiconducting polymer. *Nature* 370: 354–357
- [CON 01] Congjun W, Moonsub S and Guyo-Sionnest P (2001) Electrochromic nanocrystal quantum dots. *Science* 291: 2390–2392
- [DAB 97] Dabbousi BO, Rodriguez-Viejo J, Mikulec FV, Heine JR, Mattoussi H, Ober R, Jensen KF and Bawendi MG (1997) (CdSe)ZnS core-shell quantum dots: synthesis and characterization of a size series of highly luminescent nanocrystallites. *J. Phys. Chem. B* 101: 9463–9475
- [DAH 03] Dahan M, Lévi S, Luccardini C, Rostaing Ph, Riveau B and Triller A (2003) Diffusion dynamics of glycine receptors revealed by single-quantum dot tracking. *Science* 302: 442–445
- [DNE 92] Dneprovskii VS, Klimov VI, Orokov DK and Vandyshev YV (1992) Strong optical nonlinearities and laser emission of semiconductor microcrystals. *Solid State Comm.* 81: 227–230
- [EFR 82] Efros AI and Efros AL (1982) Interband absorption of light in a semiconductor sphere. *Sov. Phys. Semicond.* 16: 772–778
- [EFR 91] Efros AL (1991) Luminescence polarization of CdSe nanocrystals. *Phys. Rev. B* 46: 7448–7458
- [EFR 97] Efros AL and Rosen M (1997) Random telegraph signal in the photoluminescence intensity of a single quantum dot. *Phys. Rev. Lett.* 78: 1110–1113
- [EIS 02] Eisler HJ, Sundar VC and Bawendi MG (2002) Color-selective semiconductor nanocrystal laser. *Appl. Phys. Lett.* 80: 4614–4616
- [EKI 85] Ekimov AI, Efros AL and Onushchenko AA (1985) Quantum size effect in semiconductor microcrystals. *Solid State Comm.* 56: 921–924
- [EKI 93] Ekimov AI, Hache F, Schanne-Klein MC, Ricard D, Flytzanis C, Krudryavtsev IA, Yazeva TV, Rodina AV and Efros AL (1993) Absorption and intensity-dependent photoluminescence measurements on CdSe quantum dots: assignment of the first electronic transitions. *J. Opt. Soc. Am. B* 10:100–107
- [EMP 96] Empedocles SA, Norris DJ and Bawendi MG (1996) Photoluminescence of single CdSe nanocrystallite quantum dots. *Phys. Rev. Lett.* 77: 3873–3876
- [EMP 97] Empedocles SA and Bawendi MG (1997) Quantum-confined Stark effect in single CdSe nanocrystallite quantum dots. *Science* 278: 2114–2117

- [FRA 98] Franceschetti A, Wang LW, Fu H and Zunger A (1998) Short-range versus long-range electron-hole exchange interaction in semiconductor quantum dots. *Phys. Rev. B* 58:R13367-R13370
- [GAC 94] Gacoin T, Boilot JP, Gandais M, Ricolleau C and Chamarro (1994) Transparent sol-gel matrices doped with quantum sized PbS particles. In Collinq RW, Tsai CC, Hirosi M, Koch F and Brus L (eds) *Microcrystalline and Nanocrystalline Semiconductor Symposium Proceedings* pp 247–252
- [GOU 98] Goupalov SV and Ivchenko EL (1998) Electron-hole long-range exchange interaction in semiconductor quantum dots. *J. Crystal Growth* 184–185, 393–397
- [GRI 90] Grigorian GB, Kazaryan EM, Efros AL and Yazeva TV (1990) Quantized holes and the absorption edge in spherical semiconductor microcrystals with a complex valence band structure. *Sov. Phys. Solid State* 32: 1031–1035
- [HUY 02] Huynh WU, Dittmerr JJ and Alivisatos AP (2002) Hybrid nanorod-polymer solar cells. *Science* 295, 2425–2427
- [KIM 97] Kimble HJ, Dagenis M and Mandel L (1997) Photon antibunching in resonance fluorescence. *Phys. Rev. Lett.* 39: 691–695
- [KLE 97] Klein DL, Roth R, Lim AKL, Alivisatos AP and McEuen PL (1997) *Nature* 389: 699–701
- [KLI 98] Klimov VI and McBranch D (1998) Femtosecond 1P-to 1S electron relaxation in strongly confined semiconductor nanocrystals. *Phys. Rev. Lett.* 80: 4028–4031
- [KLI 99] Klimov VI, Schawrz ChJ, McBranch D, Leatherdale CA and Bawendi MG (1999) Ultrafast dynamics of inter- and intraband transitions in semiconductor nanocrystals: implications for quantum-dot lasers. *Phys. Rev. B* 60: R2177-R2180
- [KLI 00a] Klimov VI, Mikhailovsky AA, McBranch DW, Leatherdale CA and Bawendi MG (2000) Quantization of multiparticle Auger rates in semiconductor quantum dots. *Science* 287: 1011–1013
- [KLI 00b] Klimov VI, Mikhailovsky AA, Xu S, Malko A, Hollingsworth JA, Leatherdale CA, Eisler HJ and Bawendi MG (2000) Optical gain and stimulated emission in nanocrystal quantum dots. *Science* 290: 314–317
- [KUR 00] Kurtsiefer C, Mayer S, Zarda P and Weinfurter H (2000) Stable solid-state source of single photons. *Phys. Rev. Lett.* 85: 290–293
- [LAB 03] Labeau O, Tamarat Ph and Lounis B (2003) Temperature dependence of the luminescence lifetime of single CdSe/ZnS quantum dots. *Phys. Rev. Lett.* 90: 257404–1,4
- [LAV 03] Lavallard P, Chamarro M, Perez-Conde J, Bhattacharjee AK, Goupalov and SV Lipovskii AA (2003) Exchange interaction and acoustical phonon modes in CdTe nanocrystals. *Solid State Comm.* 127: 439–442
- [LIP 89] Lippens PE and Lannoo M (1989) Calculation of the band gap for small CdS and ZnS crystallites. *Phys. Rev. B* 39: 10935–10942
- [LOU 00] Lounis B, Bechtel HA, Gerion D, Alivisatos P and Moerner WE (2000) Photon antibunching in single CdSe/ZnS quantum dot fluorescence. *Chem. Phys. Lett.* 329: 399

- [MAL 02] Malko V, Mikhailovsky AA, Petruska MA, Hollingsworth JA, Htoon H, Bawendi MG and Klimov VI (2002) From amplified spontaneous emission to microring lasing using nanocrystal quantum dot solids. *Appl. Phys. Lett.* 81: 1303–1305
- [MIC 00a] Michler P, Kiraz A, Becher C, Schoenfeld WV, Petroff PM, Zhang L, Hu E and Imamoglu A (2000) A quantum dot single-photon turnstile device. *Science* 290: 2282–2284
- [MIC 00b] Michler P, Imamoglu A, Mason MD, Carson PJ, Strouse GF and Buratto SK (2000) Quantum correlation among photons from a single quantum dot at room temperature. *Nature* 406: 968–970
- [MIC 97] Micic OI, Cheong HM, Fu H, Zunger A, Sprague JR, Mascarenhas A and Nozik AJ (1997) Size-dependent spectroscopy of InP quantum dots. *J. Phys. Chem. B* 101: 4904–4912
- [MIK 02] Mikhailovsky AA, Malko AV, Hollingsworth JA, Bawendi MG and Klimov VI (2002) multiparticle interactions and stimulated emission in chemically synthesized quantum dots. *Appl. Phys. Lett.* 80: 2380–2382
- [MOR 01] Moreau E, Robert I, Gerard JM, Abram I, Manin L and Thierry-Mieg V (2001) Single-mode solid-state single photon source based on isolated quantum dots in pillar microcavities. *Appl. Phys. Lett.* 79: 2865–2867
- [MUR 93] Murray CB, Norris DJ and Bawendi MG (1993) Synthesis and characterization of nearly monodisperse CdE (E=S,Se,Te) semiconductor nanocrystallites. *J. Am. Chem. Soc.*, 115: 8706–8715
- [MUR 95] Murray CB, Kagan CR and Bawendi MG (1995) Self-organization of CdSe nanocrystallites into three-dimensional quantum dot superlattices. *Science* 270: 1335–1338
- [NIR 95] Nirmal M, Norris DJ, Kuno M and Bawendi MG (1995) Observation of the “dark exciton” in CdSe quantum dots. *Phys. Rev. Lett.* 75: 3728–3731
- [NIR 96] Nirmal M, Dabbousi BO, Bawendi MG, Macklin JJ, Trautman JK, Harris TD and Brus LE (1996) Fluorescence intermittency in single cadmium selenide nanocrystals. *Nature* 383: 802–804
- [NOR 01] Norris DJ, Yao N, Charnock FT and Kennedy TA (2001) High-quality manganese-doped ZnSe nanocrystals. *Nano-Letters* 1: 3–7
- [PER 01] Perez-Condé J, Bhattacharjee, Chamarro M, Lavallard P, Petrikov VD and Lipovskii AA (2001) Photoluminescence Stokes shift and exciton fine structure in CdTe nanocrystals. *Phys. Rev. B* 64: 113303–1,4
- [RAM 93] Ramaniah LM and Nair SV (1993) Optical absorption in semiconductor quantum dots: a tight-binding approach. *Phys. Rev. B* 47: 7132–7139
- [RIC 96] Richard T, Lefebvre P, Mathieu H and Allegre J (1996) Effects of finite spin-orbit splitting on optical properties of spherical semiconductor quantum dots. *Phys. Rev. B* 53: 7287–7298
- [ROM 94] Romestain R and Fishman G (1994) Excitonic wave function, correlation energy, exchange energy, and oscillator strength in a cubic quantum dot. *Phys. Rev. B* 49: 1774–1781
- [PAV 00] Pavesi L, Dal Negro L, Mazzoleni C, Franzo G and Priolo F (2000) Optical gain in silicon nanocrystals. *Nature* 408: 440–444

- [POI 03] Poitras CB, Lipson M, Megan HD, Hahn Z and Krauss TD (2003) Photoluminescence of colloidal quantum dots embedded in a monolithic microcavity. *Appl. Phys. Lett.* 82: 4032–4034
- [SPA 87] Spanhel L, Haase M, Weller H and Henglein A (1987) Photochemistry of colloidal semiconductors. Surface modification and stability of strong luminescing particles. *J. Am. Chem. Soc.* 109: 5649–5655
- [VAH 90] Vahala KJ and Sercel PC (1990) Application of total-angular-momentum basis to quantum-dot band structure. *Phys. Rev. Lett.* 65: 239
- [WAN 90] Wang Y and Herron N (1990) Quantum size effects on the exciton energy of CdS clusters. *Phys. Rev. B* 42: 7253–7255
- [XIA 89] Xia JB (1989) Electronic structures of zero-dimensional quantum wells. *Phys. Rev. B* 40: 8500–8507
- [YUM 87] Yumoto J., Fukushima S and Kubodera K (1987) Observation of optical bistability in CdS_xSe_{1-x} glass with 25-psec switching. *Optics Lett.* 12: 832–834
- [ZUN 98] Zunger A (1998) Electronic-structure theory of semiconductor quantum dots. *MRS Bulletin* 23: (2) 35–42

Chapter 10

Nano-Biophotonics

10.1. Introduction

Since the beginnings of molecular biology, our view of signaling processes has been enriched by a large amount of molecular detail [GIL 02]. Starting from a stimulus, a signaling process is a cascade of molecular events which leads a cell to take a decision: gene expression, cell division, etc. These cascades are often depicted as block diagrams where each elementary step is sketched (protein interaction, recruitment ...). Between these steps one can find arrows representing the flux of biological information (Figure 10.1).

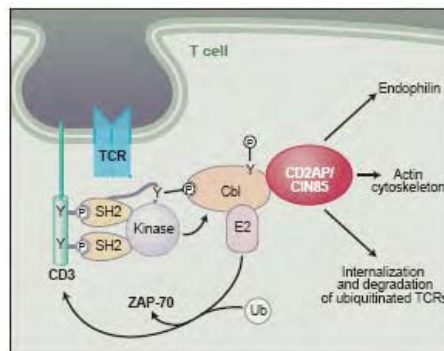


Figure 10.1. Block diagram found in biology: arrows represent the flux of biological information between elementary steps. Case of the CD2AP/CIN85 protein involved in T cell responses (from [MAL 03])

Although these block diagrams provide a structured and coherent view of signaling processes in the cell, they do not provide any information concerning space (where precisely are the interactions localized?), time (what is the dynamic of molecular displacement and interaction dynamics?) and structure (is there any structural modification at the nanoscale?) which nowadays are fundamental to a detailed understanding of cell machinery. A precise description of information flux in the cell is difficult to obtain because of the multitude of molecules involved at various spatial and temporal scales.

Although it provides a nanometer resolution, the electronic microscope is unable to work on living samples. However, optical techniques are well adapted to work on living cells and tissues.

With this constraint, instruments have to exhibit dedicated characteristics such as:

- *High sensitivity*: molecular concentrations found in signaling processes are often very low and require high sensitivity (down to the single molecule level) together with large optical magnification. It is also important to find an efficient and specific contrast mechanism to detect the molecules of interest.

- *High spatial and temporal resolving power*: the cell volume exhibits a variety of sub-structures and one aims at localizing the molecular signal with the best accuracy; furthermore a good temporal resolution (μs to ms) is needed to describe most of the biological dynamics.

- *Cell innocuousness*: any relevant study should not perturb the cell and keep it in its natural physiological state.

Although local probe techniques are making progress, they still have limitations in connection with the accurate monitoring of the distance between the probe and the soft biological sample. Optical techniques and especially far field microscopy are still nowadays the best compromise in terms of sensitivity, spatial and temporal resolution, innocuousness and ease of implementation.

Within this framework, this chapter will focus on optical methods and techniques dedicated to studying cell architecture and dynamics through the accurate localization of molecular entities (lipids and proteins).

The first section will briefly present the sizes of cell constituents. The second section will focus on contrast mechanisms that can be generated to study biomolecules at work. Special emphasis will be given to techniques which take advantage of the interaction between ultrashort laser pulses and the biological medium. The third and final section will focus on the spatial resolution problem and will present recent advances for reducing the observation volume below the

diffraction limit. Such techniques use non linear optics or nanophotonic structures located in the vicinity of bio-molecules.

As the nano-biophotonics field is progressing at a great pace, the examples chosen by the authors are far from exhaustive and are subject to change quickly. Nevertheless, the goal of this chapter is to give to physicists some insight into the world of nano-biophotonics.

10.2. The cell: scale and constituents

The spatial and temporal scales found in the cell are very broad and will dictate the properties and characteristics of the optical tools necessary to perform nano-biophotonic studies.

Briefly, a eukaryotic cell has a diameter of $20\mu\text{m}$. Its intracellular volume is separated from the extracellular space by the plasma membrane which is made of a lipid bilayer (thickness 5nm).

The intracellular volume is partitioned into organelles such as the nucleus (which contains genetic information), the Golgi and the endoplasmic reticulum (which synthesize, sort and transport the elementary constituents). As important elementary constituents, proteins are a few nm and exhibit three-dimensional structures which play a crucial role in their functions. They can be localized both in the intracellular space and in the plasma membrane (membrane protein). For more information, the reader should consult a textbook of biology [ALB 02; LOD 03].

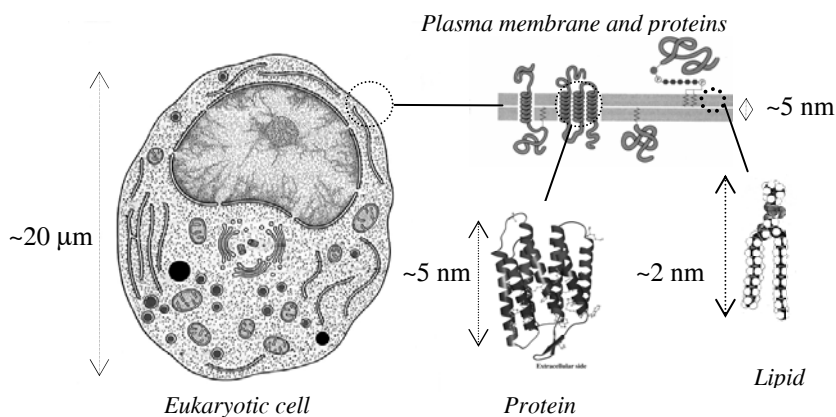


Figure 10.2. The eukaryotic cell and its constituents (typical sizes)

10.3. Origin and optical contrast mechanisms

To probe the cell and its constituents, one needs a contrast mechanism. This can be the simple refraction or absorption of incoming light by the sample (as in standard vision) or it can be more complex-light matter interaction such as fluorescence. In any case, the micron scale of the cell requires us to use microscope objective lenses to concentrate and collect the light. A microscope objective lens is a complex association of lenses and can be simply described by its magnification¹ and numerical aperture (NA). If n stands for the refractive index in which the objective is used, NA is simply related to the maximum angle of focalization θ_{\max} taken from the optical axis²:

$$NA = n \sin \theta_{\max} \quad (1)$$

Furthermore, the Airy disk³ stands for the minimum area an objective can focus an incident beam of wavelength λ . The radius of the Airy disk is given by:

$$w_{\min} = 0.61 \frac{\lambda}{NA} \quad (2)$$

Finally, the resolving power⁴ $d_{x,y}$ of a microscope objective in the plane transverse to the optical axis is still given by equation (2) in the case of a point source⁵.

Along the optical axis, the depth of field d_z gives the distance over which the sample is in focus and is given by:

$$d_z = n \frac{\lambda}{(NA)^2} \quad (3)$$

After these basics, let us discuss the contrast mechanisms used in microscopy.

1 Modern objectives, whose aberrations are corrected at infinity, mention a magnification which is achieved when they are used with their nominal tube lens whose focal length is manufacturer dependent (Leica: 200mm; Nikon: 200mm; Olympus: 180mm; Zeiss: 160mm).

2 An objective with an NA greater than the refractive index n produces evanescent waves.

3 For a wavelength of $\lambda=0.5\mu\text{m}$ and a numerical aperture $NA=1.2$ in water ($n=1.33$), the minimum focal spot diameter is $2w_{\min}=\lambda$.

4 This resolving power is also known as the Rayleigh criterion and stipulates that an imaging optical setup can separate two point sources if they are distant from more than w_{\min} .

5 In the case of bright field microscopy, when the light shone on a sample comes from a condenser whose numerical aperture is $NA_{\text{condenser}}$ the resolving power is given by $d=1.22\lambda/(NA_{\text{condenser}}+NA_{\text{objective}})$.

10.3.1. Classical contrast mechanisms: bright field, dark field, phase contrast and interferometric contrast

Conventional microscopy uses white light to illuminate the sample and uses refraction (phase difference when beams are crossing the sample) and absorption as contrast mechanisms. So called bright field microscopy uses as a spatial contrast the absorption of light and generates a magnified image in the detection plane (known as image plane). Because biological samples exhibit low contrast, various specialized techniques have been developed to improve bright field contrast. A detailed discussion of these techniques is beyond the scope of this chapter, but we recommend that the interested reader consults a reference textbook [MUR 01] or the internet (<http://micro.magnet.fsu.edu/primer>).

Briefly, these specialized techniques use two concepts:

– *Dark field*: The scattered beams at large angles (high spatial frequencies) crossing the sample carry information relating to strong phase or amplitude gradients and are used to generate an image which emphasizes the contours of the sample.

– *Phase contrast and differential interference contrast (DIC)*: These techniques use the phase difference between a set of two beams crossing the sample⁶ to create an interference pattern which reveals the thickness of the sample.

These conventional contrasts have a limited resolving power (equation (2)) and are unable to distinguish two nano-objects separated by a distance below the diffraction limit and which furthermore present a very faint contrast (absorption or refraction). Figure 10.3 shows neuron cells observed with various contrast mechanisms available in classical transmission microscopy (dark field and phase contrast).

⁶ These classes are “scattered” and “non-scattered” beams in the phase contrast and beams with different polarization states in the difference interference contrast (DIC).

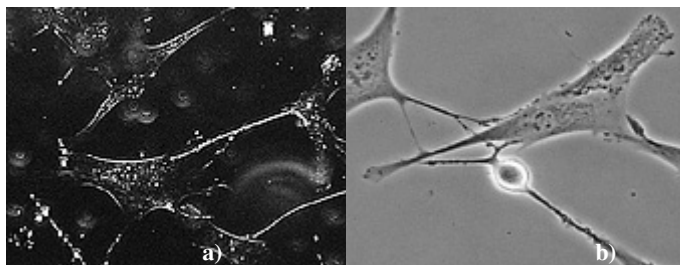


Figure 10.3. Neuron cells imaged with the dark field (A) and the phase contrast technique (B) (from <http://www.zeiss.de/>)

10.3.2. The fluorescence contrast mechanism

Fluorescence is a very efficient contrast mechanism which is widely used in live optical microscopy, especially in the detection of molecular species.

Fluorescence is the process of light emission from molecules experiencing electronic transitions following photo-activation⁷.

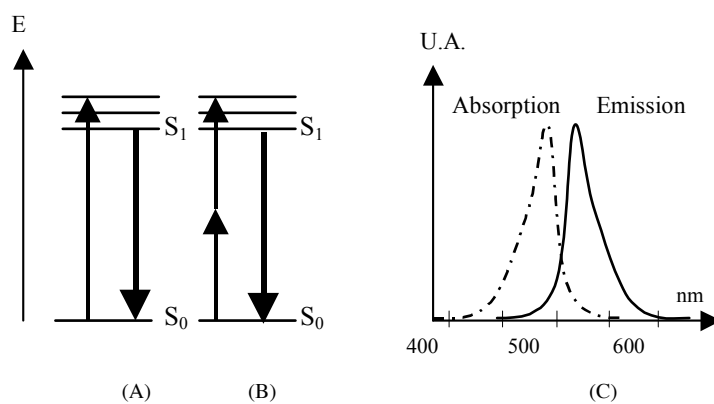


Figure 10.4. Jablonski diagram of 1-photon (A) and 2-photon (B) fluorescence processes. (C) Typical fluorescence absorption and emission spectra of a dye molecule

⁷ Fluorescence is a sub-class of luminescence which indicates the various processes leading to molecular light emission (chemical, mechanical, biological, etc.).

As depicted by the schematic Jablonski diagram in the energy space, the excitation beam is absorbed and populates the S_1 electronic state from which the luminescence is produced through a radiative relaxation to S_0 (Figure 10.4A–B). The spectral shift between the absorption and emission maxima (Figure 10.4C) is called the Stokes shift. The optical instruments which use the fluorescence contrast often require strong optical filtering to separate fluorescence from the excitation light. If the transition from the fundamental level S_0 to the excited level S_1 corresponds to the absorption of a single photon, the resulting fluorescence is called a 1-photon fluorescence process (Figure 10.4A).

If the transition from S_0 to S_1 requires the simultaneous absorption of two photons, the resulting fluorescence is called a 2-photon absorption or fluorescence process⁸ (Figure 10.4B). Note that in this case the excitation wavelength is twice the wavelength of maximum absorption shown in Figure 10.4C. 2-photon fluorescence is a quadratic process in excitation field intensity and is very unusual as compared to a 1-photon process; to be observed it requires high peak power that can be found in ultrashort laser pulses⁹.

The success of fluorescence contrast is mainly due to the excellent quantum efficiency¹⁰ of some dyes together with the ability to hybridize these dyes with various bio-molecules (lipids and proteins).

Since the discovery of the green fluorescent protein (GFP) and the possibility of including its genome in a host cell to tag a specific protein [BRE 97; TSI 98], fluorescence microscopy has been enjoying a strong revival. The resulting GFP chimer protein is produced by the cell and possesses the properties of the native protein together with being fluorescent. Figure 10.5 shows a confocal microscopy image of HeLa cells expressing a membrane protein merged with GFP.

8 The expression “2-photon fluorescence” should more accurately be replaced by “2-photon absorption” as 2 photons are absorbed from the excitation field.

9 The 1-photon absorption cross-section of a dye molecule is around $\sigma_1=10^{-16}\text{cm}^2$ whereas it goes down to $\sigma_2=10^{-49}\text{cm}^4\cdot\text{s}$ in the case of a 2-photon process.

10. As an example, the quantum efficiency of Fluoresceine and Rhodamine dye reaches 0.9 (ratio between the number of absorbed and emitted photons).

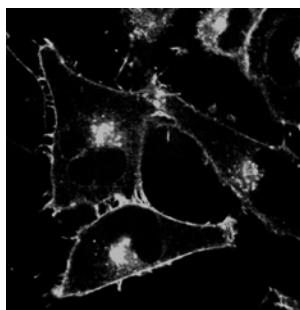


Figure 10.5. 1-photon fluorescent image of the ABC1 membrane protein merged with GFP. The Golgi and the plasma membrane are visible (courtesy Yannick Hamon – CIML)

One drawback of fluorescence is the photobleaching of dye molecules when they are excessively illuminated with the excitation beam¹¹. Semiconductor quantum dots are less subject to photobleaching and offer an attractive alternative to labeling biomolecules [ALI 04].

10.3.2.1. The lifetime contrast

It is possible to use the excited electronic state lifetime of the fluorescent molecule to generate a contrast. This lifetime contrast is known as FLIM (Fluorescence Lifetime Imaging Microscopy) and has the interesting property of being independent of the dye concentration inside the sample. FLIM images are obtained by recording the dye lifetime for each point in the sample. This lifetime is dependent on the local dye environment together with the physiological conditions of the cell (Figure 10.6).

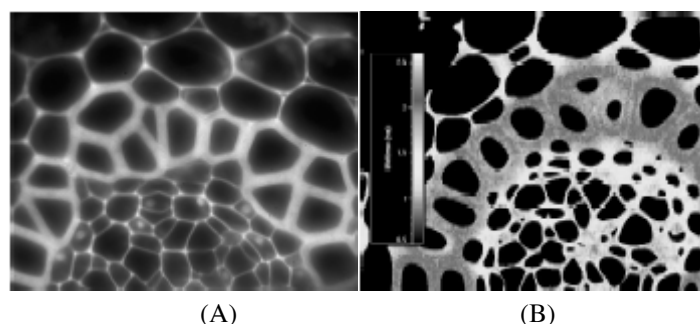


Figure 10.6. Fluorescent image (A) and FLIM image (B) of plant tissue (convallaria). The lifetime range is between 0.5ns and 2.5ns (from <http://www.lambert-instruments.com>)

¹¹ Typically a fluorescent molecule emits between 10^4 and 10^6 photons before it photobleaches.

This technique is of particular interest when studying fluorescence resonant energy transfer¹² (FRET) between two fluorescent molecules. Instead of monitoring the increase in fluorescence of the acceptor when FRET occurs, it is much more interesting to study the lifetime decrease of the donor.

The FLIM technique generally uses sub-picosecond laser pulses to detect the nanosecond lifetime of dye molecule and its variation.

10.3.2.2. *Resolving power in fluorescence microscopy*

The optical resolution achievable in fluorescence microscopy is essentially limited by the diffraction limit given by equation (2). Therefore, it is impossible to distinguish two molecular emitters separated by a distance less than $d_{x,y}=w_{\min}$ in the plane perpendicular to the optical axis. This Rayleigh criterion deals with the ability of the optical system to separate two entities, nevertheless it does not forbid localizing a single emitter with an accuracy better than $d_{x,y}$.

This case is precisely the one found in single molecule detection where a nanometer size emitter appears as a diffraction pattern (Airy disk) in the microscope image plane. This Airy disk is well described by $(J_1(r)/r)^2$, where J_1 is the first order Bessel function and r the transverse spatial coordinate.

If the signal to noise ratio is good enough, it is possible to follow the Airy disk center with a precision much better than the diffraction limit (Figure 10.7).

It is therefore possible to follow the trajectory of a single fluorescent molecule with an accuracy of a few tens of nm. In this specific case, far field optics can even reach a resolution of a few nm¹³.

12 FRET: when two fluorescent molecules are a few nm apart, an electromagnetic energy transfer can occur from the acceptor molecule to the donor molecule. This energy transfer is possible if the absorption band of the acceptor overlaps the emission band of the donor and follows a law in $1/r^6$.

13 In single particle tracking (fluorescent molecules and beads) [NIS 03] and [YIL 04] claim a precision of a few nm.

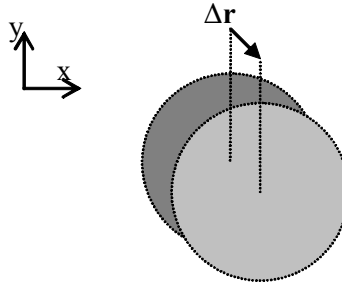


Figure 10.7. Super resolution in single particle tracking: the Airy disk center can be localized with a nm accuracy if the signal to noise ratio is good enough

Confocal microscopy

To achieve the best transverse resolution $d_{x,y}$, one has to clearly identify the Airy disk corresponding to a single fluorescent molecule. This is a hard task when fluorescent light also comes from emitters located beyond or above the depth of field d_z . This is often the case in 1-photon fluorescence where all the emitters located in the excitation path are activated. The classical technique for getting rid of this parasitic fluorescence is to place a pinhole in front of the detector (Figure 10.8A). This so called “confocal” set-up aims at stopping the fluorescent light coming from emitters located above or under the depth of field area. Furthermore the pinhole spatially filters a transverse area corresponding to the image of the pinhole in the object plane. In all, this spatial filtering defines an “observation volume” whose best transverse¹⁴ and longitudinal extension are given by [PAW 95].

$$d_{xy}^{confoc} = 0.4 \frac{\lambda}{NA} \quad ; \quad d_z^{confoc} = 1.4n \frac{\lambda}{(NA)^2} \quad (4)$$

One can see that transverse extension is slightly better than in wide field microscopy (w_{min} in equation (2)) whereas the longitudinal extension is slightly larger than the depth of field d_z . Nevertheless, the signal to noise ratio coming from this confocal observation volume¹⁵ is excellent. In confocal microscopy the image is built by raster scanning the observation volume through the sample.

¹⁴ One speaks of “best resolution” when the pinhole radius divided by the optical magnification equals w_{min} . For a larger pinhole, the observation volume is larger.

¹⁵ In a first approximation one can consider that the transverse and longitudinal extensions of the optimal observation volume are equal to $2d_{xy}^{confoc}$ and $2d_z^{confoc}$ respectively. For a

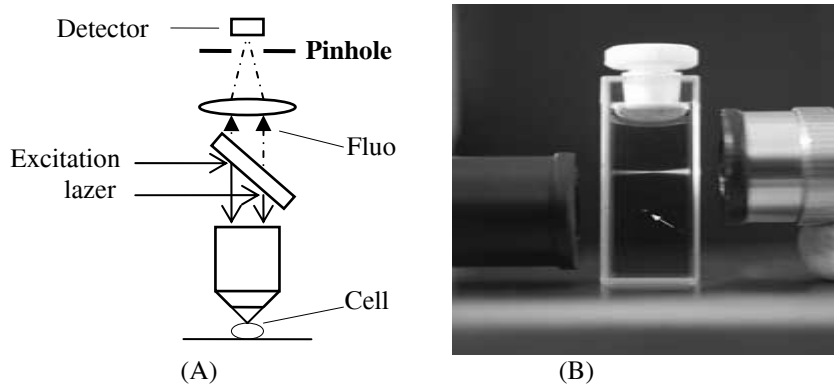


Figure 10.8. Confocal microscopy set-up (A), in the case of 2-photon fluorescence the confocal pinhole can be removed. (B) 1-photon fluorescence (top) and 2-photon fluorescence (arrow) (from Bio-Rad website: <http://www.microscopy.bio-rad.com>)

In the case of 2-photon fluorescence [DEN 90; DIA 02], the confocal pinhole can be removed because this unlikely process takes place only at the very focal plane where the excitation beam is the sharpest (Figure 10.8B). It is interesting to note that, without a confocal pinhole, the 2-photon observation volume is twice as large as in the 1-photon case (essentially because the excitation wavelength is twice as large). This is the same for the resolution, which is degraded by a factor of 2. Nevertheless, it is possible to recover the 1-photon resolution by using a pinhole¹⁶.

One real advantage of 2-photon fluorescence is its ability to excite simultaneously chemically different fluorescent molecules with the same infra-red (IR) pulse. This is possible because the 2-photon absorption cross-sections of common fluorescent probes spectrally overlap [ZIP 03].

10.3.3. Non-linear microscopy

In non-linear microscopy the contrast mechanism uses light-matter interaction, which belongs to the field of non-linear optics (see Chapter 5 in this book). Advances in this field take advantage of recent progress in ultra-fast laser systems and the associated strong optical peak power which it is possible to generate. As

$\lambda=0.5\mu\text{m}$ wavelength and a 1.2 numerical aperture in water one gets $2d_{xy}^{\text{confoc}} = 0.33\mu\text{m} \approx 2/3 \lambda$ and $2d_z^{\text{confoc}} = 1.3 \mu\text{m} \approx 2.5 \lambda$.

¹⁶ Nevertheless, photobleaching in 2-photon fluorescence is larger than in the 1-photon case.

discussed above, 2-photon fluorescence is a good example of a non-linear contrast mechanism.

10.3.3.1. Second harmonic generation (SHG)

SHG is a non-linear process where a fundamental wave (pulsation ω) interacts with a non centro-symmetric medium to generate a harmonic wave (pulsation 2ω). The harmonic field is coherent with the fundamental field and is generated in specific directions which follow the phase matching condition. These specific directions are related to the distribution and orientation of the induced dipoles in the interaction volume [MER 01] (Figure 10.9).

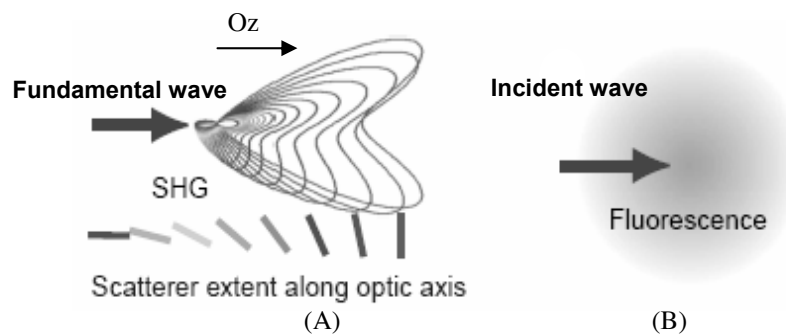


Figure 10.9. (A) Relation between the generated harmonic wave and the orientation of the induced dipoles. (B) On the contrary fluorescence (1 or 2 photons) has an isotropic radiation pattern [ZIP 03]

This effect can be used to image the cell membrane (Figure 10.10).

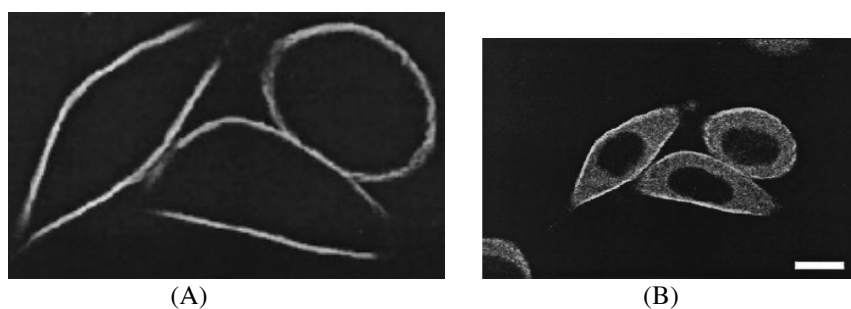


Figure 10.10. Non-linear molecules (Di-6-ASBPS) are introduced in a cell. The molecules inserted in the membrane create a non centro-symmetric medium and generate SHG (A) whereas the molecules in the cytoplasm have no privileged directions and generate only fluorescence (B) (after [MOR 01])

In the previous example, exogenous non-linear molecules are used to create SHG but it is possible to use endogenous structures such as collagen, which naturally present a non centro-symmetric structure to generate SHG efficiently.

Using high peak power it is also possible to generate third harmonic generation (THG) [MUL 98].

10.3.3.2. *Coherent anti-Stokes Raman scattering (CARS)*

Contrary to SHG which is a non-resonant process, stimulated Raman scattering uses vibrational molecular levels to generate a contrast mechanism which reveals the local density of a specific molecular bond.

This process, known as CARS (Coherent Anti-Stokes Raman Scattering), does not require labeling or staining and can be used directly on fresh living samples. Although four wave mixing processes are not new in microscopy [DUC 82], advances in ultrafast laser systems have revolutionized the technique [ZUM 99].

10.3.3.2.1. Spontaneous Raman

In Raman scattering, an incoming laser optical wave (pulsation ω_L) experiences an inelastic scattering by a molecule and is converted into a Stokes wave (pulsation ω_S) and an anti-Stokes wave (pulsation ω_{AS}). The frequency shift between the incoming and the scattered waves depends on the molecular vibrational levels (pulsation Ω_R) such that $\omega_L - \omega_S = \omega_{AS} - \omega_L = \Omega_R$. In the photon picture, Stokes and anti-Stokes waves are associated to an absorption process which starts from the fundamental and the excited vibrational levels respectively (Figure 10.10A–B). Note that the upper levels involved in the CARS process are *a priori* virtual (dashed lines in Figure 10.11) but can be real (electronic levels) in the resonant Raman case.

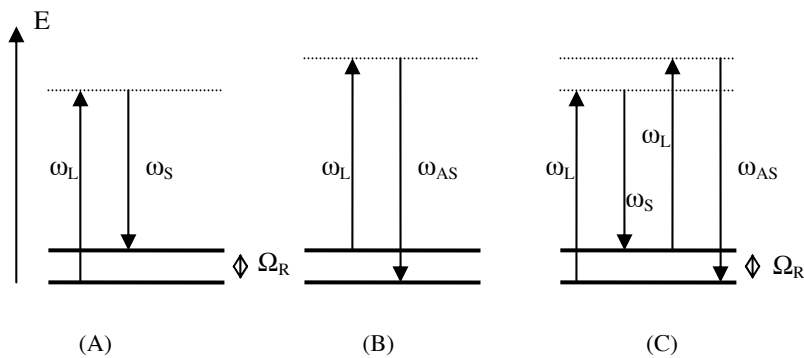


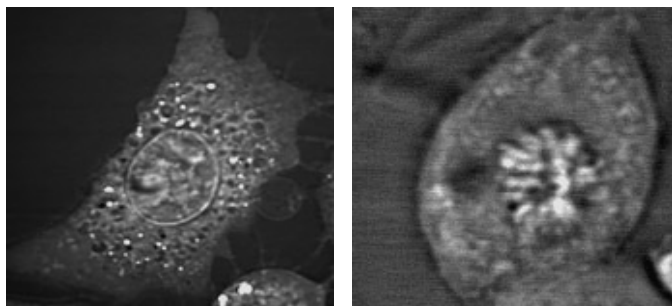
Figure 10.11. Spontaneous Raman: Stokes wave generation (A) and anti-Stokes wave generation (B). CARS process: (C) the four wave mixing process creates the anti-Stokes wave

Inelastic scattering which creates the anti-Stokes wave is very unlikely because it starts from the vibrational excited level. For this reason only the Stokes wave can be detected in practice. The spectral positions of the Stokes line give valuable information on the molecular bond and their density in the observed sample; such information is the essence of Raman scattering. Using such a technique in living tissue it has been possible to reveal the localization of a cancerous cell tumor [CHO 02]. This inelastic scattering process is very weak¹⁷ compared to fluorescence and cannot be implemented at a sub-cellular level¹⁸.

10.3.3.2.2. CARS

The essence of CARS is to populate the excited vibrational level by means of stimulated emission. This non-linear optical process can be produced at the focal point of a microscope objective lens if the Laser and Stokes waves are overlapping spatially and temporally and are such that $\omega_L - \omega_S = \Omega_R$. In this case a four wave mixing process takes place, generating an anti-Stokes wave whose pulsation is $\omega_{AS} = 2\omega_L - \omega_S - \omega_R$.

In practice, one must tune the frequency difference between the Laser and Stokes pulses to match the desired vibrational chemical bond. After careful tuning to overlap these two pulses in time and space, one simply raster scans the sample, as in confocal microscopy, to build an image of the anti-Stokes signal (Figure 10.12).



(A)

(B)

Figure 10.12. CARS images: (A) NIH-3T3 cells: when $\omega_L - \omega_S$ is tuned to the CH_2 vibration, one can distinguish the nucleus membrane and the mitochondria. (B) Nucleus image: when $\omega_L - \omega_S$ is tuned to a DNA vibration, chromosomes can easily be seen (after [CHE 02])

¹⁷ Raman cross-sections are in the 10^{-31} – 10^{-29} cm^2 range. The largest values are obtained in resonant Raman. This should be compared with the absorption cross-section of a good dye which reaches $\sigma_1 = 10^{-16}$ cm^2 .

¹⁸ Spontaneous Raman can be strongly enhanced (up to 10^{14}) by metallic nanoparticles. This effect is known as SERS (Surface Enhanced Raman Scattering) and is interesting in nanobiophotonics [KNE 02].

The spatial resolution of a CARS microscope is similar to the resolution of 2-photon fluorescence.

We have shown some contrast mechanisms that are able to build images with molecular information on bio-samples. All of these techniques are fundamentally limited by the laws of diffraction. As we will see in the next section, there are some clever techniques which allow us to push the ability of these optical systems further.

10.4. Reduction of the observation volume

We learned from Optics books that the resolution of optical microscopes is limited by the laws of diffraction [ABB 73]. At best, a confocal microscope reaches the resolution given by equation (4) and conventional optical methods are unable to distinguish two identical objects when separated by a distance smaller than this limit value. However, as explained above, the diffraction limit does not prevent us from detecting single molecules that are much smaller than the diffraction limit if they are sufficiently far apart. Moreover, when spectrally different, they can be *a priori* “separable” whatever their inter-distance (in this case the resolution depends on the signal to noise ratio). Reduction of the observation volume is still a crucial problem for resolving small details or detecting identical single molecules at high concentration. In biology this is the case for most fluorescently-labeled molecules. When the surface concentration is larger than a few tens of molecules per μm^2 or the volume concentration larger than a few tens of nanoMoles/l, molecules cannot be optically separated.

How can the observation volume be reduced below the limit imposed by diffraction? Optical methods based on non-linear [HEL 03] and near field optics [LAN 01] have recently been proposed to bypass this limit.

For photo-excitation the size and shape of the observation volume depend on both the properties of the excitation field and the optical system which collects the light. To describe these characteristics it is appropriate to introduce the Molecular Detection Efficiency function (MDE). In the linear regime it is defined for every spatial coordinate \mathbf{r} as the product of excitation intensity I_e by the collection efficiency function (CEF):

$$MDE(\mathbf{r}) = CEF(\mathbf{r}) \cdot I_e(\mathbf{r}) \quad (5)$$

The MDE function gives locally the power emitted by a point source which is collected by collection optics. The methods which are proposed to reduce the observation volume aim at modifying the excitation and/or collection efficiency.

10.4.1. Far field methods

The optical resolution of a microscope is related to the size of the smallest focus spot (equations (2) and (4)). By using shorter optical wavelengths and higher numerical aperture objectives, it is theoretically possible to reduce this spot. However, living samples are easily damaged for optical wavelengths below 350nm and the half aperture angle is technically limited to 75° ¹⁹.

10.4.1.1. 4Pi microscopy

The numerical aperture of the microscope's collection system can be increased by combining the aperture of two apposite objectives (Figure 10.13B). These techniques are called 4Pi [HEL 92] or I5-M [GUS 99]. They lead at best to a sevenfold increase in the axial resolution. Two contra-propagating fields are focussed at the same position by two apposite objectives.

The central spot has a width of $\sim\lambda/4n \approx 100\text{nm}$ along the optical axis but is surrounded by interference fringes with a period of $\sim\lambda/2n \approx 200\text{nm}$, whose number and amplitude increase as the numerical aperture decreases. To reduce the side-lobes' contribution different methods have been proposed: spatial filtering, 2-photon excitation, and using the difference between the excitation and fluorescence wavelengths. This latter strategy is based on the fact that when excitation and fluorescence wavefronts interfere on the sample and the detector, respectively, the associated side-lobes do not coincide anymore. When combined with image restoration, such methods yield the optical resolution down to $\sim 100\text{nm}$ in the three spatial dimensions. 4Pi microscopy requires a precise adjustment of the two apposite objectives, which can make its implementation difficult. This technique of far field optics is remarkable.

¹⁹ Some manufacturers propose NA=1.45 objectives working in a n=1.5 immersion medium.

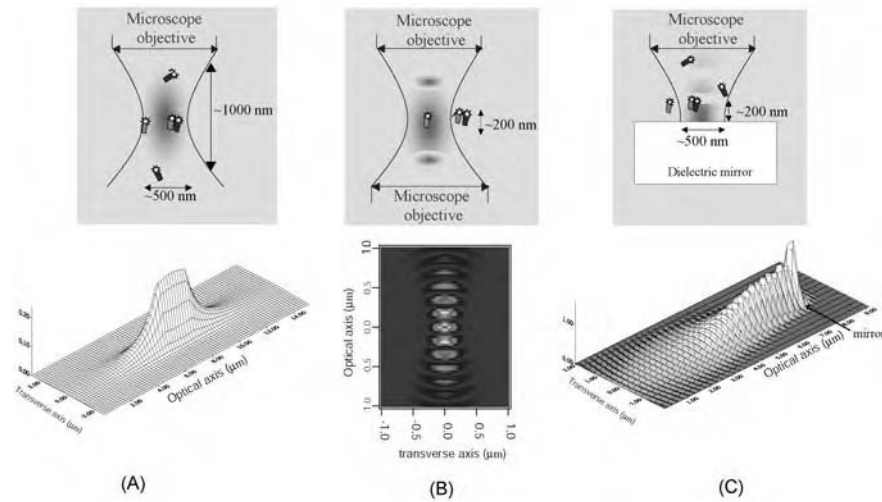


Figure 10.13. Detection volume (MDE) obtained in confocal microscopy (A), in 4Pi microscopy using two opposite objectives (B) and in a set-up using a mirror at the focal plane of a confocal microscope (C)

10.4.1.2. Microscopy on a mirror

In our group we proposed a method that combines high numerical aperture and high axial resolution. We used a mirror located at the focal plane of the objective lens, in order to reflect both the excitation and emission beams [LEN 02; RIG 03]. The interference of the excitation incident and reflected beams gives rise to an axial modulation of the excitation intensity with a period of $\sim \lambda/2n \approx 200$ nm, as in 4Pi microscopy. Single fluorescent molecules diffusing through the collection volume emit a fluorescent signal that fluctuates with time. The diffusion of the molecules through a bright fringe produces a fluorescence fluctuation whose duration depends on interfringe spacing and the diffusion coefficient. The temporal analysis of these fluctuations, which is called fluorescence correlation spectroscopy (FCS), provides information on a molecule's dynamics, diffusing in a volume as small as $\sim \lambda/2n$ along the optical axis. Moreover, because the mirror redirects the fluorescence beam towards the objective, the collected signal is enhanced (>fourfold) as compared to the standard confocal set-up. Figure 10.13C shows the MDE obtained in the presence of a mirror.

10.4.1.3. Stimulated emission depletion: STED

Far field linear methods are not suitable for reducing the observation volume below $\lambda/2n$. In free space, a possible method consists of using a non-linearity

between the excitation field and the signal to be detected (e.g. the fluorescence). In 1994 Hell and Wichmann [HEL 94] proposed using the saturation of a two-state electronic transition to locally forbid fluorescence emission.

The method consists of depleting a fluorescent molecular state (first excited) by a focussed beam which exhibits a non-zero intensity point. In one *modus operandi*, which is called stimulated emission depletion (STED) [KLA 00], fluorophore, which are first excited by a focussed pulse to a state S_1 (Figure 10.14A), are stimulated down to their ground state S_0 by a second beam with a donut shape²⁰ (Figure 10.14C). Only fluorophores which are in the central region of the donut emit a fluorescence signal that can be detected. Because depletion is a non-linear effect, the non-depleted central region can be smaller than the diffraction limit²¹.

This method enables us to reduce the observation volume down to²² 0.67×10^{-18} l (Figure 10.14C). The observation volume can be scanned through the sample, as in confocal microscopy, and high resolution images can be obtained. One of the current obstacles to STED microscopy rests in the limited number of “good” fluorophores that can be efficiently depleted. Nevertheless, this method has opened a new window in microscopy.

20 Such a shape is obtained by placing a phase mask before the microscope objective.

21 Superresolution is obtained by virtue of non-linearity, whereas the excitation and depletion beams are diffraction-limited.

22 The non-depleted final volume is roughly a sphere with a 100nm diameter.

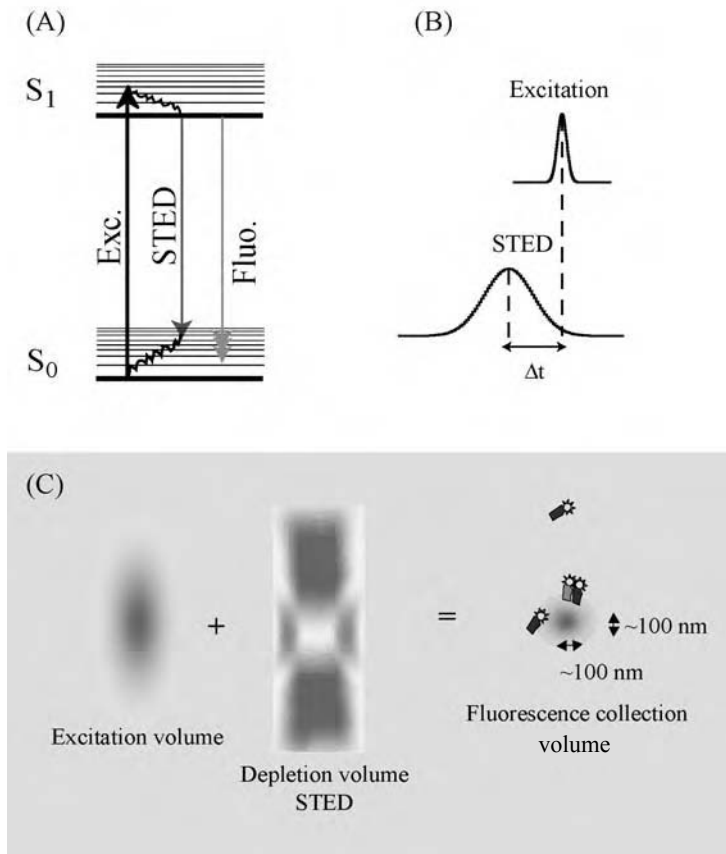


Figure 10.14. Scheme of Stimulated Emission Depletion (STED) microscopy. (A) Fluorophore energy diagram. One molecule, which is excited in state S_1 can be brought down its fundamental level S_0 either by spontaneous or stimulated emission. (B) To saturate depletion, the STED pulse must be intense and longer than the fluorescence lifetime of the molecule in the state S_1 . Excitation and depletion pulses are synchronized but temporally delayed to deplete the S_1 state before spontaneous relaxation. (C) The depletion beam is superimposed on the excitation beam but exhibits zero-intensity at the focus point. The saturated depletion reduces strongly the size of the fluorescence collection volume (from [HEL 03])

10.4.2. Near field methods

To circumvent the diffraction limit, near field methods can alternatively be used. The advent of near field microscopy (in particular Atomic Force Microscopy –

AFM), which uses a very sharp tip to scan the surface of the sample²³, has opened the way for nanometric observation.

The diffraction limit as expressed by equation (2) is only correct for far field, in other words when the propagating waves can propagate and be focussed. By using evanescent waves located in the vicinity of dielectric or metallic structures, whose curvature radii are smaller than the wavelength²⁴, high intensity spots whose extensions are much smaller than the diffraction limit can be obtained.

10.4.2.1. NSOM

Near field scanning optical microscopy (NSOM) enables fluorescence imaging to be performed with a resolution down to a few tens of nm²⁵. The size of the NSOM tip's aperture (Figure 10.15A) reduces the size of the detection volume in order to detect single molecules at a concentration of up to 100/ μm^2 [GAR 00].

Most NSOM applications in biology are concerned with isolated and fixed samples²⁶, for example fluorescent chromosomes [MOE 96] or cytoskeleton isolates [BET 93]. To our knowledge, there has been no report on live cells in physiological conditions, despite the efforts of a few teams.

10.4.2.2. TIRF

Total Internal Reflection Fluorescence (TIRF) also benefits from the properties of the evanescent field. At low angles (below the critical angle), total internal reflection results when light propagating within a high optical index medium (e.g. glass) reaches an interface with a lower optical index medium (e.g. aqueous solution). Although the light is fully reflected, an evanescent field is generated which extends beyond the interface into the aqueous solution over a distance in the order of 100nm²⁷ (Figure 10.15B). This method can be used to image the contact area between a cell and a substrate [TOO 01] (Figure 10.16) or to analyze ligand-receptor associations [LIE 03].

23 Tip to sample distance is in the order of a few nm.

24 There is theoretically no limit if evanescent waves with sufficiently large wave vectors are present.

25 See Chapter 7 on near field optics.

26 The biological sample is fixed due to a chemical which makes it more rigid.

27 The evanescent wave penetrates over a distance $d = \lambda / 4\pi(n_1^2 \sin^2 \theta_1 - n_2^2)^{-1/2}$ where n_1 is the optical index of the high index medium, n_2 the optical index of the low index medium and θ_1 the incident angle to the normal.

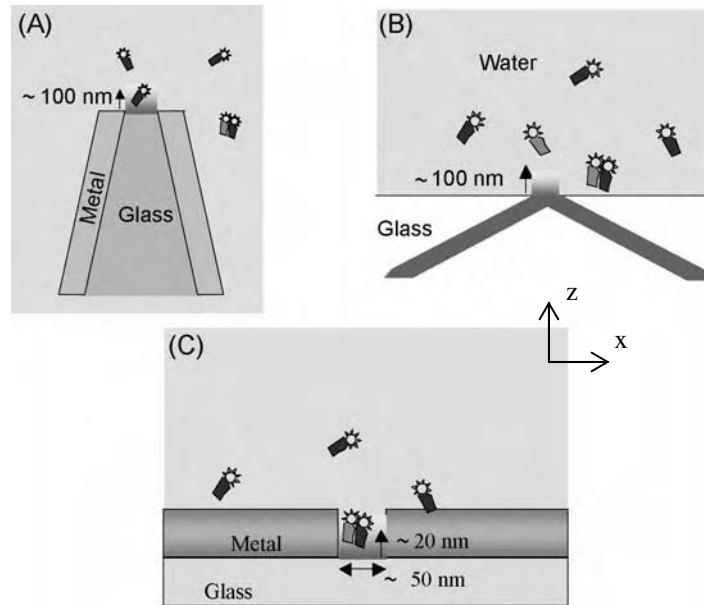


Figure 10.15. Near field methods and reduction of the observation volume. (A) NSOM. (B) TIRF. (C) Single-molecule detection in sub-wavelength metallic apertures

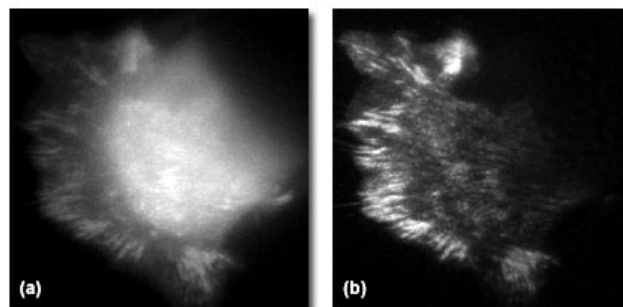


Figure 10.16. Images of a fluorescently-labeled cell (a) wide field fluorescence image; (b) TIRF image. In TIRF, the only region which is close to the cover-slip surface (a few tens of nm above) is observed (from Nikon Microscopy: <http://www.microscopyu.com>)

10.4.2.3. Nanoholes

TIRF uses a planar observation interface and therefore its transverse resolution (in x,y plan – see Figure 10.15) is diffraction-limited. The shaping of

excitation/detection volumes is also possible in 3D due to structures with “defects”, whose size is smaller than the optical wavelength. For example, sub-wavelength apertures in metallic films can be used to define nanometric detection volumes [LEV 03] (Figure 10.15c). In this example, a focussed beam illuminates a single nanohole; because the excitation field is evanescent inside the hole, the detection volume can be as small as 10^{-21} l. Because of such structures, single molecules can be detected up to 100 μ M concentration, making studies of low affinity molecular associations possible. Moreover, when the aperture diameter is about one third of the light wavelength (150 nm) the detected fluorescence count rate per molecule is drastically increased (up to 6.5) as compared to larger holes or open solution [RIG 05]. By taking benefit of this significant enhancement, such apertures could serve as efficient nano-optical sources or nano-wells for fast and highly parallel molecular analysis at high concentration.

10.5. Conclusion

By presenting a few examples we have shown that optical microscopy enables us to study the organization of biological objects both spatially and temporally. While fluorescence makes the detection of single molecules possible, label-free methods can produce complementary information, based on vibrational contrast for example. Even if optoelectronic systems can be efficiently used to perform fast single spot measurements, crucial improvements need to be made to increase the speed of imaging scanners and high-sensitivity cameras. The development of new fluorescent probes is also an important area.

Because classical optical systems are spatially limited by the laws of diffraction, the detailed architecture of live cells can only be tackled by new methods. In this chapter we presented a few strategies which have been proposed in wide and near field optics to bypass the diffraction limit. These new tools will be of benefit in biology and will hopefully reveal the details of information fluxes in the cell, and finally replace the arrowheads in Figure 10.1.

10.6. References

- [ABB 73] Abbe E. 1873. Beiträge zur Theorie des Mikroskops und der mikroskopischen Wahrnehmung. *Arch. Mikroskop. Anat.* 9: 413–420.
- [ALB 02] Alberts B, Johnson A, Lewis J, Raff M, Roberts K, Walter P. 2002. *Molecular Biology of the Cell*, Garland Science Publishing.
- [ALI 04] Alivisatos P. 2004. The use of nanocrystals in biological detection. *Nat. Biotechnol.* 22 (1): 47–52.

- [BET 93] Betzig E, Chichester RJ. 1993. Single molecules observed by near field scanning optical microscopy. *Science* 262 (5138): 1422–1428.
- [BRE 97] Brejc K, Sixma TK, Kitts PA, Kain SR, Tsien RY, Ormo M, Remington SJ. 1997. Structural basis for dual excitation and photoisomerization of the *Aequorea victoria* green fluorescent protein. *Proc. Natl. Acad. Sci. USA* 94 (6): 2306–11.
- [CHE 02] Cheng JX, Jia YK, Zheng G, Xie XS. 2002. Laser-scanning coherent anti-Stokes Raman scattering microscopy and applications to cell biology. *Biophys. J.* 83 (1): 502–9.
- [CHO 02] Choo-Smith LP, Edwards HG, Endtz HP, Kros JM, Heule F, Barr H, Robinson JS, Jr., Bruining HA, Puppels GJ. 2002. Medical applications of Raman spectroscopy: from proof of principle to clinical implementation. *Biopolymers* 67 (1): 1–9.
- [DEN 90] Denk W, Strickler JH, Webb WW. 1990. Two-photon laser scanning fluorescence microscopy. *Science* 248 (4951): 73–76.
- [DIA 02] Diaspro A (ed). 2002. *Confocal and Two-Photon Microscopy, Foundations, Applications and Advances*, New York: Wiley-Liss.
- [DUC 82] Ducan MD, Reintjes J, Manuccia TJ. 1982. Scanning coherent anti-stokes Raman microscope. *Opt. Lett.* 7 (8): 350–352.
- [GAR 00] Garcia-Parajo MF, Segers-Nolten GM, Veerman JA, Greve J, van Hulst NF. 2000. Real-time light-driven dynamics of the fluorescence emission in single green fluorescent protein molecules. *Proc. Natl. Acad. Sci. USA* 97 (13): 7237–7342.
- [GIL 02] Gilman AG, Simon MI, Bourne HR, Harris BA, Long R, Ross EM, Stull JT, Taussig R, Arkin AP, Cobb MH *et al.* 2002. Overview of the Alliance for Cellular Signaling. *Nature* 420 (6916): 703–706.
- [GUS 99] Gustafsson MGL, Agard DA, Sedat JW. 1999. I5M: 3D widefield light microscopy with better than 100 nm axial resolution. *J. Microsc.* 195 (1): 10–16.
- [HEL 92] Hell S, Stelzer EHK. 1992. Properties of a 4Pi confocal fluorescence microscope. *J. Opt. Soc. Am. A* 9 (12): 2159–2166.
- [HEL 94] Hell SW, Wichmann J. 1994. Breaking the diffraction resolution limit by stimulated emission: stimulated-emission-depletion fluorescence microscopy. *Opt. Lett.* 19 (11): 780–782.
- [HEL 03] Hell SW. 2003. Toward fluorescence nanoscopy. *Nature Biotech.* 21 (11): 1347–1355.
- [KLA 00] Klar TA, Jakobs S, Dyba M, Egner A, Hell SW. 2000. Fluorescence microscopy with diffraction resolution barrier broken by stimulated emission. *Proc. Natl. Acad. Sci. USA* 97 (15): 8206–8210.
- [KNE 02] Kneipp K, Kneipp H, Itzkan I, Dasari RR, Feld MS. 2002. Surface-enhanced Raman scattering and biophysics. *J. Phys.: Condens. Matter.* 14 (18): R597–R624.
- [LAN 01] de Lange F, Cambi A, Huijbens R, de Bakker B, Rensen W, Garcia-Parajo M, van Hulst N, Figdor CG. 2001. Cell biology beyond the diffraction limit: near field scanning optical microscopy. *J. Cell. Sci.* 114 (23): 4153–4160.

- [LEN 02] Lenne PF, Etienne E, Rigneault H. 2002. Subwavelength patterns and high detection efficiency in fluorescence correlation spectroscopy using photonic structures. *Appl. Phys. Lett.* 80 (22): 4106–4108.
- [LEV 03] Levene MJ, Korlach J, Turner SW, Foquet M, Craighead HG, Webb WW. 2003. Zero-mode waveguides for single-molecule analysis at high concentrations. *Science* 299(5607): 682–686.
- [LIE 03] Lieto AM, Cush RC, Thompson NL. 2003. Ligand-receptor kinetics measured by total internal reflection with fluorescence correlation spectroscopy. *Biophys. J.* 85 (5): 3294–3302.
- [LOD 03] Lodish HF. 2003. *Molecular Cell Biology*. New York: WH Freeman and Company.
- [MAL 03] Malissen B. 2003. Immunology. Switching off TCR signaling. *Science* 302 (5648): 1162–1163.
- [MER 01] Mertz J, Moreaux L. 2001. Second harmonic generation by focussed excitation of inhomogeneously distributed scatterers. *Opt. Commun.* 196 (16): 325–330.
- [MOE 96] Moers MH, Kalle WH, Ruiter AG, Wiegant JC, Raap AK, Greve J, de Grooth BG, van Hulst NF. 1996. Fluorescence *in situ* hybridization on human metaphase chromosomes detected by near field scanning optical microscopy. *J. Microsc.* 182 (Pt 1): 40–45.
- [MOR 01] Moreaux L, Sandre O, Charpak S, Blanchard-Desce M, Mertz J. 2001. Coherent scattering in multi-harmonic light microscopy. *Biophys. J.* 80 (3): 1568–1574.
- [MUL 98] Muller M, Squier J, Wilson KR, Brakenhoff GJ. 1998. 3D microscopy of transparent objects using third-harmonic generation. *J. Microsc.* 191 (3): 266–274.
- [MUR 01] Murphy DB. 2001. *Fundamentals of Light Microscopy and Electronic Imaging*, New York: Wiley-Liss.
- [NIS 03] Nishiyama M, Higuchi H, Ishii Y, Taniguchi Y, Yanagida T. 2003. Single molecule processes on the stepwise movement of ATP-driven molecular motors. *Biosystems* 71 (1–2): 145–156.
- [PAW 95] Pawley JB. 1995. *Handbook of Biological Confocal Microscopy*, New York: Plenum.
- [RIG 03] Rigneault H, Lenne PF. 2003. Fluorescence correlation spectroscopy on a mirror. *J. Opt. Soc. Am. A* 20 (10): 2203–2214.
- [RIG 05] Rigneault H, Capoulade J, Dintinger J, Wenger J, Bonod N, Popov E, Ebbesen T, Lenne PF. 2005. Enhancement of single molecule fluorescence detection in subwavelength apertures. *Phys. Rev. Lett.* 95 (11): 117401–117404
- [TOM 01] Toomre D, Manstein DJ. 2001. Lighting up the cell surface with evanescent wave microscopy. *Trends Cell. Biol.* 11 (7): 298–303.
- [TSI 98] Tsien RY. 1998. The green fluorescent protein. *Annu. Rev. Biochem.* 67: 509–44.
- [YIL 04] Yildiz A, Tomishige M, Vale RD, Selvin PR. 2004. Kinesin walks hand-over-hand. *Science* 303 (5658): 676–678.

- [ZIP 03] Zipfel WR, Williams RM, Webb WW. 2003. Nonlinear magic: multiphoton microscopy in the biosciences. *Nature Biotechnol.* 21 (11): 1369–1377.
- [ZUM 99] Zumbusch A, Holtom GR, Xie XS. 1999. Vibrational microscopy using coherent anti-Stokes Raman scattering. *Phys. Rev. Lett.* 82 (20): 4014–4017.

List of Authors

Maria CHAMARRO
Paris Nanosciences Institute, France
chamarro@gps.jussieu.fr

Frédérique DE FORNEL
Optical Near Field Team
LPUB-CNRS
Dijon, France
ffornel@u-bourgogne.fr

Claude DELALANDE
Pierre Aigrain Laboratory
École Normale Supérieure
Paris, France
claude.delalande@lpa.ens.fr

Philippe DELAYE
Charles Fabry Laboratory of the Optical Institute
CNRS and Paris Sud University
Orsay, France
Philippe.delaye@iota.u-psud.fr

Alain DEREUX
Physics Laboratory
University of Bourgogne
Dijon, France
adereux@u-bourgogne.fr

Yannick DUMEIGE
Optronics Laboratory
ENSSAT – CNRS
Lannion, France
yannick.dumiege@enssat.fr

Robert FREY
Charles Fabry Laboratory of the Optical Institute
CNRS and Paris Sud University
Orsay, France
Robert.Frey@iota.u-psud.fr

Jean-Michel GÉRARD
CEA-CNRS-UJF Nanophysics and Semiconductors
Grenoble, France
gerard@drfmc.ceng.cea.fr

Pierre-François LENNE
Mosaic Team
University of Aix-Marseille III
Marseille, France
lenne@fresnel.fr

Ariel LEVENSON
Photonics and Nanostructures Laboratory
CNRS
Marcoussis, France
ariel.levenson@lpn.cnrs.fr

Jean-Michel LOURTIOZ
Fundamental Electronics Institute
CNRS and Paris Sud University
Orsay, France
Jean-Michel.Lourtioz@ief.u-psud.fr

Dominique PAGNOUX
Optical Communications and Microwaves Research Institute
University of Science and Techniques of Limoges
Limoges, France
pagnoux@ircom.unilim.fr

Fabrice RAINERI
Photonics and Nanostructures Laboratory
CNRS
Marcoussis, France
fabrice.raineri@lpn.cnrs.fr

Hervé RIGNEAULT
Mosaic Team, Fresnel Institute
University of Aix-Marseille III
Marseille, France
herve.rigneault@fresnel.fr

Gérald ROOSEN
Charles Fabry Laboratory of the Optical Institute
CNRS and Paris Sud University
Orsay, France
Gerald.roosen@iota.u-psud.fr

Anne TALNEAU
Photonics and Nanostructures Laboratory
CNRS
Marcoussis, France
anne.talneau@lpn.cnrs.fr

Pierre VIKTOROVITCH
Electronics, Optoelectronics and Microsystems Laboratory
École Centrale de Lyon, CNRS
Ecully, France
pierre.viktorovitch@ec-lyon.fr

Index

A, B

air fraction 111, 112
attenuation 121, 127
Auger
 constant 281
 effect 279-281
 ionization 279
 recombination 279, 285
biological labeling 266, 284
birefringence 116, 118, 119, 123,
170-171
 form 180-181
Bloch 29, 33-35, 36, 40-41, 43, 50,
51, 55, 65, 72-76, 86, 88
Bragg 28, 31, 36, 37, 38, 39, 40, 45,
46

C, D

chromatic dispersion 110, 114, 116,
117, 118, 121-123, 127
confinement 25, 26, 27, 35, 57-59,
66, 70, 73, 74, 75
 coupling 18, 22, 23, 29-31, 33-35,
40-41, 44-45, 51-55, 60, 61, 65, 66,
68-71, 73, 74, 77-78, 81
diffraction 29, 30, 40, 41, 43, 47, 51,
52, 64

diodes 135, 149, 153
dipole 208-212

F, G

field
 local 196-203
 optical near 207-235
fluorescence microscopy 296, 298-
303
forbidden bands 25, 27
 four wave mixing 193, 194-196,
203
Green's function, 243, 244
guided mode 219, 227-228, 230

H, I

Heisenberg uncertainty principle 240,
241
heterowires 260-262
InP 75, 80, 82

K, L

Kerr effect 159, 160, 175-177, 185,
195-196, 204
lattices (direct, reciprocal) 18, 29, 49-
53, 56, 60, 62, 74, 75, 76
laser 33, 47, 64, 73-77
 thresholdless 136, 153

lifetime 21-22, 34-35, 38, 39, 41, 43, 45, 55, 63, 68, 71, 74, 75, 78, 79, 279, 281, 282

Local Density of States (LDOS) 242, 244-245, 247-249

localized defect 36, 37, 44-45, 62-64, 69, 73, 75

losses 28, 38, 39, 43, 45, 55, 58, 66-67, 70, 71, 74, 75, 77, 79, 81, 89, 93-94, 96, 97, 102, 103, 104, 116

M, N

Maxwell equations 17, 19-20, 21, 28, 29, 33, 41, 43, 50

membrane 40, 55, 58-60, 61, 65, 74, 75, 76, 78, 80

merit factor 21-22, 25, 26, 27, 35, 38, 43-44, 55, 58, 64

microcavity 27, 36-40, 44-45, 47, 62-64, 67, 71, 72, 73, 75

microdisks 140, 141, 143, 144, 145, 147, 149

micropillar 140, 143, 145, 147, 148, 149, 150

near field microscopies 212, 217-227

nonlinear

microscopy 303-307

optics 159-187, 192-198

susceptibilities 202, 203

O, P

optical

contrast 296-307

phase matching 160, 168, 170-172, 173, 178-184

reconfiguration 184-186

photoluminescence 138, 147, 148

Photon Scanning Tunneling Microscope (PSTM) 240, 246-257, 259-261, 262

photonic crystal 140, 141, 143, 144, 148, 153

cavities 207-208

waveguides 229-230

Photonic Integrated Crystals (PICs) 85, 96, 102, 103

plasmons 211-212, 224, 232-235, 240, 246, 247, 249-253, 255-256, 257, 258, 262

polarization 111, 113, 119, 123

Purcell effect 136, 141, 145, 147-150, 152

refraction 56, 57, 64

S, T

Scanning Near field Microscope (SNOM) 240, 242, 247-249, 250

single photon sources 149, 150-153

spatial

resolution 294, 307

solitons 176, 186

spontaneous emission 135-137, 140

total internal reflection 110, 112, 114, 115, 125, 128, 208, 211, 213-217, 218, 223

two photon absorption 192, 195-196

V

velocity

group 20, 25, 26, 31, 33, 34, 35,

36, 52, 65-67, 69

light 52, 55

phase 20, 34, 53